Journal of Fluids Engineering

Published Monthly by ASME

VOLUME 130 • NUMBER 2 • FEBRUARY 2008

FLUIDS ENGINEERING DIVISION

Editor
J. KATZ (2009)

Assistant to the Editor
L. MURPHY (2009)

Associate Editors
M. J. ANDREWS (2009)
S. BALACHANDAR (2008)
A. BESKOK (2008)
S. L. CECCIO (2009)
D. DRIKAKIS (2008)
P. DUPONT (2010)
I. EAMES (2010)
C. HAH (2009)
T. J. HEINDEL (2010)
J. KOMPENHANS (2009)
J. A. LIBURDY (2010)
P. LIGRANI (2008)
R. MITTAL (2009)
T. J. O'HERN (2008)
U. PIOMELLI (2010)
Z. RUSAK (2010)
D. SIGINER (2008)
Y. ZHOU (2008)

PUBLICATIONS COMMITTEE
Chair, **B. RAVANI**

OFFICERS OF THE ASME
President, **SAM Y. ZAMRIK**
Executive Director, **V. R. CARTER**
Treasurer, **T. D. PESTORIUS**

PUBLISHING STAFF

Managing Director, Publishing
P. DI VIETRO

Manager, Journals
C. MCATEER

Production Coordinator
A. HEWITT

RESEARCH PAPERS

Flows in Complex Systems

Fundamental Issues and Canonical Flows

Multiphase Flows

(Contents continued on inside back cover)

Transactions of the ASME, Journal of Fluids Engineering (ISSN 0098-2202) is published monthly by The American Society of Mechanical Engineers, Three Park Avenue, New York, NY 10016. Periodicals postage paid at New York, NY and additional mailing offices.
POSTMASTER: Send address changes to Transactions of the ASME, Journal of Fluids Engineering, c/o THE AMERICAN SOCIETY OF MECHANICAL ENGINEERS, 22 Law Drive, Box 2300, Fairfield, NJ 07007-2300.
CHANGES OF ADDRESS must be received at Society headquarters seven weeks before they are to be effective. Please send old label and new address.

STATEMENT from By-Laws. The Society shall not be responsible for statements or opinions advanced in papers or ... printed in its publications (B7.1, Par. 3).
COPYRIGHT © 2008 by the American Society of Mechanical Engineers. Authorization to photocopy material for internal or personal use under those circumstances not falling within the fair use provisions of the Copyright Act, contact the Copyright Clearance Center (CCC), 222 Rosewood Drive, Danvers, MA 01923, tel: 978-750-8400, www.copyright.com. Request for special permission or bulk copying should be addressed to Reprints/Permission Department.

Canadian Goods & Services Tax Registration #126148048.

This journal is printed on acid-free paper, which exceeds the ANSI Z39.48-1992 specification for permanence of paper and library materials. ♾™
♻ 85% recycled content, including 10% post-consumer fibers.

Downloaded 03 Jun 2010 to 171.66.16.159. Redistribution subject to ASME license or copyright; see http://www.asme.org/terms/Terms_Use.cfm

(**Contents continued**)

Journal of Fluids Engineering **Volume 130, Number 2** **FEBRUARY 2008**

Techniques and Procedures

The ASME Journal of Fluids Engineering is abstracted and indexed in the following:

Applied Science & Technology Index, Chemical Abstracts, Chemical Engineering and Biotechnology Abstracts (Electronic equivalent of Process and Chemical Engineering), Civil Engineering Abstracts, Computer & Information Systems Abstracts, Corrosion Abstracts, Current Contents, Ei EncompassLit, Electronics & Communications Abstracts, Engineered Materials Abstracts, Engineering Index, Environmental Engineering Abstracts, Environmental Science and Pollution Management, Excerpta Medica, Fluidex, Index to Scientific Reviews, INSPEC, International Building Services Abstracts, Mechanical & Transportation Engineering Abstracts, Mechanical Engineering Abstracts, METADEX (The electronic equivalent of Metals Abstracts and Alloys Index), Petroleum Abstracts, Process and Chemical Engineering, Referativnyi Zhurnal, Science Citation Index, SciSearch (The electronic equivalent of Science Citation Index), Shock and Vibration Digest, Solid State and Superconductivity Abstracts, Theoretical Chemical Engineering

Mathieu Rouméas
e-mail: mathieu.roumeas@yahoo.fr

Patrick Gilliéron
e-mail: patrick.gillieron@renault.com

Groupe "Mécanique des Fluides et
Aérodynamique,"
Direction de la Recherche Renault,
1 Avenue du Golf (TCR AVA 058),
78288 Guyancourt, France

Azeddine Kourta
Institut de Mécanique des Fluides de Toulouse,
Groupe EMT2,
Avenue du Professeur Camille Soula,
31400 Toulouse, France
e-mail: kourta@imft.fr

Separated Flows Around the Rear Window of a Simplified Car Geometry

A 3D numerical simulation based on the lattice Boltzmann method is carried out on a simplified car geometry (initially proposed by Ahmed, Ramm, and Falting, 1984, SAE Technical Paper series No. 840300) to analyze and establish a method for controlling the near-wake flow topology of a generic blunt body model. The results indicate the existence of a complex flow topology consisting of transverse and longitudinal vortices emanating from flow separations that occur on the top and the lateral edges of the slanted rear window, respectively. The topology of each structure is detailed and the numerical results are compared with the experimental results in the literature. The results presented in this paper can then be used to develop and parametrize active control solutions conducive to improving the aerodynamic performances of automobile vehicles.

[DOI: 10.1115/1.2829566]

Keywords: lattice Boltzmann method, Ahmed body, 3D separation, longitudinal vortices, automobile aerodynamics

1 Introduction

One solution to meet new fuel emissions and fuel consumption requirements (Corporate Average Economy Fuel) would be to reduce the aerodynamic drag of motor vehicles. In this context, fluidic actuator systems (blowing, suction, or synthetic jets) have recently been studied to replace commonly used passive systems such as spoilers or fins [1–5]. Recent results suggest that the eventual use of such active flow control devices in the automotive industry could dramatically improve the aerodynamic and aeroacoustic performances of the moving vehicle, with a negligible impact on vehicle geometry.

Active solutions need an external energy source in order to control the flow around the vehicle without necessarily interfering with its shape. Many flow control techniques have been developed in university and industrial laboratories, where significant results have been found on simplified geometries [2]. For instance, blowing devices installed on an ONERA D profile are capable of displacing or even eliminating flow separations [4]. Similar results have been obtained by Tensi et al. [5] on a cylindrical body. Many studies demonstrate that suction and/or blowing techniques offer a promising alternative for reducing the aerodynamic drag of an automotive vehicle [3].

The implementation of such solutions on an automotive vehicle, however, requires a better understanding of the physical phenomena encountered in the near-wake flow, and an identification of the parameters that contribute toward the formation and development of aerodynamic drag.

The flow which develops around an automotive vehicle is fully turbulent and three dimensional. The separations that occur at the radiator grille, on the bottom and top of the A pillars, at the underbody inlet or outlet, on the rotating wheels, on the sidewalls, and on the top and side edges of the rear window, interact, and contribute toward the complex nature of the near-wake flow [3]. Furthermore, secondary internal flows, occurring inside the engine compartment and underbody, also contribute toward the aerodynamic forces applied to the vehicle [4].

In this context, a 3D numerical simulation is conducted to represent and analyze the main vortices that appear on a simplified vehicle geometry near-wake flow. The objective is twofold: firstly, to obtain a reliable representation of the vortices by comparing the numerical results with the experimental data in the reference works and secondly, to analyze the topology of these structures in order to understand how they can be optimally controlled.

A simplified car geometry initially proposed by Ahmed et al. [6–11] is used for the purposes of this study. The rear window is inclined at 25 deg with respect to the horizontal, a configuration conducive to reproducing the longitudinal vortices that contribute to the near-wake flow on an automobile geometry [6]. Experimental [7,9] and numerical results [10] found in the literature are used to validate the numerical results.

In the first part, the computation code and the numerical simulation methods are detailed. The results obtained on the simplified geometry are then analyzed and presented in the second part.

2 Numerical Simulation

The 3D numerical simulation used in this study is based on POWERFLOW code with a lattice Boltzmann method (LBM). Unlike conventional numerical schemes based on discretizations of macroscopic continuum equations, the LBM is based on microscopic models and mesoscopic kinetic equations. The fundamental principle of the LBM is to construct simplified kinetic models that incorporate the essential physics of microscopic or mesoscopic processes such that the macroscopic-averaged properties conform to the desired macroscopic equations. The basic premise for using these simplified kinetic-type methods for macroscopic fluid flows is that the macroscopic fluid dynamics are the result of the collective behavior of many microscopic particles in the system and that the macroscopic dynamics are not sensitive to the underlying details as is the case in microscopic physics.

2.1 Algorithm. The fluid particles are distributed on a Cartesian lattice of computation nodes, described in Fig. 1. For each lattice node, a distribution function $[f_i]_{i=1,\ldots,N}$ is associated with a discrete velocity distribution $[\mathbf{V}_i]_{i=1,\ldots,N}$ representing N possible velocities of motion (Fig. 1). One particle placed on one node may stay at this node (energy level 0: $\bar{e}=0$, represented by triangle (Fig. 1)), moved toward an adjacent node in horizontal or vertical plane (energy level 1: $\bar{e}=1$, circle), or moved to a farthest node

---

Contributed by the Fluids Engineering Division of ASME for publication in the JOURNAL OF FLUIDS ENGINEERING. Manuscript received July 27, 2006; final manuscript received August 30, 2007; published online January 24, 2008. Review conducted by Paul Durbin.

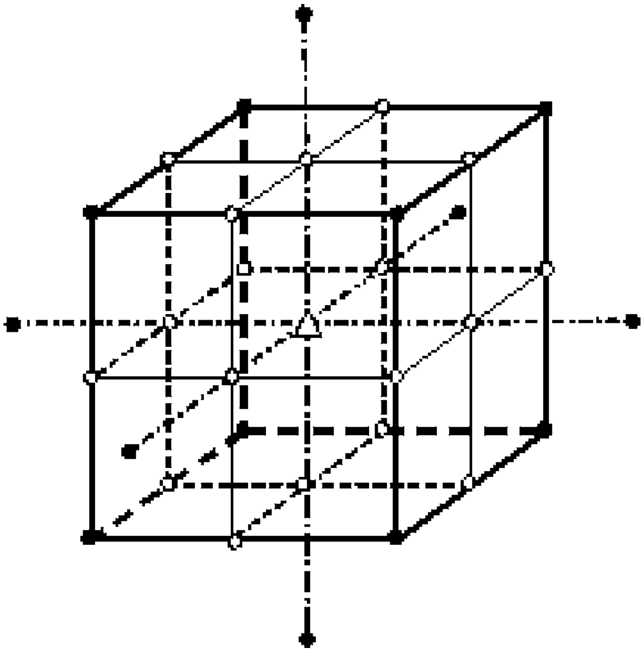

Fig. 1 Definition of a velocity lattice with 34 velocities on three energy levels (△, Level 0; ○, Level 1; and ●, Level 2), Chen et al. [15]

(energy level 2: $\bar{e}=2$, black dot). The model gives 34 possible combinations and is called 34 velocities model (2 possibilities for Level 0, 18, for Level 1, and 14 for Level 2). More details concerning the algorithm can be found in Ref. [12]. The kinetic energy is then given by $\bar{e}=\frac{1}{2}\Sigma_{i=1}^{N}V_i^2$.

The macroscopic variables (density ρ and momentum density ρu) are defined as particle velocity moments of the distribution function f_i.

$$\rho(r,t)=\sum_{i=1}^{N} f_i(\mathbf{r},t)$$

$$\rho(r,t)\mathbf{u}(r,t)=\sum_{i=1}^{N}\mathbf{V}_i f_i(\mathbf{r},t) \tag{1}$$

The objective of the simulation is therefore to determine the distribution $[f_i]_{i=1,\ldots,N}$ of particles for each node on the lattice. This distribution is obtained according to the Boltzmann equation (Eq. (2)) governing the particle dynamics at the microscopic (mesoscopic) level [13–15]:

$$f_i(\mathbf{r}+\mathbf{V}_i\Delta t,t+\Delta t)-f_i(\mathbf{r},t)=\Omega_i(\mathbf{r},t) \tag{2}$$

where f_i is the particle velocity distribution function along the ith direction and Ω_i is the collision operator, which represents the rate of variation of f_i resulting from the collision, whereas Δt and $V_i\Delta t$ are the time and space increments, respectively. The right-hand side (RHS) depends on ΔT but to simplify Eq. (2) for farther developments, this time increment is set equal to 1.

In the Boltzmann equation (2), the distribution function f_i evolves in two phases. During the first phase, i.e., the propagation phase, each particle is considered as an independent entity. N possibilities of motion, associated with N velocities $[V_i]_{i=1,\ldots,N}$, are attributed to each node on the lattice (left-hand term of Eq. (2)). In the second phase, a collision model is used to describe the impacts that occur between the particles and to redistribute the particles on the lattice (right-hand term of Eq. (2)). This type of simple description of the particle dynamic, with the help of the Chapman–Enskog development [12], leads to Navier–Stokes equation solutions.

At this level, the problem consists in determining a collision model $[\Omega_i]_{i=1,\ldots,N}$. The representation selected for this term is that proposed by Bhatnagar–Gross–Krook (BGK) [16], in which the collision is associated with a relaxation of the excited state of the particles before impact and a state of equilibrium after the impact. The collision term is then obtained according to Eq. (3):

$$\Omega_i(\mathbf{r},t)=\frac{f_i(\mathbf{r},t)-f_i^{\mathrm{eq}}(\mathbf{r},t)}{\tau_r} \tag{3}$$

in which τ_r is the relaxation time and $\mathbf{f}_i^{\mathrm{eq}}$ the distribution of particles in a state of equilibrium at the node defined by the position $\mathbf{r}$ at date t.

In the BGK representation [16], the collision model is then completely characterized by the state of equilibrium $\mathbf{f}_i^{\mathrm{eq}}(\mathbf{r},t)$ and by the relaxation constant τ_r (Eq. (3)). These two parameters are indicated by Chen et al. [17]:

$$f_i^{\mathrm{eq}}=\rho\omega_i\left[1+\frac{\mathbf{V}_i\cdot\mathbf{u}}{T}+\frac{(\mathbf{V}_i\cdot\mathbf{u})^2}{2T^2}-\frac{|\mathbf{u}|^2}{2T}+\frac{(\mathbf{V}_i\cdot\mathbf{u})^3}{6T^3}-\frac{\mathbf{V}_i\cdot\mathbf{u}}{2T^2}|\mathbf{u}|^2\right]$$

$$\tau_r=\frac{\nu}{T}+\frac{1}{2} \tag{4}$$

in which T represents the temperature, ν the viscosity, and ω_i the weighting coefficients associated with each ith direction. All variables are in nondimensional form [12].

The general algorithm for the LBM is thus defined in four stages. The first consists in propagating the distribution function in time $t+1$ (left-hand term of Eq. (2)). In the second stage, the collisions between the particles are modeled (right-hand term of Eq. (2)). The collision operator $[\Omega_i]_{i=1,\ldots,N}$ is then defined by Eqs. (3) and (4) applied to time $t-1$. The third stage consists in determining the associated values of density and density momentum according to Eq. (1). Finally, the fourth stage consists in initiating iteration on the basis of the macroscopic values determined in the third stage (Eq. (4)).

As in the case of all numerical space-time discretization methods, the LBM is not capable of resolving all turbulence scales. The computation code therefore uses a turbulence model, which introduces a turbulent viscosity into the initial model.

2.2 Turbulence Model. The turbulence model is the renormalization group (RNG) k-ε model originally developed by Yakhot and Orszag [18]. The equations describing the transport of kinetic energy and dissipation applied by the model are resolved on the same lattice as the Boltzmann equations. The discretization diagram used is a second order in space (Lax–Wendroff finite difference model), associated with a time-explicit integration diagram [19].

Close to the wall, a specific velocity law is applied to limit the computational workload [19]. The velocity is then described by a logarithmic law according to Eq. (5):

$$\frac{u}{u^+}=\frac{1}{\kappa}\log\left(\frac{y^+}{\varsigma}\right)+C \tag{5}$$

with

$$u^+=\sqrt{\frac{\tau_p}{\rho}}$$

$$y^+=y\frac{u^+}{\nu} \tag{6}$$

in which u represents the tangential velocity, κ the Karman constant ($\kappa=0.41$), C a constant applied by the model ($C=5$), τ_p the wall shear stress, y and u^+ the distance and friction velocity on the wall, respectively, ν the kinematic viscosity, and ς a correction term to make allowance for the adverse pressure gradient. This

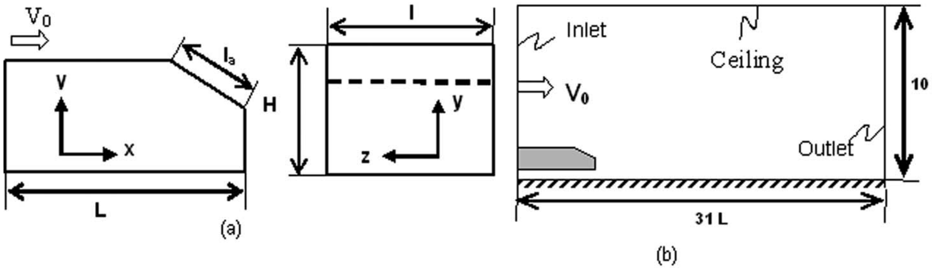

Fig. 2 Schematic of the numerical simulation setup: (*a*) studied geometry and (*b*) simulation volume

equation is applicable for values of y^+ between 30 and 300.

A validation of this numerical method can be found in the literature on numerous applications (pipe flow [19], flow past a cylinder [20], NACA 12 profile [21]).

2.3 Numerical Simulation Protocol. The numerical simulations presented in this paper were conducted on a simplified vehicle geometry initially proposed by Ahmed et al. [5]. In order to limit the computation time, the front part is not represented. The flow separations that develop on the front rounded surface of the Ahmed body, experimentally demonstrated by Gilliéron et al. [22], are not represented; the simulation exclusively focuses on the vortices, which appear on the rear window and on the base of the vehicle. The consequence of this limitation is that the boundary layer thicknesses on roof and sides cannot be exactly reproduced. However, as stated by Ahmed et al. [6], the interference between the rear end and the fore body flow is weak; this would be a consequence of the relatively long midsection. This statement has been confirmed by Krajnovic and Davidson [23,24] with large eddy simulation (LES) calculations. In computations done on the complete body, along the roof after the leading edge separation and reattachment, a classical boundary layer is found. Hence, to obtain the main important characteristics at the rear body (the separation and longitudinal vortices), the length of the present body is fixed in such a way that the boundary layer thickness at the end of the roof be equivalent to the one of the complete Ahmed body.

The geometry is represented in Fig. 2(*a*). Length L, width l, and height H correspond to $L=1.044$ m, $l=0.389$ m, and $H=0.288$ m, respectively. In this analysis, length $l_a=0.222$ m is inclined at an angle of 25 deg with respect to the horizontal. Finally, the lower part is positioned at $h=0.17H$ from the floor of the numerical wind tunnel (Fig. 2(*a*)). The geometry is located in a rectangular numerical section of length, width, and height equal to $31L$, $20L$, and $10H$, respectively (Fig. 2(*b*)). These dimensions ensure that there is no interaction between the boundary conditions imposed at the limit of the computational domain, and the development of the near-wake flow. The outlet condition, downstream from the geometry (*outlet* Fig. 2(*b*)) and on the upper part (*ceiling* Fig. 2(*b*)), is a free flow condition [25] on pressure and velocity. The flow is advected from left to right and a uniform velocity $V_0=40\ \mathrm{m\ s^{-1}}$ is applied to the left-hand surface of the simulation domain (Dirichlet velocity condition, *inlet* Fig. 2(*b*)). The Reynolds number associated with length L of the geometry is $\mathrm{Re}=2.8\times 10^6$. Finally, symmetry conditions are applied on the side surfaces of the simulation domain [25,26].

The simulation volume is subdivided into parallelepiped domains. Inside each domain, the volume mesh is Cartesian, uniform and the resolution is halved as it moves away from the surface. Each block B_k is associated with a resolution level δx_k defined by

$$\delta x_k = 2^k \delta x_0 \tag{7}$$

in which δx_0 represents the most refined resolution, i.e., the size of an elementary computation cube in the block having the highest resolution.

In the present case, 12 levels (0–11) of blocks have been created: The fourth most refined levels are located in areas generating high gradient and flow separations close to the geometry (B_0, B_1, B_2, and B_3, Fig. 3). The geometry is hence completely contained in block B_3 with resolution $\delta x_3=2\times 10^{-3}$ m (Fig. 3(*b*)), and the first computation node, at the end of the roof, is located at $y^+=120$, with y^+ defined by

$$y^+ = y\frac{u^+}{\nu} \tag{8}$$

in which y represents the distance perpendicular to the wall, ν the viscosity of the fluid, and u^+ the friction velocity defined according to parietal friction constraint τ_ω formulated by

$$\tau_p = \rho u^{+2} \tag{9}$$

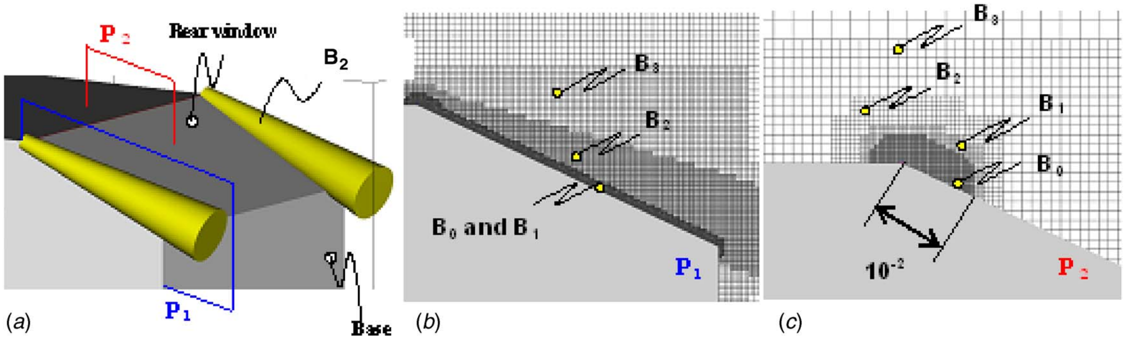

Fig. 3 Schematic of the volume mesh distribution around the geometry: (*a*) block B_2 perspective, (*b*) cross section in longitudinal plane P_1 situated on left-hand side edge, and (*c*) cross section in longitudinal median plane P_2 on upper edge of rear window

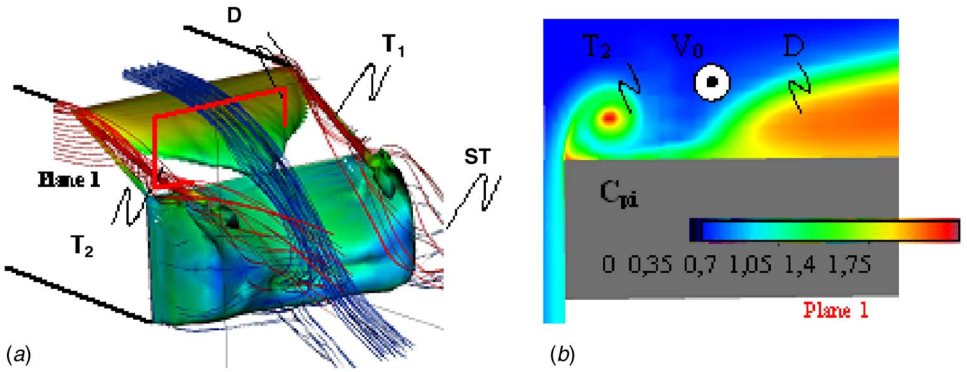

Fig. 4 Near-wake flow topology: (*a*) isosurface $C_{pi}=1.22$ and (*b*) total pressure loss field measured in transverse Plane 1 (defined in (*a*))

The boundary layer thickness represents around 2×10^{-2} m at the end of the roof, and ten computation points are used to characterize the boundary layer on block B_3. The mesh is refined on the separation lines, on the top and side edges of the rear window. On level B_0 located on the rear window lateral edges (B_0, Fig. 3(*b*)) and at the end of the roof (B_0, Fig. 3(*c*)), the distance between two consecutive computation nodes is therefore $\delta_0=2.5\times10^{-4}$ m. At the upper part of the rear window, block B_0 spreads over 10^{-2} m downstream from the upper edge of the rear window to obtain a better representation of the static pressure gradient associated with the separation (Fig. 3(*c*)). Finally, an intermediate conical block is created at the side edges, at a resolution of 10^{-3} m, in order to represent the velocity and pressure gradients in the longitudinal vortices (B_2, Fig. 3(*a*)). The mesh size then increases as it moves away from the geometry, from blocks B_4 to B_{12}. The number of nodes in the computational domain is 16.7×10^6 of which 15×10^6 are distributed close to the geometry, whereas the body surface is meshed with 1.2×10^6 triangular cells. According to the Courant–Friedrichs–Lewy (CFL) criterion, the computation time step is equal to 1.354×10^{-6} s for the finest mesh (block B_0) and the simulation is conducted over 500,000 iterations, corresponding to 0.7 s of real time. Convergence is attained after 50,000 time steps and the numerical results are averaged on 0.61 s (50,000–500,000 iterations).

From one block to the next one (B_i to B_{i+1}), the mesh density is divided by 2. The finer mesh is used near the wall and in the region with high gradient. So moving from the wall to the freestream, the mesh density decreases. This technique accelerates the computational convergence. In fact, the time step is defined by $\Delta t=\mathrm{CFL}c_s|\mathbf{\Delta x}|$, where c_s is the sound celerity, in this case given by $c_s=\sqrt{[(D+2)/D]T}(|\mathbf{\Delta x}|/\Delta t)$, D the degree of freedom equal to 4 and $|\mathbf{\Delta x}|$ is the cell size. From this expression, it can be easily obtained that the CFL number is equal to 0.794.

The CFL number is kept constant all over the computational domain; thus, the time step is proportional to the cell size. So the time step is doubled from one block to the next one. This procedure increases the convergence and for the present computation, only 50,000 iterations are needed. The convergence is based on the drag coefficient error. The convergence is attempted when the relative error is smaller than 1%.

3 Numerical Results

The results obtained are analyzed and compared with the experimental [7,9] and numerical results [10] found in the literature. Firstly, the near-wake flow topology is analyzed according to the total pressure loss isosurface, characterized by the total pressure loss coefficient C_{pi}:

$$C_{pi}=\frac{P_{i0}-P_i}{\frac{1}{2}\rho V_0^2} \tag{10}$$

Each of the structures identified is then analyzed according to pressure and vorticity fields, parietal visualizations, and velocity profiles.

The total pressure loss isosurfaces (Fig. 4(*a*)) indicate the development of longitudinal and transversal vortices on the near-wake flow. These vortices are associated with significant total pressure losses ($C_{pi}>1$, Fig. 4(*b*)). The streamlines emanating from the roof separate along the upper edge of the rear window, roll up in a separated region annotated D (Fig. 4(*a*)), and contribute to the wake flow. The associated total pressure loss coefficients C_{pi} are close to 1.5 in the separated zone D (Fig. 4(*b*)). The results in Fig. 4(*a*) therefore suggest that the flow reattaches itself on the bottom of the rear window, which effectively concurs with the results proposed by Ahmed et al. [6]. Likewise, the streamlines emanating from the lateral side of the geometry separate along the lateral edges of the rear window and roll up into two counter-rotating longitudinal vortices annotated T_1 and T_2 in Fig. 4(*a*). The volume energy loss associated with the vorticity at the vortex center is characterized by average total pressure loss coefficients close to $C_{pi}=1.75$ (Fig. 4(*b*)). Finally, the fluid emanating from the lateral sides, from the underbody, and from the rear window separates around the base periphery and forms a transversal vortical ring (annotated *ST* in Fig. 4(*a*)). The flow topology in the separated region D and in the longitudinal vortices T_1 and T_2 is analyzed more specifically in the following developments.

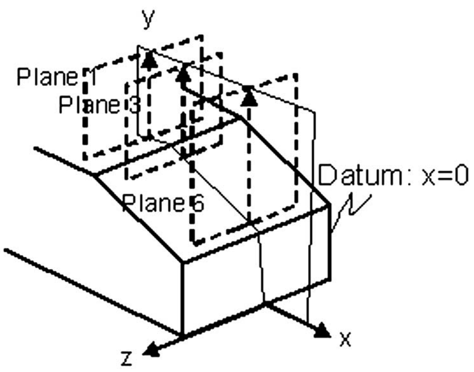

Fig. 5 Definition of measurement planes on rear window and end of roof

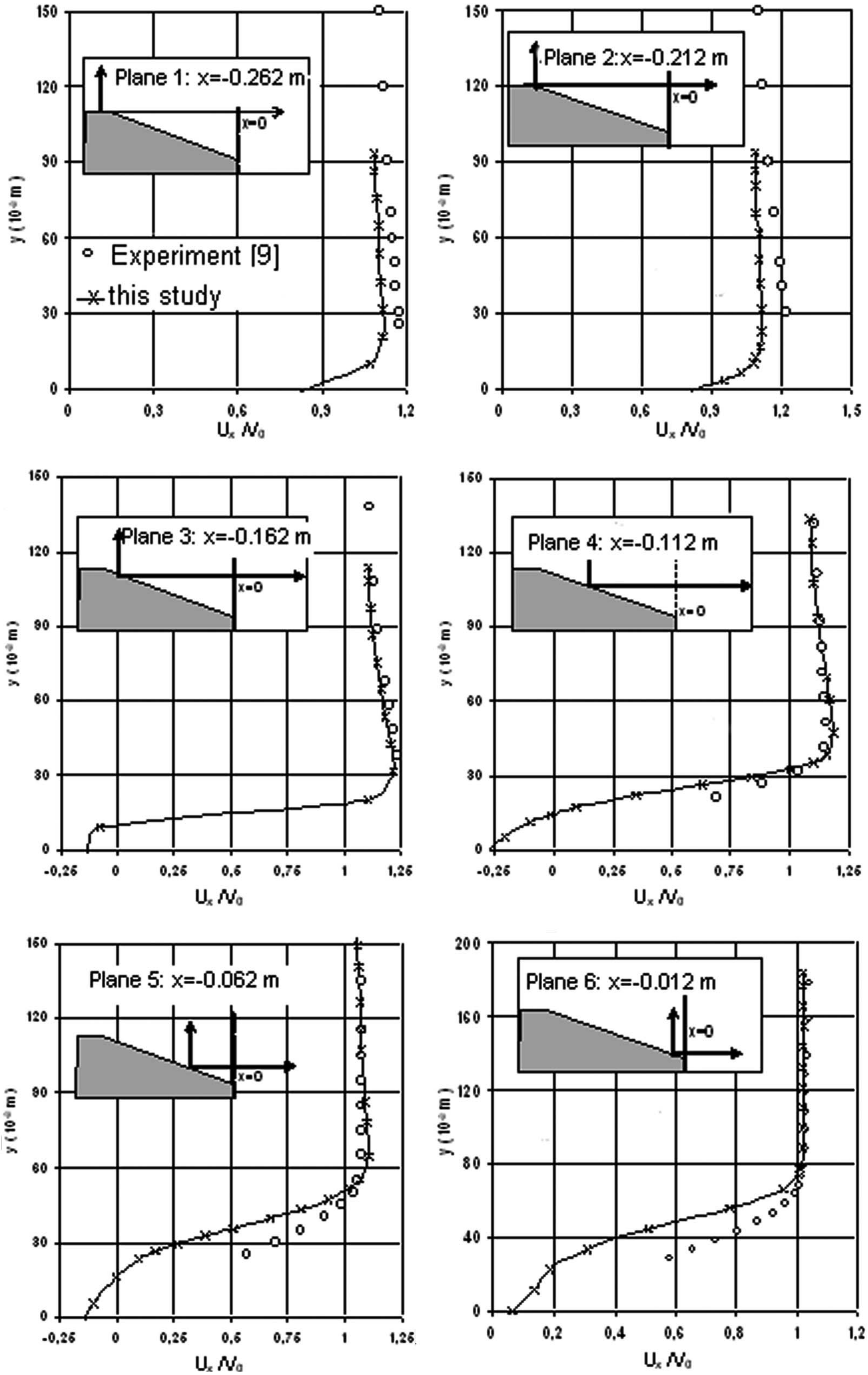

Fig. 6 Longitudinal velocity profiles in the vertical direction measured in longitudinal median plane

3.1 Separated Region Analysis. The separated region D is analyzed on the longitudinal velocity profiles in the vertical direction (Fig. 6), measured on the median longitudinal plane, at the end of the roof (Plane 1 for $x=-0.262$ m), at the top of the rear window (Plane 2 for $x=-0.212$ m), at the first part of the rear window (Plane 3 for $x=-0.162$ m), in the middle of the rear window (Plane 4, $x=-0.112$ m), at the last part of the rear window (Plane 5, $x=-0.062$), and at the bottom of the rear window (Plane

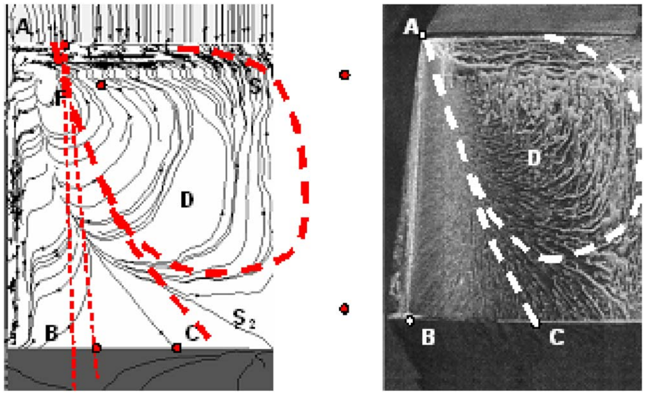

(*a*) (*b*)

Fig. 7 Friction line traces noted on left-hand part of rear window: (*a*) present numerical results and (*b*) experimental results, Gilliéron et al. [22]

6, $x=-0.012$ m). For each of the velocity measurements, the datum point of the horizontal axis ($O\mathbf{x}$) is placed on the base and the datum point of the vertical axis ($O\mathbf{y}$) is located at any point of the surface ($y=0$ on the geometry, see Fig. 5). The numerical results are then compared to profiles obtained by laser doppler anemometer (LDA) [9].

At the end of the roof (Plane 1, Fig. 6 and at the top of the rear window (Plane 2, Fig. 6), the numerical simulation slightly underestimates the velocity near the wall ($\Delta V_x=3$ m s^{-1}) with respect to the profiles obtained on LDA [9]. Near the wall, experimental data do not exist to perform comparison in the boundary layer. Further downstream, in Planes 3 and 4 located on the rear window, close to the separation line, the numerical and experimental results are more consistent (Fig. 6). The separation is indeed fixed by the sharp-edged geometry and the longitudinal velocity profiles are less sensitive to the upstream flow [10]. The velocity appears negative close to the wall of the geometry ($V_x=-5$ m s^{-1} at $y=0$, Plane 3), which typifies a fluid recirculation under the separated region *D* (Fig. 4(*a*)). At the end of the rear window (Planes 5 and 6), the flow reattaches itself to the wall and the longitudinal velocity becomes positive ($V_x=+3$ m s^{-1}, Plane 6). The computation code is then able to predict both the separation and attachment of the fluid, respectively, on the top and bottom of the rear window (Planes 3–6). This aspect, a common problem in the numerical representation of the flow around fastback geometry [27,28], is correctly processed by the code. On the last profiles (Planes 5 and 6), however, the computation code overestimates the velocity deficit in the boundary layer close to the reattachment. The results obtained in the separated boundary layer are associated with the logarithmic law used to define the velocity evolution close to the wall (Eq. (5)). This law is not adapted to the separated region [29].

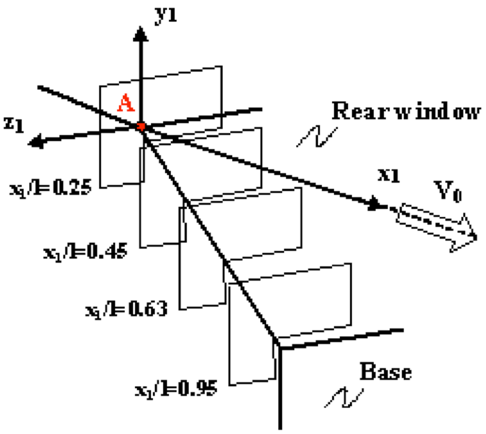

Fig. 8 Definition measurement planes

The accuracy of the present results has been evaluated by determining the differences with experimental results considered as a basis of comparison. The maximum error is less than 15%. It is equal, respectively, to 5%, 9%, 1%, and 3% for Profiles 1–4. In the external region, the error is less than 1% but it can reach 11–13% in the separation zone (Profiles 5 and 6) where the computation is less accurate. The results obtained in the symmetry plane are representative of the situation in other regions in the domain.

The turbulent kinetic energy has been compared to experimental data [12]. Before and at the beginning of the separation region, the agreement with experiment is good. However, due to the fact that the size of the separation zone is underestimated by the present numerical simulation, the agreement in the reattachment region is poor. This is due to the fact that k-ϵ turbulent model is, as known, not able to predict correctly the separation zone. So, complete comparison [12], both for mean velocity and turbulent kinetic energy, has been done. Agreement is globally good for the mean velocity but quite poor for the turbulent kinetic energy. The present results are in good agreement with LES results [10].

The friction line traces on the rear window, illustrated in Fig. 7(*a*), however, indicate that the computation code correctly represents the physical phenomena highlighted in the experiments conducted by Gilliéron et al. [22] at a Reynolds number $\mathrm{Re}=0.7\times10^6$ (Fig. 7(*b*)). In view of the flow symmetry, only the rear left-hand part of the rear window is represented (seen from the rear).

The streamlines issued from the lateral side of the geometry separate along the lateral edges of the rear window, roll up into the

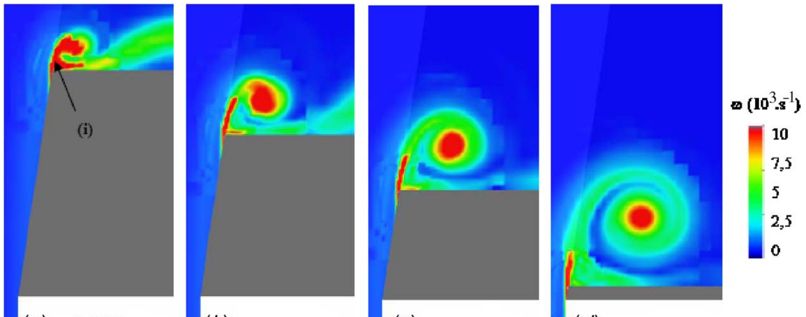

(*a*) $x_1/l=0,25$ (*b*) $x_1/l=0,45$ (*c*) $x_1/l=0,63$ (*d*) $x_1/l=0,95$

Fig. 9 Vorticity fields measured in transverse planes located on longitudinal vortex T_2 for various coordinate: (*a*) $x_1/l=0.25$, (*b*) $x_1/l=0.45$, (*c*) $x_1/l=0.63$, and (*d*) $x_1/l=0.95$

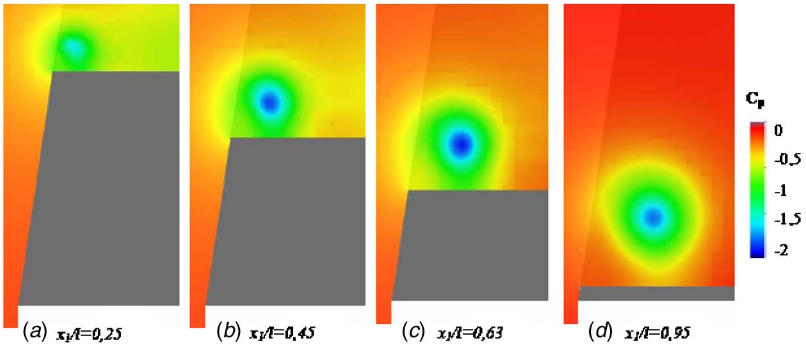

(a) x_1/l=0,25 (b) x_1/l=0,45 (c) x_1/l=0,63 (d) x_1/l=0,95

Fig. 10 Static pressure loss coefficient fields measured in transverse planes located on longitudinal vortex T_2 for various coordinate: (*a*) $x_1/l=0.25$, (*b*) $x_1/l=0.45$, (*c*) $x_1/l=0.63$, and (*d*) $x_1/l=0.95$

longitudinal vortex T_2 (Fig. 4(*a*)), and reattach themselves on the rear window along attachment line AC (Figs. 7(*a*) and 7(*b*)). A portion of the fluid then moves toward the side edge and separates again along the separation line annotated AB (in Figs. 7(*a*) and 7(*b*)). The friction lines therefore indicate the existence of a secondary counter-rotating longitudinal vortex along the lateral edge as observed by Krajnovic and Davidson [10]. Angle $B\hat{A}C$ noted in Fig. 7(*a*) is equal to 27 deg, as opposed to 22 deg in the experimental results [22] (Fig. 7(*b*)). The friction line field also indicates a significant interaction between the longitudinal vortex T_2 and the separated region D. A portion of the fluid emanating from the attachment line AC feeds the parietal recirculation flow under the separated region whereas the friction lines roll up around a singular focus point F (Fig. 7(*a*)). The momentum conservation therefore forces the streamlines to converge toward this center and to escape into the wake flow through a secondary vortex. This vortex shown by Spohn and Gilliéron [7] does not appear, however, in the numerical results presented herein. Finally, considering the symmetry of the flow with respect to the longitudinal median plane, two singular saddle type points appear on the median plane (annotated S_1 and S_2 in Fig. 7(*a*)).

These results effectively concur with the above-mentioned experimental results found in the literature, and can be used to validate the numerical simulation for the representation of the separated region on the rear window. The following step therefore consists of representing the longitudinal vortices, which interact with the separated zone to form the near-wake flow.

3.2 Longitudinal Vortex Analysis. Vortices T_1 and T_2 (Fig. 4(*a*)) are analyzed according to the total pressure loss, vorticity, and velocity fields measured in the transversal planes defined in Fig. 8. The results are compared with experimental and numerical results found in the literature.

The time-averaged vorticity magnitude measured on the vortex axis is close to $\omega=13\times10^3\ \mathrm{s}^{-1}$ (Fig. 9) and decreases along the length of the rear window. This rotational movement in plane (y_1z_1) is supplied by the fluid emanating from the lateral side of the geometry, separating along the side edge of the rear window. The vortex center is then characterized by a depression zone associated with the fluid rotation, at static pressure loss coefficients C_p close to $C_p=-1.7$ (Fig. 10), comparable to those observed by Beaudoin et al. [8]. The space-averaged total pressure loss coefficient, measured in the vortex cross section, corresponds to $C_{pi}=1.5$, with the maximum values noted in the vortex core ($C_{pi}=1.75$, Fig. 4(*b*)). These values correspond to those noted by Gilliéron et al. [22] on the same geometry and more generally with those measured by total pressure loss tomography on the fastback geometry vehicle [30].

The vorticity (Fig. 9 and static pressure fields (Fig. 10) are measured in the transverse planes distributed along the left-hand side edge of the rear window (seen from the rear). The datum point of the x axis is fixed at point A (Fig. 8), in the upper left-hand corner of the rear window. The results therefore show three phases in the vortex development.

On the upper part of the rear window and as far as abscissa

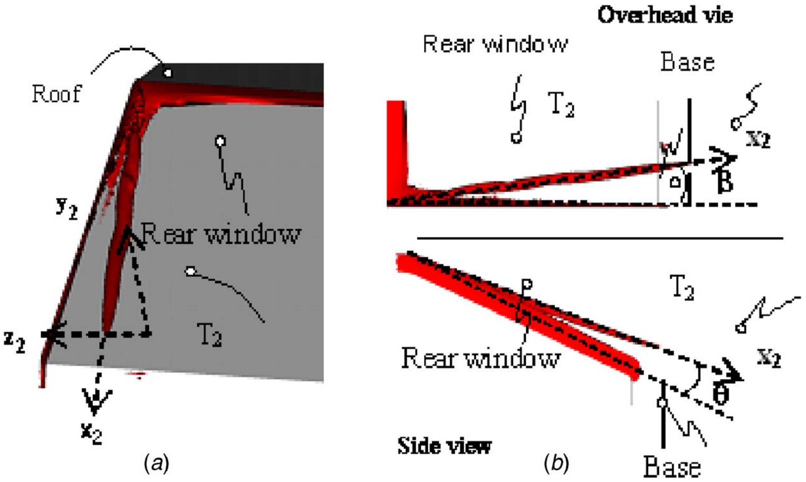

Fig. 11 Vorticity isocontour surface ($\omega=10^4\ \mathrm{s}^{-1}$): (*a*) definition of coordinate system associated with vortex T_2, and (*b*) determination of vortex axis position with respect to rear window

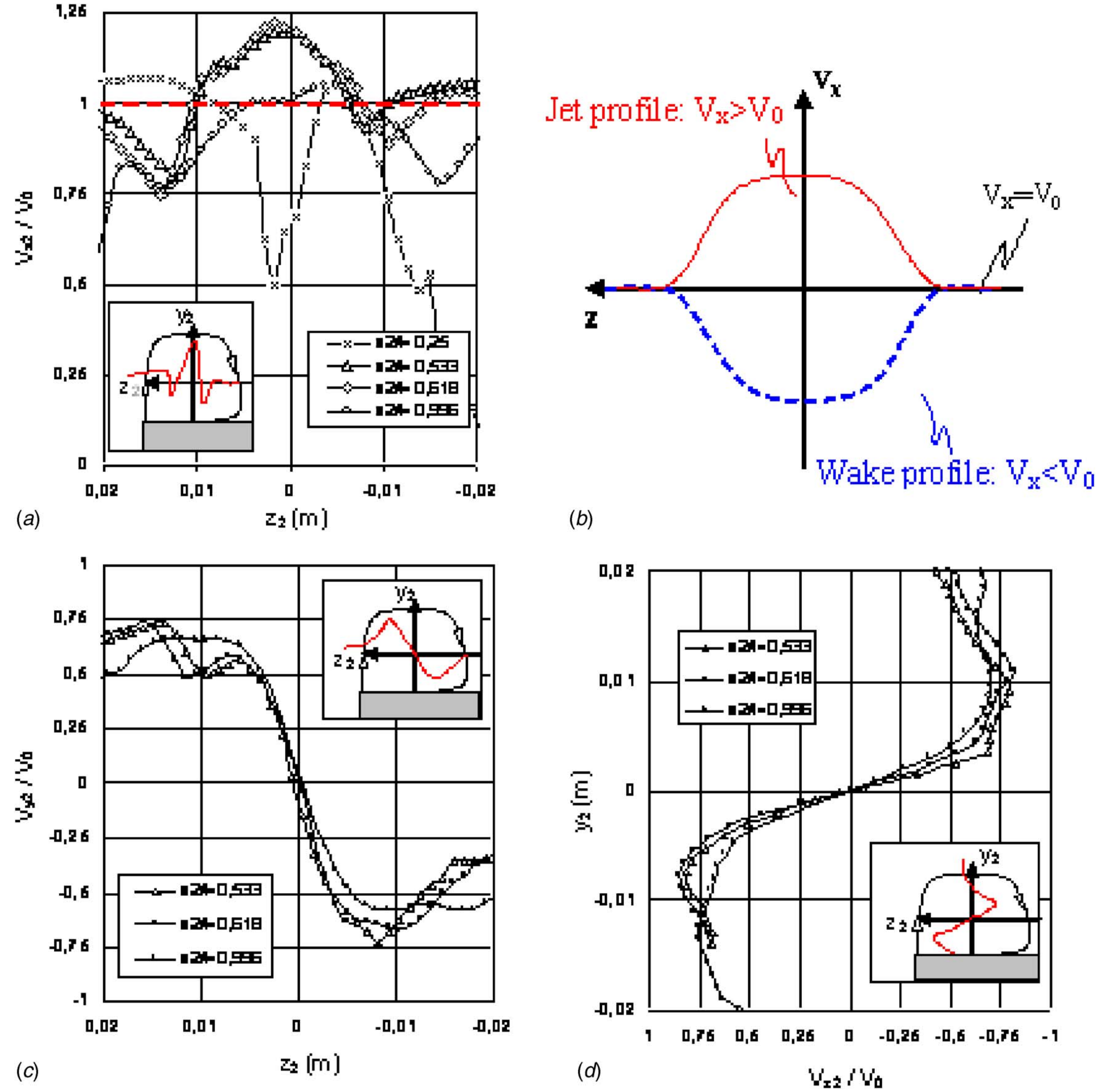

Fig. 12 Velocity profiles in the longitudinal left-hand vortex T_2 for different coordinates: (*a*) axial velocity transverse profile $V_{x2}(y_2=0,z_2)$, (*b*) schematic diagram of jet and wake-type vortices, (*c*) azimuthal velocity profile in the transverse direction ($V_{y2}(y_2=0,z_2)$, and (*d*) azimuthal velocity transverse profile in the vertical direction ($V_{z2}(y_2,z_2=0)$

$x_1/l=0.25$, the vortex core does not appear clearly and the vorticity fields only highlight the shear layer, which develops on the lateral edge of the rear window ((i) in Fig. 9(*a*)). These results concur with those of Lehugeur et al. [31], who characterized the vortex core formation along the rear window through Q criterion fields obtained by 3D-particle image velocity (PIV).

At coordinate $x_1/l > 0.45$, the vorticity fields (Fig. 9(*b*)) reveal the existence of a well-established structure with a quasicircular vortex cross section, and the depression zone in the vortex core is clearly distinct (Fig. 10(*b*)). The vorticity magnitude and the static pressure loss coefficient, measured at the vortex center, are close to $\omega=15\times10^3\ \mathrm{s}^{-1}$ and $C_p=-2$, respectively. These values remain constant until $x_1/l=0.63$. The vortex formation phase, at the top of the rear window, has also been highlighted by Lehugeur and Gilliéron [11] (by LBM numerical means) and by Beaudoin et al. [8] (by experimental means). The static pressure loss values are also comparable ($C_p=-1.7$ [11] and $C_p=-1.67$ [8]).

Finally, at the bottom of the rear window (at coordinate $x_1/l=0.95$, Figs. 9(*d*) and 10(*d*), the vorticity and static pressure loss coefficients decrease, with $\omega=11.10^3\ \mathrm{s}^{-1}$ and $C_p=-1.6$. The vortex separates from the wall and moves away from the side edge. Feeding of the vortex by lateral separation is no longer preponderant and the vortex dynamics are governed by dissipation conditions.

The vorticity (Fig. 9) and static pressure loss coefficient fields (Fig. 10) also show that the vortex axis is not parallel to the side edge. The inclinations, noted between the vortex axis and the left-hand side edge, are similar to those indicated by Lehugeur and Gilliéron [11]: $\theta=7$ deg and $\beta=7$ deg (Fig. 11 where the vortex is highlighted by the vorticity isocontour $\omega=10^4\ \mathrm{s}^{-1}$). This information is used to define a coordinate system (x_2,y_2,z_2) associated with the vortex axis, represented in Fig. 11(*a*). The datum point of the coordinate system is the upper left-hand corner of the rear window, and axis (Ox_2) and plane (y_2z_2) therefore represent the vortex axis and the cross section plane, respectively (Fig. 11(*a*)).

Vortex T_2 is then analyzed through the velocity profiles measured in a cross section plane in the vortex core. The axial velocity profile, represented by $V_{x2}(y_2=0,z_2)$, is given in Fig. 12(*a*). The

Table 1 Drag coefficient

Authors	Study	Re	$\bar{C}_x$
Ahmed et al. [6]	Experimental	2.8×10^6	0.24
Gilliéron and Chometon [34]	Numerical (FLUENT)	4.2×10^6	0.28
Lienhart and Becker [9]	Experimental	2.8×10^6	0.285
Krajnovic and Davidson [10]	Numerical (LES)	2.8×10^6	0.292
Present study	Numerical (LBM)	2.8×10^6	0.31

azimuthal velocity profiles along the horizontal axis ($V_{y2}(y_2=0,z_2)$) and the vertical axis ($V_{z2}(y_2,z_2=0)$) are indicated in Figs. 12(*c*) and 12(*d*), respectively, for different coordinates ($x_2/l=0.533$, $x_2/l=0.618$, and $x_2/l=0.955$ in which l represents the rear window length).

The results in Fig. 12(*a*) reveal a maximum value of the longitudinal velocity in the vortex core (V_{x2} close to $1.2V_0$ at the vortex core). This velocity overshoot is characteristic of swirling jet structure [32] as opposed to a wake structure where the vortex core sustains a velocity deficit with respect to the main flow velocity (see Fig. 12(*b*)). Two longitudinal velocity minima appear on either side of the vortex core at coordinate $x_2/l>0.533$ (Fig. 12(*a*)), the position of which corresponds to the position of the azimuthal velocity extrema (Fig. 12(*c*)). This result concurs with the results obtained by Lehugeur and Gilliéron [11]. It is also of interest to note that the velocity profile measured at coordinate $x_2/l=0.25$ (Fig. 12(*a*)) does not have an established structure. The maximum axial velocity value is not detected at the vortex center ($z_2=0$), and the minima do not appear distinctly, in particular, at $z_2<-0.02$, due to the presence of the separated layer close to the vortex core. These results confirm the observations in Figs. 9(*a*) and 10(*a*): The vortex is not established on the top of the rear window, which once again concurs with the results of Lehugeur et al. [31].

The azimuthal velocity (horizontal profile in Fig. 12(*c*) and vertical in Fig. 12(*d*)) exhibits a linear evolution close to the vortex center, which highlights a constant shear zone indicative of a block rotation in the vortex core [11,32,33]. The azimuthal velocity extrema along the horizontal axis (Fig. 12(*c*)) and vertical axis (Fig. 12(*d*)) do not, however, have the same values: The maximum velocity (minimum, respectively) is close to 25 m s^{-1} (respectively, -25 m s^{-1}) in the horizontal profiles versus 32 m s^{-1} (respectively, -30 m s^{-1}) in the vertical profiles. The presence of the separated boundary Layer *D* (Fig. 4(*a*)) and of the geometry wall influences the structure of the vortex, which does not develop freely, and the vortex must therefore be considered as asymmetric.

The extrema values of the azimuthal velocity do not vary significantly along the rear window, which confirms the observations made on the pressure and vorticity fields: At $x/l>0.45$, the vortex is in a quasiuniform state [31].

Drag coefficient has been computed and compared to previous experimental and numerical studies. The value proposed by Ahmed et al. is the lower one. It was obtained by extrapolation of results corresponding to three experiments for different angles of the rear window (0 deg, 12.5 deg, and 30 deg). Table 1 presents drag coefficient. The value obtained in the present study is higher than the other one. This is due to the fact that the first part of the body is not considered here.

4 Conclusions

The near-wake flow of a simplified 3D fastback vehicle is studied according to a numerical approach based on the original LBM. The results obtained concur with the experimental and numerical results found in the literature and the various longitudinal and transversal separated vortices forming the wake are correctly reproduced.

The results show the formation of a separated layer on the rear window. The velocity profiles measured in the median longitudinal plane of the geometry indicate that the flow separates at the end of the roof and reattaches itself at the bottom of the rear window. These profiles effectively concur with the profiles measured experimentally in the reference works. The friction line field also reveals a strong interaction between the separated region and the longitudinal vortices, which feed the parietal fluid recirculation under the separated layer.

The topology of the longitudinal vortices is also analyzed. The axial and azimutal velocity profiles measured in the vortex core indicate a swirling jet structure, in accordance with the results found in the literature. After a formation phase on the top of the rear window, the longitudinal vortex structure appears in a columnar state along the side edge.

The results herein and the comparisons conducted with the experimental results constitute a validation of the computation code for the representation of bluff body near-wake flow characteristic of automotive vehicle wake. The numerical simulation presented can therefore be used to develop and parametrize active control solutions with a view to improve the aerodynamic performances of automobile vehicles. In this context, the topological results presented can be used to determine the control objectives: A reduction of aerodynamic drag consists therefore in finding solutions capable of limiting (even eliminating) the development of the longitudinal vortices and the separated layer development on the rear window.

References

[1] Gad-El-Hak, M., 1996, “Modern Developments in Flow Control,” Appl. Mech. Rev., **9**, pp. 365–379.

[2] Gilliéron, P., 2002, “Contrôle des Écoulements Appliqués à l’Automobile. Etat de l’Art,” Mécanique & Industries, **3**, pp. 515–524.

[3] Hucho, W. H., 1998, “Aerodynamics of Road Vehicle,” Annu. Rev. Fluid Mech., **25**, pp. 485–537.

[4] Ivanic, T., and Gilliéron, P., 2004, “Reduction of the Aerodynamic Drag Due to Cooling System: An Analytical and Experimental Approach,” SAE Paper No. 2005-01-1017.

[5] Tensi, J., Boué, I., and Paillé, F., 1999, “Effets Comparés sur L’écoulement Autour d’un Cylindre a Faible Nombre de Reynolds d’un Soufflage Pariétal Amont et en aval du Décollement,” *14eme Congrès Français de Mécanique*, Toulouse, France.

[6] Ahmed, S. R., Ramm, R., and Falting, G., 1984, “Some Salient Features of the Time Averaged Ground Vehicle Wake,” SAE Technical Paper series No. 840300.

[7] Spohn, A., and Gilliéron, P., 2002, “Flow Separations Generated by a Simplified Geometry of an Automotive Vehicle,” *Congrès IUTAM Symposium on Unsteady Separated Flows*, Toulouse, France, Apr. 8–12.

[8] Beaudoin, J. F., Cadot, O., Aider, J. L., Gosse, K., Paranthoën, P., and Hamelin, B., 2004, “Cavitation as a Complementary Tool for Automotive Aerodynamics,” Exp. Fluids, **37**, pp. 763–768.

[9] Lienhart, H., and Becker, S., 2003, “Flow and Turbulent Structure in the Wake of a Simplified Car Model,” SAE Paper No. 20030-01-0656.

[10] Krajnovic, S., and Davidson, L., 2004, “Contribution Large-Eddy Simulation of the Flow Around a Simplified Car Model,” *SAE International Congress and Exposition*, Detroit, MI, Paper No. 2004-01-0227.

[11] Lehugeur, B., and Gilliéron, P., 2005, “Characterization of Longitudinal Vor-

tices in the Wake of a Simplified Car Model," Paper No. AIAA-2005-5383.

[12] Rouméas, M., 2006, "Contribution à l'Analyse et au Contrôle du Sillage Épais par Aspiration ou Soufflage Continu," Ph.D. thesis, Thèse de Doctorat, INP Toulouse, France.

[13] Frisch, U., D'Humières, U., and Pommeau, Y., 1986, "Lattice-Gas Automata for Navier-Stokes Equation," Phys. Rev. Lett., **56**, pp. 1505–1508.

[14] Chen, S., Chen, H., Martinez, D., and Matthaeus, W., 1991, "Lattice Boltzmann Model for Simulation of Magnetohydrodynamics," Phys. Rev. Lett., **67**, pp. 3776–3779.

[15] Chen, S., Chen, H., and Matthaeus, W., 1992, "Recovery of the Navier-Stokes Equations Using a Lattice-Gas Boltzmann Method," Phys. Rev. A, **45**, R5339–R5342.

[16] Bhatnagar, P. L., Gross, E. P., and Krook, M., 1954, "A Model for Collision Processes in Gases. Small Amplitude Processes in Charged and Neural One-Component Systems," Phys. Rev., **94**(3), pp. 511–525.

[17] Chen, H., Teixeira, C., and Molvig, K., 1997, "Digital Physics Approach to Computational Fluid Dynamics: Some Basic Theoretical Features," Int. J. Mod. Phys. C, **8**(4), pp. 675–684.

[18] Yakhot, V., and Orszag, S. A., 1986, "Renormalization Group Analysis of Turbulence. Basic Theory," J. Sci. Comput., **1**, pp. 1–51.

[19] Pervaiz, M., and Teixeira, M., 1999, "Two Equation Turbulence Modeling With the Lattice-Boltzmann Method," *Proceedings of ASME PVP Division Conference, Second International Symposium on Computational Technologies for Fluid/Thermal and Chemical Systems With Industrial Applications*, Boston.

[20] Li, Y., Shock, R., Zhang, R., and Chen, H., 2004, "Numerical Study of Flow Past an Impulsively Started Cylinder by Lattice Boltzmann Method," J. Fluid Mech., **519**, pp. 273–300.

[21] Shock, R. A., Mallick, S., Chen, H., Yakhot, V., and Zhang, R., 2002, "Recent Results on Two Dimensional Airfoils Using Lattice Boltzmann-Based Algorithm," J. Aircr., **39**(3), pp. 434–439.

[22] Gilliéron, P., Laurent, J., and Chometon, F., 2000, "Analyse des Écoulements de Culot par Vélocimétrie Laser: Application à l'Automobile," *7ième Congrès de Vélocimétrie Laser*, September.

[23] Krajnovic, S., and Davidson, L., 2005, "Flow Around a Simplified Car, Part 1: Large Eddy Simulation," ASME J. Fluids Eng., **127**, pp. 907–918.

[24] Krajnovic, S., and Davidson, L., 2005, "Flow Around a Simplified Car, Part 2: Understanding the Flow," ASME J. Fluids Eng., **127**, pp. 919–928.

[25] Chen, H., Teixeira, C., and Molvig, K., 1998, "Realization of Fluid Boundary Conditions via Discrete Boltzmann Dynamics," Int. J. Mod. Phys. C, **9**(8), p. 1281–1292.

[26] Yu, D., Mai, R., and Shyy, W., 2002, "A Multi-Block Lattice Boltzmann Method for Viscous Fluid Flow," Int. J. Numer. Methods Fluids, **39**, pp. 99–120.

[27] 2001, *Ninth Joint ERCOFTAC/IAHR/QNET-CFD Workshop on Refined Turbulence Modelling*, S. Jakirkic, R. Jester-Zürker, and C. Tropea, eds., Darmstadt, Allemagne.

[28] 2002, *Ninth Joint ERCOFTAC/IAHR/QNET-CFD Workshop on Refined Turbulence Modeling*, R. Manceau, and J. P. Bonnet, eds., Poitiers, France.

[29] Chassaing, P., 2000, "Turbulence en Mécanique des Fluides: Analyse du Phénomène en vue de sa Modélisation à l'Usage de l'Ingénieur," CEPADUES edition, pp. 441–484.

[30] Gilliéron, P., 1998, "La Technique des Tomographies de Pertes de Pression d'Arrêt," Aérodynamique Appliquée, cycle d'approfondissement, CNAM niveau C, CNAM Médias, 1998/2001.

[31] Lehugeur, B., Gilliéron, P., and Ivanic, T., 2005, "Characterization of C-Pillar Vortices by 3D PIV," *Workshop on Particle Image Velocimetry in Car Industry*, Gurgliasco, Italy.

[32] Ivanic, T., Foucault, E., and Pécheux, J., 2003, "Dynamic of Swirling Jets Flows," Exp. Fluids, **35**, pp. 317–324.

[33] Lambourde, N. C., and Bryer, D. W., 1961, "The Bursting of Leading-Edge Vortices: Some Observations and Discussion of the Phenomenon," Aero. Res. Counc., Report & Memoranda, **3282**, pp. 1–35.

[34] Gilliéron, P., and Chometon, F., 1997, "Modélisation de l'Écoulement Tridimensionnel Décollé Stationnaire Autours du corps de Ahmed," Groupe utilisateurs Fluent, Paris, Oct.

A Differential Quadrature Solution of MHD Natural Convection in an Inclined Enclosure With a Partition

Kamil Kahveci
e-mail: kamilk@trakya.edu.tr

Semiha Öztuna
e-mail: semihae@trakya.edu.tr

Mechanical Engineering Department,
Trakya University,
22030 Edirne, Turkey

Magnetohydrodynamics natural convection in an inclined enclosure with a partition is studied numerically using a differential quadrature method. Governing equations for the fluid flow and heat transfer are solved for the Rayleigh number varying from 10^4 *to* 10^6, *the Prandtl numbers (0.1, 1, and 10), four different Hartmann numbers (0, 25, 50, and 100), the inclination angle ranging from* 0 deg to 90 deg, *and the magnetic field with the x and y directions. The results show that the convective flow weakens considerably with increasing magnetic field strength, and the x-directional magnetic field is more effective in reducing the convection intensity. As the inclination angle increases, multicellular flows begin to develop on both sides of the enclosure for higher values of the Hartmann number if the enclosure is under the x-directional magnetic field. The vorticity generation intensity increases with increase of Rayleigh number. On the other hand, increasing Hartmann number has a negative effect on vorticity generation. With an increase in the inclination angle, the intensity of vorticity generation is observed to shift to top left corners and bottom right corners. Vorticity generation loops in each region of enclosure form due to multicelluar flow for an x-directional magnetic field when the inclination angle is increased further. In addition, depending on the boundary layer developed, the vorticity value on the hot wall increases first sharply with increasing y and then begins to decrease gradually. For the high Rayleigh numbers, the average Nusselt number shows an increasing trend as the inclination angle increases and a peak value is detected. Beyond the peak point, the foregoing trend reverses to decrease with the further increase of the inclination angle. The results also show that the Prandtl number has only a marginal effect on the flow and heat transfer.* [DOI: 10.1115/1.2829567]

Keywords: natural convection, MHD, PDQ, enclosure, vorticity, stream function

1 Introduction

Natural convection in enclosures has received considerable attention in recent years because of numerous applications in engineering. The primary interest of previous studies has been a simple rectangular enclosure. However, in many practical cases, enclosures with partitions are used to modify heat transfer. Natural convection in an enclosure with a centrally located partition was analyzed by Dzodzo et al. [1]. Their results indicate that partitioning the enclosure vertically reduces the convective heat transfer up to 64%. In addition, the results of Tong and Gerner [2] show that placing a partition midway between the vertical walls of an enclosure produces the greatest reduction in heat transfer. Kahveci [3,4] studied natural convection in an enclosure partitioned with a finite thickness partition and found that the average Nusselt number decreases with an increase of the distance between the hot wall and the partition, and the thickness of the partition has a little effect on natural convection. Kahveci [5] also found that with increasing aspect ratio, heat transfer shows an increasing trend and gets a maximum value. Beyond the maximum point, the foregoing trend reverses to decrease with further increase of the aspect ratio. Elsherbiny et al. [6] found that the thermal boundary conditions at the end walls influence the effect of partitions in reducing the heat transfer rate across the enclosure. Acharya and Tsang [7] studied the effect of the inclination angle of an enclosure with a centrally located partition on natural convection. Their results show that the inclination angle has a strong influence on the magnitude of the maximum Nusselt number. Khan and Yao [8], comparing natural convection of water and air in a partially divided enclosure, suggested that the average Nusselt number for water is slightly higher than that for air in the same conditions. The effect of using a horizontal partition in an enclosure was analyzed by Nag et al. [9], and they found that the higher the value of the position of the partition along the wall, the more the attenuation in heat transfer. The numerical examination of the radiation-convection interaction presented by Mezrhab and Bchir [10] shows that the radiation standardizes the temperature in the two parts of the enclosure. Yucel and Ozdem [11] concluded from their numerical investigation on natural convection in the partially divided enclosures that increasing the number of the partitions causes the average Nusselt number to decrease. The effect of a vertical partial partition in an enclosure on natural convection was investigated by Öztuna [12]. The results show that an increase in the partition height brings about a significant decrease in the average Nusselt number. Wang et al. [13] investigated convection in a partially divided enclosure with a combined horizontal temperature and concentration gradient and found that the partition ratio has a strong effect on both the mass transfer rate and flow pattern.

The previous studies of partitioned enclosures investigate natural convection in the absence of a magnetic field. On the other hand, natural convection for an electrically conducting fluid under the influence of a magnetic field is of great importance in many industrial applications such as crystal growth, metal casting, and

---

Contributed by the Fluids Engineering Division of ASME for publication in the JOURNAL OF FLUIDS ENGINEERING. Manuscript received January 12, 2007; final manuscript received July 16, 2007; published online January 24, 2008. Review conducted by Malcolm J. Andrews.

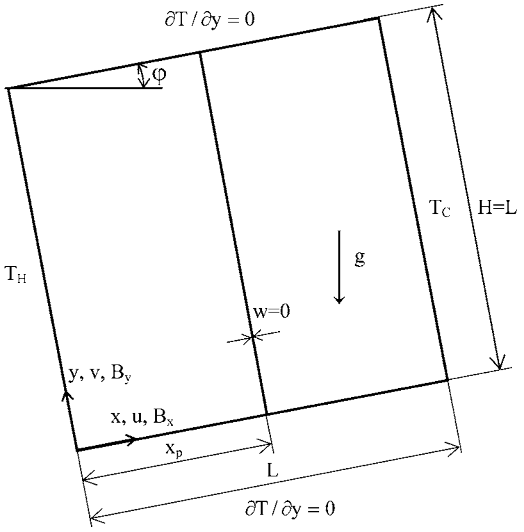

Fig. 1 Geometry and coordinate system

liquid metal cooling blankets for fusion reactors. A magnetic field imposed on electrically conducting fluid creates the Lorentz force in the plane perpendicular to the magnetic field vector, oriented in the direction opposite to the fluid velocity, thus retarding the motion perpendicular to the magnetic field.

In this study, MHD natural convection in an inclined enclosure with a partition was investigated numerically to reveal the effect of the various governing parameters on the flow and heat transfer. For the simulation of natural convection, mostly the low order methods such as finite difference, finite element, and finite volume methods were used in the previous studies, and, in general, the low order methods need a large number of grid points to ensure a reliable accuracy. However, the polynomial differential quadrature (PDQ) method [14–16] is an efficient discretization technique to obtain accurate numerical solutions using a considerably small number of grid points as compared with the low order methods. Therefore, the numerical solution of the problem was obtained by using the PDQ method.

2 System and Model Equations

The geometry and the coordinate system used in the analysis are shown in Fig. 1. The square enclosure is bounded by two isothermal walls at temperatures T_H and T_C and two adiabatic walls. A thin partition subdivides the enclosure into two regions. The fluid is an incompressible Newtonian fluid with the Boussinesq approximation.

The dimensionless variables used are as follows:

$$x = \frac{x^*}{L} \quad y = \frac{y^*}{L} \quad u = \frac{u^*}{\alpha/L} \quad v = \frac{v^*}{\alpha/L}$$

$$p = \frac{L^2}{\rho_o \alpha^2}(p^* + \rho_o g y^*) \quad T = \frac{T^* - T_C}{T_H - T_C} \tag{1}$$

where u^* and v^* are the dimensional velocity components, p^* is the dimensional pressure, T^* is the dimensional temperature, ρ is the fluid density, and α is the thermal diffusivity of the fluid.

The magnetic field induced by the electric current density is assumed to be negligible because the electric current density induced by fluid motion is very small. The Joule heating of the fluid and the effect of viscous dissipation are also considered to be negligible. Under these assumptions, the dimensionless governing equations in the vorticity-stream function formulation are as follows:

$$\frac{\partial^2 \psi}{\partial_x^2} + \frac{\partial^2 \psi}{\partial_y^2} = -\omega \tag{2}$$

$$u\frac{\partial \omega}{\partial x} + v\frac{\partial \omega}{\partial y} = \Pr\left(\frac{\partial^2 \omega}{\partial x^2} + \frac{\partial^2 \omega}{\partial y^2}\right) + \mathrm{Ra}\Pr\left(\frac{\partial T}{\partial x}\cos\phi - \frac{\partial T}{\partial y}\sin\phi\right) + \mathrm{Ha}^2\Pr\left(\delta\frac{\partial u}{\partial x} - \frac{\partial v}{\partial x} + \delta^2\frac{\partial u}{\partial y} - \delta\frac{\partial v}{\partial y}\right) \quad \delta = B_y/B_x \text{ or} \tag{3a}$$

$$u\frac{\partial \omega}{\partial x} + v\frac{\partial \omega}{\partial y} = \Pr\left(\frac{\partial^2 \omega}{\partial x^2} + \frac{\partial^2 \omega}{\partial y^2}\right) + \mathrm{Ra}\Pr\left(\frac{\partial T}{\partial x}\cos\phi - \frac{\partial T}{\partial y}\sin\phi\right) + \mathrm{Ha}^2\Pr\left(\delta^2\frac{\partial u}{\partial x} - \delta\frac{\partial v}{\partial x} + \delta\frac{\partial u}{\partial y} - \frac{\partial v}{\partial y}\right) \quad \delta = B_x/B_y \tag{3b}$$

$$u\frac{\partial T}{\partial x} + v\frac{\partial T}{\partial y} = \frac{\partial^2 T}{\partial_x^2} + \frac{\partial^2 T}{\partial_y^2}. \tag{4}$$

Here, δ is the ratio of magnetic field strengths of x and y directions, and the Prandtl, Rayleigh, and Hartmann numbers are defined as

$$\Pr = \frac{v}{\alpha} \quad \mathrm{Ra} = \frac{g\beta L^3 \Delta T^*}{v\alpha} \quad \mathrm{Ha}_i = \mathrm{LB}_i\sqrt{\frac{\sigma}{\mu}} \quad i = x, y \tag{5}$$

where g is the gravitational acceleration, β is the coefficient of thermal expansion, v is the kinematic viscosity of the fluid, B is the magnetic induction, and σ is the electric conductivity.

The boundary conditions for the problem are

$$\psi(x,0) = 0 \quad \psi(x_p,y) = 0 \quad \psi(x,1) = 0 \quad \psi(0,y) = 0 \quad \psi(1,y) = 0 \tag{6}$$

$$\left.\frac{\partial T}{\partial y}\right|_{x,0} = 0 \quad T(x_p^-,y) = T(x_p^+,y) \quad \left.\frac{\partial T}{\partial x}\right|_{x_p^-,1} = \left.\frac{\partial T}{\partial x}\right|_{x_p^+,1}$$

$$\left.\frac{\partial T}{\partial y}\right|_{x,1} = 0 \quad T(0,y) = 1 \quad T(1,y) = 0 \tag{7}$$

Physically, there is no boundary condition for the vorticity. However, an expression can be obtained from the Taylor series expansion of the stream function equation as $\omega_{\text{wall}} = -\partial^2\psi/\partial\eta^2$, where η is the outward normal variable to the surface. This equation is adapted as the boundary condition for the vorticity in this study.

3 Computational Method

After discretization by the PDQ method, the governing equations become as follows:

$$\sum_{k=0}^{N_x} b_{i,k}\psi_{k,j} + \sum_{k=0}^{N_y} \bar{b}_{j,k}\psi_{i,k} = -\omega_{i,j} \tag{8}$$

$$\sum_{k=0}^{N_y} \bar{a}_{j,k}\psi_{i,k}\sum_{k=0}^{N_x} a_{i,k}\omega_{k,j} - \sum_{k=0}^{N_x} a_{i,k}\psi_{k,j}\sum_{k=0}^{N_y} \bar{a}_{j,k}\omega_{i,k} = \mathrm{Ra}\Pr\left[\cos\varphi\sum_{k=0}^{N_x} a_{i,k}T_{k,j} - \sin\varphi\sum_{k=0}^{N_x} \bar{a}_{j,k}T_{i,k}\right] + \Pr\left[\sum_{k=0}^{N_x} b_{i,k}\omega_{k,j} + \sum_{k=0}^{N_y} \bar{b}_{j,k}\omega_{i,k}\right] + \mathrm{Ha}_i^2\Pr(1+\delta)\delta\left[\sum_{k=0}^{N_x} b_{i,k}\psi_{k,j} + \sum_{k=0}^{N_y} \bar{b}_{j,k}\psi_{i,k}\right] \tag{9}$$

Table 1 Grid dependency for Ra=10^6 and Pr=1 and Ha=0

Mesh size	Nu_a	$\lvert\psi\rvert_{\max}$
18×18	4.25	11.6
22×22	4.28	11.8
26×26	4.32	11.8
31×31	4.32	11.8

$$\sum_{k=0}^{N_y}\bar{a}_{j,k}\psi_{i,k}\sum_{k=0}^{N_x}a_{i,k}T_{k,j}-\sum_{k=0}^{N_x}a_{i,k}\psi_{k,j}\sum_{k=0}^{N_y}\bar{a}_{j,k}T_{i,k} = \left[\sum_{k=0}^{N_x}b_{i,k}T_{k,j}+\sum_{k=0}^{N_y}\bar{b}_{j,k}T_{i,k}\right] \tag{10}$$

where the indices i and j indicate a grid point, and N_x and N_y represent the total number of the grid points in the x and y directions, respectively. The discretized equations (Eqs. (8)–(10)) are solved by the successive over-relaxation (SOR) iteration method. The following nonuniform grid point distribution called Chebshyev-Gauss-Lobatho is used in the solution procedure of the problem:

$$x_i=\frac{1}{2}\left[1-\cos\left(\frac{i}{N_x}\pi\right)\right]\quad i=0,1,2,\ldots,N_x$$

$$y_j=\frac{1}{2}\left[1-\cos\left(\frac{j}{N_y}\pi\right)\right]\quad j=0,1,2,\ldots,N_y \tag{11}$$

To ensure convergence of the numerical algorithm, the criteria $|\Phi_{i,j}^{m}-\Phi_{i,j}^{m+1}|<10^{-5}$ is applied to all dependent variables over the solution domain where Φ represents a dependent variable, ω, ψ, T, and the index m indicates the current iteration.

A series of grid systems of up to 31×31 points are performed to obtain a grid independent mesh size. It suggests that when the mesh size is above 26×26, Nu_a and $|\psi|_{\max}$ remain the same. The results for the case of Ra=10^6, Pr=1, and Ha=0 are shown in Table 1. Depending on this observation, the mesh size is selected as 31×31 in this work.

For the validation of the numerical code, the solution for the nonpartitioned square enclosure case is also obtained by the PDQ method, and the results are compared with the benchmark results obtained by de Vahl Davis [17] through a standard finite difference method (see Table 2). It can be concluded from Table 2 that there is a very good agreement between the results of the PDQ method for the grid 31×31 and the benchmark results of de Vahl Davis [17] based on the low order methods for the grids up to 81×81.

4 Results and Discussions

The computational results are obtained for the Rayleigh number in the range of 10^4 and 10^6, the Prandtl number ranging from 0.1 to 10, the Hartmann number ranging from 0 to 100, and the inclination angle in the range of 0 deg to 90 deg. The velocity profiles for Pr=1 and Ha=0 are shown in Fig. 2. It can be noticed that the velocity components are linear throughout the core regions. Furthermore, the comparison of the velocity components reveals that the flow in the vertical direction is faster because of the buoyancy-induced acceleration experienced by the fluid particles transported in this direction.

The streamlines and isotherms are shown in Figs. 3–6 for various values of the inclination angle. It may be observed that the flow on both sides of the enclosure is single cellular for the small values of inclination angle. In addition, it is seen that flow patterns are symmetrical on both regions of enclosure because the temperature gradients along the x direction are almost the same. As the inclination angle increases, single-cellular flows break down for the x-directional magnetic field case, and multicellular flows form in the flow fields for the higher values of the Hartmann number. With an increase in the strength of the magnetic field, the convection strength is reduced. This result is consistent with the results of Ece and Büyük [18], who investigated natural convection in a nonpartitioned enclosure under the magnetic field. In addition, as it is seen from the figures, isotherms gradually become linear with increasing magnetic field strength. The core of streamlines moves toward the top of the cold wall and the bottom of the hot wall as the magnetic field strength increases. It can be seen from the figures that the x-directional magnetic field is more effective in retarding the motion as compared to that for the y-directional case. This is expected because the main flow is at the y direction. As it is expressed before, magnetic field retards the fluid motion perpendicular to the magnetic field. Therefore, the x-directional magnetic field retards the fluid motion in the y direction, while the y-directional magnetic field retards it in the x direction.

A circulatory gyre pattern for natural convection in a partitioned enclosure can also be seen using the vorticity contours. As observed in Figs. 7–10, there is an existence of near-stagnant interior cores in each region of the enclosure along with the distinct boundary layers near the vertical walls. Higher values of the vorticity on the walls indicate the intense convection effect on the fluid structure. Vorticity takes lower values as a result of weak circulation when Hartmann number is increased. With increase in the inclination angle, the intensity of vorticity generation is observed to shift to top left corners and bottom right corners. These changes indirectly indicate the variations in the velocity gradients due to the varying inclination angle. For the x-directional magnetic field case, vorticity generation loops because of multicellular flow are clearly seen in Fig. 10.

Variation of the values of the vorticity along the hot wall with the Rayleigh number is seen in Fig. 11 for various values of the inclination angle. The vorticity values increase with an increase in the value of the Rayleigh number, resulting in a strong circulatory motion. Circulation becomes weaker depending on the boundary layer developed along the hot wall. Thus, the vorticity value along the hot wall represents a sharp increase near the leading edge and then begins to decrease gradually toward the trailing edge. The vorticity values show a wavy variation in the case of multicellular flow. A negative value of vorticity at the y-directional magnetic field for inclination angle φ=90 deg is due to counterclockwise circulation.

Table 2 Validation of the numerical code (nonpartitioned case)

	Ra=10^4		Ra=10^5		Ra=10^6	
	de Vahl Davis	Present	de Vahl Davis	Present	de Vahl Davis	Present
$\lvert\psi\rvert_{\max}$	—	5.07	9.61	9.60	16.75	16.72
Nu_a	2.24	2.24	4.52	4.52	8.80	8.82
$\mathrm{Nu}_{\max}$	3.53	3.53	7.72	7.70	17.93	17.56
$\mathrm{Nu}_{\min}$	0.59	0.59	0.73	0.73	0.99	0.98

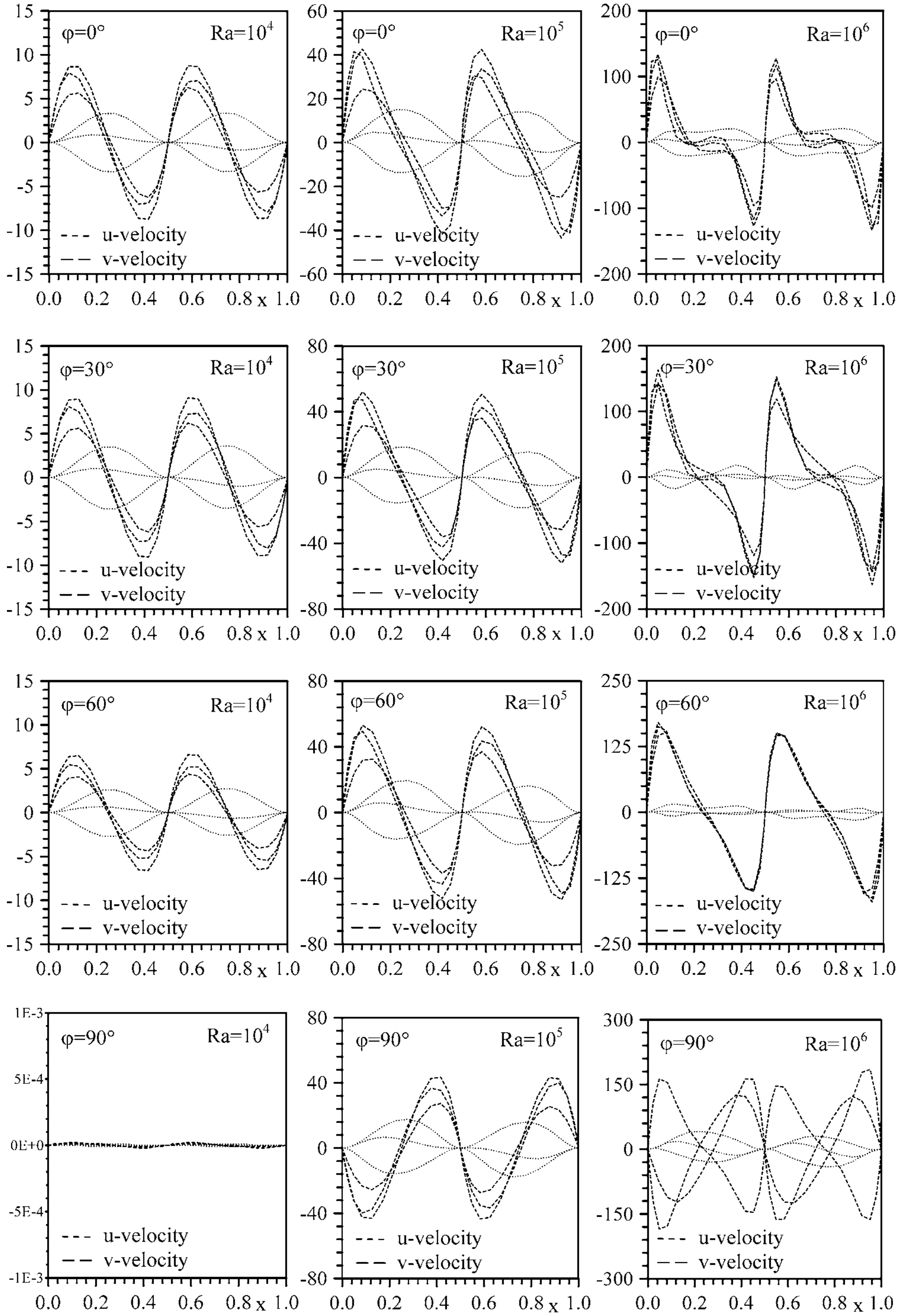

Fig. 2 Distributions of the velocities along the lines $y=0,0.5,0.75$ for Pr=1 and Ha=0

Variation of vorticity along the hot wall with the Hartmann number is shown in Fig. 12 for various values of inclination angle. As seen from the figure, vorticity shows a decreasing trend with increasing Hartmann number depending on the weakening circulation. For the y-directional magnetic field case, this decreasing trend becomes stronger with increasing Hartmann number.

For the vertical enclosure case, the variation of position where vorticity takes a maximum value along the hot wall with the Rayleigh and Hartman numbers is shown in Fig. 13. The maximum value of vorticity closes to the leading edge for both x-directional and y-directional magnetic field cases when the Rayleigh number is increased. The same trend is seen when the Hartmann number is increased. However, the position where vorticity obtains its maximum value approaches a constant value when the Hartmann number is increased further. Similar variations for position where the vorticity takes a maximum value with the Rayleigh and Hartmann numbers is observed for other inclination angles (not shown here) where multicellular flow does not occur.

Variation of the local Nusselt number along the hot wall with the Rayleigh number is presented in Fig. 14 for various values of the inclination angle. For the low Rayleigh numbers, the isotherms are evenly spaced between the vertical walls of the enclosure, indicating that the conduction heat transfer is dominant. As the Rayleigh number increases, a gradually strengthening circula-

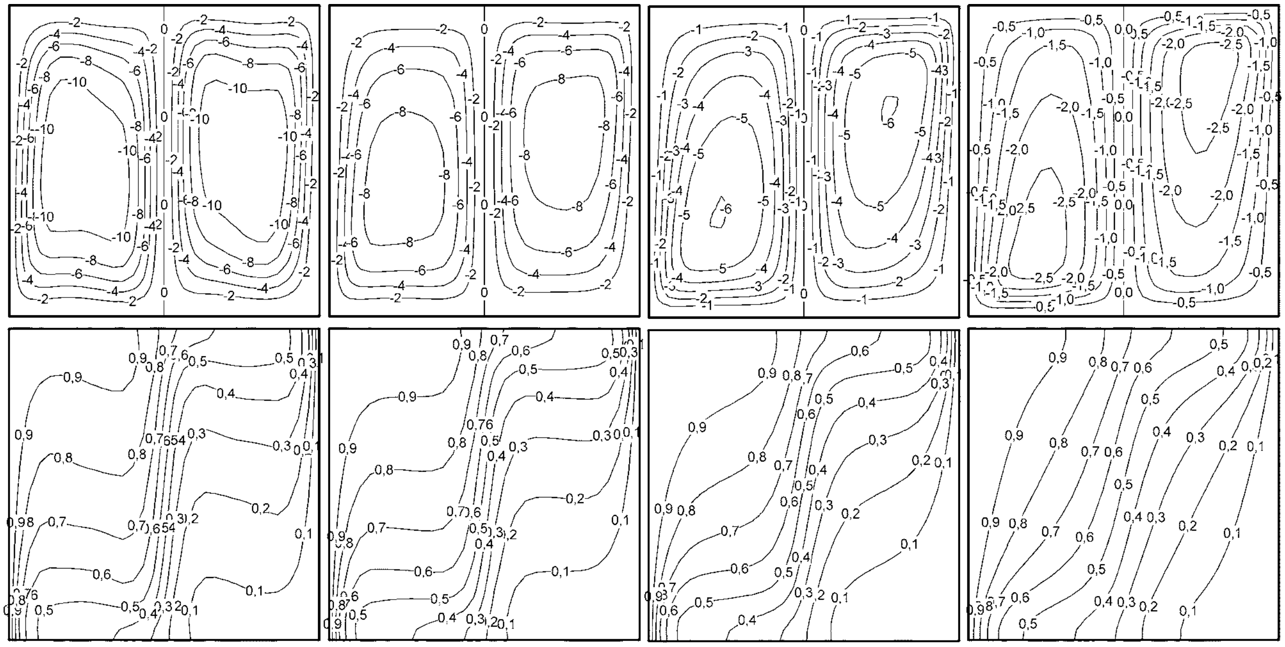

a) Ha=0 b) Ha=25 c) Ha=50 d) Ha=100

x-directional magnetic field

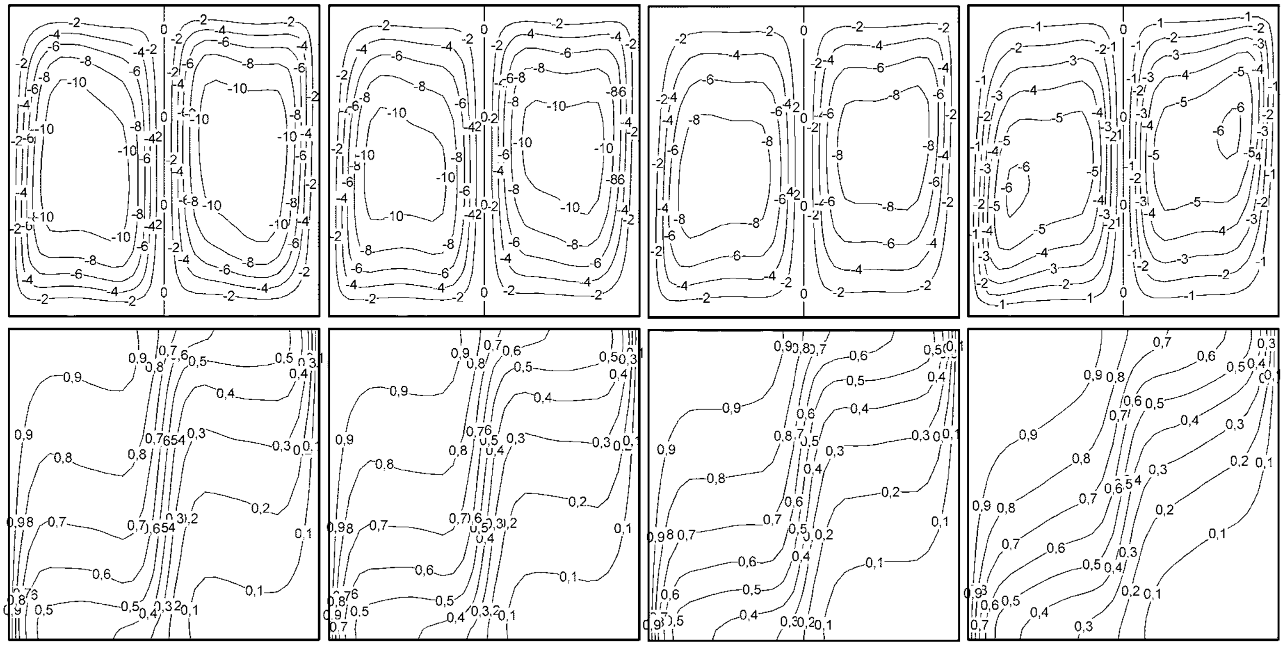

a) Ha=0 b) Ha=25 c) Ha=50 d) Ha=100

y-directional magnetic field

Fig. 3 Streamlines and isotherms for Ra=10^6, Pr=1, and φ=0 deg

tion begins to develop on both sides of the enclosure. This results in an increase of the local Nusselt number, as seen from Fig. 14. The *x*-directional magnetic field yields the smaller local Nusselt numbers when it is compared with the *y*-directional magnetic field. The isotherms in the core region for a vertical enclosure are nearly horizontal, while they are oblique for an inclined enclosure. Therefore, for a vertical enclosure, the temperature of the fluid directed from the partition to the base of the hot surface is colder, while the temperature of the fluid in the lower part of the hot surface is higher than the corresponding fluid temperature in an inclined enclosure. As a result, the local Nusselt number for a vertical enclosure shows higher changes along the hot wall compared with the corresponding local Nusselt number for an inclined enclosure. For the high inclination angles, multicellular flows with three cells occur on both sides of the enclosure for the *x*-directional magnetic field case as a result of the breakdown of the single-cellular flows. One of these three cells is in the middle of the enclosure and rotates clockwise, while the other two are in the lower and upper parts of the enclosure and rotate counter-clockwise. For this multicellular flow case, the local Nusselt num-

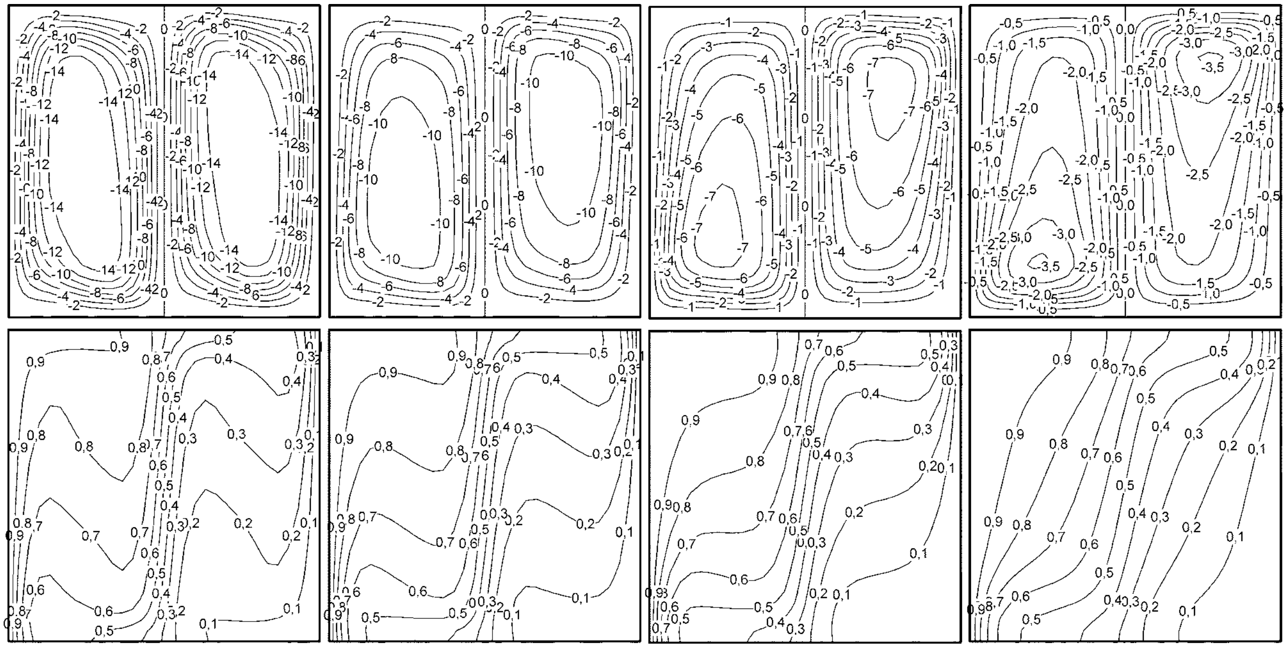
a) Ha=0 b) Ha=25 c) Ha=50 d) Ha=100

x-directional magnetic field

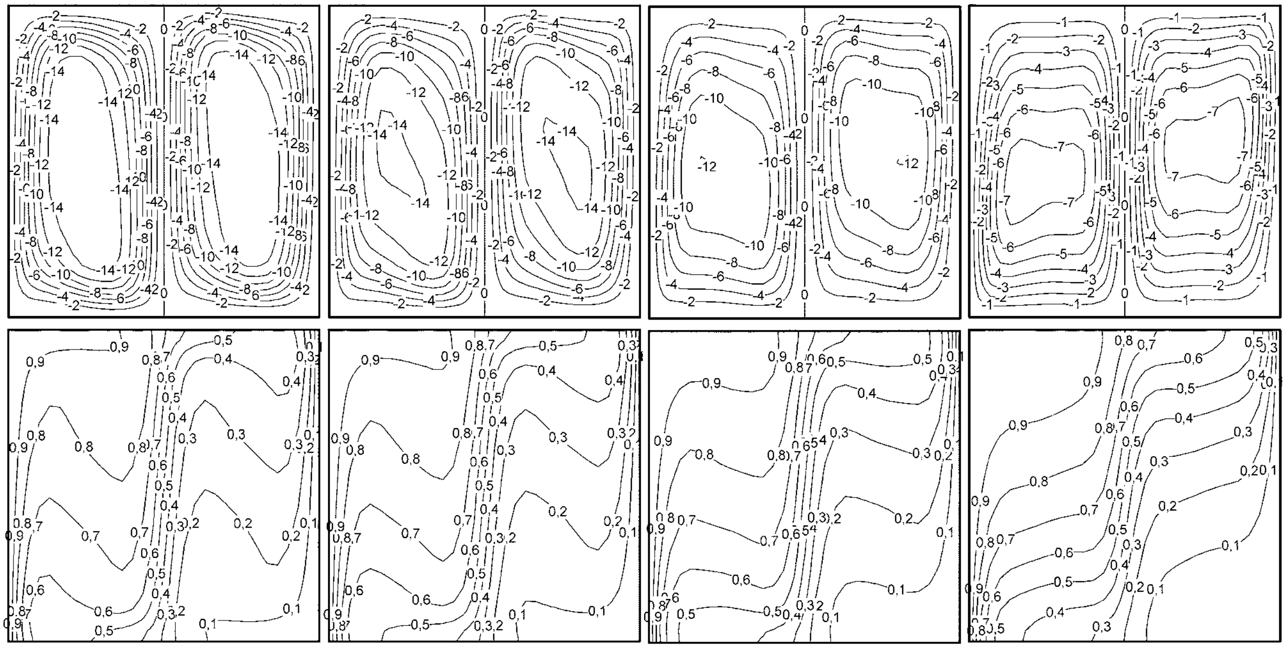
a) Ha=0 b) Ha=25 c) Ha=50 d) Ha=100

y-directional magnetic field

Fig. 4 Streamlines and isotherms for Ra=10^6, Pr=1, and φ=30 deg

ber shows an increasing trend with increasing *y* in the lower part of the enclosure because of the counterclockwise rotating circulation cell. The clockwise cell, which is in the middle of the enclosure, causes a decrease in the local Nusselt number. The local Nusselt number begins to increase again in the upper part of the enclosure due to the cell rotating counterclockwise and eventually shows a decrease toward the trailing edge of the hot wall. For the inclination angle $\varphi=90$ deg, a counterclockwise circulation cell forms the flow fields for the *y*-directional magnetic field case; therefore, the local Nusselt number shows an increasing trend with increasing *y*.

The effect of the Prandtl number on the local Nusselt number along the hot wall is shown in Fig. 15 for various values of the inclination angle. As the Prandtl number increases, the local Nusselt number along the hot surface increases in a little amount especially in the lower part of the enclosure for the cases except

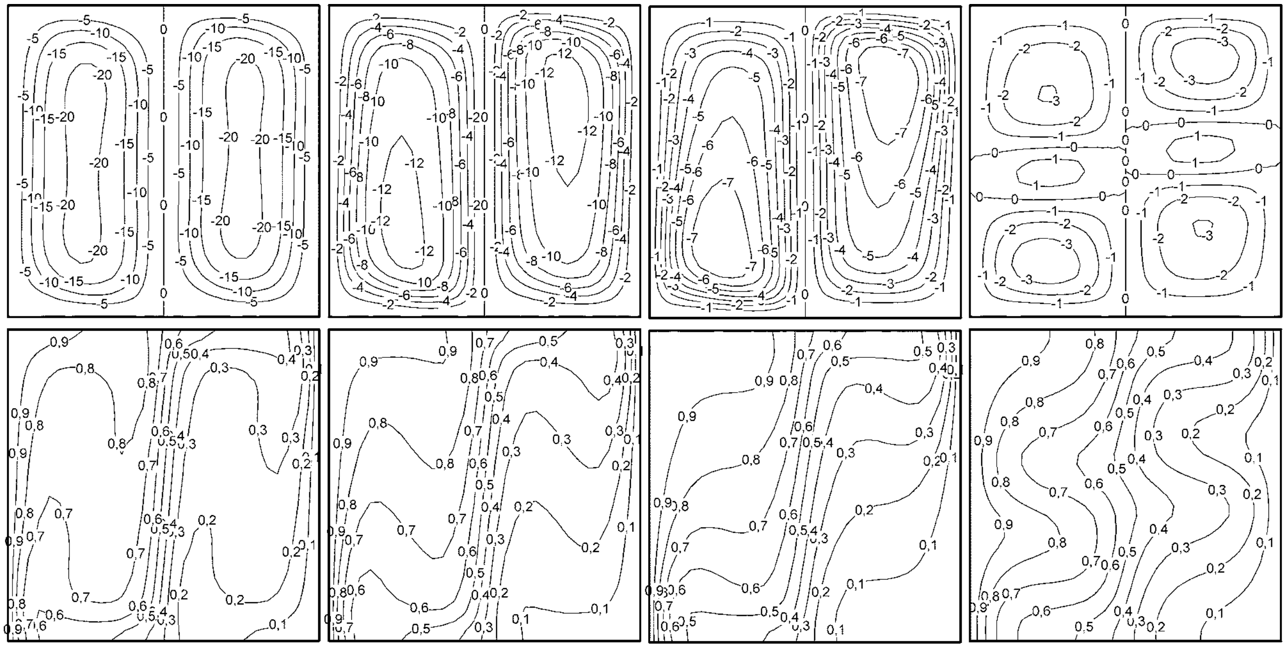

a) Ha=0 b) Ha=25 c) Ha=50 d) Ha=100

x-directional magnetic field

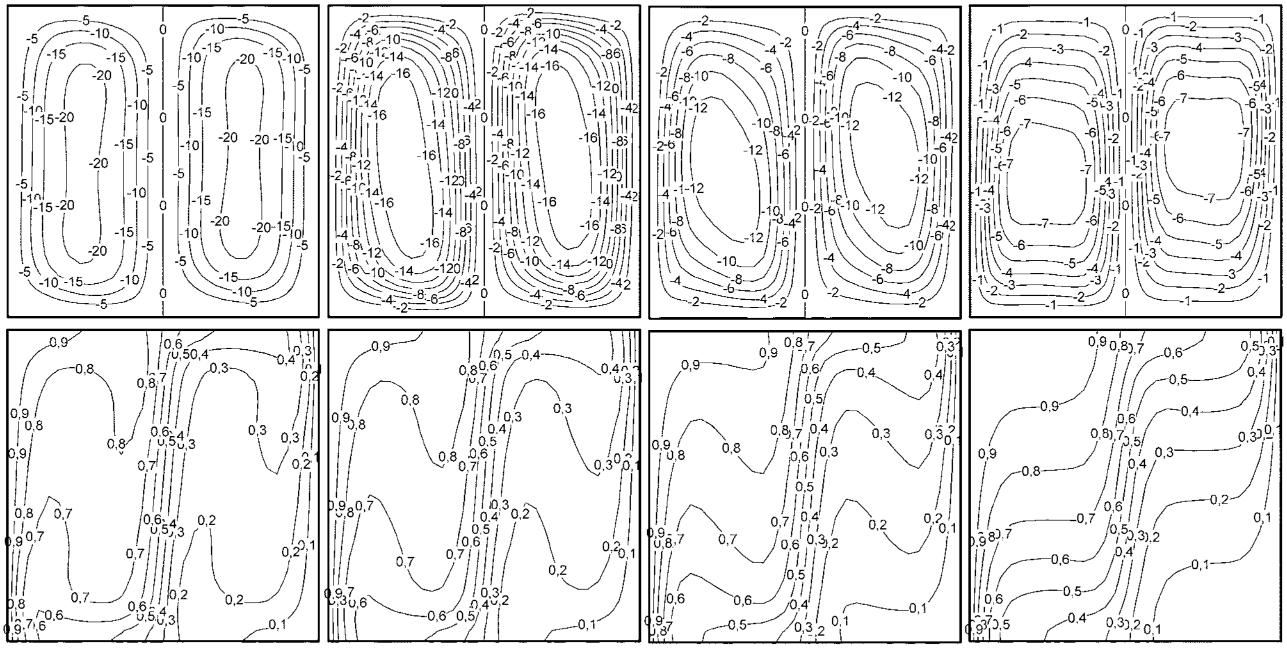

a) Ha=0 b) Ha=25 c) Ha=50 d) Ha=100

y-directional magnetic field

Fig. 5 Streamlines and isotherms for $Ra=10^6$, $Pr=1$, and $\varphi=60$ deg

for $\varphi=90$ deg. This is because of the fact that the thermal boundary layer along the hot wall becomes relatively thinner as the Prandtl number increases, causing higher heat flux. For the $\varphi=90$ deg, the difference between the maximum and minimum values of the local Nusselt number decreases with increasing Prandtl number.

Variation of the local Nusselt number along the hot wall with the Hartmann number is shown in Fig. 16. Because of the retarding effect of the magnetic field on convective flow, the local Nusselt number decreases in the existence of a magnetic field. The damping of the local Nusselt number increases with increasing Hartmann number. As stated before, multicellular flows form the flow fields for the $\varphi=90$ deg if the enclosure is under the x-directional magnetic field. Therefore, the local Nusselt number along the hot wall shows a wavy variation for this case. For the y-directional magnetic field case, single-cellular counterclockwise

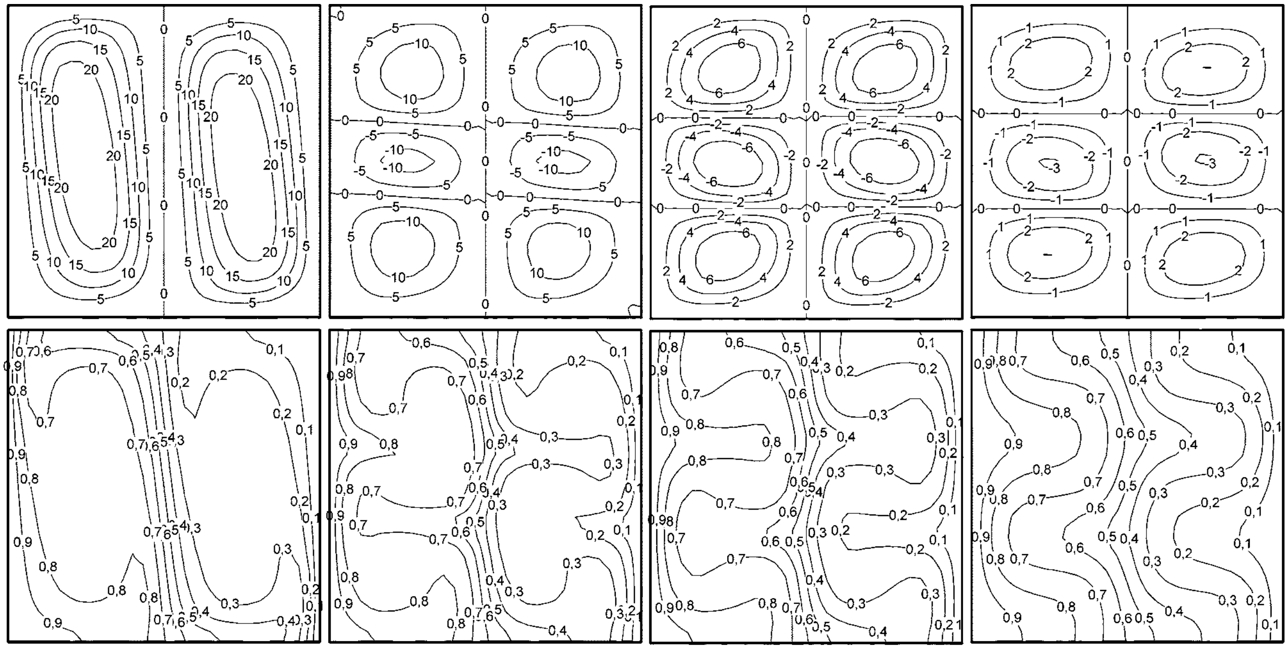

a) Ha=0 b) Ha=25 c) Ha=50 d) Ha=100

x-directional magnetic field

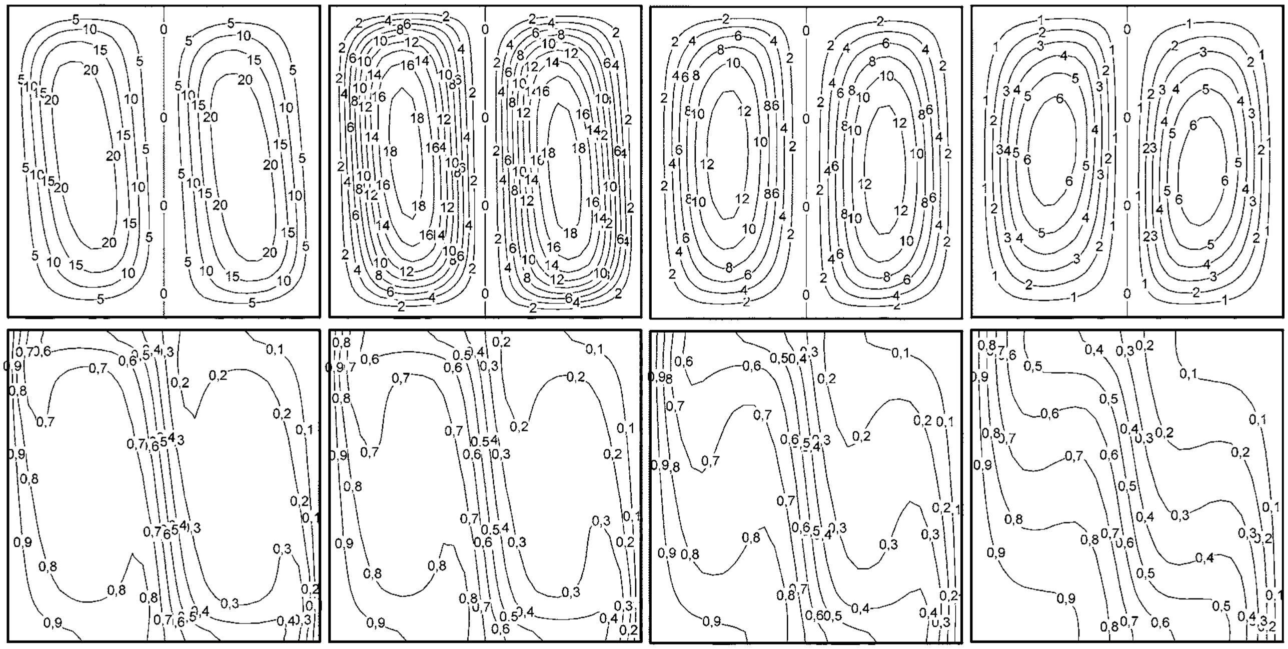

a) Ha=0 b) Ha=25 c) Ha=50 d) Ha=100

y-directional magnetic field

Fig. 6 Streamlines and isotherms for $Ra=10^6$, $Pr=1$, and $\varphi=90$ deg

flows form the flow fields on both sides of the enclosure. Therefore, the local Nusselt number shows an increasing trend with increasing y and takes lower values with increasing magnetic field strength.

Variation of the average Nusselt number with the Rayleigh number is shown in Fig. 17 for various values of the inclination angle. The average Nusselt number remains nearly constant with increasing Hartmann number for the low values of the Rayleigh number. For the high values of the Rayleigh number, heat transfer decreases when a magnetic field exists in the flow field. As can be seen from Fig. 17, the damping in heat transfer increases with increasing strength of the magnetic field. The maximum decrease takes place for $Ra=10^5$ for the low values of the Hartmann number and for $Ra=10^6$ for the high values of the Hartmann number.

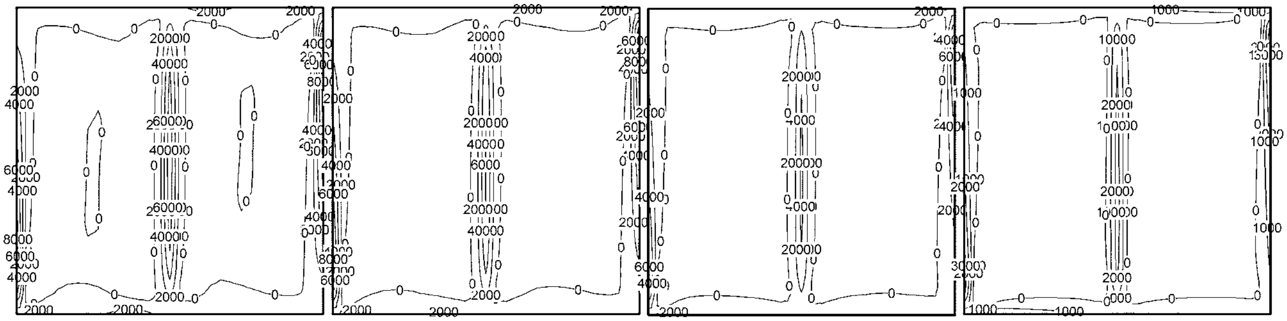

x-directional magnetic field

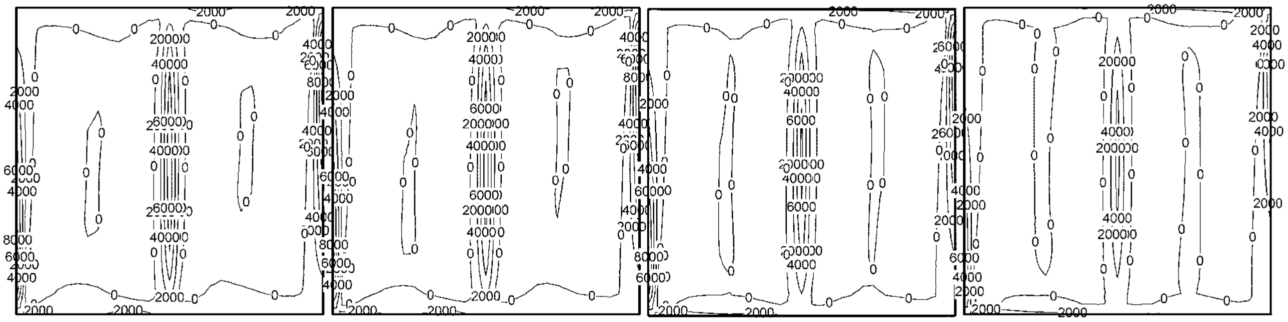

y-directional magnetic field

a) Ha=0 b) Ha=25 c) Ha=50 d) Ha=100

Fig. 7 Vorticity contours for Ra=10^6, Pr=1, and φ=0 deg

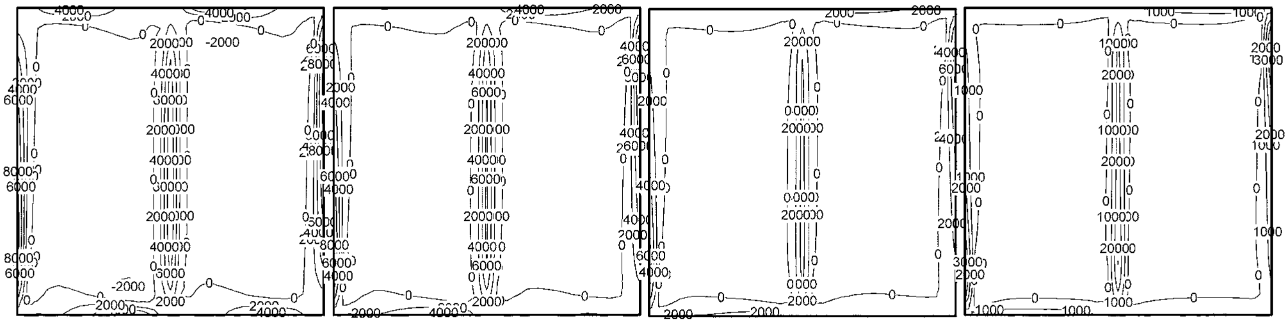

x-directional magnetic field

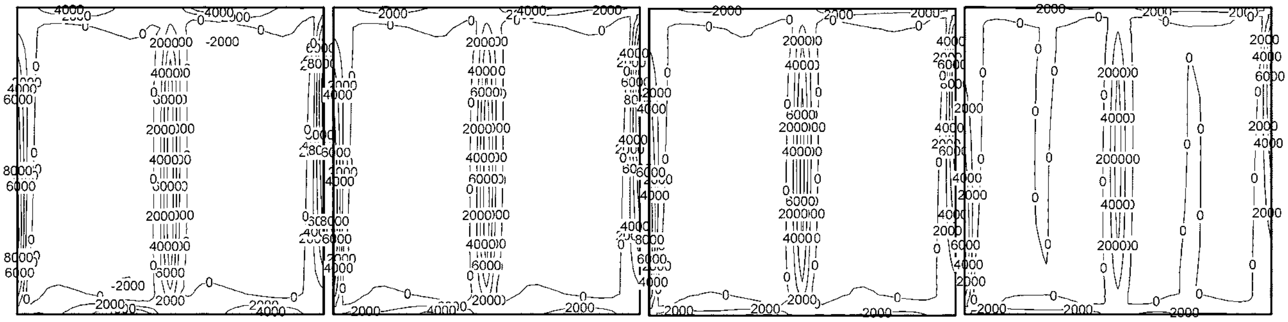

y-directional magnetic field

a) Ha=0 b) Ha=25 c) Ha=50 d) Ha=100

Fig. 8 Vorticity contours for Ra=10^6, Pr=1, and φ=30 deg

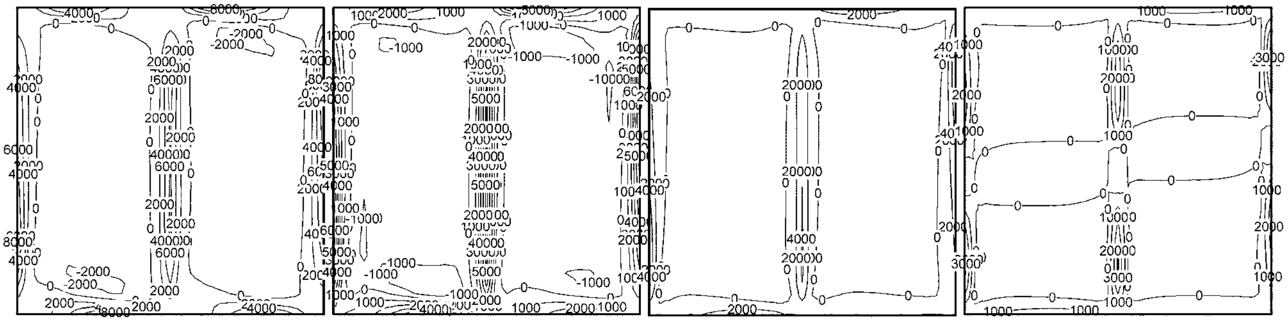

x-directional magnetic field

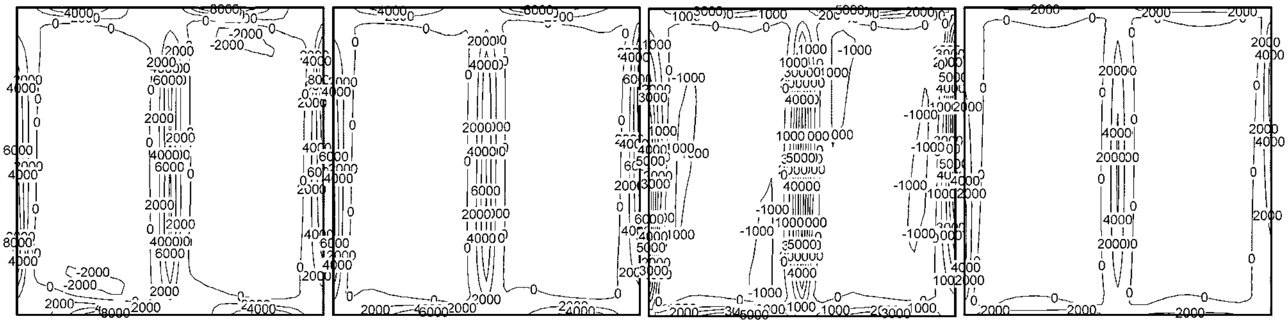

y-directional magnetic field

a) Ha=0 b) Ha=25 c) Ha=50 d) Ha=100

Fig. 9 Vorticity contours for Ra=10^6, Pr=1, and φ=60 deg

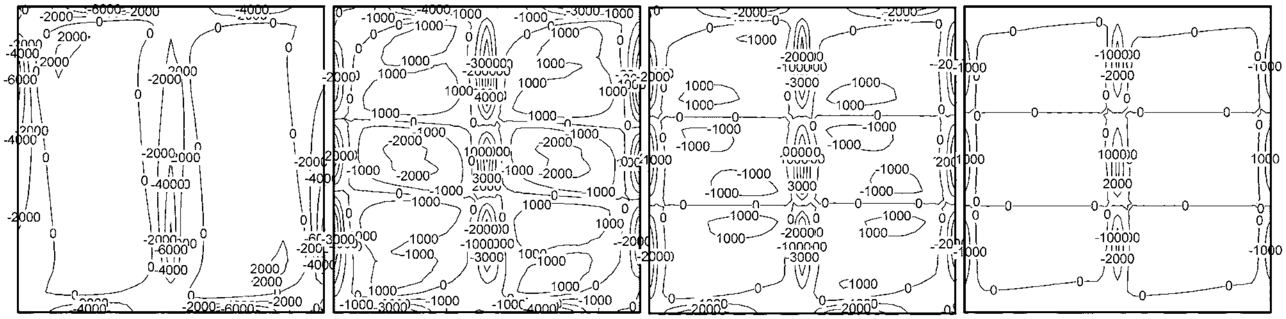

x-directional magnetic field

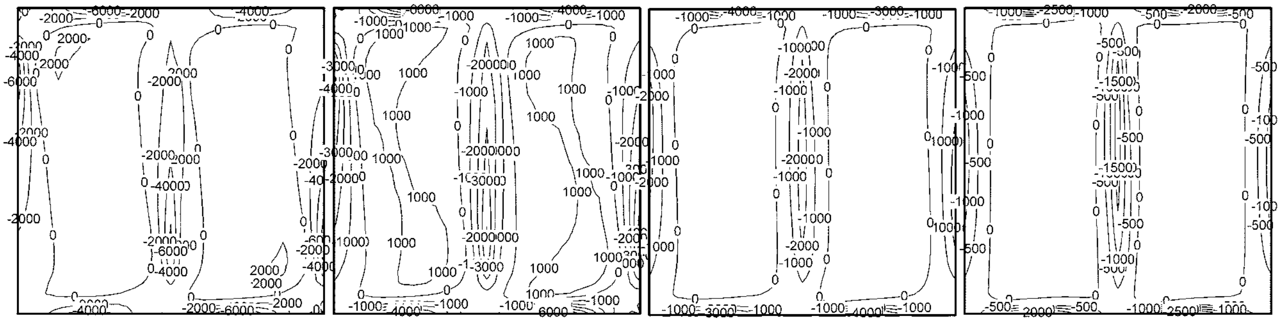

y-directional magnetic field

a) Ha=0 b) Ha=25 c) Ha=50 d) Ha=100

Fig. 10 Vorticity contours for Ra=10^6, Pr=1, and φ=90 deg

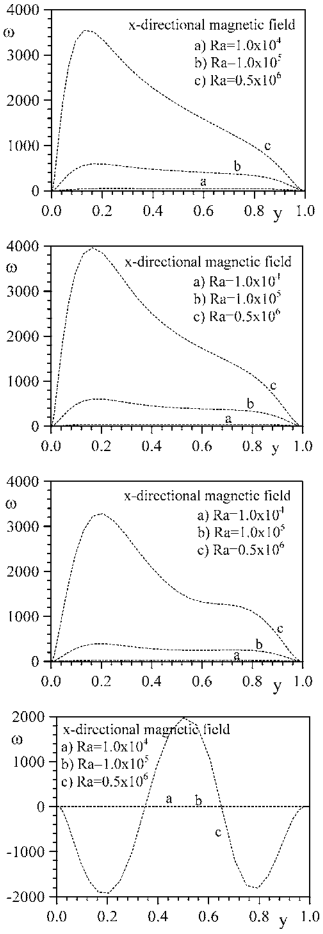

Fig. 11 Variation of the vorticity along the hot wall with the Rayleigh number for Pr=1 and Ha=50

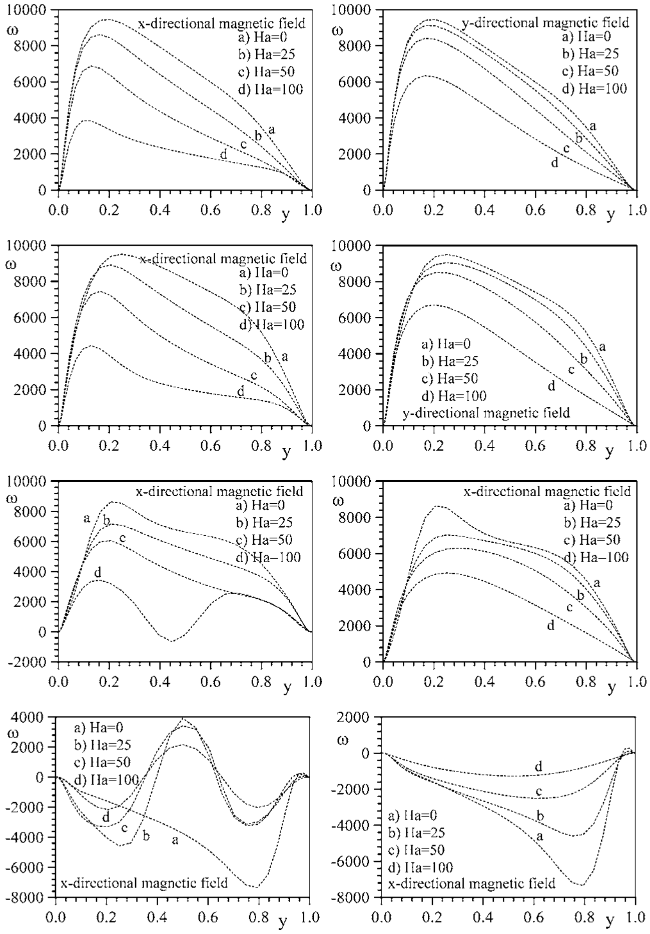

Fig. 12 Variation of the vorticity along the hot wall with the Hartmann number for Pr=1 and Ra=10^6

The effect of the inclination angle on the average Nusselt number is shown in Fig. 18 for various values of the Hartmann number. For the low values of the Rayleigh number, the average Nusselt number decreases with increasing inclination angle. As for the high values of the Rayleigh number, the average heat transfer rate shows an increasing trend with increasing inclination angle, and a peak value is detected. Beyond the peak point, the foregoing trend reverses to decrease with the further increase of inclination angle. The maximum heat transfer takes place at $\varphi=0$ deg for Ra=10^4 and at $\varphi=30$ deg for Ra=10^5 and 10^6. As seen in Fig. 18, the effect of the inclination angle on the average heat transfer rate diminishes as the Hartmann number increases because of its higher retarding effect.

Various correlations for the average Nusselt number are available in the literature for the vertically partitioned enclosures in the absence of a magnetic field. One of them is suggested by Ander-

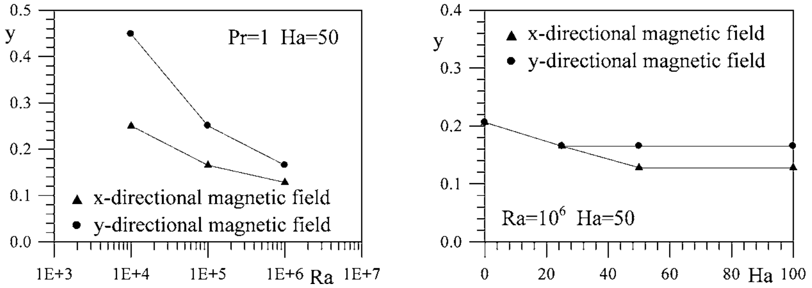

Fig. 13 Variation of location of maximum values of vorticity along the hot wall for $\varphi=0$

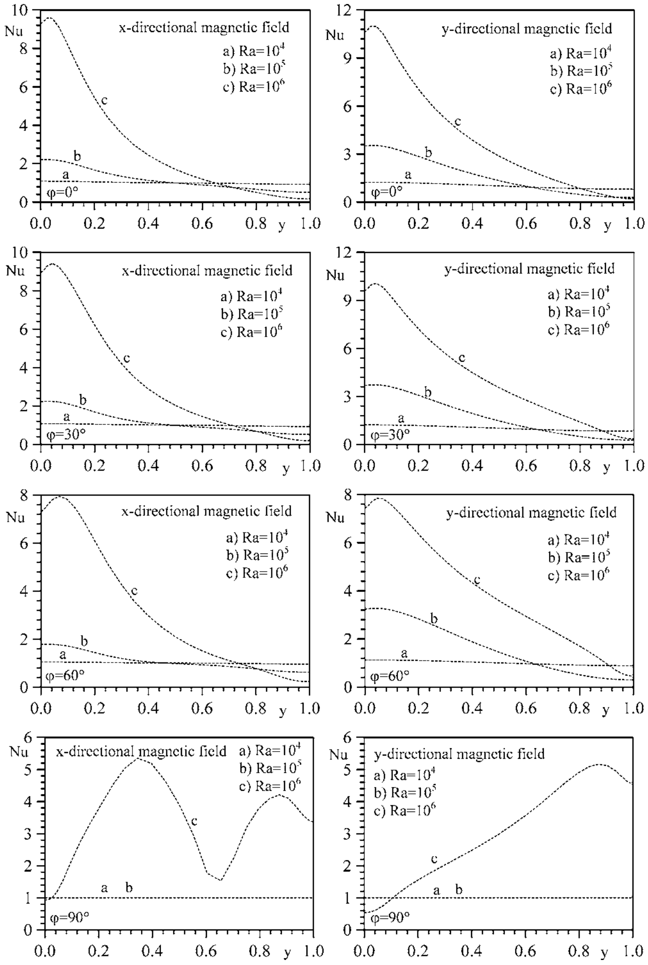

Fig. 14 Variation of the local Nusselt number with the Rayleigh number for Pr=1 and Ha=50

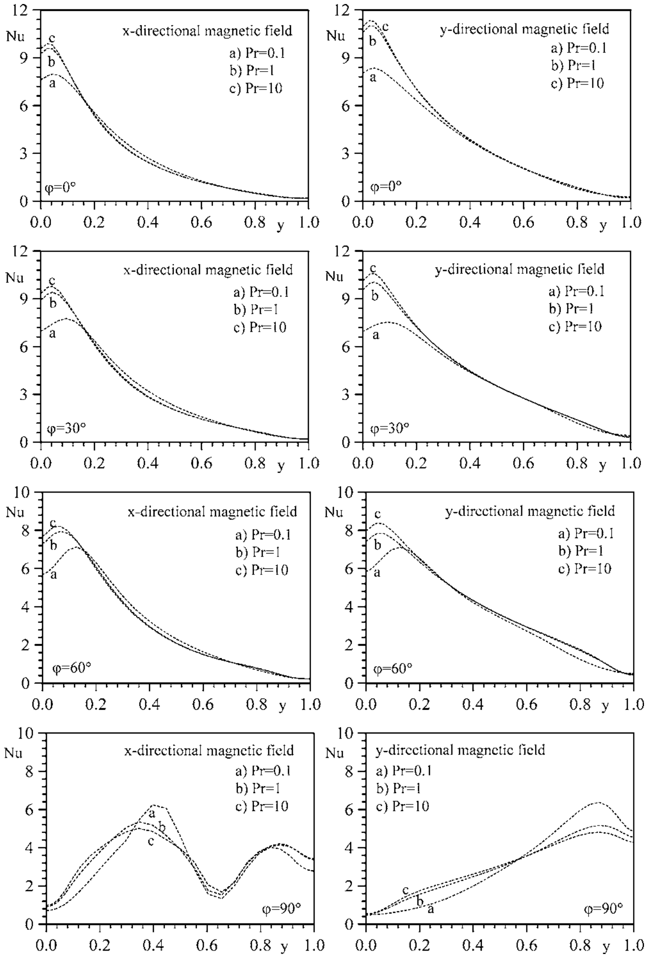

Fig. 15 Variation of the local Nusselt number with the Prandtl number for Ra=10^6 and Ha=50

son and Bejan [19] based on their experimental results as $\mathrm{Nu}_a = 0.201\,\mathrm{Ra}^{0.276}(N+1)^{-1/4}$. Here, N is the partition number. Another correlation is given by Nishimura et al. [20] as $\mathrm{Nu}_a = 0.297\,\mathrm{Ra}^{1/4}(N+1)^{-1}$. The comparison of the values of the average Nusselt number, which belongs to the correlations given above and to this study, is presented in Fig. 19 along with the values of the average Nusselt number for the x-directional magnetic field case. It may be observed from Fig. 19 that the numerical results are in good agreement with those of the correlations.

5 Conclusion

The buoyancy driven MHD flow in an inclined enclosure with a thin partition is investigated numerically by the PDQ method. The results show that the magnetic field suppresses the flow and, therefore, heat transfer considerably, and the x-directional magnetic field is more effective in damping the convective flow when it is compared with the y-directional magnetic field. It is also found that with an increase in the inclination angle, multicellular flows begin to develop inside the enclosure for the x-directional magnetic field case as a result of the breakdown of the single-cellular flows. The vorticity generation intensity increases with an increase of Rayleigh number. On the other hand, increasing Hartmann number has a negative effect on vorticity generation. Vorticity generation intensity is shifted to top left corners and bottom right corners with increasing inclination angle. Vorticity generation loops in each region of enclosure form due to the multicellular flow for the x-directional magnetic field case when the inclination angle is increased further. In addition, depending on the boundary layer developed, the vorticity value on the hot wall increases first sharply with increasing y and then begins to decrease gradually. It is also observed that as the inclination angle increases, the heat transfer increases first with inclination angle and passes through a maximum and then begins to decrease especially for the high values of the Rayleigh number. The maximum heat transfer takes place at $\varphi=0$ deg for Ra=10^4 and at $\varphi=30$ deg for Ra=10^5 and 10^6. The results also show that the flow and heat transfer show little dependence on the Prandtl number.

Nomenclature

a = first-order weighting coefficient
B = magnetic induction, T
b = second-order weighting coefficient
g = gravitational acceleration, m^2/s
H = height of the enclosure, m
Ha = Hartmann number, $\mathrm{Ha}=LB\sqrt{\sigma/\mu}$
i,j = grid point indices
L = width of the enclosure, m
N_x, N_y = grid point numbers in x, y directions
Nu = Nusselt number, $\mathrm{Nu}=-(\partial T/\partial\eta)|_{\eta=0}$
Pr = Prandtl number, $\mathrm{Pr}=\nu/\alpha$
p = dimensionless pressure, $p=L^2(p^*+\rho_o g y^*)/(\rho_o\alpha^2)$
Ra = Rayleigh number, $\mathrm{Ra}=g\beta L^3\Delta T^*/(\nu\alpha)$
T = dimensionless temperature $=(T^*-T_C)/(T_H-T_C)$

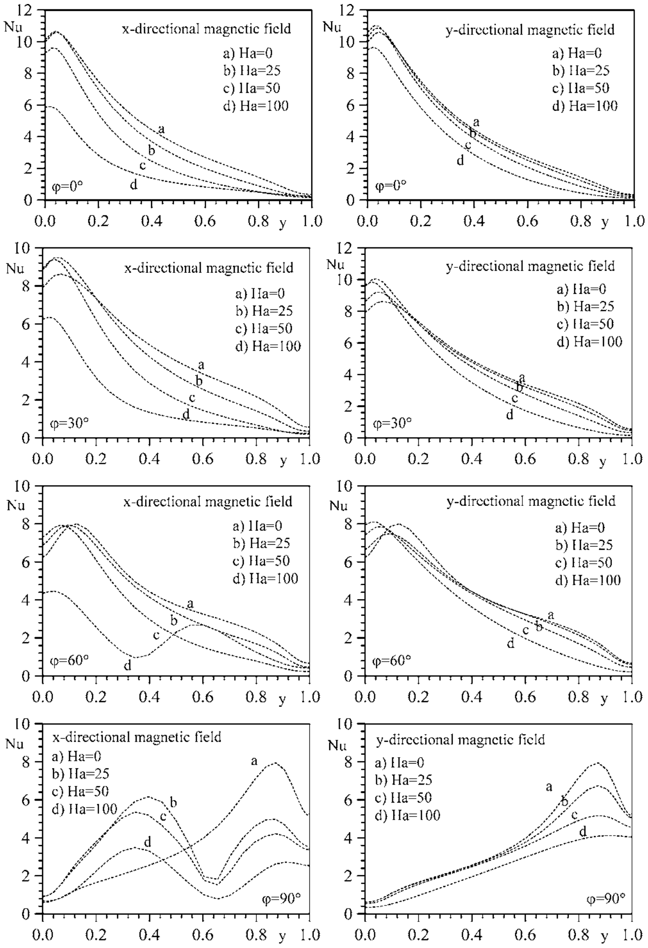

Fig. 16 Variation of the local Nusselt number with the Hartmann number for Ra=10^6 and Pr=1

u,v = dimensionless velocity components in x,y directions
w = width of the partition, m
x,y = dimensionless coordinates=$(x^*,y^*)/L$
α = thermal diffusivity, m^2/s
β = thermal coefficient of volume expansion, 1/K
δ = ratio of magnetic field strengths of x and y directions
Φ = dependent variable
ϕ = inclination angle
υ = kinematic viscosity, m^2/s
η = outward direction normal to the surface
ρ = density, kg/m^3
σ = electrical conductivity, $1/(\Omega\ m)$
ω = dimensionless vorticity=$\omega^* L^2/\alpha$
ψ = dimensionless stream function=ψ^*/α

Subscripts

a = average
C = cold
H = hot
p = partition
x = x direction
y = y direction

Superscripts

$*$ = dimensional quantities
m = current iteration
$\bar{\ }$ = in the y direction

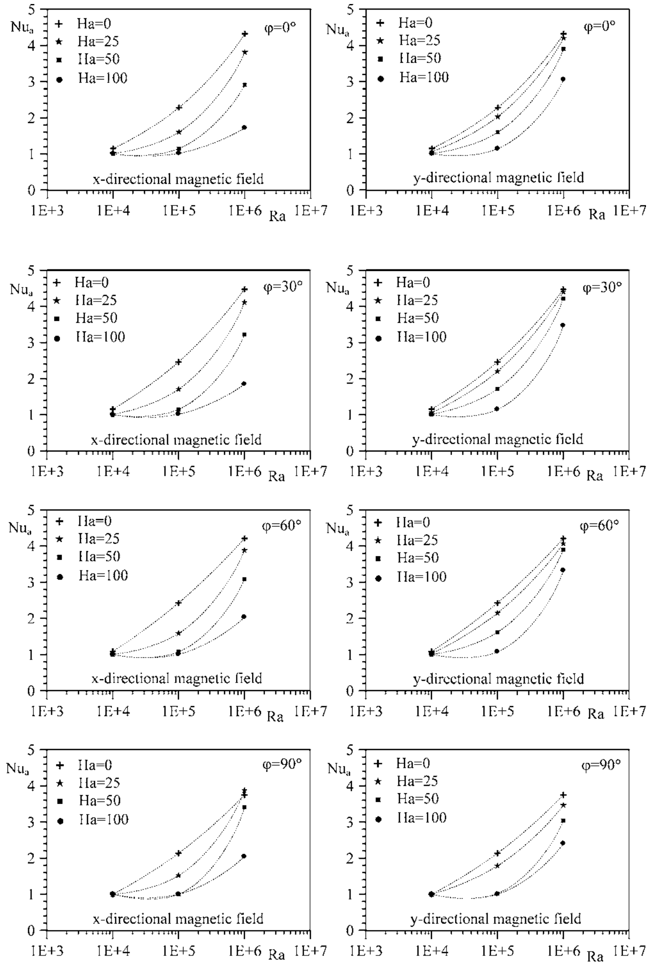

Fig. 17 Variation of the average Nusselt number with the Rayleigh number

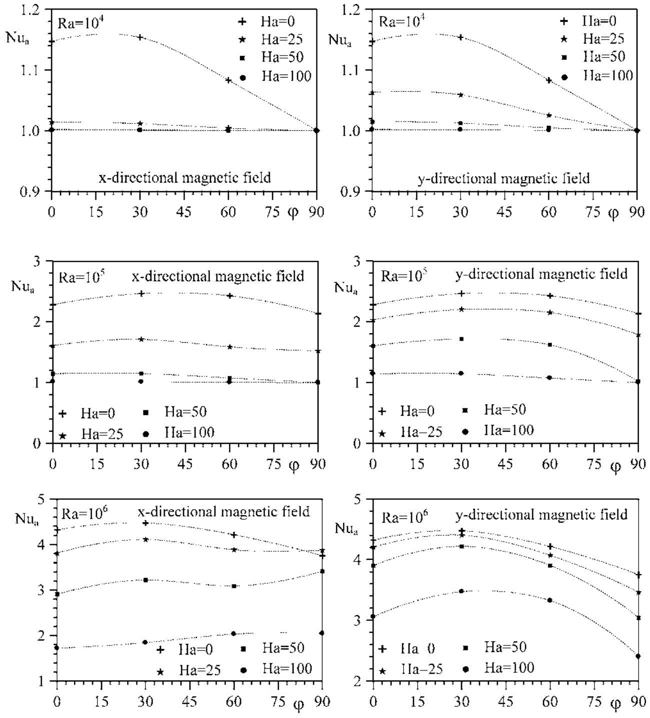

Fig. 18 Variation of the average Nusselt number with the inclination angle

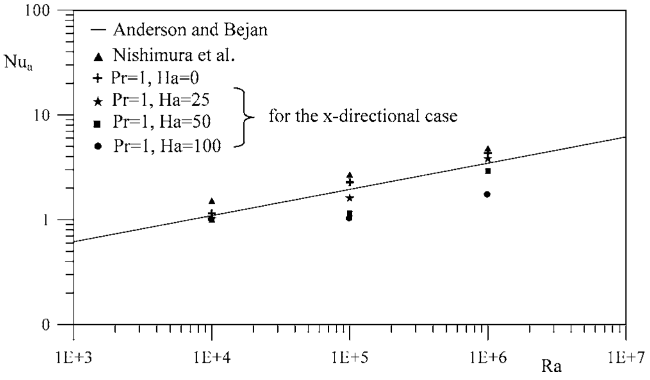

Fig. 19 A comparison for the average Nusselt number

References

[1] Dzodzo, D. M. C., Dzodzo, M. B., and Pavlovic, M. D., 1999, "Laminar Natural Convection in a Fully Partitioned Enclosure Containing Fluid With Nonlinear Thermophysical Properties," Int. J. Heat Fluid Flow, **20**, pp. 614–623.

[2] Tong, T. W., and Gerner, F. M., 1986, "Natural Convection in Partitioned Air-Filled Rectangular Enclosures," Int. Commun. Heat Mass Transfer, **10**, pp. 99–108.

[3] Kahveci, K., 2007, "Numerical Simulation of Natural Convection in a Partitioned Enclosure Using PDQ Method," Int. J. Numer. Methods Heat Fluid Flow, **17**(4), pp. 439–456.

[4] Kahveci, K., 2007, "Natural Convection in a Partitioned Vertical Enclosure Heated With a Uniform Heat Flux," ASME J. Heat Transfer, **129**, pp. 717–726.

[5] Kahveci, K., 2007, "A Differential Quadrature Solution of Natural Convection in an Enclosure With a Finite Thickness Partition," Numer. Heat Transfer, Part A, **51**(10), pp. 979–1002.

[6] Elsherbiny, S. M., Holland, K. G. T., and Raithby, G. T., 1981, "Effect of the Thermal Boundary Condition on Natural Convection in Vertical and Inclined Air Layers," *Proceedings of the 20th ASME-AIChE National Heat Transfer Conference*, Milwaukee, Wisconsin HT 16, pp. 127–133.

[7] Acharya, S., and Tsang, C. H., 1985, "Natural Convection in a Fully Partitioned Inclined Enclosure," Numer. Heat Transfer, **8**, pp. 407–428.

[8] Khan, J. A., and Yao, G.-F., 1993, "Comparison of Natural Convection of Water and Air in a Partitioned Rectangular Enclosure," Int. J. Heat Mass Transfer, **36**, pp. 3107–3117.

[9] Nag, A., Sarkar, A., and Sastri, V. M. K., 1993, "Natural Convection in a Differentially Heated Square Cavity With a Horizontal Partition Plate on the Hot Wall," Comput. Methods Appl. Mech. Eng., **110**, pp. 143–156.

[10] Mezrhab, A., and Bchir, L., 1998, "Radiation-Natural Convection Interactions in Partitioned Cavities," Int. J. Numer. Methods Heat Fluid Flow, **8**, pp. 781–799.

[11] Yucel, N., and Ozdem, A. H., 2003, "Natural Convection in Partially Divided Square Enclosures," Heat Mass Transfer, **40**, pp. 167–175.

[12] Öztuna, S., 2007, "A Differential Quadrature Solution of Natural Convection in an Enclosure With a Partial Partition," Numer. Heat Transfer, Part A, **52**, pp. 1009–1026.

[13] Wang, L. W., Kung, Y. C., Wu, C. Y., Kang, M. F., and Wang, S. L., 2004, "Thermosolutal Convection in an Inclined Rectangular Enclosure With a Partition," J. Mech., **20**, pp. 233–239.

[14] Belman, R. E., Kashef, B. G., and Casti, J., 1972, "Differential Quadrature: A Technique for the Rapid Solution of Nonlinear Partial Differential Equations," J. Comput. Phys., **10**, pp. 40–52.

[15] Shu, C., 1992, "Generalised Differential-Integral Quadrature and Application to the Simulation of Incompressible Viscous Flows Including Parallel Computation," Ph.D. thesis, University of Glasgow.

[16] Shu, C., 2000, *Differential Quadrature and Its Application in Engineering*, Springer-Verlag, New York.

[17] de Vahl Davis, G., 1983, "Natural Convection in a Square Cavity," Int. J. Numer. Methods Fluids, **3**, pp. 249–264.

[18] Ece, M. C., and Büyük, E., 2006, "Natural-Convection Flow Under a Magnetic Field in an Inclined Rectangular Enclosure Heated and Cooled on Adjacent Walls," Fluid Dyn. Res., **38**, pp. 564–590.

[19] Anderson, R., and Bejan, A., 1983, "Heat Transfer Through Single and Double Vertical Walls in Natural Convection: Theory and Experiment," Int. J. Heat Mass Transfer, **24**, pp. 1611–1620.

[20] Nishimura, T., Shiraishi, M., Nagasawa, F., and Kawamura, Y., 1998, "Natural Convection Heat Transfer in Enclosures With Multiple Vertical Partitions," Int. J. Heat Mass Transfer, **31**, pp. 1679–1698.

P. P. Vlachos
Mechanical Engineering Department,
Virginia Tech,
Blacksburg, VA 24061

D. P. Telionis
Engineering Science and Mechanics Department,
Virginia Tech,
Blacksburg, VA 24061

The Effect of Free Surface on the Vortex Shedding From Inclined Circular Cylinders

Spectral analysis of laser Doppler velocimetry measurements and flow visualization are employed to study the wake of inclined cylinders piercing a free surface. The results indicate that the free surface affects vortex shedding almost two to three cylinder diameters below the free surface. Variation of the vortex axis inclination and cells of shedding were visually observed. These effects induce a phase difference in the vortex-shedding mechanism. Streamwise vortical structures are formed along the primary vortex axis. Furthermore, for the case of the highest Froude number, evidence is provided that vortex shedding is suppressed in the region near the free surface. [DOI: 10.1115/1.2829578]

Introduction

Circular-cylinder wakes have attracted many researchers who produced an endless list of publications (see reviews by Williamson [1,2]). This is due partly to the simplicity of setting up an experimental or computational investigation of the problem and to the great practical interest that it presents. The flow involves the interactions of the free stream with the boundary layers, the separated shear layers, and the vortices that form and shed in the wake. Macroscopically, it appears that the flow develops in a two-dimensional fashion, but a closer look reveals subtle three-dimensional patterns, for example, the streamwise vortical instabilities, which ride on the separated shear layers [3,4]. It has been demonstrated by several authors such as Ramberg [5] and many others that dominant three-dimensional effects in the wake of a circular cylinder depend on the end conditions. End disturbances in the spanwise direction could trigger oblique shedding and totally violate the two-dimensional character of the flow [6]. In the present study, we focus on the asymmetry of the end conditions introduced by a cylinder attached to a flat horizontal wall and piercing a free water surface.

Apart from the formation of vortical structures with their axis aligned with the free stream (braids), the three-dimensional character of the flow is manifested in the form of the oblique shedding process. Hammache and Gharib [6] showed how oblique shedding depends on the end conditions. They were able to control the angle of the vortex shedding by employing two transverse circular cylinders upstream from the main cylinder and thus reproduce both types of shedding. However, their work was limited in a range of very small Reynolds numbers ($\mathrm{Re}=40-160$) where the onset of the initial wake instabilities is observed. For higher values of the Reynolds number (>1000), the wake is affected by the shear layer instabilities and by upstream turbulence. In order to understand the three-dimensional character of the flow, the effects of yaw on the vortex-shedding mechanism have been studied extensively. Ramberg [5] investigated such effects for Re ranging from 160 to 1000, and showed that there exists a relation between the vortex shedding frequency and the angle of the shed vortex axes.

The wake of an inclined cylinder is governed by the so called “independence principle,” which states that the Strouhal frequency is linked to the free-stream velocity component normal to the cylinder axis. This principle relates the Strouhal frequency to the Re number by a universal relation, which according to the early work by Roshko [7] is proportional to 1/Re. This relation is valid for all cases, with and without inclination. More recent studies [8] show better agreement of experimental data for a wider range of the Re number, if an expansion in powers of $1/\sqrt{\mathrm{Re}}$ replaces 1/Re. Spanwise changes in the vortex-shedding frequency correspond to different shedding modes and subsequently they result in the inclination of the vortex axis, i.e., oblique vortex shedding.

A great amount of work has been carried to explore the behavior of free-surface vorticity. However, research is needed in order to understand the fundamentals of the interaction of a free surface with bluff-body wakes. Such flows are found in many engineering applications, such as offshore structures, ship wakes, risers, and others. For a cylinder piercing a free surface, the latter represents an end condition more compatible with the two-dimensional character of the flow. This is because on a solid wall, all the vortex lines must bend and align parallel to the wall. In contrast, vortex lines can terminate on a free surface because it represents a stress-free interface that allows a vorticity component normal to it. The process whereby a vortex tube rearranges its geometry so that its vortex lines terminate along the free surface is often called “vortex reconnection.” As an additional consequence, we can assume that a flat (undisturbed) free surface acts as a mirror plane for the vorticity parallel to itself, and thus induces velocities that propel the vortex. If we take into consideration the effect of surface deformation, then we have to account for the generation of secondary vorticity and vorticity flux. All these effects constitute a behavior of vorticity that is not observed in the interaction with solid boundaries. More discussion on these effects can be found in Rood [9–11].

Lang and Gharib [12] investigated the problem but focused on the effect of varying free surface conditions. In their case, the free surface was contaminated by surfactants, and thus it was no longer a stress-free interface. As a result, the vorticity had the tendency to align with the free surface. Vlachos and Telionis [13,14] used time resolved digital particle image velocimetry (DPIV) to investigate the streamwise and spanwise vorticity variations and free-surface turbulence characteristics for a vertical, free-surface piercing cylinder. The results provided indication of vortex suppression near the free surface. However, this work focused only on vertical cylinders and did not consider oblique shedding. Stern et al. [15] studied the interaction of a flat plate piercing a free surface. However, the flat plate was aligned with the free stream, and the main objective was the understanding of the boundary layer development in the neighborhood of the surface. In the present effort, we focus on the character of the vortex-shedding mechanism as it is affected by the presence of the free

---

Contributed by the Fluids Engineering Division of ASME for publication in the JOURNAL OF FLUIDS ENGINEERING. Manuscript received February 8, 2007; final manuscript received July 1, 2007; published online January 24, 2008. Review conducted by James A. Liburdy.

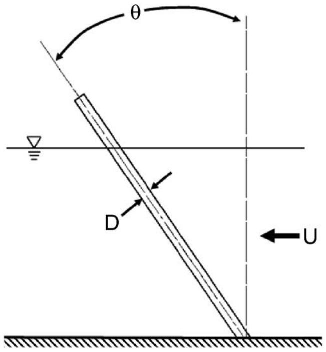

Fig. 1 Inclination of the cylinder with respect to the free-stream velocity. This is a side view of the experimental setup. The flow is depicted from right to left, to be consistent with the flow visualizations.

surface. Oblique and parallel vortex-shedding mechanisms are investigated qualitatively and quantitatively, using flow visualizations and laser doppler velocimetry (LDV).

Experimental Setup

Experiments were conducted in the free-surface water tunnel facility of the Engineering Science and Mechanics Department at Virginia Tech. This tunnel has a 610×610 mm^2 test section. For the free-stream velocities under consideration in the presence of free surface, the mean turbulence intensity was on the order of 1%. A circular cylinder with a diameter of 15.87 mm was mounted on the floor of the tunnel, piercing the free surface. The aspect ratio of the cylinder, namely, the ratio of the depth to the diameter was $L/D=20$. Three cylinder inclinations and three Froude numbers were considered: $a=0$ deg, 30 deg, and −30 deg, as shown in Fig. 1, and Froude numbers Fr=0.3, 0.65, and 1.06. Here, we define the Froude number as $\mathrm{Fr}=U/(gD)^{1/2}$, where U is the free-stream velocity and D the diameter of the cylinder. In Fig. 1, the free stream is shown in the unconventional direction of right to left to match with the flow visualizations. In our experimental setup, it is not easy to change the Froude number while keeping the Reynolds number fixed. For the values of the Froude numbers chosen, the Reynolds number based on the diameter of the cylinder varied between $\mathrm{Re}_D=1700$ and 6000. It is well known that in this range of Reynolds numbers, its effect on the flow characteristics is negligible. The boundary layer is laminar; separation location and the vortex-shedding process are practically unaffected. We have confirmed earlier in our experimental facilities that the shedding frequency and shedding patterns do not depend on the Reynolds number for $\mathrm{Re}_D=1000-20{,}000$, if both ends of the cylinder are mounted on the tunnel walls. The phenomena studied here are therefore dominated by the inclination of the cylinder and the free-surface effects that are characterized by the Froude number.

Flow Visualizations

Flow visualizations using hydrogen bubbles released from a wire placed across the cylinder span and in a plane parallel to the primary vortex-shedding axes were performed in order to expose the vortex-shedding structure and inclination. In addition, particle flow visualizations were used to observe the flow structure in planes parallel to the free surface. For either of these visualizations, a Cu-vapor pulsing laser was employed as a light source with a mean output power of 36 W, energy per pulse of 5.5 mJ, emitting a green-yellow (516 nm and 572 nm wavelength) beam. Especially coated optics were used to form a 1–2-mm-thick laser sheet, and deliver it in the test section. Planes of laser sheets were directed either normal to the vertical direction or parallel to the axis of the model and in the direction of the stream. A gray-scale charge-coupled device (CCD) camera, acquiring up to 1000 fps with a resolution of 256×256 pixels and 8 bit dynamic range (256 shades of gray), was used to acquire the images. The camera was synchronized with the laser at frequencies from 30 Hz to 50 Hz. For all cases, 10 s of data were digitally recorded.

Hydrogen-Bubble Flow Visualizations. Hydrogen bubbles are excellent tracers for monitoring instantaneous characteristics of the flow field, since their relative time scale is usually less than 10^{-4} s. A detailed discussion of the properties, behavior, and applications of hydrogen bubbles in flow visualizations can be found in Lian and Su [16]. Lu and Smith [17,18] employed hydrogen bubbles to investigate the bursting characteristics of a turbulent boundary layer, while Utami and Ueno [19] used them to investigate characteristics of a turbulent open channel flow. Techet et al. [20] employed hydrogen bubbles in a way similar to the present study, namely, to visualize the vortex-shedding characteristics in the wake cylinder. However, in their experiments, the bubbles were generated using the lead precipitation method, while in the present study we employed electrolysis.

One issue that needs to be considered is the rising terminal velocity of the bubble. This can be calculated from the balance of the drag forces and the buoyancy forces. The terminal velocity U of a rising bubble is given by

$$U = gd^2(\rho - \rho_h)/12\mu \tag{1}$$

where g is the acceleration of gravity, d is the diameter of the bubble, ρ is the liquid density, ρ_h is the gas density, and μ is the fluid viscosity For a bubble diameter of 0.01 mm, the terminal velocity is in the order of 8×10^{-5} m/s, which is extremely small compared to the velocities under consideration in the present study. The bubble velocity deficit because of the wake of the wire is not a factor in this case either, since the objective is to qualitatively determine the time variation of the vortex inclination and not to perform accurate velocity measurements.

In this study, the hydrogen bubbles were generated using the method of electrolysis. A platinum wire of about 20 μm in diameter was stretched along the span of the cylinder, approximately one diameter away from the center, namely, at $x=0$, $y=12$ mm, as shown in Fig. 2. Placing the wire not too close to the cylinder allows the bubbles to follow the roll-up of the shear layer, without getting trapped in the dead water region. The distinct patterns of the vortex shedding are thus revealed. Moreover, any streamer vortices, i.e., vortices with their axis in the direction of the stream (braids), that ride on shear layers can be more easily identified. The plane of the laser sheet was parallel to the free stream and was passed through the axis of the cylinder (Fig. 2). The field of view was adjusted to fit the full depth of the test section, resulting to a 1.3×1.3 mm^2 pixel size.

Particle Flow Visualizations. Neutrally buoyant 30 μm hollow glass spheres were used as flow tracers. Because of their diameter and specific gravity, any lag of the particle velocity to respond to flow accelerations is negligible. The plane of the laser sheet was positioned parallel to the free surface, i.e., along an x-y plane, one diameter below the free surface. Attempts to acquire images closer to the free surface were unsuccessful because of the light reflections from the free surface, which saturated the images. These reflections are visible even one diameter below the surface, especially for the case of the highest Fr numbers. The camera was placed underneath the test section, and its field of view was adjusted to 3.65 cylinder diameters, as shown in Fig. 2.

Laser Doppler Velocimetry Measurements

In order to investigate the effect of the cylinder inclination and the free surface on vortex shedding, a TSI fiber-optic LDV system was employed to acquire velocity time series at different locations along the spanwise direction of the cylinder. The flow was seeded

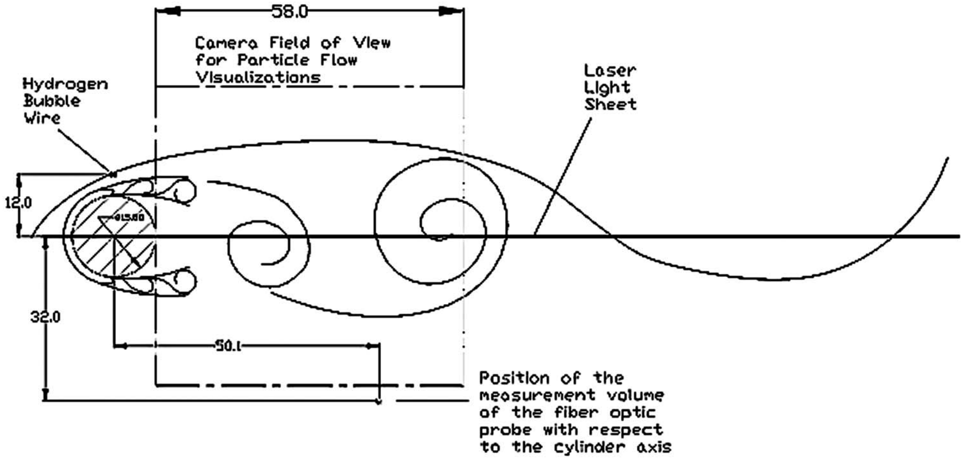

Fig. 2 Schematic representation of the position of the hydrogen-bubble wire and the fiber-optic LDV probe with respect to the cylinder axis. This sketch represents a cut normal to the *z* axis of Fig. 1, i.e., a top view of the experimental setup. Here, the flow is from left to right. (All dimensions are in mm)

with 1 μm diameter, neutrally buoyant polystyrene particles. The data rate of the LDV signal was carefully kept above 1000 Hz, and a "sample-and-hold" approach was used for the reconstruction of the signal. Since the main frequencies under consideration do not exceed 15 Hz, the "random arrival" problem of the LDV measurements is not an issue. The sampling frequency of the data acquisition system was set at 128 Hz. Analog-to-digital conversion was carried with a 12 bit ± 10 V D/A board, resulting in an accuracy of ± 48 mV. Only the x component (streamwise) of the velocity was acquired; therefore, there was no need to run the measurements in coincidence mode. Traversing of the LDV probe allowed measurements from $0.5D$, with D the cylinder diameter, above the bottom, to $0.5D$ diameters below the free surface, covering 19 diameters. Based on the positioning accuracy of the traversing scales and the implemented feedback using linear variable displacement transducers (LVDTs), the overall accuracy of the traversing system is estimated in the order of ± 20 μm. For the cases of the inclined cylinders, the axis of translation of the LDV measuring volume was carefully kept parallel to the axis of the cylinder. For all cases, the LDV measurement volume was placed 3.15 diameters downstream and 1.25 diameters away from the center of the cylinder, namely, at $x=3.15D$, $y=1.25D$. (Fig. 2). Finally, a Hewlett Packard signal analyzer was also used for real time monitoring of the velocity signals and the calculation of power spectra.

Results and Discussion

Hydrogen-Bubbles Flow Visualization. Results from the hydrogen-bubble flow visualizations are presented first. Representative instants of the flow field demonstrate the general characteristics of the vortex-shedding process. The corresponding instances of the flow field depicted were chosen approximately within one shedding cycle to illustrate representative patterns of the evolving flow field. However, these present a limited view of the phenomena under consideration. A more complete understanding can be achieved only by animating the entire sequence of these visualizations.

Each column of frames in Figs. 3–5 presents instantaneous visualizations for the same parameters. The first column in each of these figures presents data for $\mathrm{Fr}=0.3$, the second for $\mathrm{Fr}=0.65$ and the third for $\mathrm{Fr}=1.06$. The results in Figs. 3–5 correspond to inclinations of $a=0$ deg, 30 deg and -30 deg, respectively. In all these figures, we have captured the trace of the vortex axis, as it intersects the laser sheet. In all the frames of Fig. 3, there is no distinct trace of a vortex axis near the floor of the tunnel. This is attributed to the effect of the horseshoe vortex. As we move up in the spanwise direction, the vortex axis is inclined with respect to the axis of the cylinder, indicating a component of vorticity parallel to the free stream. However, after the 50% of the span, the inclination of shedding changes, the vortex axis becomes almost parallel to the cylinder, and the vortex finally reconnects normally to the free surface. In the second frame of this column, i.e., Fig. 3(*b*), the vortex axis is almost uniformly parallel to the cylinder axis and a much smaller effect of the horseshoe vortex is observed. In the third frame (Fig. 3(*c*)), the vortex clearly reconnects normal to the free surface; however, oblique shedding is now encountered a few diameters below the free surface. Animation of the complete sequence shows the unsteady character of the flow. Alternations of the inclination occur inconsistently and with no repeatable pattern. Furthermore, the existence of "braid" vortices is observed throughout the span of the cylinder but with no obvious periodicity. Braids are clearly obvious in the animation in the form of local rotation about axes aligned with the stream. In the still frames presented in this paper, braids appear as discontinuities of the trace of bubbles.

In the second case of zero inclination, for $\mathrm{Fr}=0.65$, presented in the second column of instantaneous frames in Fig. 3, the behavior is changing. In all three frames, Figs. 3(*d*)–3(*f*), the inclination of the shedding is consistently oblique, emphasizing the three-dimensional character of the flow. This becomes more evident by carefully observing the animation of the whole sequence. Braid vortices are also present along the span of the cylinder. What is very interesting is the fact that there exists a phase difference in the vortex-shedding processes as a function of the spanwise distance. This can be seen clearly in all three frames of Fig. 3, where strong discontinuities of the trace of the vortex are present in the midspan region. Because the vortex reconnects normal to the free surface, the change of the slope of the inclination is sharper in the vicinity of the free surface if compared to the lower Froude number case.

Data for zero inclination and $\mathrm{Fr}=1.06$ are presented in the third column of Fig. 3. The inclination of the vortex is alternating between different instants, with abrupt changes in the slope, showing discontinuities or a wavy pattern. This can be indicative of a variation in the development of the shear layer instabilities with respect to the span, leading to vortex dislocations. An interesting feature is the formation of a surface depression, which is not affected by vortex shedding, and is thus invariant in time. This is due to the low base pressure in the near wake region, which results in free-surface deformation. The formation of the surface

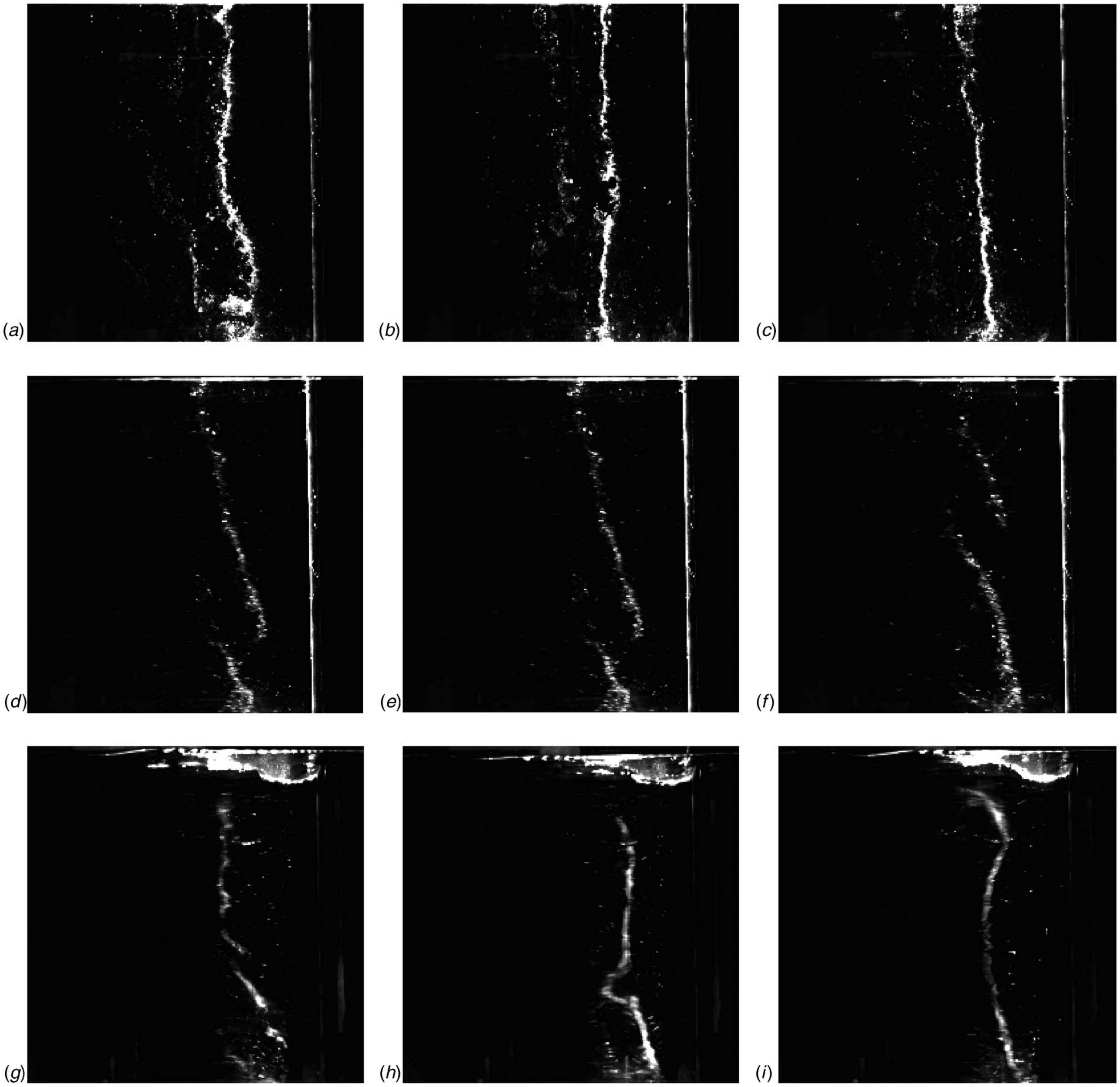

Fig. 3 Hydrogen bubbles. (*a*) Inclination *a*=0 deg, Fr=0.3; (*b*) inclination *a*=0 deg, Fr=0.3; (*c*) inclination *a*=0 deg, Fr=0.3; (*d*) inclination *a*=0 deg, Fr=0.65; (*e*) inclination *a*=0 deg, Fr=0.65; (*f*) inclination *a*=0 deg, Fr=0.65; (*g*) inclination *a*=0 deg, Fr =1.06; (*h*) inclination *a*=0 deg, Fr=1.06; and (*i*) inclination *a*=0 deg, Fr=1.06.

depression behaves as an obstacle, which accelerates the flow around it. As a result, there is no distinct trace of the vortex core in the region near the free surface, indicating suppression of the vortex shedding or extension of the vortex formation length further downstream. Because of the high free-stream velocity, the time scale of the life of the bubbles is reduced, making their observation harder.

A visual comparison of the three cases shows that the intensity of the oblique shedding is increasing as the Fr number increases. The boundary conditions imposed by the solid wall (no slip) and the free surface (free slip) dictate the character of the shedding in their neighborhood. The asymmetry introduced from the different character of the boundary conditions at the two ends enhances the three-dimensional effects.

The observations for the 0 deg cylinder inclination are mostly valid for the inclined cylinder flows as well. Thus, we are going to focus the remaining discussion only on additional features and major differences.

The frames displayed in Fig. 4 correspond to the inclination of 30 deg. For the first case of Fr=0.3, vortex shedding occurs almost parallel to the cylinder axis for the major part of the cylinder length, as shown in the frames of Fig. 4. However, since the cylinder is inclined and the vortex needs to reconnect normal to the free surface, the slope is forced to change, as the vortex aligns with the normal to the free-surface direction (Fig. 4(*c*)). Comparison with the frames of Fig. 3 shows that the effect of the horseshoe vortex now extends higher above the floor of the tunnel, affecting vortex shedding almost up to 25% of the cylinder length from the base of the cylinder. For the case of Fr=0.65 (Fig. 4), the existence of a wavy pattern of the vortex axis is initially observed. For the case of Fr=1.06, the size of the surface depression in the wake is smaller than the depression observed for 0 deg inclination, allowing the vortex to reconnect to the free surface. Further-

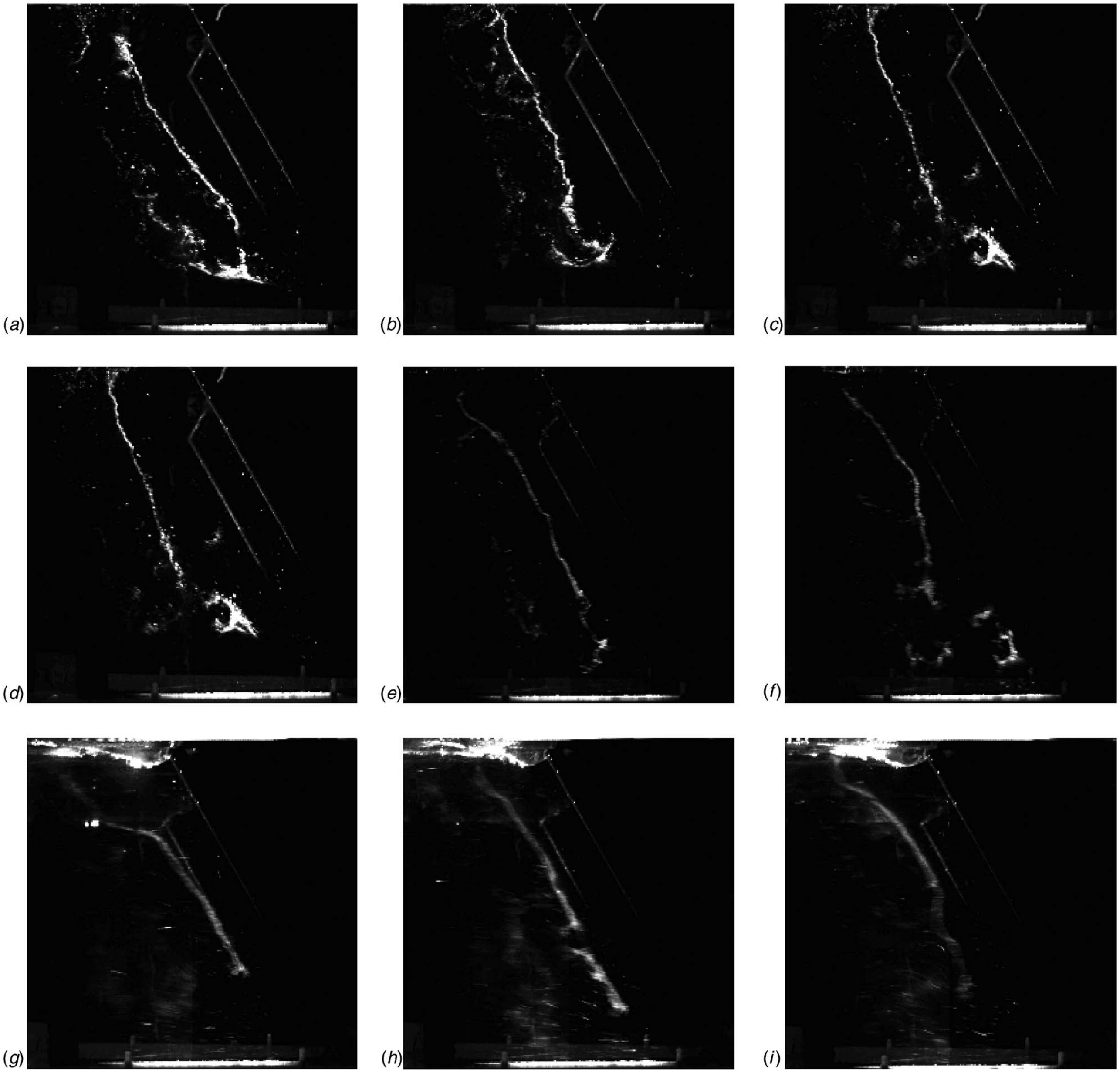

Fig. 4 Hydrogen bubbles. (*a*) Inclination $a=30$ deg, Fr=0.3; (*b*) inclination $a=30$ deg, Fr=0.3; (*c*) inclination $a=30$ deg, Fr=0.3; (*d*) inclination $a=30$ deg, Fr=0.65; (*e*) inclination $a=30$ deg, Fr=0.65; (*f*) inclination $a=30$ deg, Fr=0.65; (*g*) inclination $a=30$ deg, Fr=1.06; (*h*) inclination $a=30$ deg, Fr=1.06; (*i*) inclination $a=30$ deg, Fr=1.06.

more, the discontinuities in vortex shedding observed in the previous inclination case are significantly reduced. We observe that for all cases of this inclination, the effect of the horseshoe vortex extends further away from the cylinder end. The opposite is true for the effects of the free surface.

The results for the case of $a=-30$ deg are presented in Fig. 5. The effect of the boundary conditions is reversed with respect to the previous case, and this can be observed for all the Froude numbers. The region near the base of the cylinder affected by the horseshoe vortex core is confined to only about one diameter from the floor of the tunnel. On the opposite end, the reconnection process affects the change of the slope significantly, in some instants extending down to 50% of the span of the cylinder. For Fr=0.3 (Fig. 5), where the intensity of the trace of the vortex core is stronger in comparison with the higher Fr number cases, a change in the phase of the vortex shedding can be clearly observed. The intermediate case of Fr=0.65 shows that there is reconnection normal to the free surface; however, phase differences are intensified as shown in frames of the second column. The increase of the Froude number to Fr=1.06 shows the formation of a stronger surface depression in the wake. Indeed, in Fig. 5, it appears that the reconnection is suppressed by the surface depression, since there is no distinct trace of the vortex in the vicinity of the free surface.

Summarizing the observations for three Fr numbers and three inclinations, we see that the increase of the Froude number results in suppression of the vortex shedding, which is significantly stronger as we change the inclination from +30 to 0 to −30. The existence of braid vortices and cells of shedding causing phase differences is noted for all cases. Finally, the primary spanwise vortex in all cases reconnects normal to the free surface with the exception of the cases where a strong free-surface depression suppresses vortex shedding, or the process of reconnection itself. These observations are not adequately documented from the indi-

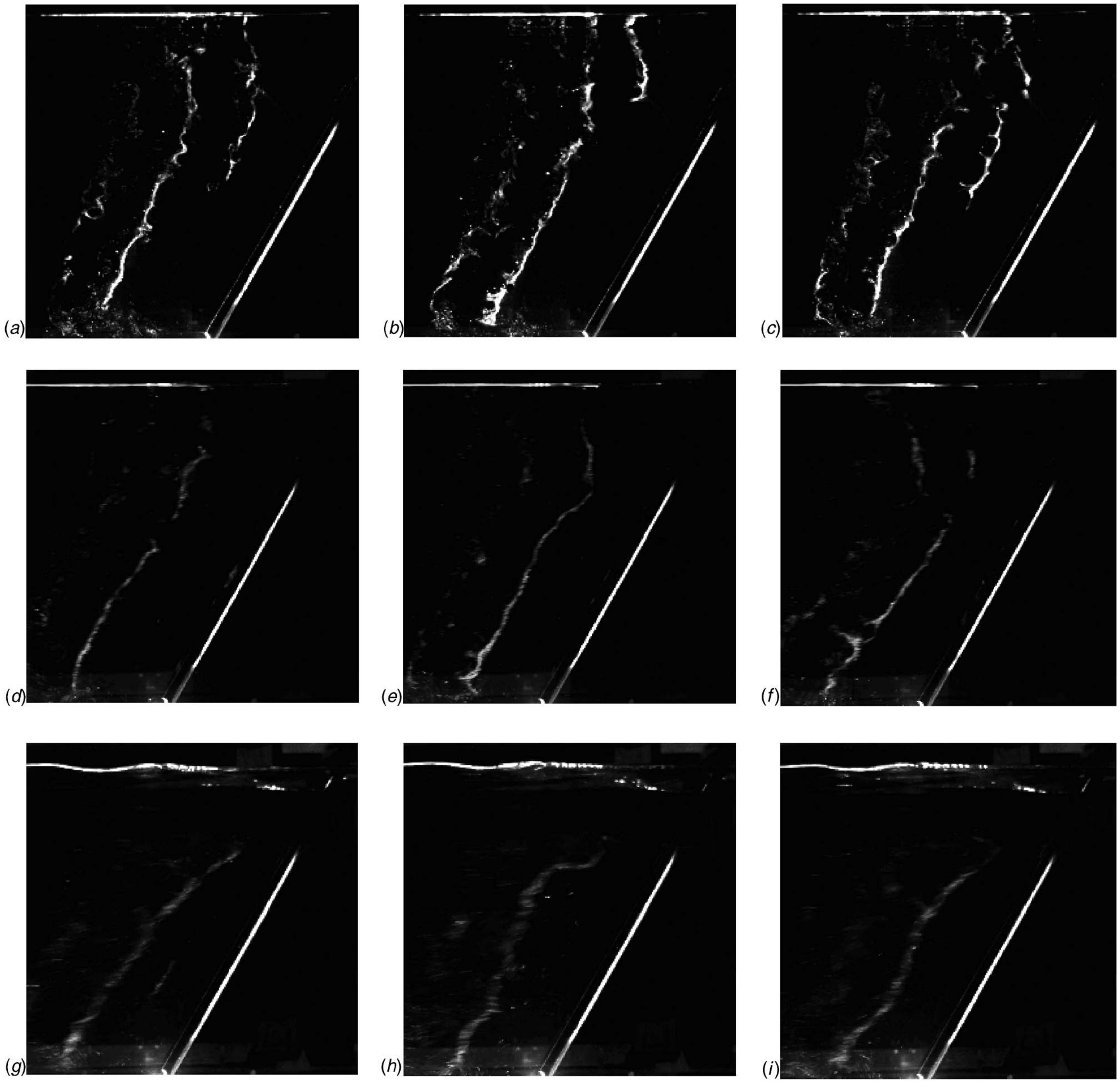

Fig. 5 Hydrogen bubbles. (*a*) Inclination $a=-30$ deg, Fr=0.3; (*b*) inclination $a=-30$ deg, Fr=0.3; (*c*) inclination $a=-30$ deg, Fr=0.3; (*d*) inclination $a=-30$ deg, Fr=0.65; (*e*) inclination $a=-30$ deg, Fr=0.65; (*f*) inclination $a=-30$ deg, Fr=0.65; (*g*) inclination $a=-30$ deg, Fr=1.06; (*h*) inclination $a=-30$ deg, Fr=1.06; and (*i*) inclination $a=-30$ deg, Fr=1.06.

vidual snapshots of the flow field presented here. Complete understanding can only be achieved by observing animations of each sequence.

Particle Flow Visualizations. Particle flow visualizations were performed for all cases of Froude number and inclination. The results presented in Fig. 6 were obtained along a plane parallel to the free surface and one diameter beneath it. The location of the vortex formation length can be determined. Instantaneous snapshots of the flow field do not provide adequate information to quantify the vortex formation length. However, comparison of different cases indicates some distinct differences.

Each row of frames in Fig. 6 corresponds to a different cylinder inclination but the three columns of frames correspond again to the three values of the Froude numbers tested. The first frame, Fig. 6(*a*), for zero inclination indicates a clear vortex-shedding pattern and an approximate vortex formation length of about 2.4 diameters downstream. This is also true for Fr=0.65 (Fig. 6(*d*)). However, for the last case of zero degrees of inclination, Fr =1.06 (Fig. 6(*g*)), there is no evidence of vortex shedding, indicating that the process is suppressed, even one diameter below the free surface. Steady wave patterns are generated in the wake near the free surface, forming a Kelvin wedge [21] with an angle that varies from 45 to 55 deg (Fig. 6).

For the case of 30 deg inclination, we note the opposite behavior. For Fr=0.3, the vortex formation extends to about three diameters, forming a larger near wake region, i.e., a region that contains very low velocities (Fig. 6(*b*)). The increase of the Froude number to 0.65 changes again the position of the formation to about 2.5 diameters (Fig. 6(*e*)), which is a significant change for such a moderate increase in the Froude number, and therefore it can be only attributed to the effect of the free surface, which is most significant in this case as it was shown by the

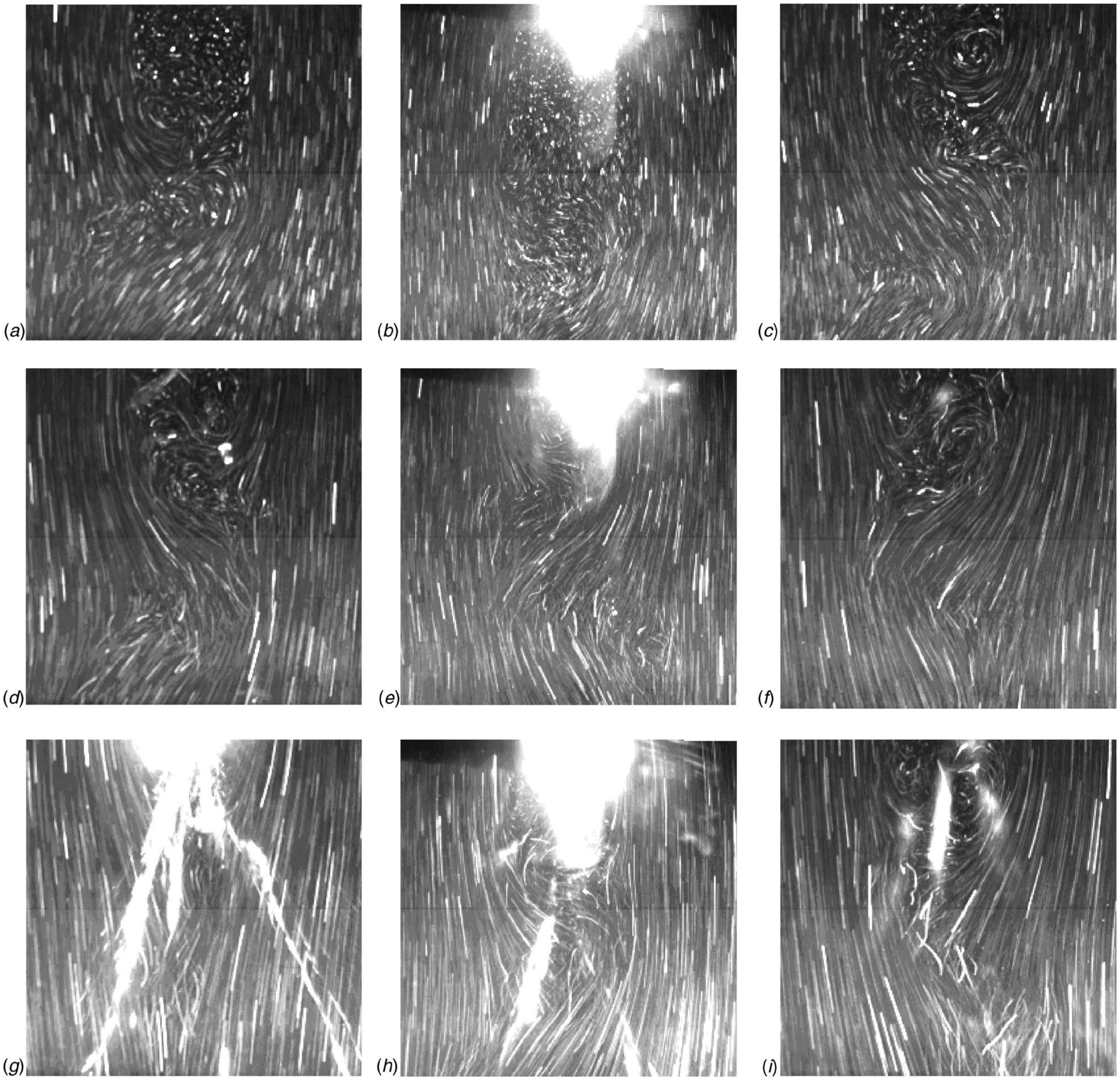

Fig. 6 Particle visualization. (*a*) *a*=0 deg, Fr=0.3; (*b*) *a*=30 deg, Fr=0.3; (*c*) *a*=−30 deg, Fr=0.3; (*d*) *a*=0 deg, Fr=0.65; (*e*) *a* =30 deg, Fr=0.65; (*f*) *a*=−30 deg, Fr=0.65; (*g*) *a*=0 deg, Fr=1.06; (*h*) *a*=30 deg, Fr=1.06; and (*i*) *a*=−30 deg, Fr=1.06

hydrogen-bubble visualizations. For the last case of Fr=1.06, the vortex formation location is approximately the same, but there is no visible wave pattern. This is because the Kelvin wedge angle increased, so it was outside of the field of view. The reflection from the free-surface depression is noticeable for all Fr numbers, which shows again that the size of the surface depression increases for the +30 inclination.

Finally, for the case of −30 deg inclination, the vortex formation position has shifted upstream to approximately one diameter for Fr=0.3 (Fig. 6(*c*)), and 1.5 for Fr=0.65 (Fig. 6(*f*)). A major difference between the 0 deg inclination and this case is observed for Fr=1.06, where for the present case we can see a vortex-shedding pattern and an approximate vortex formation point at 1.5 diameters downstream (Fig. 6(*i*)). There is also a steady wave pattern reflected from the free surface with an approximate wedge angle of about 40–45 deg.

The particle flow visualizations show that the inclination affects the vortex formation length. The influence of the free surface is noticeable for the higher Fr numbers only. In the case of 0 deg inclination and Fr=1.06, vortex shedding is entirely suppressed at the depth of one diameter, in agreement with the evidence provided by bubble visualization. However, both positive and negative inclinations counteract the effect of the free surface and allow the vortex to be formed.

Laser Doppler Velocimetry Frequency Measurements

LDV measurements were performed in order to quantify the variation of the vortex-shedding frequency with respect to the elevation for different inclinations. In Fig. 7, the power spectrum estimates are displayed in the form of contours of the reduced frequency (Strouhal number, $\mathrm{St}=fD/U$) and the elevation of each successive measurement plane (elevation). As in Fig. 6, the three columns of frames correspond to the three Froude numbers tested and the three rows correspond to the three inclinations. The logarithm of the power for a range of two decades is presented in color

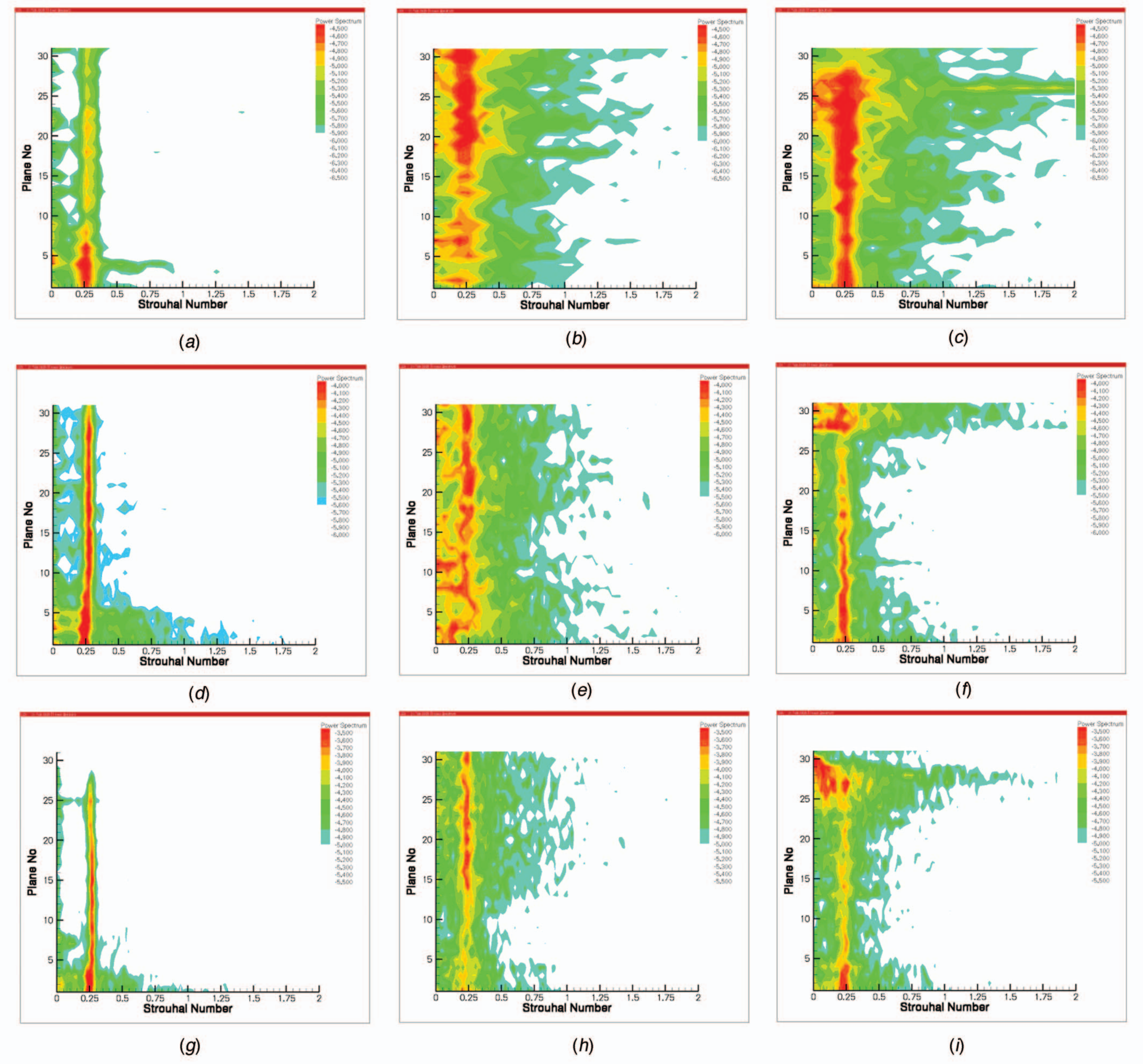

(*a*) (*b*) (*c*)

(*d*) (*e*) (*f*)

(*g*) (*h*) (*i*)

Fig. 7 Power spectra contours as a function of the elevation. (*a*) Inclination $a=0$ deg, Fr=0.3; (*b*) inclination $a=30$ deg, Fr =0.3; (*c*) inclination $a=-30$ deg, Fr=03; (*d*) inclination $a=0$ deg, Fr=0.65; (*e*) inclination $a=30$ deg, Fr=0.65; (*f*) inclination $a=-30$ deg, Fr=0.65; (*g*) inclination $a=0$ deg, Fr=1.06; (*h*) inclination $a=30$ deg, Fr=Fr=1.06; and (*i*) inclination $a=-30$ deg, Re =Fr=1.06.

contours, with the very small values that are attributed to noise being removed. This is essentially a measure of the amplitude of the oscillation. For the power spectrum estimation, the Welch periodgram was employed with the Bartlett windowing function, 75% overlapping, and step frequency of 0.5 Hz.

In Fig. 7(*a*), the power spectra for the case of $a=0$ deg inclination and Fr=0.3 are presented. A very distinct dominant frequency at approximately St=0.25 is present. However, the amplitude is reduced as the elevation increases, suggesting that the end effects influence the strength of the vortices shed but not the frequency. In the region of the horseshoe vortex, a relatively broad band of frequencies, extending almost five diameters above the tunnel floor, is present. The region between 5 and 15 diameters above the floor is less affected from the asymmetry of the boundary conditions, showing distinct peak values of the vortex-shedding frequency, but also significant modes at lower frequencies (St =0.05). The increase of the Fr number to 0.65 (Fig. 5(*d*)) demonstrates similar trends. The most dominant mode is again in the neighborhood of St=0.25. The effect of the horseshoe, vortex is more dominant and a wide range of frequencies is covering that region, extending up to approximately five to six diameters from the floor. The energy content has increased by half a decade, and as we approach the free surface, the Strouhal number shifts to 0.27. Within three diameters beneath the free surface, the energy decreases, suggesting weakening of the vortex-shedding process. For Fr=1.06, a very clear shedding frequency at St=0.27 exists throughout the span, but in the region of five diameters below the free surface the shedding frequency vanishes, showing further evidence of the vortex-shedding suppression observed in the flow visualizations. The horseshoe vortex dominates again a region three to four diameters from the base of the cylinder.

The inclination of 30 deg is considered in the next set of frames (Fig. 7(*b*)). For Fr=0.3, the picture is drastically different. The effect of the boundary conditions is inverted. The horseshoe vortex region contains less energy, and the vicinity of the free surface is characterized by a dominant vortex-shedding process. The prevailing Strouhal number is around 0.24. However, the peaks are broader than the ones observed for the 0 deg inclination. The increase of the Froude number to Fr=0.65 results in power spectra distributions with many dominant frequencies, varying between 0.06 and 0.26. Overall, there is energy content with almost one decade difference in frequencies up to St=0.75. This proves that the positive inclination results in a more violent flow field but the vortex-shedding process is also enhanced. The final Froude number for this inclination (Fr=1.06) presents a very distinct peak frequency at 0.22 that spans with very small variation the entire length of the cylinder. About eight diameters from the floor, the energy content is reduced. Generally, the 30 deg inclination demonstrates a reduction of the energy contained in the area of the horseshoe vortex.

Finally, the power spectra for the case of 30 deg inclination are presented in Fig. 7(*c*). The case of Fr=0.3 (Fig. 7(*c*)) indicates a wider range of frequencies; however, the dominant mode is approximately at St=0.24. An interesting feature is that even though vortex shedding is not suppressed in the vicinity of the free surface, the amplitude is drastically reduced. Furthermore, in the cases of higher Froude numbers, we observe a shift toward lower frequencies (Figs. 7(*f*) and 7(*i*)). Reduction of the vortex-shedding frequency indicates increase in the effective width and length of the wake. Even more interesting is the fact that at 16 diameters, the effect of the free surface becomes very dominant, generating a very broad spectrum with high-energy content. For Fr=1.06, the free surface influences a region approximately three diameters below, shifting the dominant frequencies to values as low as St =0.04.

The measured Strouhal numbers range primarily from 0.22 to 0.27. The equation proposed by Williamson [8] for the St–Re relation for higher Re numbers

$$\mathrm{St} = 0.2731 - \frac{1.1129}{\sqrt{\mathrm{Re}}} + \frac{0.4821}{\mathrm{Re}} \qquad (2)$$

predicts St numbers of 0.246, 0.255, and 0.258, respectively, for the three Reynolds numbers that correspond to the Froude numbers tested. This shows a very good agreement with the measurements presented for regions away from the ends. This indicates that the small variation in the Strouhal number can be attributed to changes in the Reynolds number and not to the Froude number variations or the end conditions. However, the broadening of the spectrum and the extent of the effects of the free surface are due to the geometry of inclination and the Froude number variation.

Conclusions

The introduction of asymmetry in the end conditions of a cylinder immersed in a stream with a free surface generate strongly three-dimensional flow fields that depend mostly on the Froude number. Analysis of hydrogen-bubble flow visualization images in conjunction with the corresponding calculated frequencies indicates that the free-surface effects on vortex shedding extend more than two to three cylinder diameters below the free surface. Discontinuities of the vortex axis and cells of shedding, which induce a phase difference in the vortex-shedding mechanism, were visually observed. Streamwise vortical structures can be identified to form along the primary vortex axis. Furthermore, particle visualizations provide evidence of vortex suppression in the region near the free surface, a finding that is most pronounced for the case of the highest Froude number and zero inclination. This was confirmed by LDV frequency measurements. In addition, positive inclination of the cylinder counteracts the effects of the free surface, recovering the vortex-shedding process, while for the negative inclination, the neighborhood of the free surface presents a broad energy spectrum.

Analyzing power spectra obtained with LDV measurements, we confirmed that the effect of the free surface is changing depending on the inclination and the Froude number, ranging from one to five diameters below the free surface. In addition, the no-slip boundary condition on the solid wall affects the flow but in reverse manner. Namely, when the horseshoe vortex is predominant, the free-surface influence is reduced and vice versa. The prevailing mode of vortex shedding is approximately at St=0.25. However, depending on the yaw angle and the free-stream velocity, values as low as 0.04 and as high as 0.3 were measured. The broadening of the spectrum indicates a less organized wake. Finally and more importantly, in the very vicinity of the free surface, significant decrease in the energy content of the shed vortices was observed and on occasion altogether suppression of vortex shedding.

Acknowledgment

The support of the Office of Naval Research, under Grant No. ONR N00014-96-1-0941, is gratefully acknowledged.

References

[1] Williamson, C. H. K., 1996, “Vortex Dynamics in the Cylinder Wake,” Annu. Rev. Fluid Mech., pp. 477–539.
[2] Williamson, C. H. K., 1995, “Vortex Dynamics in the Wake of a Cylinder,” *Fluid Vortices*, S. I. Green, ed., pp. 155–234.
[3] Bernal, L. P., and Roshko, A., 1986, “Streamwise Vortex Structures in a Plane Mixing Layers,” J. Fluid Mech., **170**, pp. 599–525.
[4] Wei, T., and Smith, C. R., 1986, “Secondary Vortices in the Wake of Circular Cylinder,” J. Fluid Mech., **169**, pp. 513–533.
[5] Ramberg, S. E., 1983, “The Effects of Yaw and Finite Length Upon the Vortex Wakes of Stationary and Vibration Circular Cylinders,” J. Fluid Mech., **128**, pp. 81–107.
[6] Hammache, M., and Gharib, M., 1991, “An Experimental Study of the Parallel and Oblique Vortex Shedding From Circular Cylinders,” J. Fluid Mech., **232**, pp. 567–590.
[7] Roshko, A., 1954, “On the Drag and Shedding Frequency of Two-Dimensional Bluff-Bodies,” *NACA Tech. Note* 3169.
[8] Williamson, C. H. K., and Brown, G. L., 1998, “A Series in $1/\sqrt{\mathrm{Re}}$ to Represent the Strouhal–Reynolds Number Relationship of the Cylinder Wake,” J. Fluids Struct., **12**, pp. 1073–1085.
[9] Rood, E. P., 1995, “Vorticity Interaction With a Free-Surface,” *Fluid Vortices*, S. I. Green, ed., pp. 155–234.
[10] Rood, E. P., 1994, “Interpreting Vortex Interactions With a Free Surface,” ASME J. Fluids Eng., **116**, pp. 91–93.
[11] Rood, E. P., 1994, “Myths, Math, and Physics of Free-Surface Vorticity,” Appl. Mech. Rev., 47(6).
[12] Lang, A. W., and Gharib, M., 1998, “On the Effects of Surface Contamination in the Wake of a Surface-Piercing Cylinder,” *Proceedings of the 1998 ASME Fluids Engineering Division Summer Meeting*, Washington, DC.
[13] Vlachos, P. P., and Telionis, D. P., 2000, “Turbulence Characteristics in the Wake of a Circular Cylinder Near the Free Surface,” *Proceedings of third ASME/JSME Joint Fluids Engineering Conference*, FEDSM2000–11320, Boston, MA.
[14] Vlachos, P. P., and Telionis, D. P., 2000, “Three-Dimensional Streamwise Vortical Structures of a Turbulent Wake Near the Free Surface,” *Proceedings of third ASME/JSME Joint Fluids Engineering Conference*, FEDSM2000–11262, Boston, MA.
[15] Stern, F., Parthasarathy, R., Huang, H. P., and Longo, J., 1994, “Effects of Waves and Free Surface on Turbulence in the Boundary Layer of a Surface-Piercing Flat Plate,” FED, 181.
[16] Lian, Q. X., and Su, T.-C., 1996, “The Application of Hydrogen Bubble Method in the Investigation of Complex Flows,” *Atlas of Flow Visualization II*, CRC, Boca Raton, FL.
[17] Lu, L. J., and Smith, C. R., 1985, “Image Processing of Hydrogen Bubble Flow Visualization for Determination of Turbulence Statistics and Bursting Characteristics,” Exp. Fluids, **3**, pp. 349–356.
[18] Lu, L. J., and Smith, C. R., 1991, “Use of Flow Visualization Data to Examine Spatial-Temporal Velocity and Burst Type Characteristics in a Turbulent Boundary Layer,” J. Fluid Mech., **232**, pp. 303–340.
[19] Utami, T., and Ueno, T., 1984, “Visualization and Picture Processing of Turbulent Flow,” Exp. Fluids, **2**, pp. 25–32.
[20] Techet, A. H., Hover, F. S., and Triantafyllou, M. S., 1998, “Vortical Patterns Behind a Tapered Cylinder Oscillating Transversely to a Uniform Flow,” J. Fluid Mech., **363**, pp. 79–96.
[21] Lighthill, J., 1978, *Waves in Fluids*, Cambridge Academic Press.

Multiobjective Design Study of a Flapping Wing Power Generator

Eriko Shimizu
Department of Mechanical Engineering,
Toyo University,
Kujirai 2100, Kawagoe,
Saitama 350-0815, Japan
e-mail: shimizu@eng.toyo.ac.jp

Koji Isogai
Department of Aerospace Engineering,
Nihonbunri University,
1727 Ooaza Ichigi,
Ooita 870-0397, Japan
e-mail: isogai@nbu.ac.jp

Shigeru Obayashi
Institute of Fluid Science,
Tohoku University,
2-1-1 Katahira, Aoba-ku, Sendai,
Miyagi 980-8577, Japan
e-mail: obayashi@ifs.tohoku.ac.jp

In conventional windmills, the high tip speed creates aerodynamic noise, and when they are used at very low Reynolds numbers, their performance deteriorates due to laminar separation. These are important issues in modern windmills. Present study deals with a new windmill concept, the "flapping wing power generator," which would solve such problems. The concept is to extract energy via the flutter phenomena and the concept has been developed by some researchers. In 2003, Isogai et al. 2003, "Design Study of Elastically Supported Flapping Wing Power Generator," International Forum on Aeroelasticity and Structural Dynamics, Amsterdam) proposed a new system. The system utilizes dynamic stall vortices efficiently and generates high power. The dynamic stall vortex is something that should be avoided in conventional windmills. They optimized the system to maximize the efficiency and obtained the set of design parameters, which achieved best efficiency. The system works at low frequencies and it enables high efficiency. To realize the system, it is necessary to consider the power and the efficiency. Thus, the present study optimized the system to maximize both the power and the efficiency. To obtain nondominated solutions, which are widely distributed in the design space, adaptive neighboring search, which is one of evolutionary algorithms, has been extended to handle multiple objectives and was used in the present study. Self-organizing map was used for the data mining. The trade-off between the power and the efficiency has been visualized. The trade-off curve was shaped by the constraints on the reduced frequency and the phase delay angle, which were imposed so that the dynamic stall phenomenon gives favorable effects on the power generation. The heaving amplitude was a parameter correlated to the objective functions. The reduced frequency and the phase delay angle change to control the heaving amplitude. Consequently, when the power is emphasized, the system undergoes a large heaving motion with a low frequency. On the other hand, when the efficiency is emphasized, the system undergoes a small heaving motion with a high frequency. Multiobjective optimization and data mining revealed the trade-off of the objective functions and the parameters correlated to the objective functions. The power obtained was comparable to that of present windmills at low tip-speed ratio region. [DOI: 10.1115/1.2829580]

Keywords: power generator, flapping wing, dynamic stall vortex, multiobjective optimization

1 Introduction

As is well known, "flutter" is a disruptive aeroelastic phenomenon that must be avoided in aeronautical/architectural structures such as aircraft and suspension bridges. The present study deals with a power generation system that extracts wind energy via the flutter phenomenon.

The idea of extracting wind energy via the flutter phenomenon is not new. "Flutter engine" by Duncan [1] might be the first machine, although it was originally built for explaining the flutter phenomenon, not as a wind power generator.

McKinney and DeLaurier [2] proposed the "wingmill," which utilized a harmonically oscillating wing to extract wind energy. The whole wing oscillates in vertical translation and in pitch with a prescribed phase delay between the two motions. The two motions are mechanically coupled. They conducted wind tunnel experiments with a working model and obtained a power generation efficiency, which was comparable to a rotary windmill.

Jones et al. [3] also presented results of their design study of a similar wingmill. They employed a panel code as the aerodynamic evaluation tool, and predicted higher efficiency than that obtained by McKinney and DeLaurier.

Recently, Isogai et al. [4] proposed a new system. In their system, the wing is supported elastically in the heaving direction while the pitching oscillation of the whole wing is mechanically driven by an electric motor with a prescribed frequency and amplitude. In Ref. [4], the system was optimized to maximize the efficiency using "complex method" proposed by Box [5].

To realize the system, it is necessary to consider the power and the efficiency. Therefore, this paper carries out multiobjective optimization of Isogai's "flapping wing power generator" to maximize both the power and the efficiency. To obtain widely distributed nondominated solutions, adaptive neighboring search (ANS), one of evolutionary algorithms, proposed by Takahashi and Kobayashi [6] has been extended and used for multiple objectives in the present study. Potential theory was used to evaluate the solutions due to the low computational cost. The nondominated solutions are analyzed by means of self-organizing map (SOM) [7,8]. SOM is a data mining technique, which is useful for visual presentation of multidimensional results. This method visualizes the trade-off of nondominated solutions in the objective function space and reveals the relationship among design variables and objective functions. To evaluate the power and the efficiency with viscous effects, numerical evaluations using Navier–Stokes simulation were conducted for several nondominated solutions.

Contributed by the Fluids Engineering Division of ASME for publication in the JOURNAL OF FLUIDS ENGINEERING. Manuscript received July 7, 2006; final manuscript received September 4, 2007; published online January 24, 2008. Review conducted by Paul Durbin.

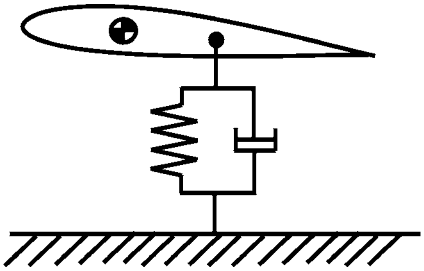

Fig. 1 Concept of flapping wing power generator

2 Model

In the flapping wing generator, the motion of the wing consists of heaving and pitching. The pitching motion is given by an electric motor at a prescribed frequency (ω) and amplitude (α_0). The pitching motion is expressed by

$$\alpha = \alpha_0 \sin \omega t \tag{1}$$

where ω is the frequency of the pitching oscillation.

The heaving motion is supported elastically (Fig. 1). In this system, the lift induced by the pitching oscillation generates the heaving oscillation, i.e., heaving oscillation is not prescribed but results from the following equation:

$$h = h_0 \sin(\omega t - \phi) \tag{2}$$

where h_0 is the amplitude of the heaving oscillation and ϕ is the phase delay angle of the heaving oscillation with respect to the pitching oscillation. This system is designed to extract energy mainly from the work done by the lift for the heaving oscillation to keep the structure simple.

The geometric definition is shown in Fig. 2. The equation of motion of this system can be derived as follows:

$$M_h \ddot{h} + \omega_h^2 M_h (1 + ig) h = L + M_w (x_{\mathrm{cg}} - a)\ddot{\alpha} \tag{3}$$

M_h is the total mass of the parts undergoing heaving oscillation, M_w is the mass of the wing, g is the damping coefficient added to the system to maintain harmonic oscillation with a constant amplitude (it is set to the generator's damping), L is the lift that acts on the wing, ω_h is the natural angular velocity of the heaving oscillation, x_{cg} is the center of gravity, and a is the position of the pitch axis. The h_0 and ϕ in Eq. (2) are obtained by solving the equation of motion (Eq. (3)).

If we assume that the aspect ratio of the present rectangular wing is large, analytical expressions of two-dimensional unsteady aerodynamic forces given in Ref. [9] can be employed to solve Eq. (3). Readers should refer to Ref. [4] for details. When the following parameters, the wing semichord length (b), the freestream velocity (U), and the amplitude of the forced pitching oscillation (α_0), are provided from a nondimensional variation of Eq. (3), we can state that the aerodynamic response of this system is governed by six design variables: the dimensionless position of the pitch axis (a^*), the dimensionless position of the center of mass of the wing (x_{cg}^*), the reduced frequency (k: $k = b\omega / U$), the damping coefficient (g), the mass ratio of the wing (μ: $\mu = M_h / \pi\rho b^2$), and the frequency ratio (ω_h / ω). To simplify the design, the position of the pitch axis is fixed at the position of the center of mass of the wing. With this assumption, the second term of the right hand side of Eq. (3) can be deleted. Thus, design variables are reduced to 5.

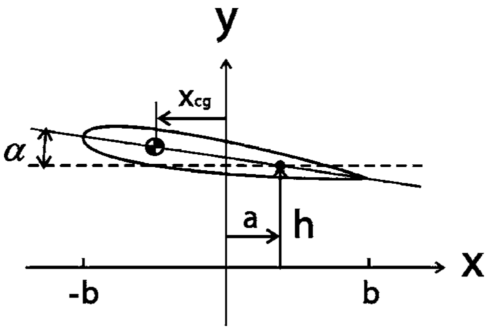

Fig. 2 Geometric definition of flapping wing power generator

Table 1 Constraints of design variables and output variables

Design variable	Constraint	Output variable	Constraint
a^*	$(-1.0, 1.0)$	h_0^*	(0.5,2.0)
k	(0,0.3)	ϕ	(100,150)
g	(0,2)	W_2	$[*, 0]$
μ	(5,200)		
ω_h / ω	(0.5,1.5)		

Assuming that the wing motion is a simple harmonic oscillation, we can obtain an analytical solution of Eq. (3) from the five design variables. The mean work provided by the aerodynamic force, i.e., the wind energy extracted from the system as power (W), is given by summing the mean work done by the lift (W_1) and the mean work done by the aerodynamic pitching moment (W_2) as follows:

$$W = W_1 + W_2 = \frac{1}{T}\int_0^T (L\dot{h} + M_\alpha \dot{\alpha}) dt \tag{4}$$

where M_α is the aerodynamic pitching moment and T is the oscillation period. W is the value after subtracting the power, which is needed to implement a pitching oscillation against aerodynamic pitching moment.

The efficiency is defined by

$$\eta = \frac{\text{power output}}{\text{extractable power from the stream}} = \frac{W}{1/2\rho U^3 (2h_s)(16/27)} \tag{5}$$

where 16/27 is the Betz coefficient [10] and h_s is the larger of the leading-edge or the trailing-edge heaving amplitude. η is the rate of the power obtained by the system against power, which is actually extractable from the freestream. The extractable power from

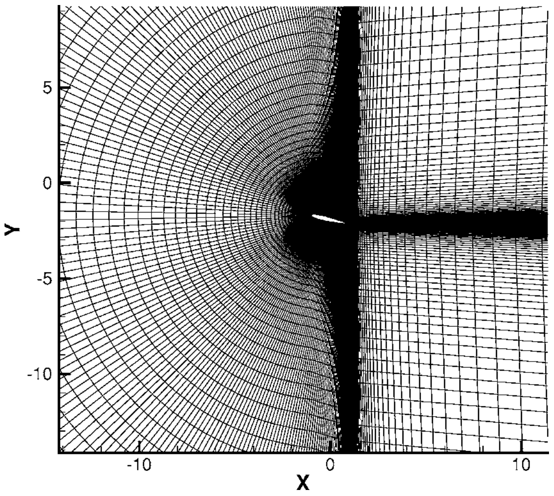

Fig. 3 Computational mesh around the airfoil

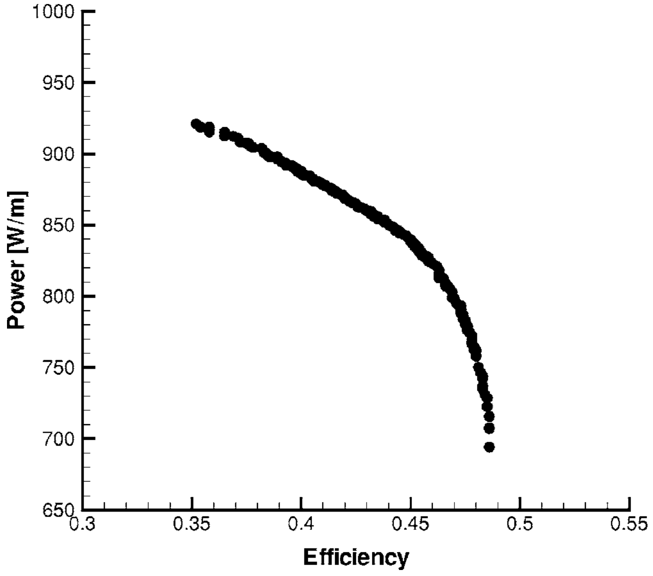

Fig. 4 Nondominated solutions plotted by power and efficiency

the flow derived from the ratio of the flow velocity before and after the wind power generator.

W and η are defined per unit span.

3 Objective Functions and Design Variables

In the current study, objectives are the maximization of the power and the efficiency (Eqs. (4) and (5)). The design variables are a^*, k, g, μ, and ω_h/ω. Output variables, h_0^*, ϕ, and W_2, are also considered for the discussion of the results.

The range of the design variables and the constraints on the output variables are shown in Table 1. The constraints for k, ϕ, and W_2 are imposed so that the dynamic stall phenomenon gives favorable effects on the power generation. According to the numerical evaluations using the Navier–Stokes simulation [11], the dynamic stall phenomenon reduces both the power and the efficiency considerably, when the system does not satisfy the constraints. By applying these constraints, it is guaranteed that the dynamic stall phenomenon increases both the power and the efficiency, beyond those predicted by the analytic evaluation [4].

4 Method

4.1 Optimization. In this study, the system is optimized by ANS-M. ANS-M is based on ANS [6] and extended for multiobjective optimization in the present study.

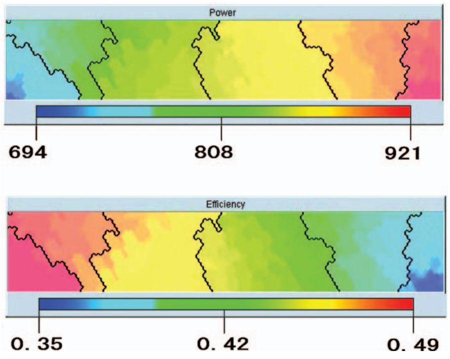

Fig. 5 SOM clustered and colored by objective functions: (*a*) power *W* and (*b*) efficiency η

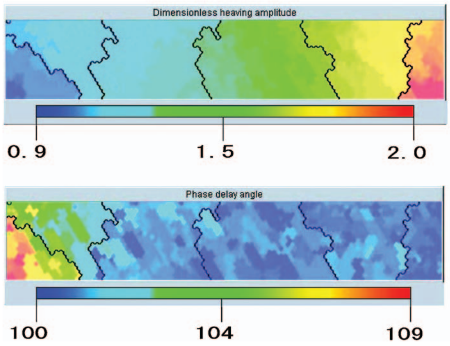

Fig. 6 SOM clustered by objective functions and colored by output variables: (*a*) dimensionless heaving amplitude h_0^* and (*b*) phase delay angle ϕ

ANS is one of evolutionary algorithms, which uses the real-coded representation of the design variables and crossoverlike mutation based on the normal distribution for generating the next searching points. This Gaussian distribution is formed based on the relative position between an individual and its neighbors. This algorithm produces clusters of individuals within the population as a result of evolution. These clusters search the design space independently and find multiple optima efficiently.

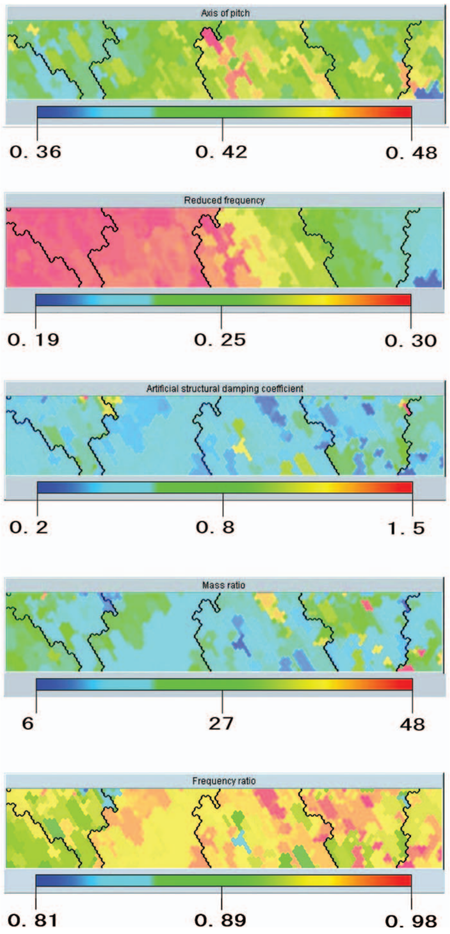

Fig. 7 SOM clustered by objective functions and colored by design variables: (*a*) axis of pitch a^*, (*b*) reduced frequency *k*, (*c*) damping coefficient a^*, (*d*) mass ratio μ, and (*e*) frequency ratio ω_h/ω

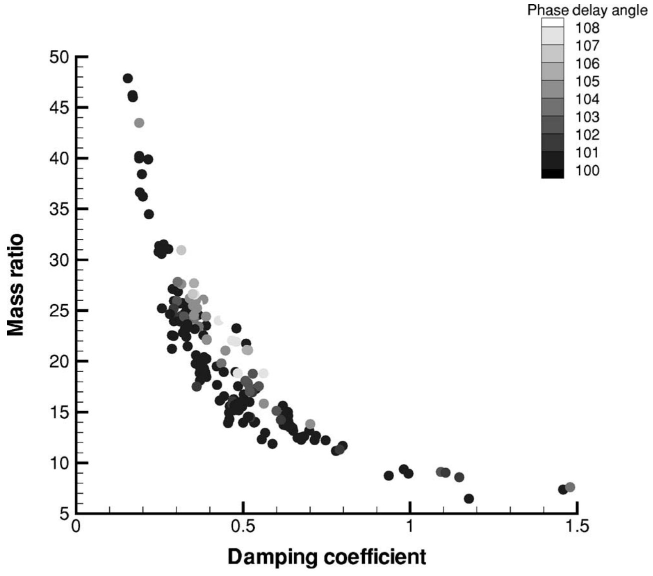

Fig. 8 Nondominated solutions plotted by damping coefficient and mass ratio colored by phase delay angle

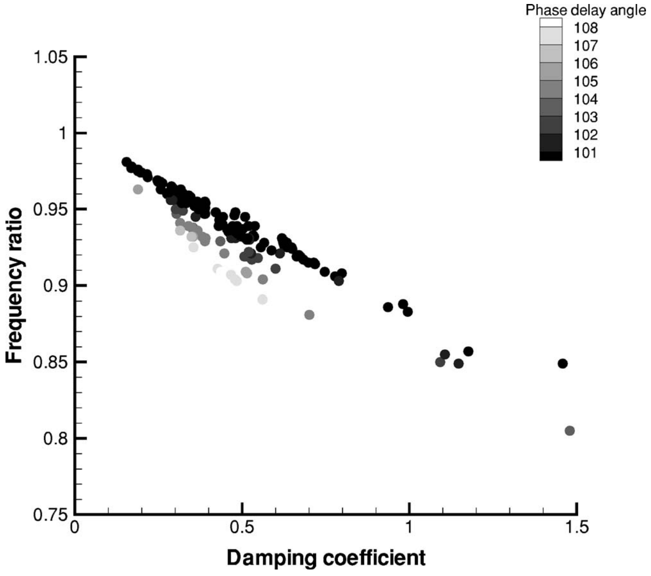

Fig. 10 Nondominated solutions plotted by damping coefficient and frequency ratio colored by phase delay angle

4.2 Data Mining. SOM [7,8] is used for the data mining. It provides a topology preserving mapping from the high dimensional space to map units. Map units usually form a two-dimensional lattice; thus, SOM is a mapping from high dimensions onto two dimensions. The topology preserving mapping indicates that nearby points in the input space are mapped to nearby units in 2D. Each unit has values of objective functions, design variables, and output variables and it is colored by each value on the map. Thus, the clustering based on the objective function values and the color specification depending on each variable value help to identify trade-offs between objective functions and the design variables correlated to the objective functions at one view.

4.3 Navier–Stokes Code. Numerical evaluation is conducted for several nondominated solutions to evaluate the power and the efficiency taking viscous effects into account. The evaluation is obtained by solving Eq. (3) using the lift predicted by the Navier–Stokes (NS) simulation.

The finite difference scheme used is the Yee–Harten total variation diminishing (TVD) [12] scheme and Baldwin and Lomax algebraic turbulence model [13] is used. The present study used the compressible Navier–Stokes code; thus, Mach number is set to be 0.3, which is a Mach number that the compressible code can handle and, at the same time, can be considered as incompressible flow. The *C*-type grid of 280×80 points (200 points on the airfoil) is used for the computation (Fig. 3), and far-field boundary is located at ten chord lengths away from the airfoil. A freestream boundary condition is prescribed at the far-field boundary and a no-slip boundary condition is given on the airfoil surface. The law of the wall coordinate y_{+1} of the grid points next to the airfoil

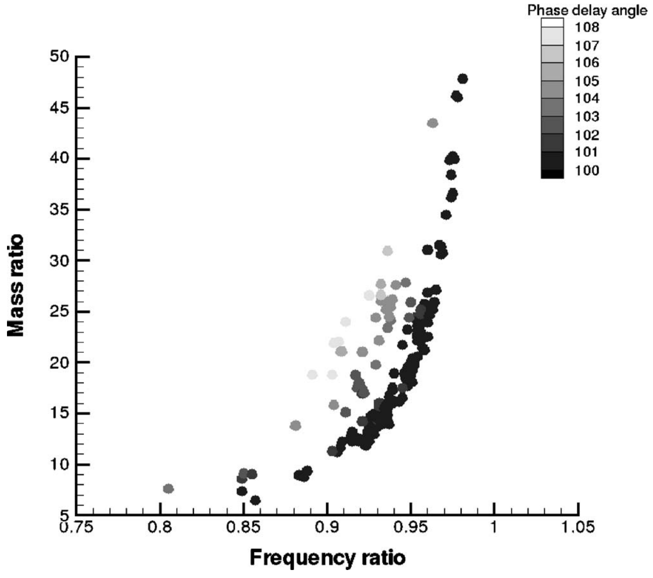

Fig. 9 Nondominated solutions plotted by frequency ratio and mass ratio colored by phase delay angle

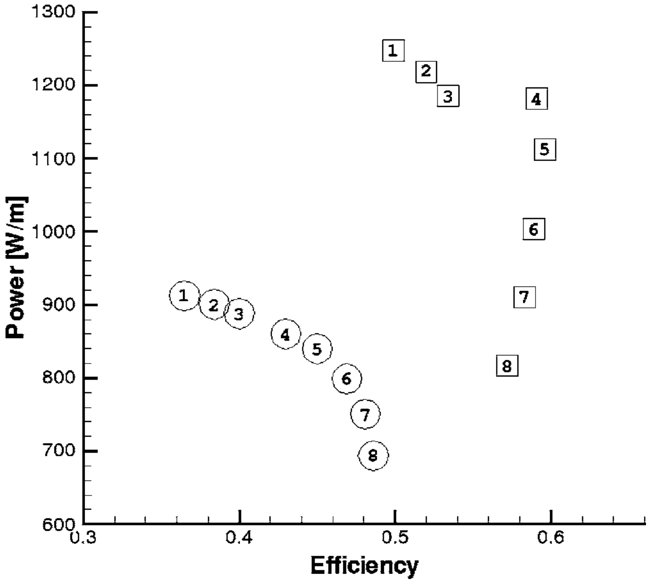

Fig. 11 Representative eight nondominated solutions plotted by the power and the efficiency. Circles show the solutions obtained by analytical evaluation and squares show the solutions recalculated by numerical evaluation.

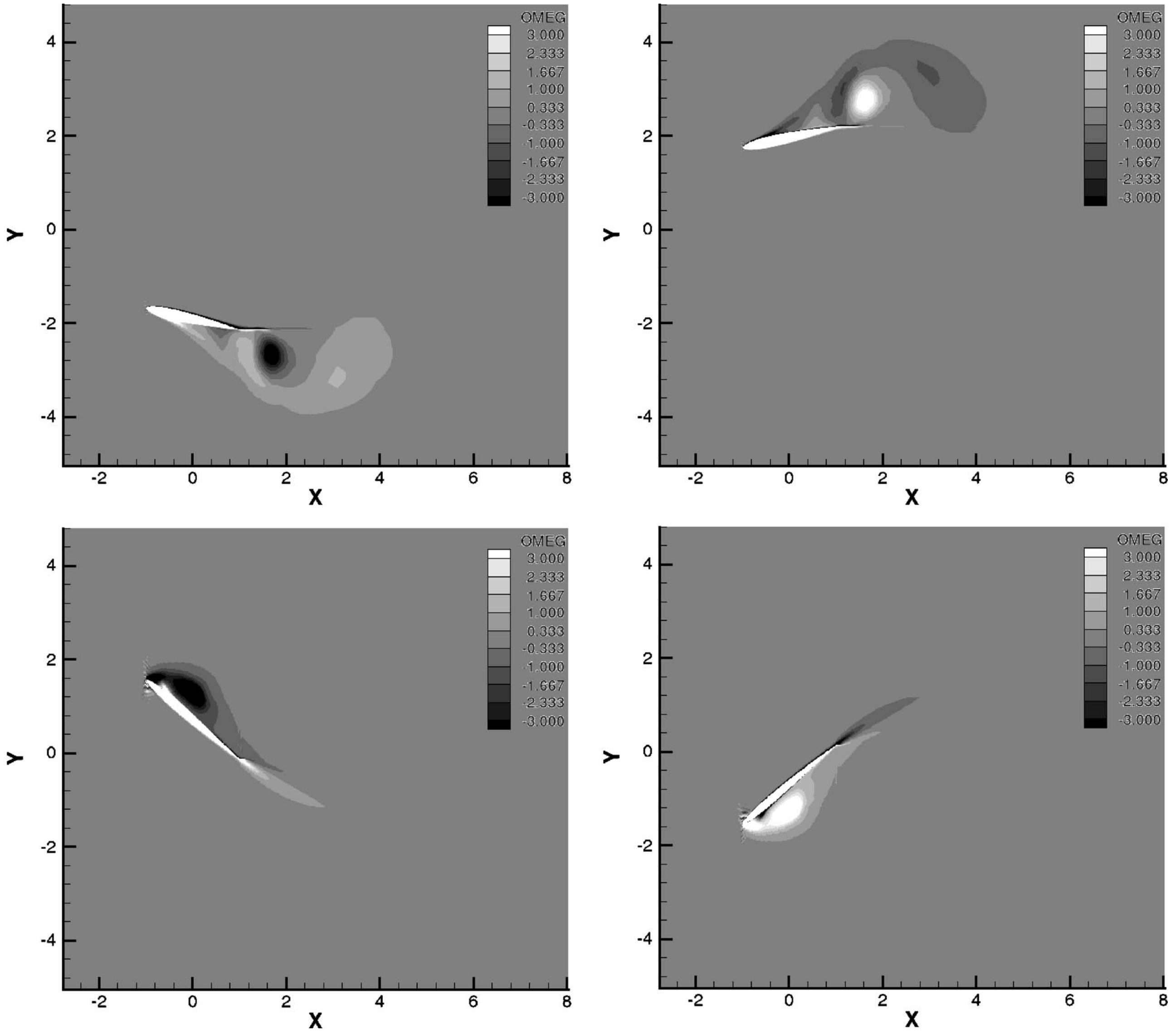

Fig. 12 Flow field (isovorticity contours) around the wing of the system: (*a*) $\omega t=\pi/24$, (*b*) $\omega t=7\pi/24$, (*c*) $\omega t=13\pi/24$, and (*d*) $\omega t=19\pi/24$

surface is 1.0. The periodic solutions are obtained after five cycles of oscillation. Readers should refer to Refs. [4,11] for details including the validation.

5 Wing Geometry and Operating Condition

The airfoil of NS simulation is a NACA0012. The semichord length (b) is 0.5 m. The amplitude of the forced pitching oscillation given by the motor (α_0) is 50 deg. The freestream velocity (U) is 15 m/s. Thus, the Reynolds number is 4.62×10^5.

6 Results

110,000 solutions were evaluated and 386 nondominated solutions were obtained after the optimization. Figure 4 shows the nondominated solutions plotted by the power and the efficiency. We can see the trade-off between the two objective functions. The power takes values up to 921 W/m and the efficiency takes values up to 0.486. Figures 5 and 6 show the resulting SOM. It is mapped by objective function values of nondominated solutions and colored by values of each variable. Black lines show the boundary between the clusters. These lines are not used in the discussion.

From Figs. 5(*a*), 5(*b*), and 6(*a*), h_0^* shows strong influence on the trade-off. The power is obtained by the multiplication of the lift and the time derivative of the heaving amplitude (Eq. (4)), and the efficiency is obtained by dividing the power by the leading-edge or the trailing-edge heaving amplitude, whichever takes a higher value (Eq. (5)). Thus, to generate high power, a large heaving amplitude is desirable, but to achieve high efficiency, a small heaving amplitude is desirable. For this reason, it is apparent that h_0^* is a parameter correlated to the objective functions.

Next, the effect of the design variables on h_0^* will be discussed. Figures 5(*b*) and 7(*b*) show that when the efficiency takes values lower than 0.45, k takes values up to 0.3. However, when the efficiency takes values higher than 0.45, k takes a constant value of 0.3. On the other hand, Figs. 5(*b*) and 6(*b*) show that when the efficiency takes values lower than 0.45, ϕ equals to 100 deg. But, when the efficiency takes values higher than 0.45, the value of ϕ changes. When we pay attention to 0.45 and look at the trade-off (Fig. 4), it seems to have different trends across this point. When the efficiency takes values more than 0.45, the trade-off curve shows rapid decrease of the power against the efficiency. $k=0.3$ is

Table 2 Values of eight nondominated solutions

	Case							
Design variable	1	2	3	4	5	6	7	8
a^*	0.450	0.429	0.409	0.442	0.430	0.404	0.389	0.392
k	0.221	0.225	0.232	0.272	0.291	0.294	0.296	0.297
g	0.155	0.634	0.338	0.390	0.483	0.600	0.381	0.487
μ	47.85	14.08	25.67	18.46	15.19	15.12	26.07	24.24
ω_h/ω	0.981	0.926	0.958	0.947	0.934	0.911	0.932	0.896
Output variable								
h_0^*	1.915	1.784	1.664	1.425	1.277	1.137	1.018	0.929
ϕ	100.0	100.5	100.5	100.7	100.4	102.2	104.6	108.8
h_{0n}^*	2.1	2.0	1.9	1.6	1.4	1.2	1.0	1.0
ϕ_n	95.74	98.00	99.68	105.9	108.0	109.6	110.9	115.7
Objective function								
W (W/m)	912.4	900.4	887.7	859.9	839.6	798.9	750.2	694.1
η	0.365	0.384	0.400	0.430	0.450	0.469	0.481	0.486
W_n (W/m)	1247	1219	1186	1182	1112	1004	909.8	817.2
η_n	0.4999	0.520	0.534	0.591	0.596	0.589	0.583	0.572
W_n/W	1.36	1.35	1.33	1.37	1.32	1.25	1.21	1.17

the upper bound of k and $\phi=100$ deg is the lower bound of ϕ. This implies that k and ϕ control h_0^* and the constraints shape the trade-off curve.

Using 2D unsteady wing theory, when k increases, the lift caused by the unsteady motion decreases. Lift increases the heaving oscillation. Therefore, when k takes high values, h_0^* takes low values; as a result, the efficiency takes high values. In this way, the system performance is affected by k.

Regarding the effect of ϕ to h_0^*, the power is obtained by Eq. (4); thus, it is desirable that the phase of the lift and the phase of the time derivative of the heaving oscillation are the same; furthermore, under the constraint of ϕ, 100 deg is closest to this situation. To see the effects of design variables, solutions were plotted by the design variables and colored by ϕ. As a result, Figs. 8–10 show that g, μ, and ω_h/ω are correlated with respect to ϕ, especially when $\phi\cong 100$ deg. It shows that when μ takes high values, the system generates high power using resonance, though damping coefficient takes small values.

From Fig. 7(*a*), a^* does not seem to affect the trade-off. The pitching axis tends to be positioned around 70% on the chord from the leading edge. This is because when it is positioned around 70% on the chord, M_α tends to take low values and thus W_2 takes small values. The total power W is the sum of W_1 and W_2, and W_2 takes negative values from the constraint. Thus, small magnitude of W_2 is desirable for high W.

Eight nondominated solutions (labeled 1–8) were chosen and recalculated using NS simulation. Figure 11 shows the chosen solutions plotted by the power and the efficiency. Circles show analytic solutions and squares show the solutions recalculated by numerical evaluation. The solutions labeled 1–8 are called Cases 1–8 in the following discussion. Solutions recalculated by numerical evaluation show high power and efficiency in comparison with the values obtained by analytic evaluation. This confirms that the constraints to utilize dynamic stall phenomenon work effectively. Figure 12 shows the flow field (isovorticity contours) around the wing in Case 1. Dark color shows clockwise vorticity and white shows counterclockwise vorticity. The dynamic stall vortices are formed on the upper/lower surface of the wing in upward/downward motion of the wing, respectively. This dynamic stall vortex helps the wing motion and increases the power of the system. This phenomenon occurs for all cases and the vortex around the wing increased the power up to 36.6%.

Table 2 shows the value of design variables, output variables, and objective functions. Variables with suffix n show that their values are predicted by numerical evaluation. Figures 13 and 14 show the solutions plotted by the output variables and the objective functions. Circles show the solutions obtained by analytical evaluation and squares show the solutions recalculated by numerical evaluation. In Fig. 13, analytical solutions show that η increases linearly, as h_0^* decreases. On the other hand, the numerical solutions show that η_n increases linearly, when h_{0n}^* takes values higher than 1.5, but at lower amplitudes, η_n slightly decreases. In Fig. 14, the analytical solutions show that W takes high values, when ϕ takes low values. Also, the numerical solutions show similar trends. When we see the values in more detail, ϕ_n takes smaller values than ϕ in Cases 1–3; on the other hand, ϕ_n take higher values than ϕ in Cases 4–8. Trends of analytical and numerical solutions are almost the same; thus, previous discussion about analytic solutions can be partly applied to numerical solutions. However, following this study, the viscous effects on the system should be revealed in more detail.

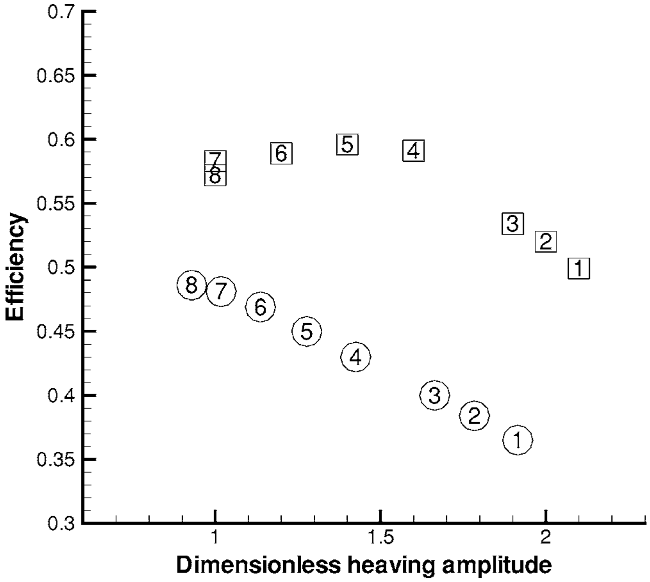

Fig. 13 Eight nondominated solutions plotted by dimensionless heaving amplitude and efficiency. Circles show the solutions obtained by analytical evaluation and squares show the solutions recalculated by numerical evaluation.

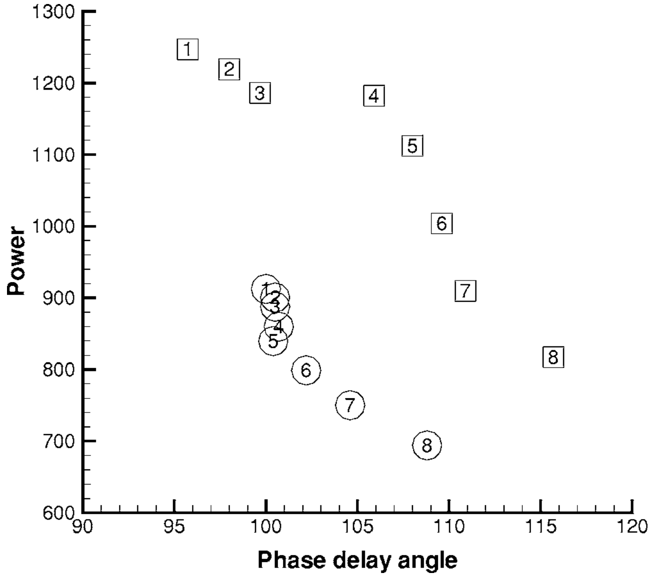

Fig. 14 Eight nondominated solutions plotted by phase delay angle and power. Circles show the solutions obtained by analytical evaluation and squares show the solutions recalculated by numerical evaluation.

In order to evaluate the potential of the present flapping wing power generator, the power coefficient C_p is compared with those of the other types of the windmill against the tip-speed ratio in Fig. 15. The C_p is defined by $C_p = W/(1/2\rho U^3 S)$, where S is the area swept by rotary wing for a windmill or the area swept by the leading edge or trailing edge for the flapping wing power generator and W is the power generated by windmill or flapping wing power generator. As seen in the figure, C_p of the present flapping wing system is about 0.35 at the tip-speed ratio of 0.58. Therefore, the present system has the potential of attaining higher performance compared with other types of windmill for the low tip-speed ratio region.

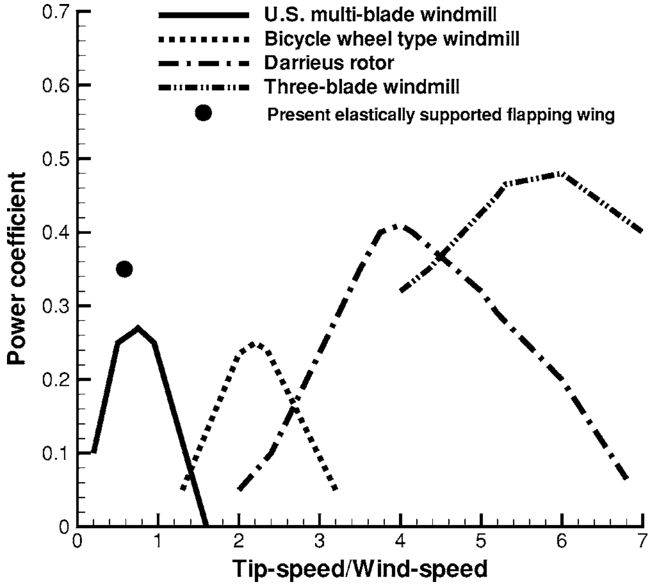

Fig. 15 Comparison with other types of windmill

7 Conclusions

The present study has conducted the multiobjective optimization of the flapping wing power generator, which is a concept that extracts wind energy via the aeroelastic response of an elastically supported rectangular wing. The results were analyzed using SOM. Multiobjective optimization revealed the trade-off of nondominated solutions between the power and the efficiency. SOM revealed the relationship among the objective functions, the design variables, and the output variables.

From the results, it was revealed that the trade-off curve is shaped by the constraints of k and ϕ, which are imposed so that the dynamic stall phenomenon gives favorable effects on the power generation, and h_0^* has a strong correlation to the objective functions. Design variables vary to change h_0^*. k controls h_0^*, when k is lower than its upper bound of 0.3. In this situation, g, μ, and ω_h/ω maintain the relationship to get ϕ close to the lower bound 100 deg to generate high power. On the other hand, ϕ controls h_0^*, when k cannot take a value more than 0.3. a^* did not seem to affect h_0^*. It tended to be located around 70% on the chord due to small negative work done by aerodynamic pitching moment.

When the power is emphasized, the system has a large heaving motion with a low frequency. On the other hand, when the efficiency is emphasized, the system has a small heaving motion with a high frequency.

In numerical evaluation, the dynamic stall vortex around the wing increased the power up to 36.6%. This proved that the constraints effectively increase the work done by lift. The values of output variables predicted by numerical evaluation were close to those predicted by the analytic evaluation. Output variables showed similar trends for objective functions as in the case of analytic evaluation.

Nomenclature

a = position of the pitch axis
a^* = dimensionless position of the pitch axis
b = wing semichord length
g = damping coefficient
h = vertical displacement of the wing
h_s = the larger of the leading-edge or the trailing-edge heaving amplitudes
h_0^* = dimensionless amplitude of the heaving oscillation
h_{0n}^* = dimensionless amplitude of the heaving oscillation predicted by numerical evaluation
k = reduced frequency ($k = b\omega/U$)
L = lift
M_α = aerodynamic pitching moment
M_h = total mass of the parts undergoing heaving oscillation
M_w = mass of the wing
Re = Reynolds number (Ub/ν)
t = time
T = oscillation period
U = freestream velocity
W = sum of the power generated by lift and by pitching moment per unit span
W_n = sum of the power generated by lift and by pitching moment per unit span predicted by numerical evaluation
W_1 = power generated by lift per unit span
W_2 = power generated by aerodynamic pitching moment per unit span
X_{cg} = position of the center of mass of the wing
x_{cg}^* = dimensionless position of the center of mass of the wing

α = angular displacement (positive nose-up) of the forced pitching oscillation
α_0 = forced pitching amplitude
η = efficiency of the system
η_n = efficiency of the system predicted by numerical evaluation
μ = mass ratio $(M_h/\pi\rho b^2)$
ν = kinematic viscosity
ω = angular velocity of the forced pitching oscillation
ω_h = natural angular velocity of the heaving oscillation
ω_h/ω = frequency ratio
ϕ = phase delay angle of the heaving oscillation with respect to the pitching oscillation
ϕ_n = phase delay angle of the heaving oscillation with respect to the pitching oscillation predicted by numerical evaluation
ρ = density of air

References

[1] Duncan, J. W., 1948, *The Fundamentals of Flutter*, ARC/R&M, London, pp. 1–36.

[2] McKinney, W., and DeLaurier, J., 1981, "The Wingmill: An Oscillating-Wing Windmill," J. Energy, **5**, pp. 109–115.

[3] Jones, K., Platzer, M. F., and Davis, S., 1999, "Oscillating-Wing Powder generator," *Proceedings of ASME/JSME FEDSM799, 1999 ASME/JSME Fluid Engineering Division Summer Meeting*, San Francisco, CA, Paper No. FEDSM99-7050.

[4] Isogai, M., Yamasaki, K., Matsubara, M., and Asaoka, T., 2003, "Design Study of Elastically Supported Flapping Wing Power Generator," *International Forum on Aeroelasticity and Structural Dynamics*, Amsterdam.

[5] Box, M. J., 1965, "A New Method of Constrained Optimization and a Comparison With Other Methods," Comput. J., **8**, pp. 42–52.

[6] Takahashi, O., and Kobayashi, S., 2001, "An Adaptive Neighboring Search Using Crossover-Like Mutation for Multimodal Function Optimization," *IEEE International Conference on System, Man and Cybernetics*, pp. 261–267.

[7] Kohonen, T., 1995, *Self-Organizing Maps*, Springer, Berlin.

[8] Obayashi, S., and Sasaki, D., 2003, in *Lecture Notes in Computer Science*, edited by C. M. Fonseca, P. J. Fleming, and E. Zitzler Springer-Verlag, Berlin, Vol. 2632, pp. 796–809.

[9] Theodorsen, T., 1935, NACA Technical Report No. 496.

[10] Johnson, G. L., 1985, *Wind Energy Systems*, Prentice-Hall, Englewood Cliffs, NJ.

[11] Isogai, K., Shinmoto, Y., and Watanabe, Y., 1999, "Effect of Dynamic Stall on Propulsive Efficiency and Thrust of Flapping Airfoil," AIAA J., **5**, pp. 1145–1151.

[12] Yee, H. C., and Harten, A., 1985, "Implicit Scheme for Hyperbolic Conservation Laws in Curvilinear Coordinates," AIAA Paper No. 85–1513.

[13] Baldwin, B., and Lomax, H., 1978, "Thin Layer Approximation and Algebraic Model for Separated Turbulent Flows," AIAA Paper No. 78–257.

Monica Sanda Iliescu
Dr. Ing.
Assistant
e-mail: msiliescu@yahoo.fr

Gabriel Dan Ciocan
Dr. Ing.
Research Associate
e-mail: gabrieldan.ciocan@orange.fr

François Avellan
Dr. Ing.
Professor
e-mail: francois.avellan@epfl.ch

Laboratory for Hydraulic Machines,
Ecole Polytechnique Fédérale de Lausanne
(EPFL),
Avenue de Cour 33bis,
CH-1007 Lausanne, Switzerland

Analysis of the Cavitating Draft Tube Vortex in a Francis Turbine Using Particle Image Velocimetry Measurements in Two-Phase Flow

Partial flow rate operation of hydroturbines with constant pitch blades causes complex unstable cavitating flow in the diffuser cone. A particle image velocimetry (PIV) system allows investigating the flow velocity field in the case of a developing cavitation vortex, the so-called vortex rope, at the outlet of a Francis turbine runner. The synchronization of the PIV flow survey with the rope precession allows applying the ensemble averaging by phase technique to extract both the periodic velocity components and the rope shape. The influence of the turbine setting level on the volume of the cavity rope and its centerline is investigated, providing a physical knowledge about the hydrodynamic complex phenomena involved in the development of the cavitation rope in Francis turbine operating regimes. [DOI: 10.1115/1.2813052]

1 Introduction

For hydraulic turbines, the operating points at partial flow rate are associated with a vortex at the runner outlet, in the draft tube cone. Cavitation develops into the low pressure zone of the vortex core, see Fig. 1. The vortex rope, a helical vortex that is cavitating in its core, appears and the cavitating volume varies with the underpressure level. The rope frequency depends on the σ level and if it comes close to one of the eigenfrequencies of the turbine or associated circuit, the resonance phenomenon may appear. The unsteady fluctuations can be amplified and lead to important damage. Jacob [1] presents a review of the effects of this operating regime on the power plant operation.

A first approach is to model the rope phenomenology. Different models are proposed. Arndt [2] makes a synthesis of the classical approaches by defining a swirl parameter to characterize the vortex rope—called the hub vortex. Qualitative correlations between the swirl number and flow visualization or pressure measurements seem to be in good agreement.

Alekseenko et al. [3] present experiments of axisymmetrical vortices in a vertical vortex chamber with tangential supply of liquid through turning nozzles. They give an analytical solution of an elementary cylindrical vortex structure considered like an infinitely thin filament, accounting for the helical shape of the vortex lines. Different laws of vorticity distribution and finally a formula for the calculation of the self-induced velocity of helical vortex rotation (precession) in a cylindrical tube is given. Okulov [4] extends this approach to a conical vortex, for a small cone opening angle. Validations are not available for this approach, and the cone angle limitation is a strong constraint in applying this model to turbine vortex ropes.

Wang et al. [5] propose two mathematical models: a partially rolled-up vortex for predicting the rope frequency and a “spiral cone cavity” for predicting the cavitation volume in the draft tube. The results are compared with the wall pressure measurements and qualitatively with rope visualizations.

Philibert and Couston [6] propose a hydroacoustic model, and the rope is represented by a pipe characterized by its length, wave celerity, and a coefficient related to the rope radius variation with the discharge. The σ influence is neglected and experimental data are needed for the model calibration.

Hocevar et al. [7] use radial basis neural networks to predict the vortex rope dynamics in a Francis turbine. The pressure spectrum is well predicted and the void fraction corresponds qualitatively to the experimental estimation. However, the method depends on the learning set and cannot predict the unstable behavior of the rope.

Zhang et al. [8], starting from Reynold’s averaged Navier-Stokes (3D RANS) numerical simulations, and Susan-Resiga et al. [9], starting from a theoretical analysis of experimental data, show that the rope origin is the absolute instability of the swirling flow at the cone inlet of the turbine draft tube. However, the rope evolution in the cone is predicted only from the point of view of its stability.

A second approach, made possible by the increase of computers’ power and of the ability of CFD codes to simulate the complex flow behavior, is the numerical simulation of the rope phenomenology. The state of the art in the numerical computation for the cavitation-free configuration is presented by Ciocan et al. [10]. They show, for the rope configuration in cavitation-free conditions, that the RANS calculation can give very accurate results, but a detailed validation is necessary before using the CFD codes for design purposes. More complex numerical investigations are presented by Paik et al. [11], comparing unsteady Reynold’s averaged Navier-Stokes (3D URANS) and direct numerical simulation (3D DNS) numerical simulations in a hydraulic turbine draft tube. Globally, the phenomenology is well predicted, but discrepancies persist in the turbulence and vortex structures in the straight diffuser downstream of the elbow. Once more, the need for detailed flow measurements to improve the draft tube phenomenology modeling is mentioned by the authors.

These approaches are based on a series of hypotheses for the rope phenomenology, which are not yet verified experimentally. Therefore, detailed measurements of the rope volume and the associated velocity fields, in addition to classical wall pressure and torque measurements, are of prime importance for quantitative

---

Contributed by the Fluids Engineering Division of ASME for publication in the JOURNAL OF FLUIDS ENGINEERING. Manuscript received June 29, 2006; final manuscript received July 1, 2007; published online January 25, 2008. Review conducted by Joseph Katz.

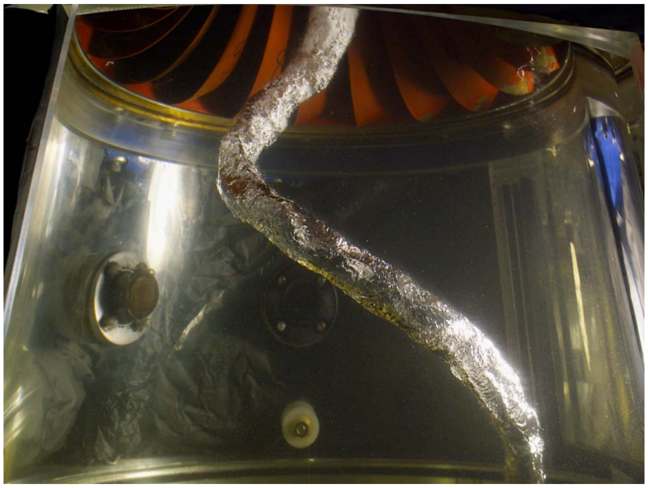

Fig. 1 Development of the vapor core rope for $\sigma=0.380$

validation. An extension of the investigation is necessary in order to demonstrate the σ influence and/or the turbine-circuit interaction influence on the rope phenomenology.

Particle Image Velocimetry (PIV) is a well established technique, see Adrian [12]. Recently, the PIV measurement technique has been applied for two-phase flows, as well in liquid-solid flows—see Kadambi et al. [13]—as in liquid-air flows (bubbly flows).

Dias and Riethmuller [14] used the PIV technique to investigate air bubbles injected into stagnant water. They measured the flow field induced by a single bubble in a water tank by means of 2D PIV, along with the contour of the bubble by the shadow detection method. If the same image is used to obtain the velocity field and the bubble contour, an error of 40% is observed for the bubble contour due to the mirror effect of the bubble boundary. Using fluorescent particles and a high-pass filter, an uncertainty of 3% for the bubble size and velocity, and 2.5% for liquid velocity at 75% confidence level, is obtained.

Lindken and Merzkirch [15] performed the reconstruction of the 3D position and volume of bubbles rising in a pipe, along with the 2D velocity field of the liquid phase. The experimental setup is made of two perpendicular laser sheets of different wavelengths, and two cameras focused on the corresponding laser sheet. The bubble sizes are evaluated from their projections on both laser sheets. Using a 532 ± 1.5 nm filter on the PIV camera, they obtained an uncertainty of 2% for the liquid velocity, 10% for the bubble shape, 5% for the bubble center, and 8% for the bubble velocity, after the rejection by a particular filtering technique of 3–5% of the images due to strong reflections. Next, Lindken and Merzkirch [16] improved this measurement method by combining three different techniques: PIV with fluorescent particles, shadowgraphy, and digital phase separation. In this way, they characterize the local modification of the turbulence in the liquid phase by the bubble passage.

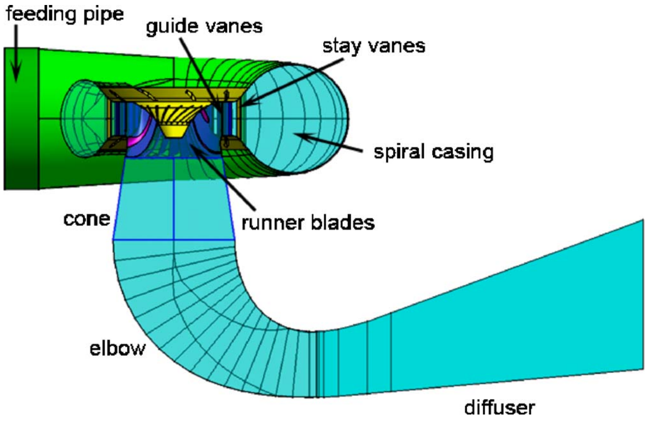

Fig. 2 Francis turbine scale model

Starting from these applications, we developed a PIV two-phase application that enables simultaneous measurements of the flow velocity field and the volume of a compact unsteady vapor cavity—the rope. Specific image acquisition and filtering procedures are implemented for the investigation of cavity volume and its evolution related to the underpressure level in the draft tube. For the first time, the development of the rope in the diffuser cone of a Francis turbine scale model is quantified.

One operating point is selected at partial flow rate operating conditions: for $\psi=1.18$ and $\varphi=0.26$, which corresponds to about 70% Q_{BEP}. To investigate the influence of the cavity size, the Thoma cavitation number is decreased from $\sigma=1.18$, cavitation-free condition, to $\sigma=0.38$, maximum rope volume, considering seven σ values. For the extreme values of σ, nine phases are acquired in order to reconstruct the rope shape by the ensemble averaging by phase technique. The measurement conditions are summarized in Table 1.

2 Scale Model of the Francis Turbine

In a Francis turbine, see Fig. 2, the flow incoming from the feed pipe is uniformly distributed along the runner inlet circumference by a spiral casing with gradually decreasing cross section. A first row of stay vanes ensures the mechanical resistance of the assembly, while a second row, of adjustable guide vanes, provides the optimum incidence angle to the flow at the runner's periphery and adjusts the turbine flow rate.

The kinetic energy of the water is then transformed into rotational energy by the runner and transmitted through the shaft to the power generator, which produces electrical energy. The residual kinetic energy at the runner outlet is transformed into pressure energy in the draft tube, composed of the cone, elbow, and diffuser, and then the flow is released in the downstream reservoir.

The investigated case corresponds to the scale model of the Francis turbines of high specific speed, $\nu=0.56$ ($n_q=88$) of a hydropower plant built in 1926, owned by ALCAN. The 4.1 m diameter runners of the machines were upgraded in the late a 80s.

Table 1 Measurement chart for $\psi=1.18$ and $\varphi=0.26$ operating point

σ	τ/T									f/n
1.180	0.38	0.44	0.50	0.56	0.61	0.65	0.69	0.75	0.81	0.300
0.780					0.61					0.300
0.650					0.61					0.300
0.630					0.61					0.300
0.600					0.63					0.300
0.520					0.63					0.309
0.380			0.46	0.53	0.60	0.68	0.73	0.78	0.83	0.360

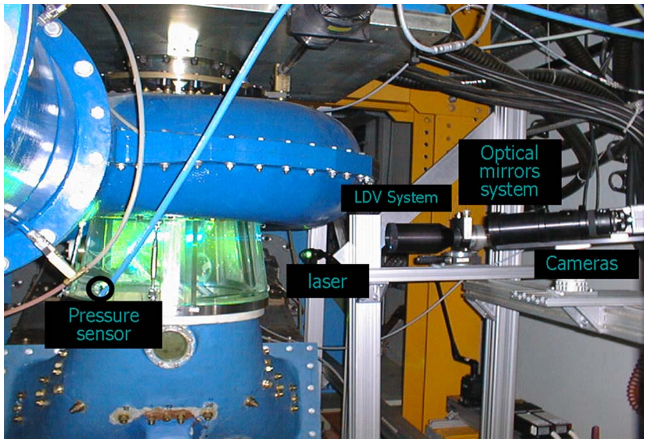

Fig. 3 Two-phase PIV setup for measuring in the diffuser cone of the Francis turbine scale model

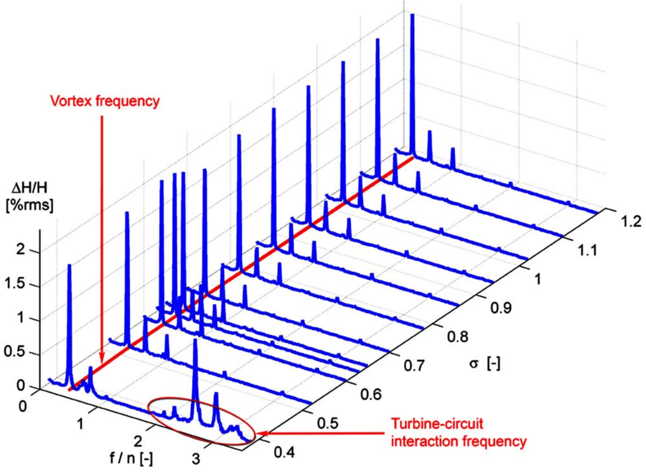

Fig. 4 Waterfall diagram of the power spectra of the wall pressure fluctuations in the diffuser cone

The elbow draft tube of the scale model turbine was especially designed for the purpose of the Flow Investigation in Draft Tubes, FLINDT Research Project EUREKA 1625, see Avellan [17].

The scale model is installed on the third test rig of the EPFL Laboratory for Hydraulic Machines and the performance tests are carried out according to the IEC 60193 standards [18].

3 Two-Phase Particle Image Velocimetry Measurements

3.1 Particle Image Velocimetry System for Two-Phase Flow Measurements. The PIV measurements have been performed with a Dantec M.T. system. The pulsed light sheet with a thickness of 3 mm is generated by two double-cavity Yttrium aluminum garnet (Nd:YAG) lasers delivering 60 mJ per pulse. An optical high power light guide is used for the positioning of the light sheet in the diffuser cone. Two charge coupled device (CCD) HiSense PIV cameras are used to visualize the illuminated zone, with a series of paired images acquired with a 150–200 μs time delay. The camera resolution is 1280×1024 pixels^2 for a 0.20×0.14 m^2 spatial domain. The measurement zone is located at the runner outlet, in the cone of the turbine, see Fig. 6.

To focus the two cameras on the same zone, an optical mirror system is used, Fig. 3. The first camera uses a 532 ± 15 nm antireflection-coated filter, focused on the laser wavelength, and the second camera has a cutoff filter (>570 nm) on the emission wavelength of fluorescent particles (RhB-580 nm). The two cameras are synchronized with the luminous flashes and then simultaneously exposed. The vector processing is performed with a FlowMap 2200 PIV specific processor, based on an 8 bit resolution cross-correlation technique. The shape of the vortex rope is determined through image processing from the first camera and the unsteady velocity field is obtained from the second one.

3.2 Particle Image Velocimetry Calibration. From the measuring field to the camera, the optical path encounters three media of different optical indices: water, polymethylmethacrylate (PMMA), and air. For minimizing the optical distortion of the images and of the laser sheet plane, the diffuser cone windows are manufactured with flat external walls, in front of the cameras and the incident laser light sheet. However, due to the conical internal surface of the draft tube cone, the image distortions remain important. Therefore, they need to be corrected through a calibration procedure, even for this 2D measurement setup.

The calibration consists in defining the coefficients of a transfer function, either linear or nonlinear, that correlates the spatial coordinates in the object plane with the corresponding positions in the recording plane. This transformation integrates the geometrical and optical characteristics of the camera setup, the perspective distortion, lens flaws, and the different media refractive indices, see Soloff et al. [19]. By acquiring images of a target with markers of well-specified spatial position, their corresponding positions in the image plane are known, and thus the geometrical transform matrix coefficients can be determined through a least squares fitting algorithm. The present measurement configuration uses a third-order polynomial function.

The calibration is performed by placing a 2D target of 200×200 mm^2 with 40×40 black dots on a white background in the measurement plane position. The test section is then filled with water for reproducing the optical configuration during measurements. The cameras are focused on the target, the calibration images are acquired, and the laser sheet is aligned with the target surface. The target is removed without modifying the optical arrangement. The accuracy of the optical arrangement after the target removal is verified by checking that the particles do not appear blurred on the image.

The estimated uncertainty for the velocity field measurement is less than 3% and it has been checked by comparing the velocity measurement obtained by both PIV and laser Doppler velocimetry (LDV), see Iliescu et al. [20].

3.3 Particle Image Velocimetry Synchronization. The rope has a 3D helical shape, see Fig. 1. A conditional sampling of the image acquisition is necessary to reconstruct the spatial position of the rope. The frequency of rope precession is influenced by the σ value, see Fig. 4 and Table 1, and can change over a revolution in certain operating conditions. Therefore, the triggering system cannot be based on the runner rotation.

The technique to detect the rope precession is based on the measurement of the pressure pulsation generated at the cone's wall by the precession of the rope. It has the advantage of working even for cavitation-free conditions when the rope is no longer visible, see Ciocan et al. [10], and for this reason, it has been selected as trigger for the PIV data acquisition. The pressure signal power spectra corresponding to the σ values are given as a waterfall diagram in Fig. 4. It can be seen that the frequency of the rope precession is decreasing with the σ value for this operating point.

As the PIV acquisition is based on the spatial position of the rope, it was necessary to validate correspondence between the wall pressure pulsation and the spatial position of the rope. For this, a second technique based on the optical detection of the rope passage with a LDV probe was used. By reducing the gain, the photomultiplier of the LDV system delivers a signal each time the rope boundary intersects the LDV measuring volume. The position of the measurement volume has been chosen close to the wall, to avoid receiving multiple signals over the same revolution, in case the rope crosses the laser beams. The wall pressure signal acquired in parallel allowed referring the rope position to the pressure signal.

Consequently, the image acquisition is triggered with the wall pressure signal breakdown given by the vortex passage. The PIV acquisition is performed at a constant phase delay value with respect to the vortex trigger signal. The influence of the vortex period variation for this kind of phase average calculation is checked and fits within the same uncertainty range as the measurement method 3%, see Ciocan et al. [10].

4 Data Processing

4.1 Image Processing. The two cameras' images are processed separately. The Camera 1 images are processed to extract the rope characteristics (position and diameter) and Camera 2 image to extract the velocity fields.

The vortex core boundary is irregular, due to vapor compressibility and pressure field fluctuations in the draft tube, which deform the vapor volume. The laser light is unevenly scattered backward and sideways at the water-vapor interface and it gives a strongly illuminated area on images from the first camera. Furthermore, the part of the rope passing in front of the laser sheet, toward the camera, is present on the image, but at a lower gray intensity. This entity also obstructs the field of view of the second camera, and fluorescent particles present in the laser plane, behind the rope, do not appear on the images used for velocity processing. Thus, a digital mask must be applied on each individual vector field for eliminating the outliers in this region.

Due to the topology of the rope, the gray intensity distribution varies drastically on the images from the first camera. In this context, an adaptive image-processing algorithm has been conceived for detecting the geometrical parameters of the rope crossing the measurement plane (see Fig. 5). The distortion correction is performed with the calibration transform prior to image processing.

Several steps are considered for enhancing the quality of the raw grayscale image:

- The image is reduced to the zone occupied by the rope, removing the excess area, which leads to improvement of the grayscale distribution;
- The gray intensity levels are balanced in the image by histogram equalization;
- The noise is removed by nonlinear adaptive bandpass filtering of the image on sliding neighborhoods of 8×8 pixels;
- The brightness is amplified by histogram shifting toward higher values, weighted logarithmically.

Starting from the improved and uniform quality images, the next step is to detect the rope shape and its dimensions at the intersection between the laser sheet and the rope.

An adaptive threshold is applied on the enhanced grayscale image, for separating the area with concentrated high intensity values from the rest, thus obtaining the position of the zone where the laser sheet crosses the rope boundary.

In parallel, another adaptive threshold is applied on the histogram of the grayscale image for separating the rope shape from the dark background in a binary image. The accuracy of the rope shape detection depends on the gray level gradient between the rope and the background. The position of the rope edge can vary with less than 1% R_{in} and this is the spatial uncertainty of the rope contour. The local minima (holes) on the binary image are filled for smoothing the rope contour. The various white spots of small area are filtered and only the shape with the largest area is kept for further processing. The boundary of this area represents the edge of the rope in the measurement plane. This area is also used like a digital mask for filtering the outliers in the velocity field.

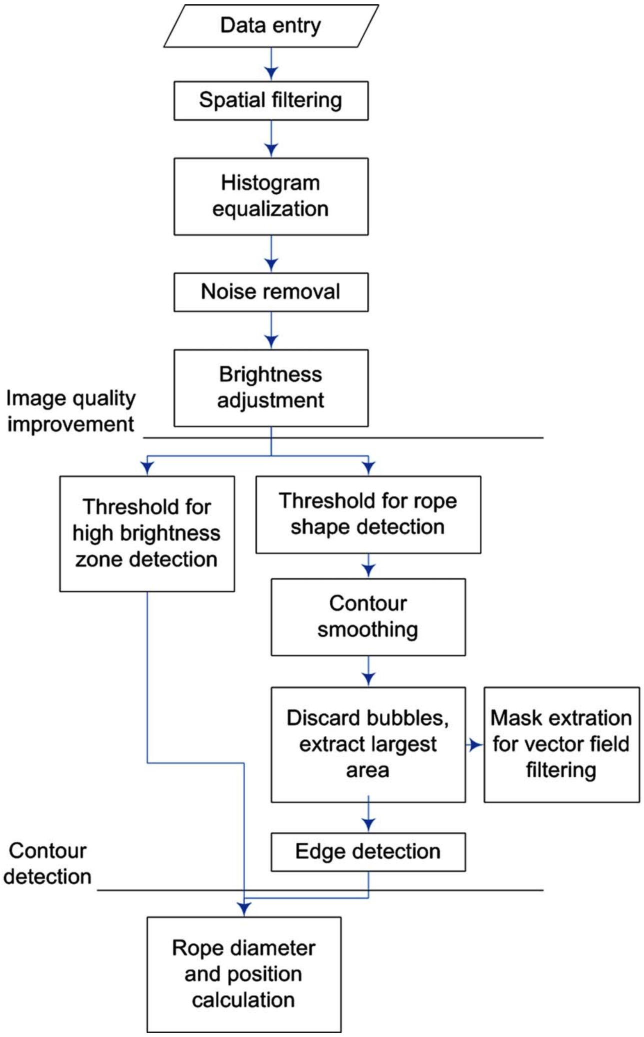

Fig. 5 Image-processing flowchart

A circular cross section of the rope was assumed throughout this evaluation. Thus, the intersection between the rope and the measurement plane is an elliptical contour. The parameters of the ellipse depend on the local geometrical characteristics of the conical rope helix (angle of incidence, local curvature radius, opening angle of the conical supporting surface). The best approximation of the real rope diameter in our case is the distance between the edges of the rope along a 45 deg direction, applied on the rope intersection with the measurement plane previously obtained. For a variation of the angle with ±10 deg, the induced error on the rope diameter is 2% R_{in}.

An example of a raw image superposed on the rope shape and the rope diameter obtained by image processing is presented in Fig. 6. A detailed description of the image-processing steps is given by Iliescu [21].

Then for each image, the rope center position and the rope diameter are available with an uncertainty of 2% R_{in}. The aberrant images are filtered on criteria of minimum/maximum dimension of the rope area and rope diameter. The rate of validated images is 95%.

4.2 Velocity Field Processing. For the Camera 2 image, the distortions of position coordinates and particle displacements are corrected through the calibration transform.

For the velocity field calculation, in order to eliminate the outliers in the region of the rope or due to the residual bubbles

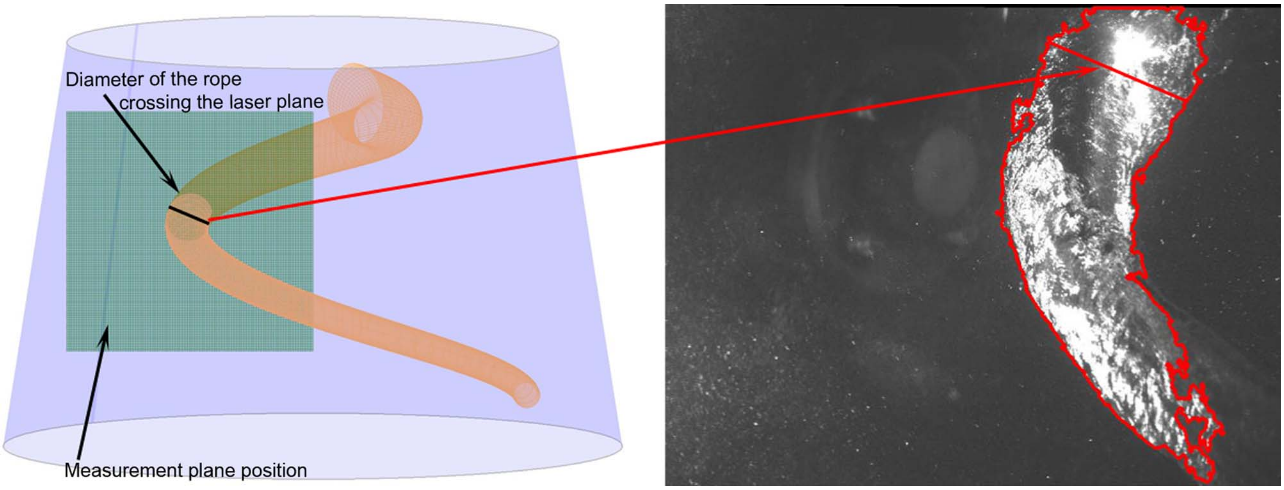

Fig. 6 Extraction of the rope diameter by image processing from each instantaneous image

shadow, a mask previously obtained by the image processing of the Camera 1 image is applied on the Camera 2 image. The raw vector maps are processed by cross correlation of the two frames from this masked image of the second camera. The results are filtered by range (vectors four times higher than the mean value are rejected) and peak (the relative height of the highest cross-correlation peak compared to the second highest is chosen 1.2) validation criteria. An example of velocity field is presented in Fig. 7; the instantaneous velocity field is superposed on the raw image for illustration. Statistical convergence is acquired with 1200 velocity fields for 3% uncertainty.

5 Flow Analysis

5.1 Velocity Phase Average. By ensemble averaging on phase of the instantaneous velocity fields, the mean velocity field is obtained in relation to the phase of the rope precession and for different volumes of the rope corresponding to σ values between 0.380 and 1.180. Assuming that the rope shape and the corresponding flow field remain constant over one revolution, the phase of the rope corresponds to its spatial angular position and the spatial velocity field can be reconstructed accordingly, see Fig. 8.

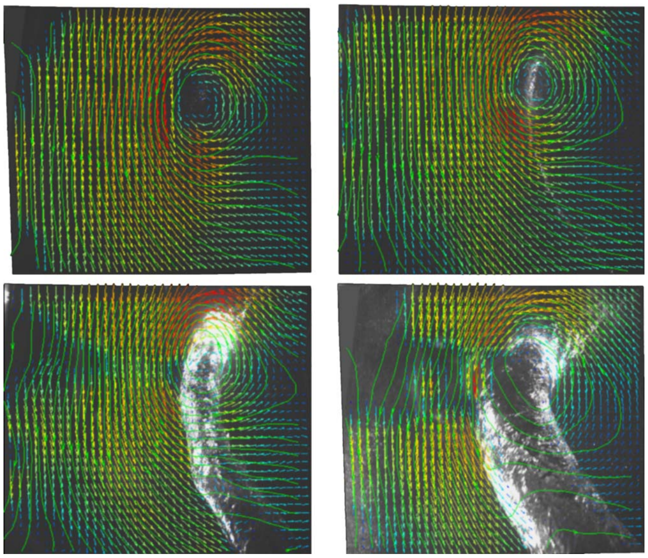

Fig. 7 Streamlines on instantaneous velocity fields for the same corresponding phase $\tau/T\sim=0.61$ and different σ values

The vortex structure is present for all the investigated σ values, and the core of this vortex, with a low pressure area set by the σ level, is cavitating and hence determines the rope volume. The cavity volume influences the flow field only locally.

As discussed by Ciocan et al. [10], the average flow velocity shows the decelerated swirling flow that develops in the central stagnation zone. The vortex encloses this zone of average velocity near zero.

The phase average velocity distribution is very similar for all σ values. While the flow rate is the same, the influence of the rope volume on the mean velocity field is comparable with the measurement uncertainty. Thus, in phase average, the flow structure is the same for all σ values, but a local modification of the velocity field and turbulent kinetic energy field in the near vicinity of the rope is expected. Unfortunately, for the moment, it is difficult to analyze this zone due to the lack of uncertainty near the rope boundary region, and strong and random reflections as well as shadows at the intersection of the rope with the laser sheet are observed.

5.2 Vortex Centerline for the Cavitation-Free Configuration. For the cavitation-free configuration, see Fig. 7 for $\sigma=1.180$, the vortex center is detected starting from the velocity field analysis. Four methods are commonly used, see Sadarjoen et al. [22], to detect its position:

- minimum of velocity
- streamline curvature centers density
- maximum of vorticity $|\nabla\times\mathbf{C}|$
- maximum of normalized helicity $\mathbf{C}\nabla\times\mathbf{C}/|\mathbf{C}||\nabla\times\mathbf{C}|$

In swirling flows, the main contribution to the vorticity is given by the mean tangential and axial components, and the vorticity profile is significant in the plane normal to the vortex filament. For the instantaneous velocity fields, the vorticity calculation is very sensitive to the relative position of the vortex and measurement plane. Consequently, computing the vorticity distribution only with the two measured velocity components does not have the proper physical meaning, nor has the helicity.

Due to the unsteadiness of the flow, an instantaneous velocity field may present zones of low velocity outside the vortex center zone. Thus, the minimum of velocity criterion, easy to implement, is not relevant in this case.

The second method, streamline curvature center density, is more consistent. By the streamline generation in each gridpoint, for each unsteady vector field, we compute the curvature centers of the streamlines, and the regions with high density of curvature centers indicate the presence of a vortex center. The center posi-

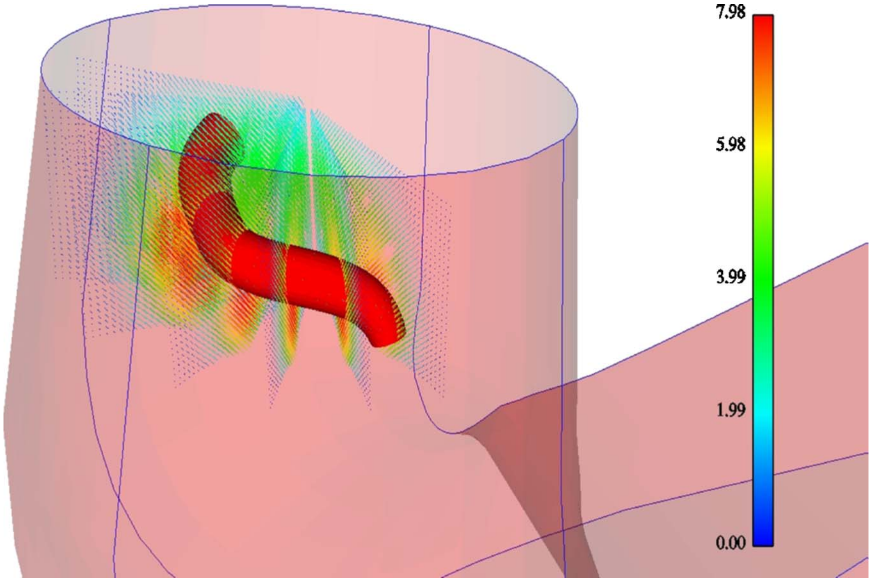

Fig. 8 Phase averaged vectors field for $\sigma=0.380$

tion is given by the mean of the curvature centers coordinates.

To speed up the computation time for the center detection, a combination of these two criteria has been used as vortex center-tracking algorithm. The streamline generation is performed only in the regions where the minimum velocity is obtained. The second method is applied afterwards to detect the vortex center. An instantaneous result, obtained by these two methods, see Fig. 9, shows a very good coherence of the center position within the measurement resolution range. The validation rate on instantaneous fields, based on coherent position criteria, is higher than 99%.

5.3 Rope Contour Phase Average. Starting from each image-processing result, for each rope precession phase and each σ value, the ensemble averaging by phase of the rope shape is performed, and thus the rope characteristics (position and diameter) in the measurement plane are determined.

Assuming that the angular velocity of the rope is constant over a rope revolution, i.e., assuming a solid body rotation of the rope, the rope precession temporal phase is transposed into angular position. In this way, the spatial position of the rope core is reconstructed in the turbine cone, see Fig. 10. Adding the measured diameters, in a plane normal to the core, leads to rendering the 3D rope shape, see Fig. 11.

For the same σ value, the rope center position and the mean

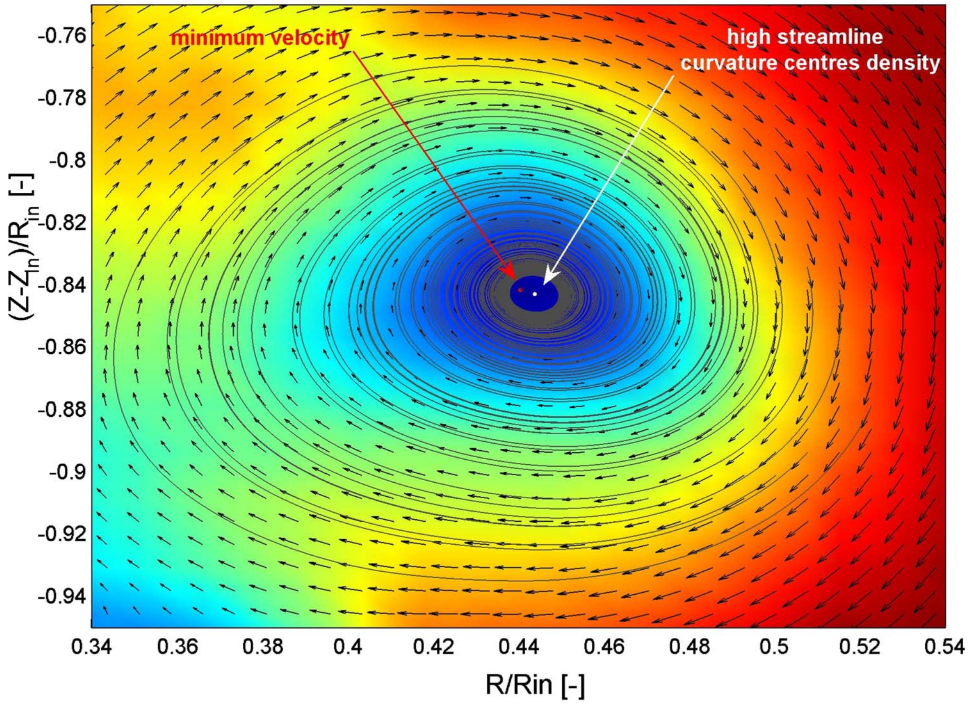

Fig. 9 Vortex center detection for noncavitating conditions

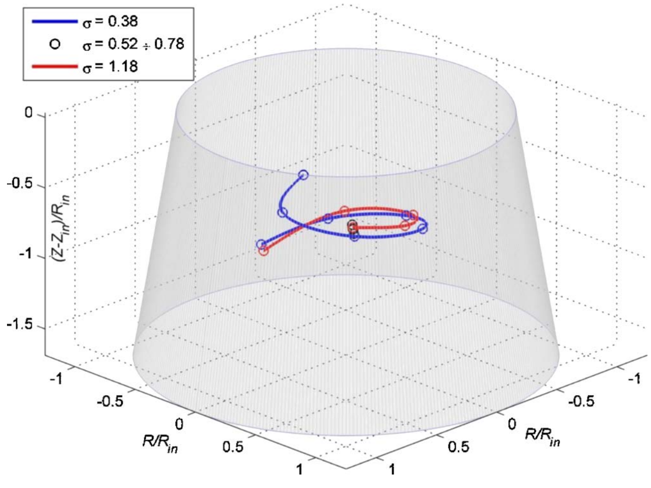

Fig. 10 Vortex centerlines for σ=0.380 and σ=1.180

value of the rope diameter are calculated, and the corresponding standard deviations are estimated for the entire measurement zone, See Fig. 12.

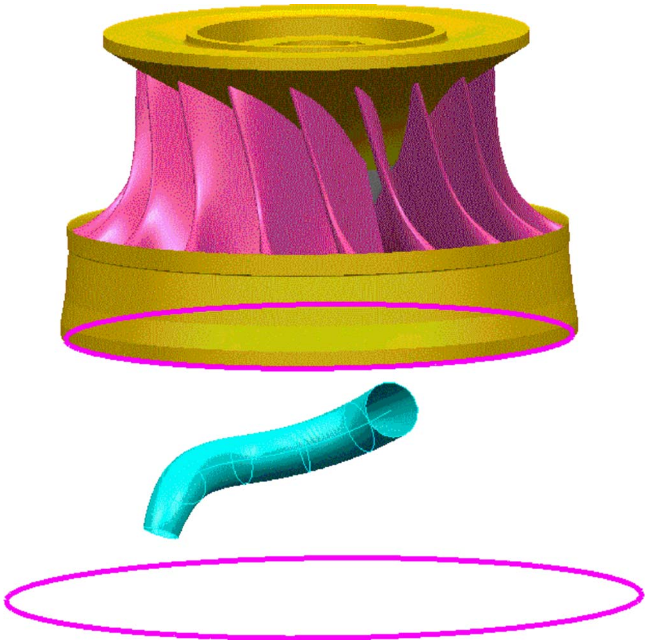

Fig. 11 Reconstruction of the rope volume

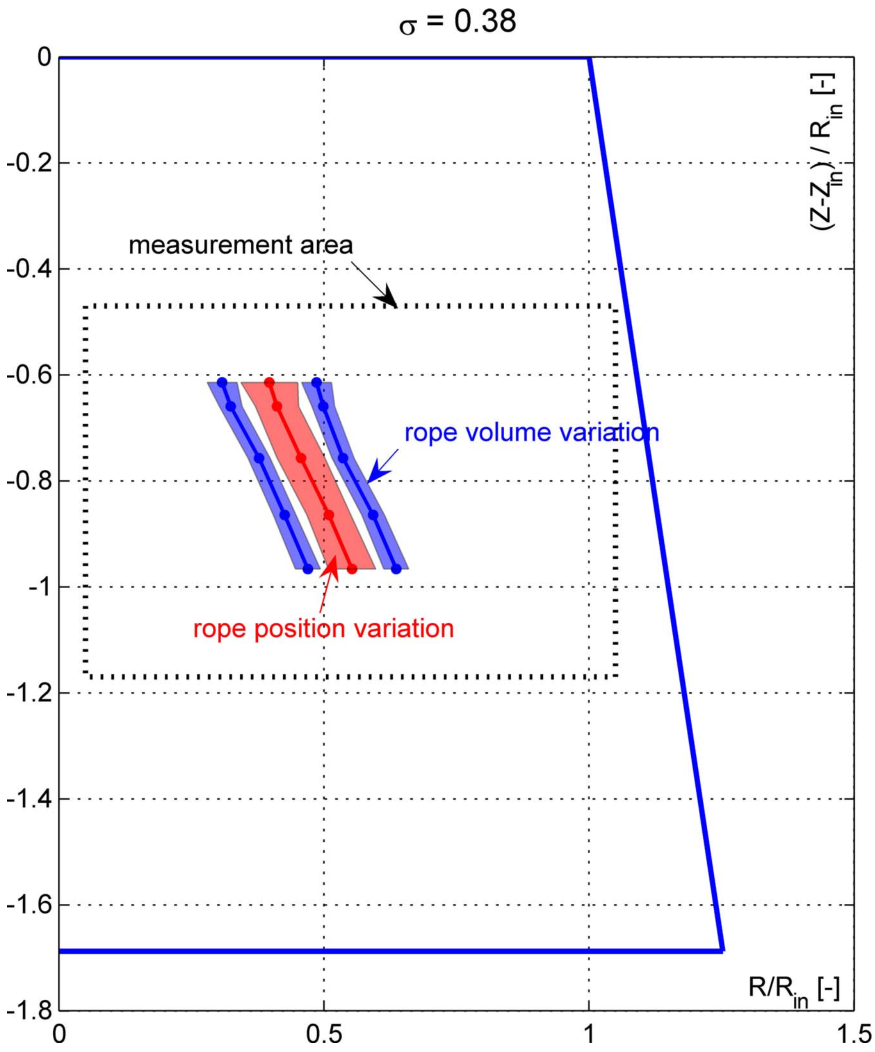

Fig. 12 Standard deviation of the rope position and rope volume

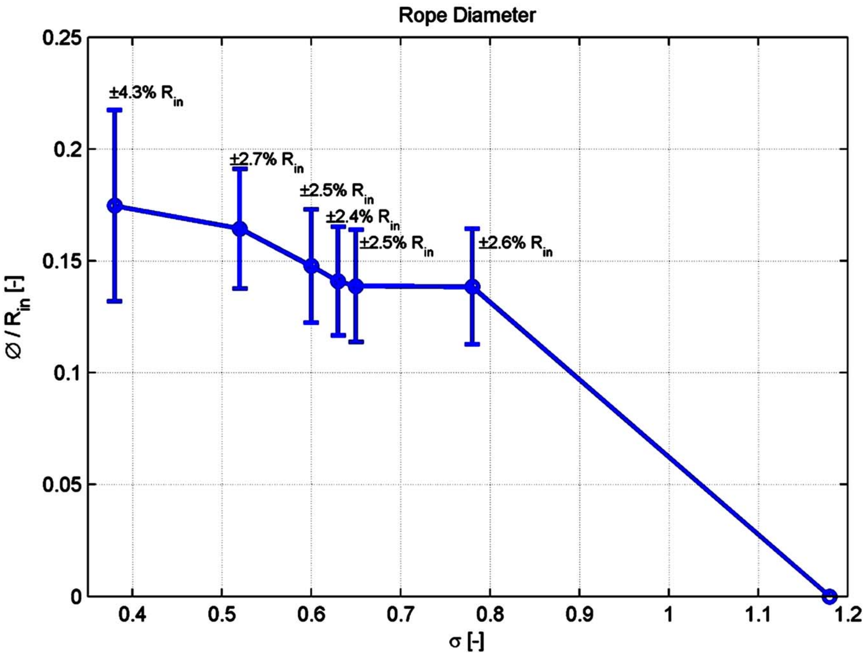

Fig. 13 Rope diameter variations versus the σ value

5.4 Flow Behavior Corresponding to σ Variation. The procedure to determine the geometrical parameter of the rope in phase average, already described, is applied for seven σ values. The rope diameters as well as the rope center position in the measurement zone are represented versus the σ value. Associated with these values, the standard deviations of the rope diameter and vortex center position are calculated, see Fig. 13.

The rope diameter decreases from low to high σ values. The standard deviation of the rope diameter is related to the rope diameter fluctuations and is a measure for the rope volume variation. This calculation is physically significant due to the axial pressure waves that act on the vapor cavity, resulting in a volume variation under the influence of the local change of pressure distribution. The standard deviations are quasiconstant for all σ values at 2.5% of $R_{\bar{1}e}$, except for the value 0.380, where it increases at 4.3% of $R_{\bar{1}e}$, see Fig. 13. For $\sigma=0.380$, the rope area referred to the local cone section area has a variation between 0.5% and 1.2%.

In fact, for the 0.380σ value, it was demonstrated by hydroacoustic simulation, see Nicolet et al. [23], that a pressure source located in the inner part of the draft tube elbow induces a forced excitation. This excitation represents the synchronous part of the vortex rope excitation. An eigenfrequency of the hydraulic system is also excited at 2.5 fn, see Fig. 4, and the plane waves, generated by the pressure source, propagate in all the hydraulic circuit. The

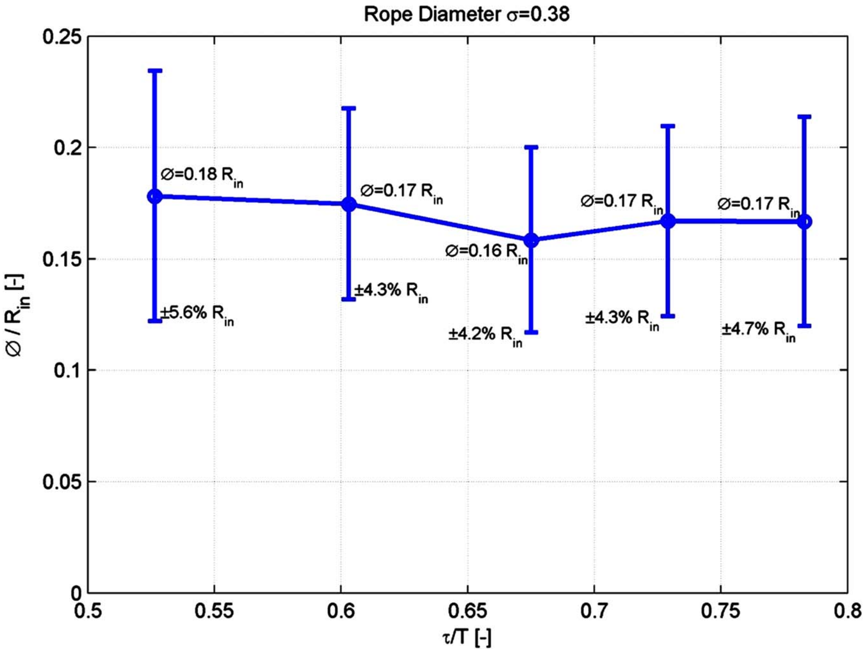

Fig. 14 Rope diameter variations versus the vortex phase τ

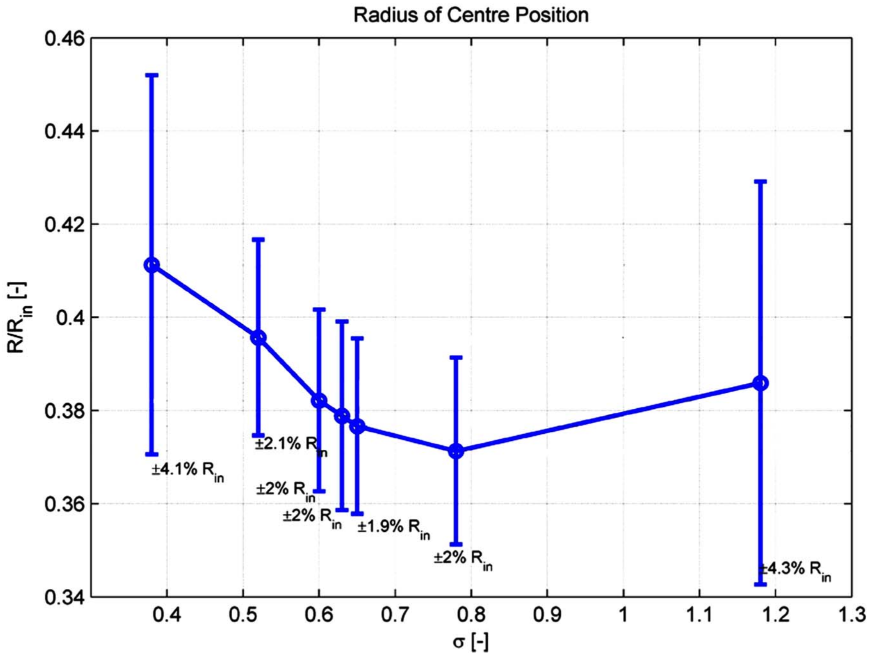

Fig. 15 Rope center variations versus the σ value

passing of the plane waves in the rope section induces successively an expansion and a contraction of the vapor volume of the rope, which explains the increase of the rope diameter standard deviation for this σ value.

For the lowest σ value, the rope diameter and its standard deviation remain virtually unchanged (the change is smaller than the measurement uncertainty) with respect to the precession phase angle over the measured domain, see Fig. 14.

The vortex center position is nearly constant between low σ values and cavitation-free conditions, see Fig. 15. For low σ values, the eccentricity of the rope position—the position of the rope center related to the cone symmetry axis—increases and thus the pressure amplitude fluctuation at the wall increases too, see Fig. 4. The standard deviation of the vortex center position is representative of the flow stability. For $\sigma=0.380$, the location of the rope center has an unsteady spatial variation of ~8% of the local radius of the cone. The resonance at this σ value induces a loss of stability of the rope position highlighted by the increase of the standard deviation of the vortex center position, i.e., it doubles from 2% to 4.1% R_{in}, except for the value 0.380, where it increases at 4.3% of R_{in}.

In the cone cross section, the rope center eccentricity (the radius of the rope center) increases following the phase evolution:

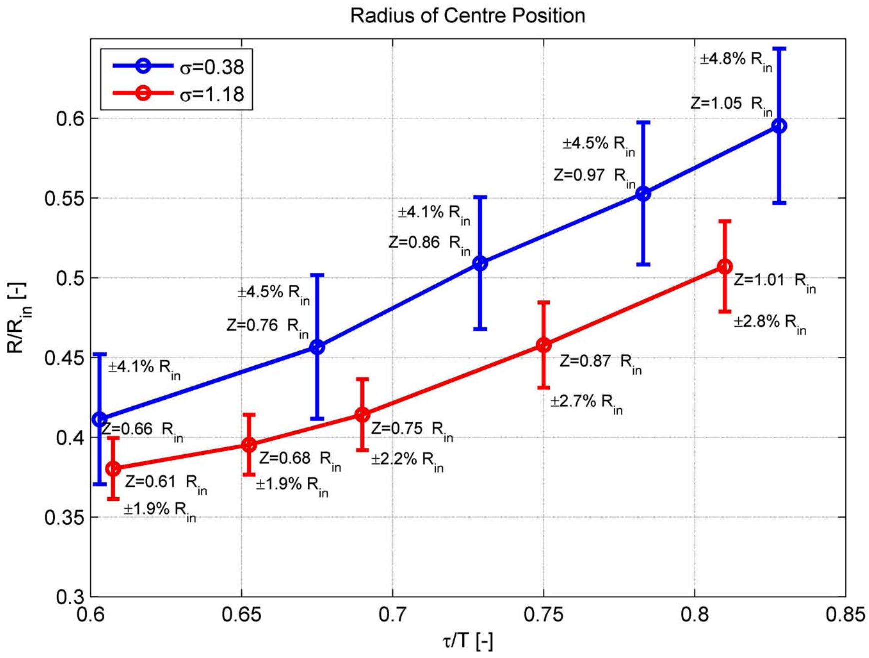

Fig. 16 Vortex position variations for σ1.180 and 0.380 values versus the vortex phase τ

the rope goes closer to the wall downstream in the cone. This evolution induces the increase of the wall pressure fluctuation synchronous with the rope rotation. The standard deviation corresponding to the rope position is quasiconstant for all phases (depth) in the measurement zone, see Fig. 16.

6 Conclusions

The PIV system gives the opportunity to survey the flow velocity field in the diffuser cone of a scale model of a Francis turbine at part load operating conditions with a precessing cavitation rope. From the experimental results, the complete description and quantification of the velocity, simultaneously with the rope boundary behavior, were obtained for different cavitation conditions.

The synchronization of the PIV acquisition with the rope position allows, by ensemble averaging, the reconstruction of the rope volume in correlation with the corresponding velocity field, in the cone of the turbine model. Image processing provides an estimation of the rope diameter and the positions of the vortex center in the measuring zone.

For a particular σ value that corresponds to a coincidence of the rope excitation with an eigenfrequency of the hydraulic circuit, the influence of the pressure source on the rope dynamics is shown.

An experimental database has been built and is now available for future validation of analytical modeling and numerical simulation of draft tube flows.

Acknowledgment

The authors wish to thank all the partners of the FLINDT II Eureka Project No. 1625: Electricité de France, Alstom Hydro, GE Hydro, VA Tech Hydro, Voith Siemens Hydro Power Generation, and the CTI, Swiss Federal Commission for Technology and Innovation, for their financial support and assistance. They also want to acknowledge the technical staff of the Laboratory for Hydraulic Machines for their efficient support.

Nomenclature

BEP = best efficiency operating point
C = mean absolute velocity (m/s)
C_p = pressure coefficient $C_p=(p-\bar{p})/1/2\rho c_{m\bar{1}}^2$ (-)
C_{ref} = mean flow reference velocity $C_{\text{ref}}=Q/\pi R_{\text{in}}^2$ (m/s)
$D_{\bar{1}e}$ = runner diameter (m)
E = specific energy (J/kg)
f_c = vortex rotation frequency (Hz)
Q = flow rate (m^3/s)
Q_{BEP} = flow rate at the best efficiency operating condition (m^3/s)
k = turbulent kinetic energy (m^2/s^2)
f_n = runner rotation frequency (Hz)
NPSE = net positive suction specific energy (J/kg)
R = local cone radius (m)
R_{in} = runner outlet radius (m)
Z = current cone elevation (m)
Z_{in} = runner outlet elevation (m)
ΔZ = cone height (m)
ω = rotational angular velocity (rad/s)
Φ = local rope diameter (m)
ψ = specific energy coefficient (-)
φ = flow rate coefficient (-)
σ = thoma number $\sigma=\text{NPSE}/E$ (-)
θ = vortex polar angle $\theta=2\pi f_c \tau$ (rad)
τ = rope phase (rad)

References

[1] Jacob, T., 1993, "Evaluation sur Modèle Réduit et Prédiction de la Stabilité de Fonctionnement des Turbines Francis," thesis, EPFL, Lausanne.

[2] Arndt, R., 2002, "Cavitation in Vortical Flows," Annu. Rev. Fluid Mech., **34**, pp. 143–175.

[3] Alekseenko, S. V., Kuibin, P. A., Okulov, V. L., and Shtork, S. I., 1999, "Helical Vortices in Swirl Flow," J. Fluid Mech., **382**, pp. 195–243.

[4] Okulov, V. L., 1995, "The Velocity Field Induced by Helical Vortex Filaments With Cylindrical or Conical Supporting Surface," Russ. J. Eng. Thermophys., **5**, pp. 63–75.

[5] Wang, X., Nishi, M., and Tsukamoto, H., 1994, "A Simple Model for Predicting the Draft Tube Surge," *Proceedings of the 17th IAHR Symposium*, Beijing, China, Sept. 15–19, Vol. 1, pp. 95–106.

[6] Philibert, R., and Couston, M., 1998, "Matrix Simulating the Gaseous Rope," *Proceedings of the 19th IAHR Symposium ()*, Singapore, Sept. 9–11, Vol. 1, pp. 441–453.

[7] Hocevar, M., Sirok, B., and Blagojevic, B., 2005, "Prediction of Cavitation Vortex Dynamics in the Draft Tube of a Francis Turbine Using Radial Basis Neural Network," Neural Comput. Appl., **14**, pp. 229–234.

[8] Zhang, R. K., Cai, Q. D., Wu, J. Z., Wu, Y. L., Liu, S. H., and Zhang, L., 2005, "The Physical Origin of Severe Low-Frequencies Pressure Fluctuations in Giant Francis Turbines," Mod. Phys. Lett. B, **19**(28–29), pp. 99–102.

[9] Susan-Resiga, R., Ciocan, G. D., Anton, I., and Avellan, F., 2006, "Analysis of the Swirling Flow Downstream a Francis Turbine Runner," ASME J. Fluids Eng., **128**, pp. 177–189.

[10] Ciocan, G. D., Iliescu, M. S., Vu, T., Nennemann, B., and Avellan, F., 2007, "Experimental Study and Unsteady Simulation of the FLINDT Draft Tube Rotating Vortex Rope," ASME J. Fluids Eng., **129**, pp. 146–158.

[11] Paik, J., Sotiropoulos, F., and Sale, M. J., 2005, "Numerical Simulation of Swirling Flow in Complex Hydroturbine Draft Tube Using Unsteady Statistical Turbulence Models," J. Hydraul. Eng., **131**(6), pp. 441–456.

[12] Adrian, R. J., 2005, "Twenty Years of Particle Image Velocimetry," Exp. Fluids, **39**, pp. 159–169.

[13] Kadambi, J. R., Charoenngam, P., Subramanian, A., Wernet, M. P., Sankovic, J., Addie, G., and Courtwright, R., 2004, "Investigations of Particle Velocities in a Slurry Pump Using PIV: Part 1, The Tongue and Adjacent Channel Flow," ASME J. Energy Resour. Technol., **126**, pp. 1–9.

[14] Dias, I., and Riethmuller, M. L., 1998, "Visualisation of the Forming Bubble and PIV Measurement of Surrounding Liquid Using Fluorescent Particles," *Proceedings of Eigth International Symposium of Flow Visualisation*, Sorrento, Italy.

[15] Lindken, R., and Merzkirch, W., 2000, "Velocity of Liquid and Gaseous Phase for a System of Bubbles Rising in Water," Exp. Fluids, **29**(7), pp. 194–201.

[16] Lindken, R., and Merzkirch, W., 2002, "A Novel PIV Technique for Measurements in Multiphase Flows and Its Application to Two-Phase Bubbly Flows," Exp. Fluids, **33**, pp. 814–825.

[17] Avellan, F., 2000, "Flow Investigation in a Francis Draft Tube: The FLINDT Project," *Proceedings of 20th I. A. H. R. Hydraulic Machinery and Systems*, Charlotte, No, Aug. 7–9, Vol. 1, Paper No. DES-11.

[18] IEC 60193 Standard, 1999, "Hydraulic Turbines, Storage Pumps and Pump-Turbines-Model Acceptance Tests," International Electrotechnical Commission, Genève, Nov.

[19] Soloff, S. M., Adrian, R. J., and Liu, Z.-C., 1997, "Distortion Compensation for Generalized Stereoscopic Particle Image Velocimetry," Meas. Sci. Technol., **8**, pp. 1441–1454.

[20] Iliescu, M. S., Ciocan, G. D., and Avellan, F., 2004, "Experimental Study of the Runner Blade-to-Blade Shear Flow Turbulent Mixing in the Cone of Francis Turbine Scale Model," *Proceedings of the 22nd IAHR Symposium on Hydraulic Machinery and Systems*, Stockholm, Sweden, Jun. 29–Jul. 2.

[21] Iliescu, M. S., 2007, "Large Scale Hydrodynamic Phenomena Analysis in Turbine Draft Tubes," thesis, EPFL, no. 3775, Lausanne.

[22] Sadarjoen, A. I., Post, F. H., Ma, B., Banks, D. C., and Pagendarm, H.-G., 1998, "Selective Visualization of Vortices in Hydrodynamic Flows," *Proceedings of IEEE Visualization*, Los Alamitos, CA, Oct. 18–23.

[23] Nicolet, C., Arpe, J., and Avellan, F., 2004, "Identification and Modeling of Pressure Fluctuations of a Francis Turbine Scale Model at Part Load Operation," *Proceedings of the 22nd IAHR Symposium on Hydraulic Machinery and Systems*, Stockholm, Sweden, Jun. 29–Jul. 2.

Performance of Two-Equation Turbulence Models for Flat Plate Flows With Leading Edge Bubbles

S. Collie

M. Gerritsen

P. Jackson

Stanford Yacht Research,
367 Panama Street,
Stanford, CA 94305-2220

This paper investigates the performance of the popular k-ω and SST turbulence models for the two-dimensional flow past the flat plate at shallow angles of incidence. Particular interest is paid to the leading edge bubble that forms as the flow separates from the sharp leading edge. This type of leading edge bubble is most commonly found in flows past thin airfoils, such as turbine blades, membrane wings, and yacht sails. Validation is carried out through a comparison to wind tunnel results compiled by Crompton (2001, "The Thin Aerofoil Leading Edge Bubble," Ph.D. thesis, University of Bristol). This flow problem presents a new and demanding test case for turbulence models. The models were found to capture the leading edge bubble well with the Shear-Stress Transport (SST) model predicting the reattachment length within 7% of the experimental values. Downstream of reattachment both models predicted a slower boundary layer recovery than the experimental results. Overall, despite their simplicity, these two-equation models do a surprisingly good job for this demanding test case. [DOI: 10.1115/1.2829596]

Keywords: turbulence, leading edge bubble, computational fluid dynamics

1 Introduction

In this study, we investigate the performance of the SST and k-ω turbulence models for thin leading edge bubbles of the type found in the flow past flat plates at shallow incidence. The numerical results are compared with the high-quality wind tunnel data obtained by Crompton [1]. The wind tunnel data allow for an accurate validation of simulation results. The test case is unique and poses a challenging assignment for two-equation turbulence models. The notable features of the flow field are unsteady shear layer flapping, shear layer transition, relaminarization, secondary recirculation, flow reattachment, and postreattachment boundary layer recovery. Each of these flow features directly challenges the assumptions from which many turbulence models are derived. The current investigation focusses on two-equation turbulence models that are generally viewed as the most practical models for industrial engineering applications. Of these models the k-ω and Shear-Stress Transport (SST) models are considered amongst the best for flows involving separation [2]. A preliminary Large Eddy Simulation (LES) study is also conducted and reported in the discussion section.

Both Crompton's study and this work were motivated by the desire to improve physical understanding and simulation of flows past yacht sails. The thin airfoil bubbles investigated here will usually exist for sails that are not supported by a mast (i.e., headsails such as genoas and jibs, or downwind sails such as spinnakers and gennakers). The bubbles significantly influence the pressure distribution and lift generated by such sails. The flexible nature of such sails is an important design consideration. Aeroelastic studies are ultimately needed to create the design that produces the desired flying shape. However, the nature of flows past downwind sails is not yet well understood, and the first question that must be answered is what sail shape provides the best aerodynamic performance. This work contributes to improving our understanding of downwind sail flows [3]. Thin airfoil bubbles occur in many other flows, such as flows past thin airfoils and membrane wings, and therefore this work is also of direct interest to a much wider range of fluid flow problems than those in the sailing community.

2 Flow Past Flat Plate at Shallow Incidence

2.1 Flow Structure. A schematic of the flow past the flat plate is provided in Fig. 1. This flow structure was first described in the experimental work of Gault [4] where he described the bubble as being vastly different from leading edge bubbles typically found on airfoils. The shear layer that separates from the leading edge is immediately unstable. Vortices are shed periodically from the tip of the plate and advected along the shear layer. Driver et al. [5] observed a similar vortex shedding in the mixing layer behind a backward facing step and referred to the phenomenon as shear layer flapping. Both the backward facing step flow of Driver et al. and the flow past the flat plate at shallow incidence involve a turbulent shear layer that separates from a point and reattaches some distance downstream. For the backward facing step of Driver et al., the performance of k-ε models have been shown to give poor results compared with the k-ω and SST models [6,7].

In Crompton's experiments, the separated shear layer was found to undergo transition within the first 2.5% of the length of the plate. Downstream of transition, turbulent kinetic energy is entrained rapidly due to high mean shear across the shear layer. This entrainment of turbulent kinetic energy causes the shear layer to thicken and curve back toward the surface of the plate. As the shear layer approaches the surface of the plate, the velocity fluctuations in the direction normal to the plate are damped. Energy from the normal fluctuations is converted to the other components of the Reynold stress tensor, with the turbulent eddies stretching in the spanwise and streamwise directions. The flow reattaches some distance, X_R, downstream of the leading edge. Here, the flow bifurcates with the bulk of the flow continuing along the length of the plate, while a smaller fraction is driven back toward the leading edge to complete the leading edge bubble. The boundary layer that forms downstream of the reattachment point is embedded with turbulent structures that are a legacy from the leading edge bubble. These mixing layer structures advect downstream

---

Contributed by the Fluids Engineering Division of ASME for publication in the JOURNAL OF FLUIDS ENGINEERING. Manuscript received June 6, 2005; final manuscript received July 26, 2007; published online January 24, 2008. Review conducted by Surya P. Vanka.

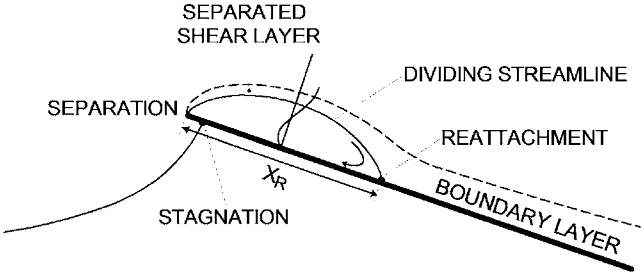

Fig. 1 Schematic of the flow past a flat plate at shallow incidence

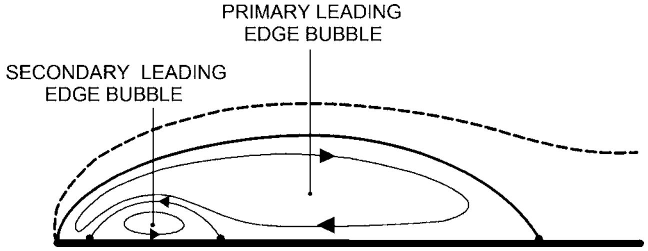

Fig. 2 Schematic of the leading edge bubble illustrating the secondary bubble near the leading edge

and interact with the development of the boundary layer.

The recovering turbulent boundary layer has a unique structure that is atypical of turbulent boundary layers; it is sluggish and prone to boundary layer separation in adverse pressure gradient flows. Naturally, the structure of the boundary layer during recovery dictates the size and structure of any trailing edge separation region that might form downstream. Consequently, the nature of the boundary layer after reattachment can have a significant impact on the lift coefficient. Naturally, the shape and structure of the separation region itself affect the pressure peak near the leading edge, which is the primary contributor to lift. The interaction between the leading edge bubble and the trailing edge separation region is as yet not fully understood.

The type of leading edge bubble found on the flat plate at shallow incidence is also known as the thin airfoil bubble. It should not be confused with the short bubble, or laminar separation bubble, which often appears on low Reynolds number airfoils due to laminar separation near the nose [8]. The primary difference between the two bubble types is that the shear layer in the thin airfoil bubble is predominantly turbulent, whereas the shear layer in the short bubble is typically laminar over more than half the length of the bubble. The difference here is that the laminar bubble separates due to the presence of an adverse pressure gradient, whereas the thin airfoil bubble is forced to separate abruptly as the flow rounds the leading edge.

2.2 Experimental Data. Of the experimental results concerned with the flat plate at shallow incidence, the thesis by Crompton [1] is the most comprehensive. Crompton presents a detailed examination of the bubble structure, which extends upon earlier work by Gault [4] and Newman and Tse [9]. The blunt plate experimental studies of Cherry et al. [10] as well as Kiya and Sasaki [11] also provide insight to separated and reattaching flows. However, these flows involve large scale unsteadiness due to the blunt rectangular shaped leading edge. Due to this difference in leading edge geometry, such flows are less suitable for the validation of sail flow simulations compared with the Crompton data.

Through the use of laser Doppler anemometry (LDA), Crompton was able to obtain accurate measurements of the velocity and turbulence statistics for the leading edge bubble. LDA measurements of the developing turbulent boundary layer in the recovery region downstream of the reattachment point were also taken. Surface pressures were recorded through static pressure tappings. Flow visualization techniques (surface tufts, china clay, and oil streakline) were used to complement the LDA and static pressure data. Unfortunately, no skin friction measurements were conducted in the experiments.

In his experiments, Crompton detected a secondary separation bubble very close to the leading edge of the plate, which had not been witnessed in previous studies (see Fig. 2). The secondary bubble is created as the reversed flow within the leading edge bubble separates due to the adverse pressure gradient that exists over the forward half of the bubble. The reversed flow is particularly prone to separate due to relaminarization of the reversed flow [1].

The wind tunnel model used in Crompton's experiments had a chord length of 160 mm and a span of 800 mm, giving an aspect ratio of 5, which was demonstrated (using oil-streakline flow visualization) to be sufficient to provide nominally two-dimensional flow [1]. The plate was constructed out of a 6 mm steel plate, giving a thickness to chord ratio of 3.75%. This thickness provided enough stiffness to minimize deflection and also facilitated the use of pressure tappings. The leading edge of the plate was chamfered at 20 deg to provide the sharp leading edge required for knife edge separation to occur exactly at the tip of the plate. A cross section of the model is illustrated in Fig. 3.

Crompton's experiments were carried out over a range of Reynolds numbers (0.1×10^5–5.5×10^5) to investigate Reynolds number dependency. The reattachment length was found to be independent of Reynolds number above 10^5. Also, the Reynolds number was not found to have an influence on the flow downstream of the reattachment point (because of the turbulent reattachment process).

The primary wind tunnel investigation was performed at a Reynolds number of 2.13×10^5, and it is at this Reynolds number that a comparison between the experiments and computational fluid dynamics (CFD) have been made. The experimental data are provided for angles of attack, $\alpha=1-5$ deg, in 1 deg intervals. At $\alpha=1$ deg, the leading edge bubble is small and similar in length to chord ratio to leading edge bubbles observed for downwind sail flows in the University of Auckland's twisted flow wind tunnel [3]. At $\alpha=5$ deg, the flow is separated for most of the plate, and at $\alpha=6$ deg, the shear layer fails to reattach. The asymmetry of the plate creates a lift force even at zero degrees of incidence, which causes the flow to curve upward (in the direction of the lift axis) near the leading edge of the plate; consequently, a small leading edge separation bubble forms at zero angle of attack. The so-called "ideal" angle of incidence, where laminar boundary layers are able to develop on both surfaces without leading edge separation, occurs at a small negative angle.

3 Computational Fluid Dynamics Model

3.1 Turbulence Models and Numerical Solvers. The software used in this study is CFX-5, an unstructured commercial CFD package [12]. In the CFX-5 solver, the Reynolds Averaged Navier-Stokes Equations (RANS) equations are discretized using a conservative and time-implicit finite volume method and are solved using an additive correction algebraic multigrid (AMG) solver, accelerated with an incomplete lower upper (ILU) factorization technique. Details of these techniques and their implementation can be found in Refs. [12,13]. Spatial interpolation is carried out using the second-order upwind advection scheme, details

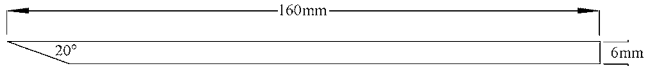

Fig. 3 Model dimensions

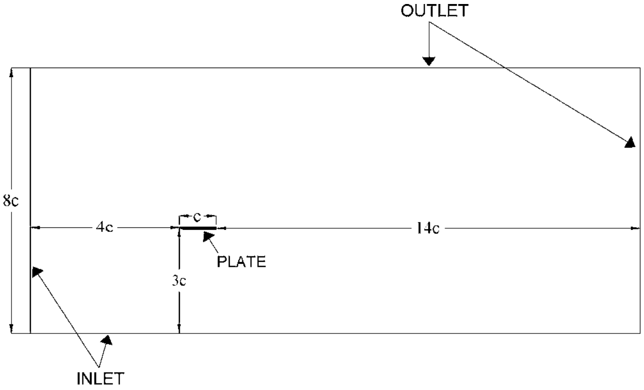

Fig. 4 Details of the domain for the flat plate

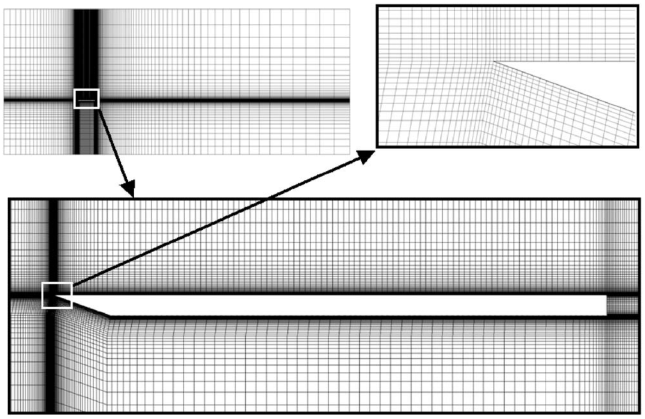

Fig. 5 Computational grid for the flat plate (medium resolution)

of which can be found in Ref. [12]. The simulations were carried out using the SST [14] and standard k-ω [15] turbulence models and all simulations converged to a steady state with all residuals decreasing by at least four orders of magnitude. Crompton [1] reported evidence of shear layer unsteadiness at the leading edge. However, in this CFD, no evidence of unsteadiness was found, even when very small time steps were used.

Simulations were also carried out using the standard k-ε model for comparative purposes. However, it was found that the algebraic wall functions used to capture the inner portion of the boundary layer in these models do not perform well for this flat plate flow. The wall functions assume that the inner boundary layer region is in turbulent equilibrium, which is not the case here, especially within the leading edge bubble. The k-ε model was found to diverge for the fine grids that were used in this study, and convergence was obtained only on grids much coarser than desired. Consequently, only results computed using the k-ω and SST models are presented in this paper.

3.2 Computational Domain and Gridding. Crompton's flat plate was modeled using the same geometry as in the experiments (Fig. 3). The computational domain is illustrated in Fig. 4. Simulations performed using a domain twice the size verified that the domain dimensions of Fig. 4 were adequate in that the proximity of the far-field boundaries did not affect the near field. At the inlet, Cartesian velocity components were specified according to the angle of incidence. The freestream turbulence intensity was set at 0.05%, which was the maximum value measured during the wind tunnel experiments [1]. The turbulent length scale was set at $0.001m$, a typical value for low turbulence wind tunnels. At the outlet, the static pressure is set at zero, and a constant gradient constraint is imposed on turbulence quantities.

Block-structured grids were generated in ICEM-HEXA [16]. Three grid resolutions were used. We refer to the grids as coarse, medium, and fine with 11,920, 49,625, and 202,435 cells, respectively. The medium and fine grids were constructed from the coarse and medium grids, respectively, by grid halving in both directions. A grid convergence study is presented in Sec. 4.1. The medium grid is illustrated in Fig. 5. In order to achieve a y^+ of around 1.0, the near-wall spacing was set at 1.0×10^{-5} m. Particular care was taken to provide high quality cells around the leading edge. The grid cells have an aspect ratio of 1:1 at the tip. The tip region is illustrated in the close-up view in Fig. 5. Along the plate, the aspect ratio of the near-wall cells is gradually increased to take advantage of the relatively small flow gradients tangential to the wall compared with those in the wall normal direction. The maximum cell aspect ratio, which occurs at the trailing edge, is set at 1:10.

4 Results

This section initially focuses on the case at $\alpha=1$ deg, for which the flow is most similar to flows past downwind sails. At this angle, the leading edge separation bubble stretches across the first 14% of the chord length (i.e., $X_R/c=0.14$), which is approximately the same as for downwind sail flows. Since the bubble at this angle is small, fewer velocity measurements were taken within the bubble at this angle than at the higher angles of attack. Therefore, we also investigated the case of $\alpha=3$ deg in order to gain a better understanding of the flow within the separation bubble. For $\alpha=3$ deg, the reattachment length $X_R/c=0.47$, which shows that the flow is separated over almost half of the plate. For $\alpha=5$ deg, the flow is almost fully separated and does not have a recovery region. We have therefore left this case out of the main discussion and refer to it only briefly when comparing the accuracy of the turbulence models in predictions of the reattachment length (Sec. 4.2).

4.1 Grid Convergence Study. A grid convergence study was performed at $\alpha=3$ deg with the SST turbulence model. At $\alpha=1$ deg the results are not as grid dependent since there the flow separation is much less severe than at $\alpha=3$ deg. Lift and drag coefficients are presented in Fig. 6 for the sequence of grids. The force coefficients are plotted against $1/N$, a nondimensional measure of the grid spacing, with N^2 as the total number of cells in the grid.

The lift and drag coefficients converge as the grid is refined. The lift from the medium grid solution is within 0.015% of the fine grid solution and the drag is within 0.0055%. Subsequent refinement is unlikely to result in improved accuracy of the solution; therefore, the medium grid was used for the simulations reported in the remainder of this paper.

4.2 Reattachment Lengths. Figure 7 presents the reattachment length data for each angle of attack (1–5 deg). At low angles of attack, the SST model captures the reattachment length accurately. However, at larger angles, it underpredicts the reattachment length. In contrast, the k-ω model consistently overpredicts the length of the leading edge bubble. The reasons and consequences of this are discussed in Secs. 4.3 and 4.4.

4.3 Comparison at $\alpha=1$ deg

4.3.1 Boundary Layer Profiles in the Leading Edge Bubble. Boundary layer velocity profiles were measured by Crompton at nine different chordwise locations along the plate using LDA. The measurement stations are located at $x/c=\{0.031, 0.125, 0.25, 0.375, 0.5, 0.625, 0.75, 0.875, 1.0\}$. Figure 8 shows the position of these measurement stations in relation to the flow field at α

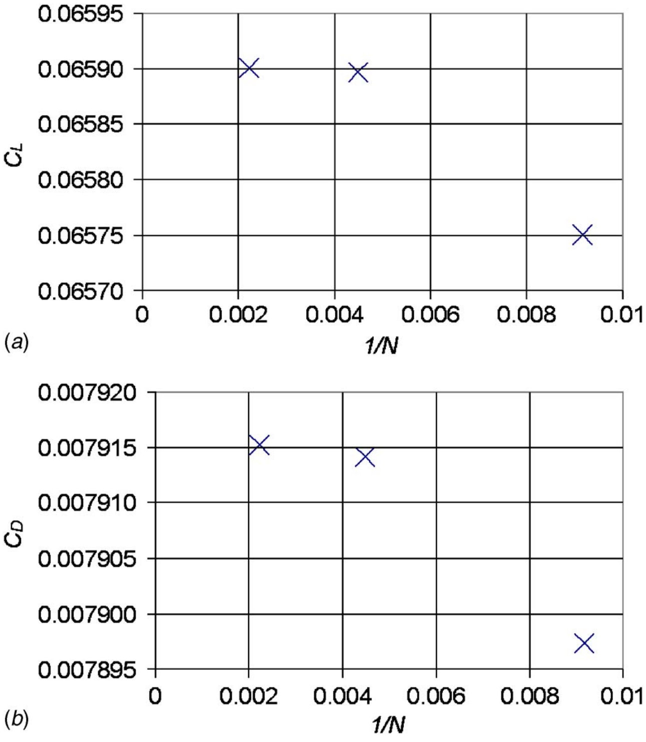

Fig. 6 Grid convergence of the lift and drag coefficients (α =3 deg)

Table 1 Reattachment lengths for the flat plate at α=1 deg

	X_R
Crompton	0.14
SST	0.1486
k-ω	0.1841

=1 deg.

Table 1 shows that the reattachment lengths computed with the SST and k-ω models differ from the experimental values. The SST model overpredicts X_R by 5.8% and the k-ω model overpredicts X_R by 24.0%. To allow a better comparison between the boundary layer profiles, the measurement stations are scaled by X_R so that each station is in the same position relative to the reattachment point. For α=1 deg only the first two measurement stations are within the leading edge bubble. The profiles at these stations are shown in Fig. 9.

The portion of the fluid forced upstream at the reattachment point is accelerated by the favorable pressure gradient and forms a reversed boundary layer. Crompton reported a maximum reversed velocity of $-0.4U_\infty$, approximately midway along the bubble. The CFD results show lower reversed velocities at the same position along the bubble, with the SST model predicting $-0.290U_\infty$ and the k-ω model predicting $-0.284U_\infty$. The measured velocities within the leading edge bubble are larger than usually experienced within short airfoil bubbles, for which the reversed flow velocity is typically below $-0.2U_\infty$ [1]. For the thin airfoil bubble, however, early transition results in a high rate of entrainment of turbulent kinetic into the bubble. Subsequently, greater velocities in both the outer and inner shear layers are observed. The turbulence models underpredict the entrainment rate and hence also underpredict the velocity magnitude throughout the leading edge bubble. This will be discussed further in Sec. 4.4, where the kinetic energy profiles within the separation bubble are presented.

Crompton reported that the reversed flow within the leading edge bubble experienced relaminarization, encouraged by the strong favorable pressure gradient, and that the inner shear layer began to show very laminarlike features. The velocity profiles within the separation bubble are presented in greater detail in Fig. 10. At x/c=0.031, in particular, the experimental data show a much more laminar profile than those provided by the CFD. To

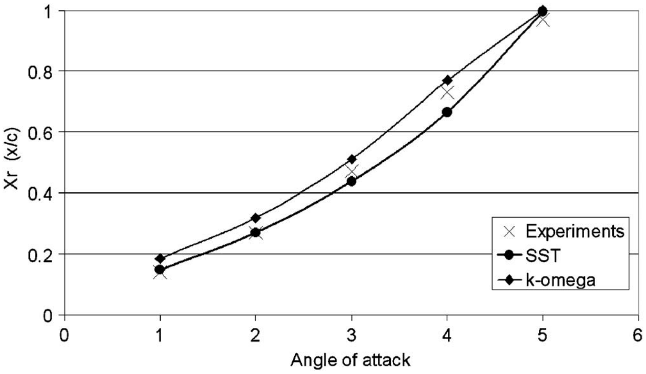

Fig. 7 Reattachment lengths versus angle of attack for the CFD compared with Crompton's data

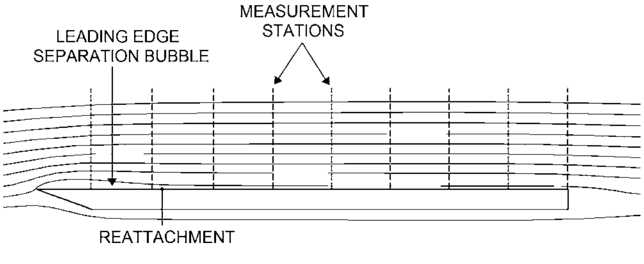

Fig. 8 Flow streamlines and the measurement stations for the flate plate at α=1 deg (SST model)

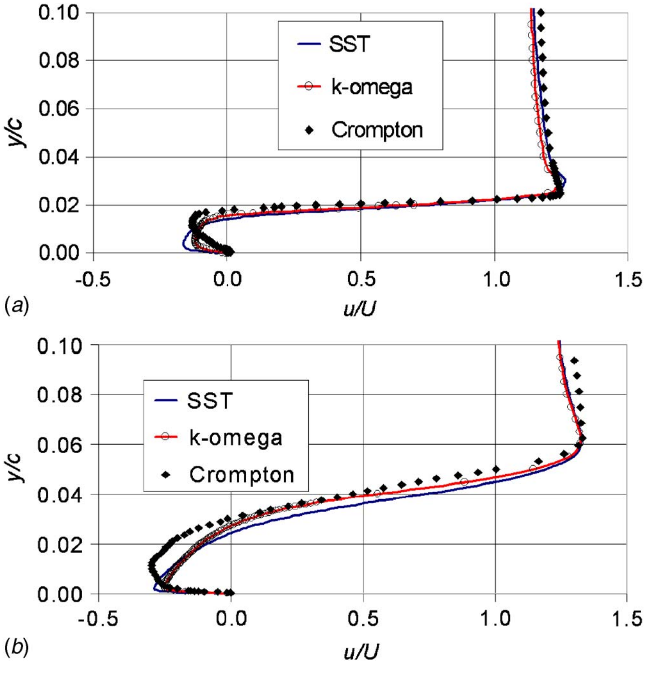

Fig. 9 Chordwise velocity profiles within the leading edge bubble (α=1 deg). (a) x/c=0.031, (b) x/c=0.125.

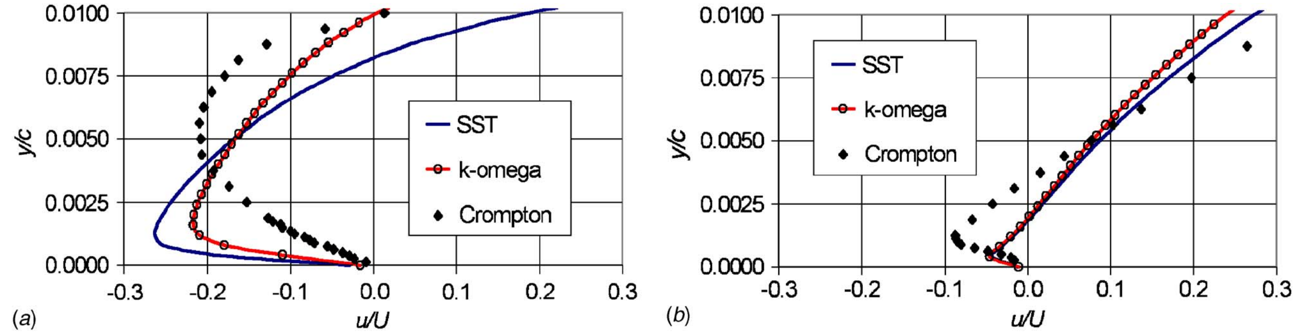

Fig. 10 Near-wall chordwise velocity profiles within the leading edge bubble (α=1 deg). (a) x/c=0.031, (b) x/c=0.125.

emulate the relaminarization process, an appropriate transition model is required, which is not provided by the turbulence models investigated.

One of the direct consequences of the more turbulentlike boundary layer profiles given by the CFD is their resistance to separation. In the simulations, the reversed boundary layer remains attached all the way to the leading edge, and there is no secondary separation of the type reported by Crompton. Crompton suggested that the form of this second bubble has significant influence on the development of the shear layer near the leading edge; consequently, its influence is likely to spread well downstream [1].

4.3.2 Boundary Layer Profiles Downstream of Reattachment. In Fig. 11, the boundary layer profiles at x/c=0.25 and 0.875 are presented using a log scale for y^+. Also plotted is a typical turbulent boundary layer at zero pressure gradient (ZPG) [17]. The wall shear stress τ_w was not provided in the experimental results; therefore, it was difficult to nondimensionalize the Crompton data. Here, y^+ and u^+ are calculated based on the τ_w values from the CFD data computed using the SST model. Any errors introduced by this approximation are likely to be small. The nondimensionalized plots in Fig. 11 follow the same trends as data compared using the raw velocity, U, and normal distance, y.

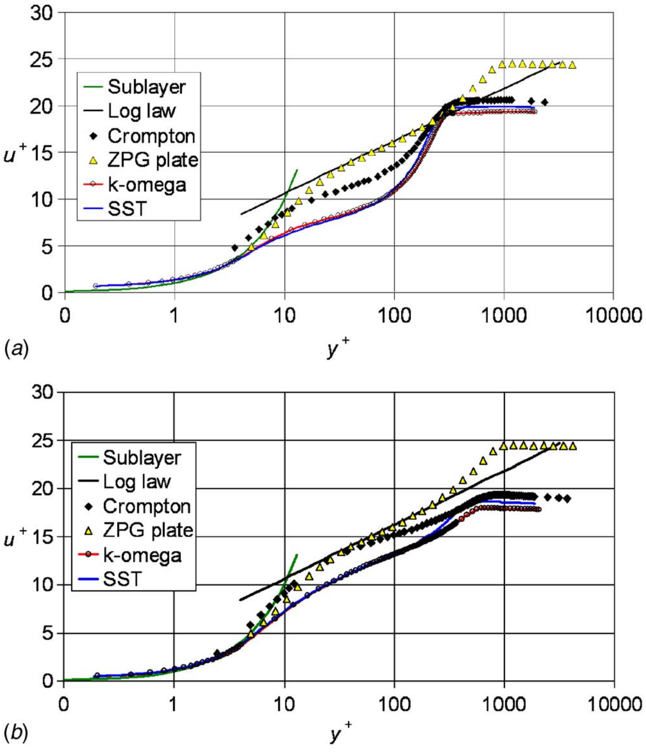

Fig. 11 Chordwise velocity profiles downstream of reattachment (log scale, α=1 deg). (a) x/c=0.250, (b) x/c=0.875.

At x/c=0.25, the boundary layer profiles given by the experiments and the CFD lie below the ZPG profile. This is expected because of the slight adverse pressure gradient the boundary layer works against. The velocities predicted by the CFD are smaller than those measured. We attribute this difference to the reattachment process.

The boundary layer profile at reattachment has a shape distinctive of reattaching turbulent shear layers. These layers are characterized by a linear increase in velocity from the wall out toward the boundary layer edge [18]. The figures show the inner structure of the recovering boundary layer developing just downstream of the reattachment point. The layer is accelerated through the inward entrainment of momentum from the outer region. Both experimental and CFD results show the sublayer developing with its characteristic thin region of steep velocity gradients. Moving further aft from the reattachment point, the boundary layer starts to show a typical turbulent boundary layer profile: The sublayer thickens, and the mixing layer structures in the outer region of the boundary layer spread and dissipate. At x/c=0.875, the inner region of the boundary layer appears to have recovered in the experiments and shows a profile similar to ZPG up to $y^+ \approx 50$. The outer region of the boundary layer—while showing its characteristic defect layer shape—still predicts low velocities and is yet to recovery fully.

The delayed postreattachment recovery of the boundary layers predicted by the CFD was also observed by So and Lai [19] for flow past a backward facing step. In their experiments, wall function based models produced better results in the recovery region than low Reynolds number turbulence models. This is not surprising because wall functions, which are based on local-equilibrium arguments, force the flow to asymptote to the log law of wall.

As a final note on the boundary layer profiles, Fig. 11 shows that the k-ω model predicts profiles that are slightly closer to the measured profiles than those predicted by the SST model. This is believed to be the consequence of the SST limiter on the eddy viscosity, which leads to less production of turbulent kinetic energy.

4.3.3 Pressure Distributions. The pressure coefficient plot for the flat plate at α=1 deg is presented in Fig. 12. In the experimental data, the pressure decreases downstream of the leading edge and reaches a minimum at $x/c \simeq 0.045$. The CFD results show a lower and flatter suction peak. They do not experience the gradual decrease in pressure over the forward half of the separation bubble that is seen in the experimental result because of the inability of the turbulence models to predict the correct transition location and resolve the secondary recirculation region. The experiments show a leading edge bubble that is shorter and fatter, indicating greater shear layer curvature. Within the leading edge bubble, the pressures, which are determined predominantly by the

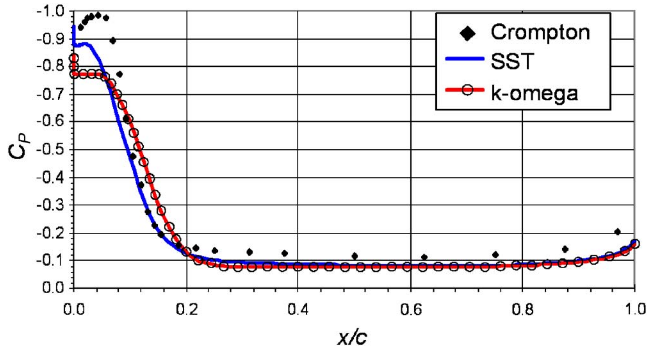

Fig. 12 Pressure coefficient plot (α=1 deg)

curvature of the outer shear layer, are lower. The shear layer is initially laminar and able to sustain a positive pressure gradient before transition. It is possible that background turbulence in the experiments may have helped to increase the curvature of the shear layer. Because the freestream turbulence intensity in the experiments was less than 0.25%, background turbulence was not likely to have caused an increase in shear layer curvature.

As shown in Fig. 12, the k-ω model predicts lower pressures than the SST model and the experimental data between $x/c=0.1$ and $x/c=0.2$. This is in agreement with the model overpredicting the length of the separation bubble.

When the C_P curves are normalized based on reattachment length, the pressure profiles compare well. The only significant differences are a larger suction at the leading edge in the experimental data and a particularly low suction peak predicted by the k-ω model. Downstream of reattachment, the pressure coefficients in the experimental results are slightly lower than in the CFD results. This is directly related to the greater velocities in both the leading edge bubble and the boundary layer in this flow region.

Table 2 Reattachment lengths for the flat plate at α=3 deg

	X_R
Crompton	0.47
SST	0.4374
k-ω	0.5096

4.4 Comparison at α=3 deg

4.4.1 Boundary Layer Profiles in the Leading Edge Bubble. The reattachment lengths for the $\alpha=3$ deg case are presented in Table 2. The SST model underpredicts X_R by 6.4% and the k-ω model overpredicts X_R by 8.4%. As before, the chordwise positions are scaled by X_R.

The velocity profiles within the separation bubble are presented in Fig. 13. At the reattachment point ($x/c=0.375$), the velocities predicted by the CFD are much lower than the experimental data in both the outer and inner shear layers. As the shear layer curves down toward the wall, the velocities in the chordwise direction are damped inappropriately. We will address this point further in the next section.

The measurement station at $x/c=0.25$ is approximately mid length of the leading edge bubble. Here, the velocities are at their maximum, both at the outside edge of the shear layer and in the reversed flow region. In the inner shear layer, the maximum reversed velocity is $-0.393U_\infty$ for the experimental results, whereas the SST model predicts $-0.252U_\infty$ and the k-ω model predicts $-0.271U_\infty$. The reversed boundary layer is notably thicker in the experiments than in the CFD results. Moving toward the leading edge, we see that at $x/c=0.125$, the reversed flow weakens due to mass flow in the direction normal to the plate mostly. In the experiments, the presence of an adverse pressure gradient also contributes to this effect.

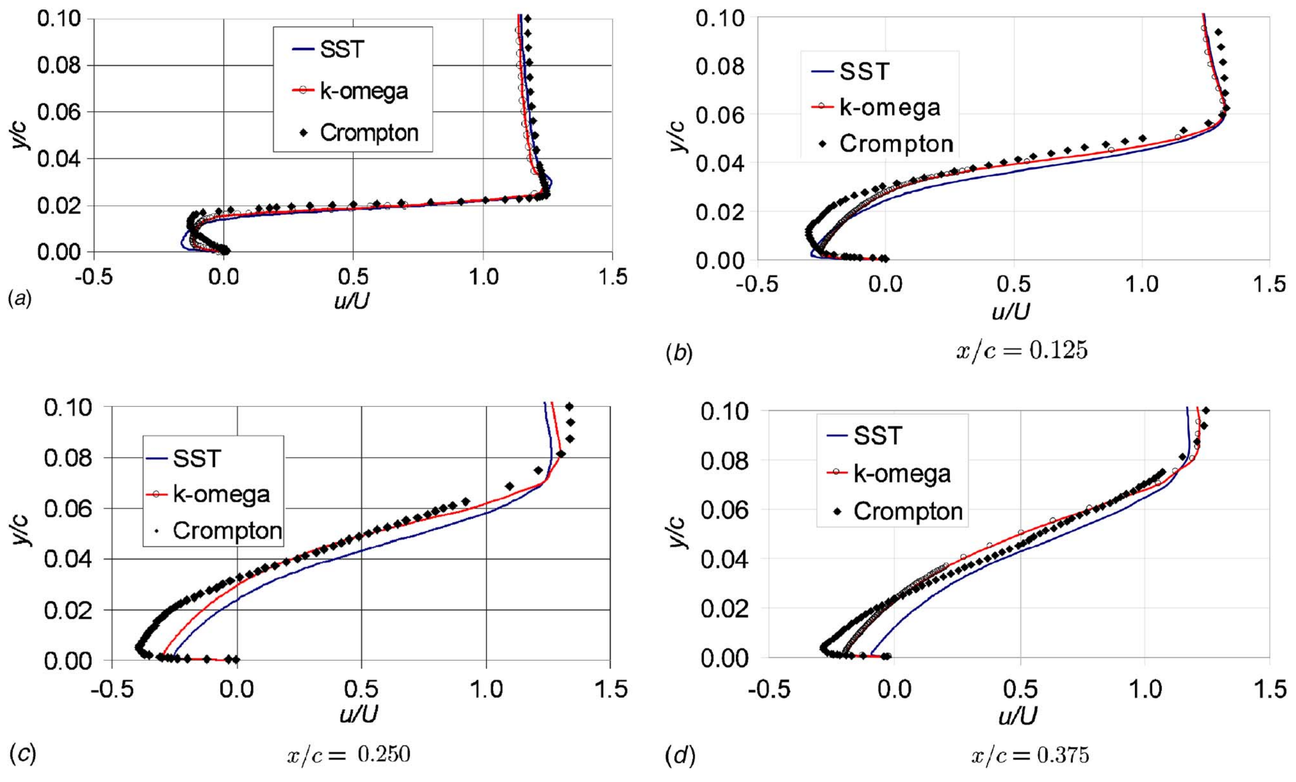

(*a*)

(*b*) $x/c = 0.125$

(*c*) $x/c = 0.250$

(*d*) $x/c = 0.375$

Fig. 13 Chordwise velocity profiles within the leading edge bubble (α=3 deg). (a) x/c=0.031, (b) x/c=0.125, (c) x/c=0.250, (d) x/c=0.375.

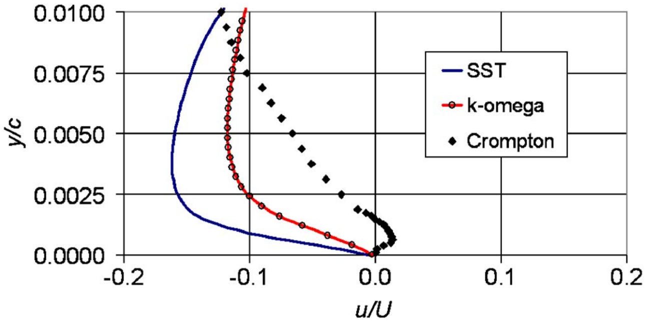

Fig. 14 Near-wall chordwise velocity profiles at $x/c=0.031$ ($\alpha=3$ deg)

At $x/c=0.031$, the secondary separation bubble presents itself in the experimental data, as shown in Fig. 14. The simulations do not show this feature, and the near-wall flow is reversed all the way to the leading edge.

4.4.2 Turbulent Kinetic Energy Profiles in the Leading Edge Bubble. In this section, we compare the turbulent kinetic energy profiles calculated by the CFD with the profiles from the experiments for the flow at $\alpha=3$ deg. Crompton's data were supplied in terms of $u_{\rm rms}$, $v_{\rm rms}$, and $w_{\rm rms}$, where rms represents the root mean square of the velocity fluctuations. From these data, the turbulent kinetic energy was calculated as $k=1/2(\overline{u'u'}+\overline{v'v'}+\overline{w'w'})$, with the normal turbulent stresses given by $\overline{u'u'}=(u_{\rm rms})$ [2]. The rms measurements cannot distinguish between turbulent fluctuations and the mean-flow unsteadiness that was observed in the shear layer. Periodicity in the rms velocities (indicating mean-flow unsteadiness) was observed as far back as $x/c=0.375$ for the $\alpha=3$ deg case. Therefore, the turbulent kinetic energy for the experimental data presented in Fig. 15 may be overestimated. Crompton reported that the vortical structures seen in the laminar shear layer were absorbed into the turbulent eddy spectrum downstream of the transition region. Therefore, the mean-flow kinetic energy associated with shear layer flapping is eventually converted into turbulent kinetic energy.

At $x/c=0.031$, the experimental turbulent kinetic energy profile shows two peaks. The first, and lower, peak is associated with the secondary separation bubble. At the outer edge of this bubble, a region of high mean shear exists, which increases production of turbulent kinetic energy. The second peak occurs at the point of inflection in the velocity profile in the outer shear layer where the mean shear is at its maximum. It is stronger than the first peak as it is driven by the large velocities around the leading edge of the plate. The maximum turbulent kinetic energy observed in the experiments is 2.5 times that predicted by the SST model and 4.0 times the maximum predicted by the k-ω model.

Naturally, care must be taken when comparing the three-dimensional experimental turbulence data to the two-dimensional simulation data. The contribution of the spanwise velocity fluctuations to the turbulent kinetic energy measured by Crompton is not negligible. However, because the turbulent energy originates from mean-flow shear, which is essentially two dimensional, we believe that the discrepancy between the simulations and the experiments cannot be fully explained by the difference in dimensionality. Our speculation is that two flow features that were not resolved by the CFD models are mostly responsible for the discrepancy: the unsteadiness at the leading edge, which feeds into the downstream turbulence spectrum, and the extra shear created by the secondary recirculation bubble.

The turbulent kinetic energy contours for the leading edge are illustrated in Fig. 16. Here, it can be seen that in the SST simulations the turbulent kinetic energy levels begin to be amplified slightly further upstream than they do for the k-ω model. While we have said that these turbulence models are not transition models, it is not true to say that they do not model transition at all. The simulations still pass from a region where the turbulent kinetic

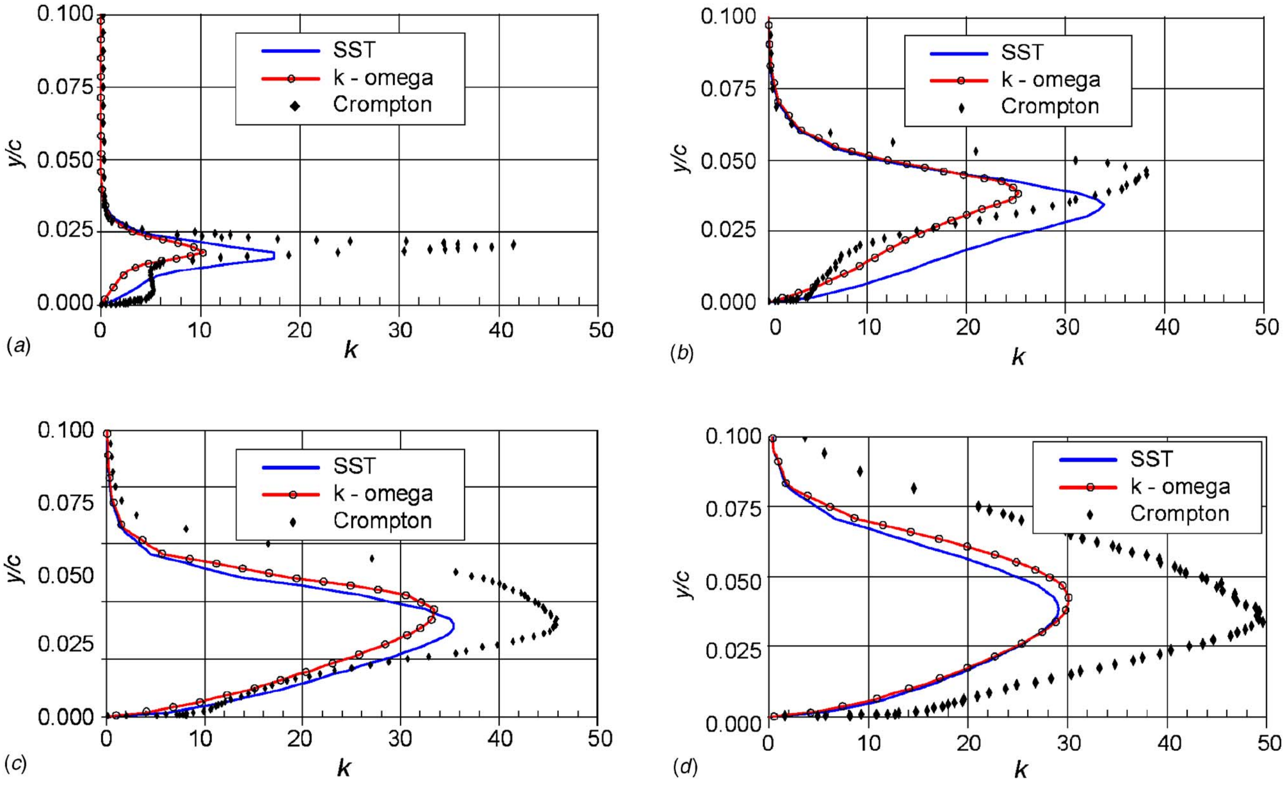

Fig. 15 Turbulent kinetic energy profiles within the leading edge bubble ($\alpha=3$ deg)

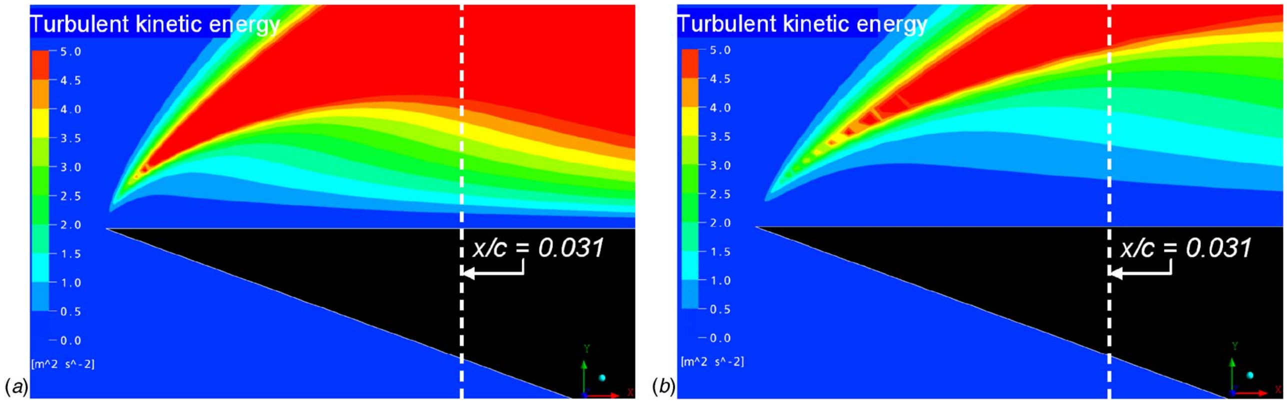

Fig. 16 Turbulent kinetic energy contours around the leading edge (α=3 deg). (a) SST, (b) k-ω.

energy is zero (i.e., a laminar region) through to a turbulent region where production terms in both the k and ω equations are positive, but they do not model the transition process appropriately. Typically, for transitional boundary layer flows, standard two-equation models will predict a transition to occur at a Reynolds number at least an order of magnitude too small [20]. Similarly, in this test case, transition occurs immediately after separation and much further upstream than the figure of 2.5%c reported by Crompton.

At $x/c=0.125$, the experiments give a peak magnitude of turbulent kinetic energy in the shear layer that is slightly lower than at the upstream station. This is due to the diminished effect of the secondary separation bubble, which extends only to $x/c=0.045$. This reduction in turbulent kinetic energy may also be associated with the diffusion of the unsteady structures that were observed in the shear layer near the leading edge. The turbulence models are in better agreement with the experiments than upstream with the SST model outperforming k-ω. In both the CFD and the experimental results, the peak in turbulent kinetic energy has widened due to the thickening of the shear layer. Near the wall, the experimental results show lower levels of turbulent kinetic energy than the CFD, which is a result of relaminarization of the reversed boundary layer.

Between $x/c=0.125$ and $x/c=0.25$, the experimental results indicate that the kinetic energy in the shear layer is still increasing and that the maximum entrainment rate has not yet been reached. The shear layer predicted by the SST model reaches a local equilibrium prematurely because the SST limiter reduces the amount of turbulent shear stress and hence the production of turbulent kinetic energy.

Between $x/c=0.250$ and $x/c=0.375$, both the SST and k-ω models predict a decrease in turbulent kinetic energy, whereas in the experimental results k continues to increase. In this region, the shear layer curves back toward the wall and decelerates as it approaches reattachment. The experimental results show a drop in vertical velocity fluctuations (v'). This energy is mostly converted to transverse (w') and streamwise (u') velocity fluctuations, and thus the kinetic energy levels are retained. The SST and k-ω turbulence models cannot emulate this transfer of energy from the vertical to transverse and streamwise fluctuations because they assume isotropy of the Reynolds stress tensor. In order to model this process, a more advanced anisotropic turbulence model is required, such as an algebraic stress model or a second-order closure model.

At $x/c=0.375$, both the SST model and the k-ω model predict peaks in turbulent kinetic energy that are approximately 1.7 times smaller than in the experimental results. In the experimental results, the kinetic energy peak is wider, which indicates that the shear layer thickness is underpredicted by the CFD.

4.4.3 Downstream of Reattachment. For the $\alpha=3$ deg case, the downstream velocity profiles are quite similar in shape to those found in the $\alpha=1$ deg case. Again, in this region, the velocities predicted by the CFD are lower than those measured in the experiments. It is likely that in the experiments the outer turbulent structures, which originate in the shear layer of the leading edge bubble, feed energy into the inner region and in this way accelerate the development of turbulence. Without these increased levels of turbulent kinetic energy, the recovery of the boundary occurs over a larger downstream distance in the CFD. It is hoped that future LES simulations will be able to help us to improve our understanding of this apparent slow postreattachment recovery of the two-equation turbulence models.

In the recovery region, the k-ω model predicts greater turbulent kinetic energy compared with SST. Consequently, the k-ω model predicts slightly steeper near-wall velocity gradients, and the turbulent boundary layer is able to recover more rapidly. The lower values of turbulent kinetic energy in the SST results are due to the SST limiter, which becomes active in regions of large mean strain.

Directly behind the square trailing edge, a small pair of steady vortices appear in the CFD results. A steady wake forms downstream. Unfortunately, the experimental data do not include flow measurements downstream of the plate.

5 Summary

5.1 Experiments Versus SST and k-ω Simulations. The experimental results show greater growth and curvature of the outer shear layer of the leading edge bubble. This is due to several phenomena that are not adequately captured by the SST and k-ω turbulence models: Firstly, there is increased entrainment in the experimental results at the leading edge due to unsteady shear layer flapping. Also, transport and production of turbulent kinetic energy dominate turbulent kinetic energy dissipation, and k continues to increase along the length of the shear layer in the experiments. The lower shear layer growth predicted by the CFD causes reattachment to be delayed and the pressure coefficient to be overpredicted within the leading edge bubble.

The reversed flow in the leading edge bubble is subject to a favorable pressure gradient, which causes relaminarization, an effect which is not captured by the turbulence models because they are designed for fully turbulent flows and are incapable of modeling transitional effects. Consequently, the models also fail to predict the secondary bubble near the leading edge. The omission of the secondary bubble in the CFD results is not believed to be an artifact of the numerics since the solutions showed excellent grid convergence and the secondary bubble was not present in the fine grid simulations.

Approaching the reattachment point, both turbulence models artificially damp turbulent kinetic energy due to the presence of the wall. In the experiments, the turbulent fluctuations normal to the wall were damped; however, the energy from this was fed into the spanwise and chordwise turbulence. The k-ω and SST models use an isotropic formulation of the Reynolds stress tensor and are thus unable to model this anisotropic effect.

Downstream of reattachment, the CFD profiles recover toward turbulent equilibrium slowly compared with the experiments. In the observed recovering boundary layer, the eddies in the outer region of the near wall originate in the separated shear layer, whereas the scales in the inner region are associated with the development of the new boundary layer. The two-equation turbulence models cannot be expected to emulate this complicated recovery process involving an irregular eddy spectrum. Also, the anisotropic effects that occur as the shear layer approaches reattachment, which leads to transfer of turbulent kinetic energy from the normal to the transverse and streamwise velocity fluctuations, cannot be captured by the turbulence models. The models instead damp the turbulent kinetic energy associated with the velocity fluctuations normal to the plate near the reattachment point. The CFD predicts a slower recovery of the boundary layer downstream of reattachment.

5.2 SST Versus k-ω. The SST model captures the leading edge bubble more accurately than the k-ω model. It predicts greater turbulent kinetic energy levels near the leading edge and therefore predicts greater shear layer growth. As a result, its predictions of the reattachment lengths are in closer agreement with the observed lengths (within 7% for both angles of attack that were investigated ($\alpha=1$ deg and $\alpha=3$ deg)), and the pressure coefficient in the vicinity of the leading edge bubble is more accurate. The shear layer predicted by the SST model has more curvature and bends back toward the plate earlier than the layer predicted by the k-ω model. However, the SST model returns lower turbulent kinetic energy values in the rear half of the leading edge bubble. This is due to the SST limiter. As a consequence, the SST model produces lower velocities in both the outer and inner shear layers compared with both the k-ω model and the experimental data.

Downstream of reattachment, the k-ω model predicts a more rapid boundary layer recovery than the SST model, but the recovery is still slower than observed in the experiments. The differences between the velocity profiles predicted by the two turbulence models are small and are a consequence of the SST limiter.

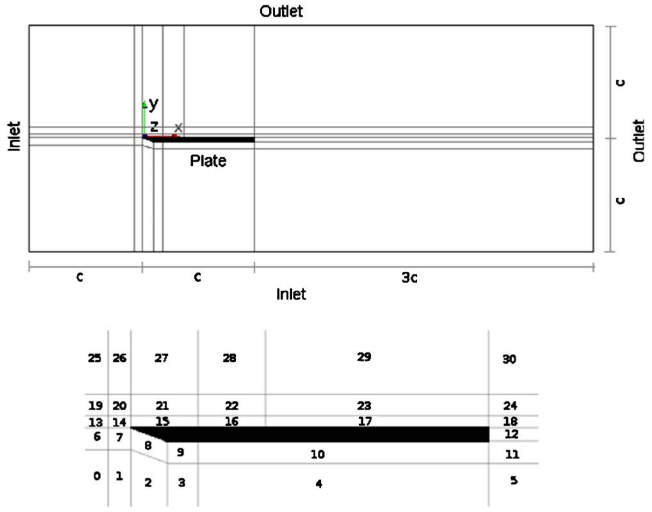

Fig. 17 Thin flat plate geometry and auxiliary block numbers

6 Discussion and Conclusions

The flow past the flat plate at shallow incidence is a complex and challenging assignment for two-equation turbulence models.

The overall flow topology of the leading edge bubble was predicted with reasonable accuracy by both the k-ω and SST turbulence models despite the fact that both turbulence models did not capture the secondary bubble. Both the k-ω and SST models underpredicted the production of turbulent kinetic energy within the leading edge bubble, which resulted in lower velocities in both the outer and inner shear layers.

A proper prediction of the recovering boundary layer downstream is particularly difficult for such turbulence models. We expect that CFD boundary layer profiles will be more susceptible to flow separation when an adverse pressure gradient is present, as is the case, for example, for curved sails. A question certainly remains over how the unsteady structures in the turbulent shear layer interact with the turbulence within the shear layer and how they affect the downstream behavior of the flow. These structures are damped by turbulence models because of the high eddy viscosities around stagnation and the leading edge. LES results would be useful here as a tool to aid the understanding of the transient behavior.

For the validation of sail flow simulations, several results from this chapter are encouraging. Firstly, the overall flow topology of the leading edge bubble and recovering boundary layer is predicted reasonably well, and the pressure coefficient plots are close to the experimental data, especially for the SST model. Secondly, despite using turbulence models that assume fully turbulent flow, the leading edge bubble was adequately captured. This is largely because the leading edge bubble involves little laminar flow, with the shear layer undergoing transition within the first 2.5% of the length of the plate. Therefore, turbulence models that do not account for transition can be much more suitably applied to the thin

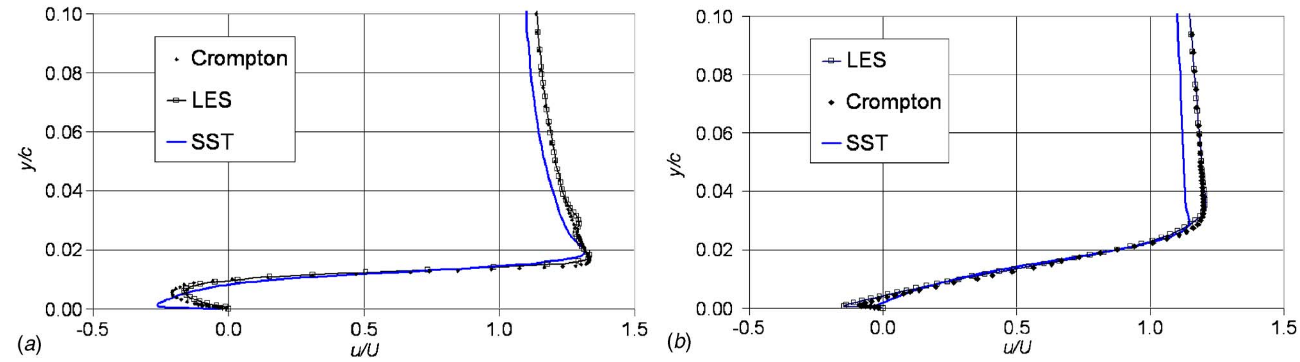

Fig. 18 LES chordwise velocity profiles within the leading edge bubble ($\alpha=1$ deg). (a) $x/c=0.031$, (b) $x/c=0.125$.

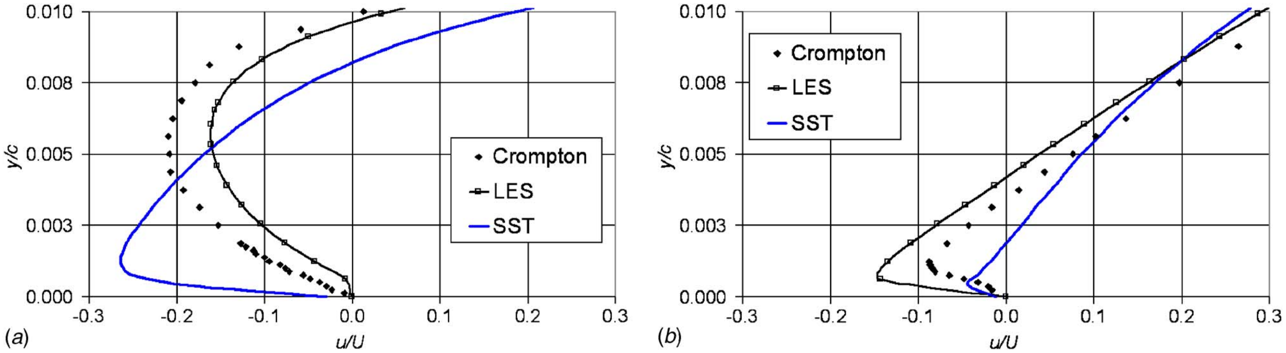

Fig. 19 LES near-wall chordwise velocity profiles within the leading edge bubble (α=1 deg). (a) x/c=0.031, (b) x/c=0.125.

airfoil bubble than the short bubble where extensive regions of laminar flow exist, both upstream of the bubble and within the separated region itself.

A correct prediction of the pressure distribution is the most important criterion for evaluating turbulence models for sail flow simulations since almost all of the lift and drag is generated from the pressure forces. Based on this method of evaluation, the SST model is preferred over the k-ω model. Considering the complexity of this flow and just how different it is to flows that modelers usually investigate and tune in their models, the results are actually quite pleasing.

6.1 Preliminary Results From LES Study. We present preliminary LES results for the plate at 1 deg angle obtained using the opensource framework OPENFOAM [21] (see also Ref. [22]). OPENFOAM's solvers are based on a cell-centered finite volume method and employ the PISO algorithm [23] with a second order time discretization. We selected the one-equation subgrid model of Horiuti [24] for its ability to deal with nonequilibrium conditions.

Figure 17 shows the computational domain and its division in subdomains used to aid the distribution of the mesh elements, and also describes the boundary conditions. The mesh has a total of 837,984 cells. We use 32 cells in the z direction, which spans 1/4th of the chord. The average y^+ value is 3.9 on the top surface, which is too high for boundary layer flows; however, more focus was placed on achieving sufficient grid density in the leading edge bubble and, in particular, the outer shear layer. To reduce computational costs, the computational domain was reduced and the grid stretched in regions away from the plate. To avoid numerical instabilities caused by grid stretching, the computational domain is partitioned into two regions. The first, which includes the flat plate and surrounding areas (regions 7–12, 14–18, and 20–24 in Fig. 17) with turbulent activity, has a fine, high-quality grid, and is discretized using a nondissipative scheme so that turbulent structures are well represented. Grid stretching is confined to the second, outer area where a dissipative scheme guarantees numerical stability.

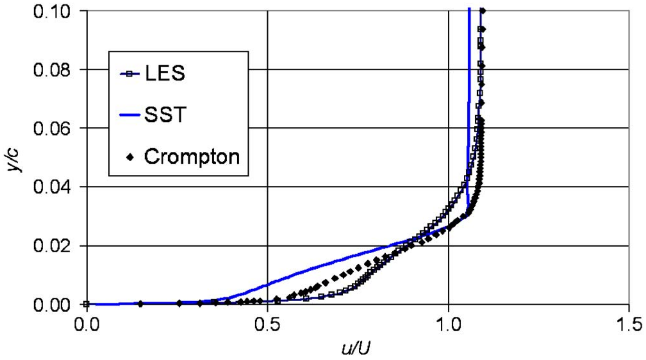

Fig. 20 LES boundary layer profile just downstream of reattachment (x/c=0.25)

The LES results are encouraging. In regions with an adequate grid density, the LES does a better job than the two-equation models at capturing the physics. For example, the maximum velocities of the outer and inner shear layers are computed more accurately. Also, the relaminarization of the leading edge bubble and the secondary bubble are captured (see Figs. 18 and 19). In the recovery region (see Fig. 20), the grid spacing used near the wall is inadequate. As a consequence, the recovery region is resolved no more accurately than with the two-equation models. Further results are presented in the thesis of Sampaio [25].

References

[1] Crompton, M. J., 2001, "The Thin Aerofoil Leading Edge Bubble," Ph.D. thesis, University of Bristol.

[2] Bardina, J. E., Huang, P. G., and Coakley, T. J., 1997, "Turbulence Modeling Validation, Testing and Development," NASA, Technical Report No. 110446.

[3] Collie, S., and Gerritsen, M., 2006, "The Challenging Turbulent Flows Past Downwind Yacht Sails and Practical Application of CFD to Them," *Second High Performance Yacht Design Conference*, Auckland.

[4] Gault, D. E., 1957, "An Investigation at Low Speed of the Flow Over a Simulated Flat Plate at Small Angles of Attack Using Pitot Static and Hot-Wire Probes," NACA, Technical Report No. TN-3876.

[5] Driver, D. M., Seegmiller, H. L., and Marvin, J. G., 1987, "Time-Dependent Behavior of a Reattaching Shear Layer," AIAA J., **25**(7), pp. 914–919.

[6] Driver, D. M., and Seegmiller, H. L., 1985, "Features of a Reattaching Turbulent Shear Layer in Divergent Channel Flow," AIAA J., **23**(2), pp. 163–171.

[7] Menter, F. R., 1992, "Improved Two-Equation k-ω Turbulence Models For Aerodynamic Flows," NASA, Technical Report No. TM-103975.

[8] Crabtree, L. F., 1957, "The Formation of Regions of Separated Flow on Wing Surfaces," Aeronautical Research Council, London, Technical Report No. R&M-3122.

[9] Newman, B. G., and Tse, M.-C., 1992, "Incompressible Flow Past a Flat Plate Aerofoil With Leading Edge Separation Bubble," Aeronaut. J., **96**, pp. 57–64.

[10] Cherry, N. J., Hiller, R., and Latour, M. E. M. P., 1983, "The Unsteady Structure of Two-Dimensional Separated-and-Reattaching Flows," J. Wind. Eng. Ind. Aerodyn., **11**, pp. 95–105.

[11] Kiya, M., and Sasaki, K., 1983, "Structure of a Turbulent Separation Bubble," J. Fluid Mech., **137**, pp. 83–112.

[12] CFX-International 2003, CFX-5 Solver and Solver Manager Version 5.6, CFX-International.

[13] Raw, M., 1996, "Robustness of Coupled Algebraic Multigrid for the Navier-Stokes Equations," *34th Aerospace Sciences Meeting and Exhibit*, Reno, NV, AIAA Paper No. 96-0297.

[14] Menter, F. R., 1994, "Two-Equation Eddy-Viscosity Turbulence Models For Engineering Applications," AIAA J., **32**(8), pp. 1598–1605.

[15] Wilcox, D. C., 1988, "Reassessment of the Scale-Determining Equation for Advanced Turbulence Models," AIAA J., **26**(11), pp. 1299–1310.

[16] ICEM-CFD-Engineering, "ICEM HEXA 4.2," http://www.icemcfd.com/

[17] Österlund, J., 1999, "Experimental Studies of Zero Pressure-Gradient Turbulent Boundary Layer Flow," Ph.D. thesis, Kungl Tekniska Högskolan.

[18] Horton, H. R., 1969, "A Semi-Empirical Theory for the Growth and Bursting of Laminar Separation Bubbles," Aeronautical Research Council, London, Technical Report No. ARC CP-1073.

[19] So, R. M. C., and Lai, Y. G., 1988, "Low-Reynolds-Number Modeling of Flows Over a Backward Facing Step," ZAMP, **39**, pp. 13–27.

[20] Wilcox, D. C., 1998, *Turbulence Modeling for CFD*, 2nd ed., Griffin, California.

[21] Weller, H., Tabor, G., Jasak, H., and Fureby, C., 1998, "A Tensorial Approach to Computational Continuum Mechanics Using Object Orientated Techniques," Comput. Phys., **12**(6), pp. 620–631.

[22] Sampaio, L. E. B., Nieckele, A. O., Gerritsen, M., and Collie, S., 2006, "Numerical Simulations of the Long Recirculation Bubbles Formed in Thin Flat Plates at Shallow Incidence," *Proceedings of the EPTT 2006, Escola de Primavera de Transicao e Turbulencia, ABCM*, Brazil Society of Mechanical Sciences and Engineering—ABCM, Rio De Janeiro, RJ, Brazil.

[23] Issa, R., 1985, "Solution of the Implicit Discretized Fluid Flow Equations by Operator-Splitting," J. Comput. Phys., **62**, pp. 40–65.

[24] Horiuti, K., 1985, "Large Eddy Simulation of Turbulent Channel Flow by One-Equation Modeling," J. Phys. Soc. Jpn., **54**(8), pp. 2855–2865.

[25] Sampaio, L. E. B., 2006, "Large Eddy Simulations of the Thin Plate Separation Bubble at Shallow Incidence," Ph.D. thesis, Department of Mechanical Engineering, Pontifícia Universidade Católica do Rio de Janeiro, RJ, Brasil, in Portuguese.

Rotational Motion of Large Particulate Doublets in Poiseuille Flow in a Capillary

E. J. McKeever

K. V. Sharp[1]

Department of Mechanical Engineering,
The Pennsylvania State University,
157 Hammond Building,
University Park, PA 16802
e-mail: ksharp@mne.psu.edu

Doublets of 48-μm-diameter polystyrene latex particles are experimentally tracked in a Poiseuille flow in a capillary tube. The rotational motion of nine doublets is observed using video microscopy with a translating stage. The particle diameter to capillary diameter ratio is 0.17, volume concentration 0.5%, and Reynolds number approximately 0.5. The rotational motions of the "large" particulate doublets are compared with theory originally developed for doublets with particle-to-tube diameters of the order of 0.04; the doublet rotations in the present experiments agree reasonably well with the earlier theory when the shear rate for the large doublet is defined based on the location of the centroid of shear rather than the shear rate at the radial center of mass of the rotating doublet. Additionally, these doublets are readily classified as primary or secondary on the basis of the rotational period. [DOI: 10.1115/1.2829581]

Keywords: doublet, capillary, microtube, Poiseuille flow, particle-laden flow

1 Background

The current trend in microfluidics is toward the use of smaller and smaller channels. Given the proposed applications of microfluidic systems [1,2] in biological-related fields (e.g., medical diagnostics, drug delivery), chemical analysis and synthesis, or even micro/nanofabrication, many of which rely on the transport of particles, there is an underlying need to understand the dynamics of particles within microfluidic systems. The fabrication of flow control devices from individual colloid particles is an example of this trend toward decreasing feature size and required transport of particles [3]. As the channels in microfluidic-application driven devices become smaller, the ratio of particle size to channel size may become significant. The flow of particle-laden fluids with large characteristic particle size to characteristic channel size ratios (d_p/D) has not been extensively studied. The work presented herein is an interesting outgrowth of our observations on particle-laden flows in capillaries with d_p/D ratios of near 0.2, and extends the range of applicability of earlier theory [4,5] on the rotational motion of doublets within Poiseuille flow.

There are also some interesting biological or biologically inspired applications of rotating and tumbling nonspherical (more spheroidal or long-chain shaped) particles or doublets [6–10]. However, the dynamics in such systems are typically even more complicated due to the potential for effects such as conformational response to shear.

One useful way to observe particle interactions in a capillary tube is to track them visually by translating the capillary tube at the speed the particles flow through it but in the opposite direction. In the present experiment, the field of view is translated such that the reference frame is nearly stationary with respect to one particle or group of particles. A number of rotating particle doublets were observed in Poiseuille flow in the capillary tube. The rotational motion of these doublets was analyzed and compared with the relevant theory, developed primarily by Jeffrey [4] and Van de Ven and Mason [5,11]. In their experiments, Van De Ven and Mason [11] used a d_p/D ratio of 0.04 and in their analysis, assumed the shear rate to be constant across a doublet. The magnitude of the shear rate required in the equations of rotation motion for a doublet was calculated based on the shear rate in the fluid flow at the location of the center of mass of the rotating doublet. In the present experiment, the d_p/D ratio was 0.17. At these higher ratios of particle-to-tube diameter, the approximation that the shear rate experienced by the doublet is constant across the doublet is not appropriate. An alternate method of calculating an appropriate shear rate for use in the rotational equations of motion is suggested based on the shear rate at the radial location of the centroid of the shear rate distribution across the doublet.

Depending on the separation distance between the particles in a rotating doublet, it was previously shown by Van de Ven and Mason [11] that doublets of colloidal particles ($d_p \sim \mathcal{O}(1\ \mu\text{m})$) in a Poiseuille flow with small particle-to-tube diameter ratios (maximum $d_p/D \sim 0.04$) could be classified as primary or secondary doublets, where a primary doublet is defined as one in which the particles are in direct contact with each other and the particles in a secondary doublet are separated by a small distance. Since the separation distance is generally too small to be visually observed, a determination of primary versus secondary must be made based on the characteristics of the rotational motion. Although the particles in the present experiments have a much larger diameter, given that the experiments are also performed with polystrene latex (PSL) suspensions for which, based on Derjaguin–Landau–Verwey–Overbeek (DLVO) theory, an interaction potential with maximum and secondary minimum can be calculated, it is hypothesized that both types of doublets are also observed in the present work. Physically, Van de Ven and Mason [11] suggested that their primary doublets were formed (and were resistant to breakup by shaking), perhaps due to the aging of the suspension, prior to the suspension even entering the experimental apparatus. Regarding secondary doublet formation, they surmised that the secondary doublets were typically formed by capture during the time that the suspension resided in the feeder syringe prior to entering the test section. So while they do not present unequivocal arguments as to why some doublets are primary and some are secondary, Van de Ven and Mason [11] do argue that the occurrence of one versus the other lies primarily in the genesis of the doublet and certain difficult-to-control aspects affecting suspension characteristics (e.g., aging) rather than in differences in flow conditions. In addition, with the larger particle diameters used in the present work, it

---

[1] Corresponding author.

Contributed by the Fluids Engineering Division of ASME for publication in the JOURNAL OF FLUIDS ENGINEERING. Manuscript received October 31, 2006; final manuscript received September 24, 2007. published online January 25, 2008. Review conducted by Theodore Heindel.

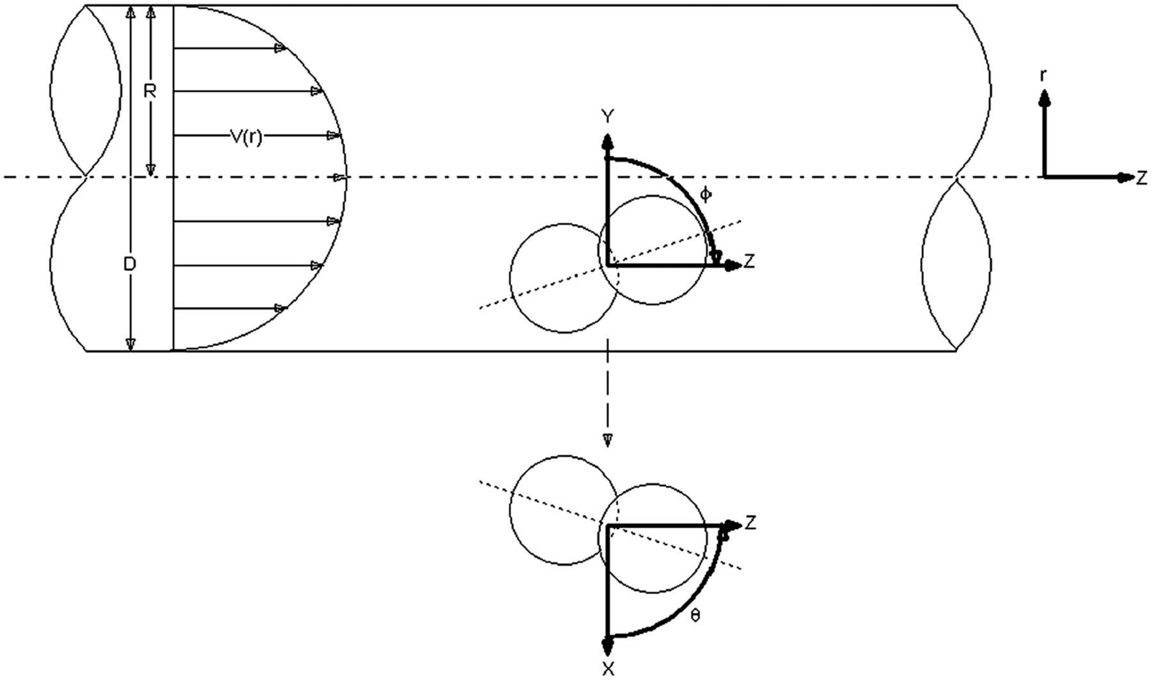

Fig. 1 Coordinate system definition. The *Y-Z* plane is the side view, and the *X-Z* plane is the bottom view. ϕ is the angle measured from the *Y* axis toward the *Z* axis, and θ is the angle measured from the *X* axis toward the *Z* axis.

is possible that the formation of primary versus secondary doublets is further influenced by nonuniform charge distribution or charge migration.

In the current work, the separation distance in a secondary doublet is estimated based on physical parameters within the experimental system. Despite the linear distribution of shear rate across a doublet, the relatively large d_p/D ratios, and the relatively large particle diameters (48 μm), it is shown that (i) the rotation rate of the particles can be predicted theoretically by defining the shear rate for the doublet as the shear rate at the centroid of shear across the doublet and (ii) the observed doublets can be readily classified as primary or secondary doublets based on the period of their rotational motion.

1.1 Rotating Doublet Theory for Small d_p/D Ratios. The theory for the rotational motion of particles and doublets flowing through a capillary tube has been proven to be quite accurate for systems in which the particle diameter to tube diameter ratio (d_p/D) is less than 0.04 [11,12]. Based on Jeffrey's original work [4], the basic rotational motion equations for spheroids in a shear flow [12] are

$$\omega = \frac{d\phi}{dt} = \frac{G}{r_e^2+1}(r_e^2\cos^2\phi + \sin^2\phi) \tag{1}$$

$$\frac{d\theta}{dt} = \frac{G(r_e^2-1)}{4(r_e^2+1)}(\sin 2\phi \sin 2\theta) \tag{2}$$

where r_e is the equivalent axis ratio, G is the shear rate, and ω is the angular velocity of the spheroid. The equivalent (ellipsoidal) axis ratio is defined as a_{ee}/b_{ee}, where $2a_{ee}$ is the length of the axis of revolution and $2b_{ee}$ is the equatorial diameter of an ellipsoid that would rotate with the same period of rotation (an "equivalent ellipsoid") [12]. The coordinate system for Eqs. (1) and (2) is shown in Fig. 1. For a spherical particle, the equivalent axis ratio r_e is 1. Goldsmith and Mason [12] showed that individual rotating spherical particles flowing through a capillary follow Eqs. (1) and (2) for d_p/D ratios less than 0.02 [12], where the value of shear rate required by Eqs. (1) and (2) is the shear rate (G) calculated at the radial location of the particle's center of mass ($r_{\text{c.m.}}$):

$$G = \frac{4Qr_{\text{c.m.}}}{\pi R^4} \tag{3}$$

Here Q is the volume flowrate, $r_{\text{c.m.}}$ is the radial location of the center of mass of the particle/doublet, and R is the radius of the capillary. Further, Goldsmith and Mason [12] assumed that since the particle diameter was small compared to the tube diameter, the linearly varying shear rate could be approximated as a constant shear rate at the center of the particle.

Equations (1) and (2) can be nondimensionalized and reduced using trigonometric substitutions to Eqs. (4) and (5) [5]:

$$\frac{d\phi}{dt^*} = \frac{1}{2}\left(1 + \frac{r_e^2-1}{r_e^2+1}\cos(2\phi)\right) \tag{4}$$

$$\frac{d\theta}{dt^*} = \frac{1}{4}\left(\frac{r_e^2-1}{r_e^2+1}\right)\sin(2\theta)\sin(2\phi) \tag{5}$$

where

$$t^* = tG \tag{6}$$

The equivalent ellipsoidal axis ratio r_e, defined as the ratio of axes in the plane of shear, and for a primary doublet (particles in direct contact) is $r_e=1.982$ [13]. Since the semiaxis of revolution (a_{ee}) for a primary doublet equals the particle diameter, this means that the equivalent diameter ($2b_{ee}$) of an ellipsoid that would rotate with the same period of rotation as a primary doublet comprised of two equal-diameter particles equals $1.009a_{ee}$ or 1.009 times the particle diameter. For a secondary doublet (particles slightly separated), r_e is found by using an asymptotic expression in terms of a nondimensional separation distance (δ^*) between particles, where h is the center-to-center distance between particles and a is the radius of the particles (here, $a_1=a_2=a$):

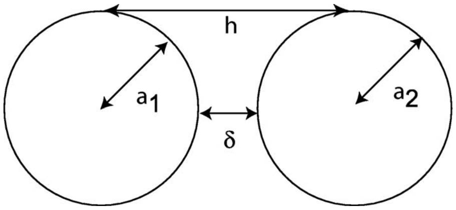

Fig. 2 Particle interaction geometry

$$r_e = 1.982 - \frac{2.923}{\ln(\delta^*)} + \frac{1.255}{\ln^2(\delta^*)} + \cdots \tag{7}$$

where

$$\delta^* = \frac{h}{a} - 2 \tag{8}$$

The geometry for a secondary doublet is shown in Fig. 2. Van De Ven and Mason [11] found that the nondimensionalized rotational motion equations worked well for predicting the motion of freely rotating doublets in Poiseuille flow, where the largest d_p/D ratio used was 0.04. Furthermore, they were able to differentiate between primary and secondary doublets by observing differences in period of revolution. In Van de Ven and Mason's work [11], the shear rate G used in Eqs. (4) and (5) was defined as the shear rate calculated at the measured distance from the capillary center to the radial center of mass of the doublet, $r_{\text{c.m.}}$. Herein, this shear rate is termed $G_{\text{c.m.}}$. The center of the doublet is defined as the point halfway between the centers of the two particles that formed the doublet. Given the d_p/D ratio less than 0.04, the shear rate varied by 16% from $r_{\text{c.m.}}-2a$ to $r_{\text{c.m.}}+2a$, which is the height of the doublet when it is orientated so that $\phi=0$ deg.

1.2 Rotating Doublet Theory for Large d_p/D Ratios. For the current experiment, the d_p/D ratio was four times as large as any used previously, namely, 0.17. Given the large (68%) variation in shear rate from $r_{\text{c.m.}}-2a$ to $r_{\text{c.m.}}+2a$ in this experiment and the "weighting" of shear rate at higher r locations, the use of $G_{\text{c.m.}}$ (shear rate calculated at the radial position of the center of mass of the doublet) in Eqs. (4)–(6) is not ideal for the prediction of rotational rates of the presently observed doublets. Rather, a more appropriate shear rate for use in Eqs. (4)–(6) is suggested, namely, the shear rate (G_{centroid}) at the location of the centroid of shear (r_{centroid}) across the height of the doublet (when the doublet is oriented with $\phi=0$ deg). For Poiseuille flow, the shear rate increases linearly from the center of the capillary to the capillary wall. Figure 3 shows the trapezoidal shape of the shear rate over the height of a doublet. The radial location of the centroid of shear (r_{centroid}) is approximated using a two-dimensional calculation based on the radial location of the doublet center of mass ($r_{\text{c.m.}}$) and represents the radial location of the centroid of the shear across the vertical height of the doublet as pictured in Fig. 3.

$$r_{\text{centroid}} = r_{\text{c.m.}} + \frac{4a^2}{3r_{\text{c.m.}}} \tag{9}$$

Equation (9) is only valid when the center of mass of the doublet ($r_{\text{c.m.}}$) is more than $2a$ from the center of the capillary. If $r_{\text{c.m.}}$ is located within $2a$ of the capillary center, then a similar geometric expression must be used to find r_{centroid}.

$$r_{\text{centroid}} = \frac{\frac{2}{3}r_{\text{c.m.}}^3 + 8a^2 r_{\text{c.m.}}}{4a^2 + r_{\text{c.m.}}^2} \tag{10}$$

Once the radial location of the centroid of shear on the doublet is calculated, Eq. (3) is used to calculate the centroidal shear rate (G_{centroid}) by replacing $r_{\text{c.m.}}$ with r_{centroid}:

$$G_{\text{centroid}} = \frac{4Qr_{\text{centroid}}}{\pi R^4} \tag{11}$$

A two-dimensional calculation is expected to underpredict r_{centroid} since this calculation is based on the projection of $r_{\text{c.m.}}$ in the object plane. Strictly speaking, for a doublet where $\theta \neq 90$ deg, the actual $r_{\text{c.m.}}$ can only be higher than $r_{\text{c.m.}}$ measured. Thus the actual r_{centroid} and thus G_{centroid} are also higher than those calculated based on the measurement. A discussion of the uncertainty for doublets with $\theta \neq 90$ deg is included in Sec. 3.

Given the relatively large dimension of the doublet compared to the capillary, there is expected to be a coupling of the particle doublet and liquid motion. However, the calculation of such coupling is extremely complex and beyond the scope of the current

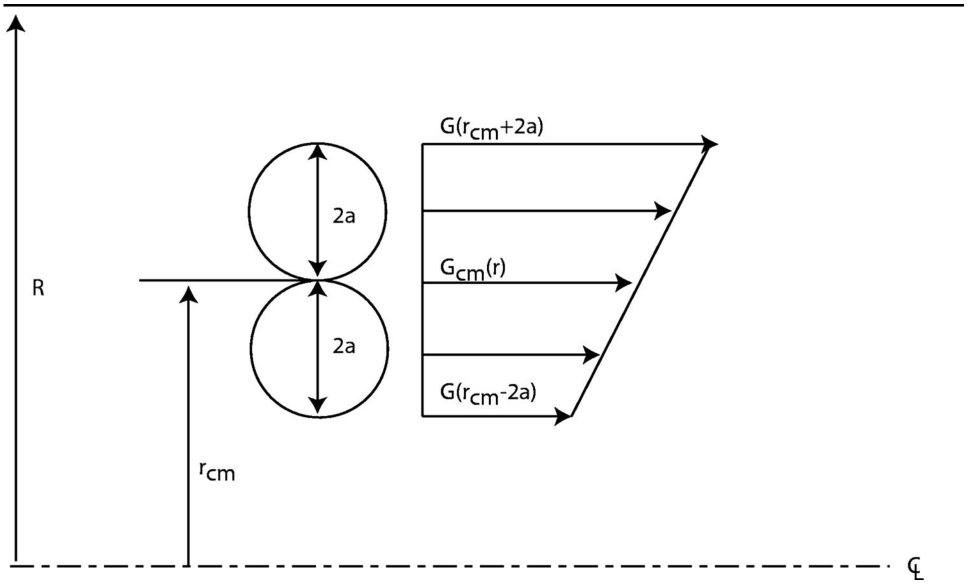

Fig. 3 Calculation of r_{centroid} based on the shape of the shear rate as a function of r. For Poiseuille flow, the shear rate increases linearly from the center of the capillary to the capillary wall. For a doublet with $r_{\text{c.m.}}$ greater than $2a$, the shear rate along the height of the doublet is trapezoidal in shape.

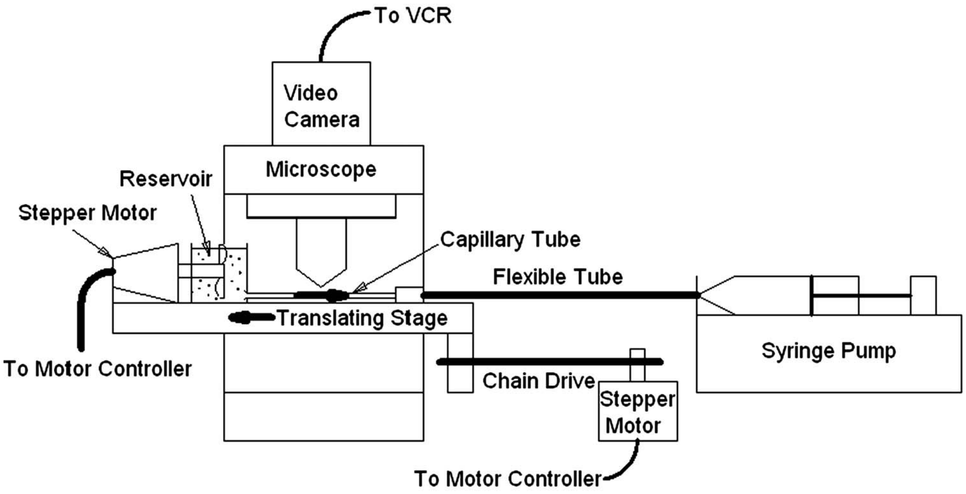

Fig. 4 Schematic of experimental setup

work. Thus, the comparison of the experimental data and theory presented herein is intended to serve as validation of a first-order estimate of the rotational motion.

2 Method of Approach

2.1 Experimental Parameters. PSL particles 48 μm in diameter were transported in a water-glycerine solution through capillary tubes with inner diameters of 279 μm. The PSL particles obtained from Duke Scientific (coefficient of variation 8%) were suspended in a 79.1% water and 20.9% glycerine solution with specific gravity close to the specific gravity of the particles (1.05). The viscosity of this solution is $1.516 \times 10^{-6}\ \mathrm{m}^2/\mathrm{s}$ [14]. With a particle concentration for the current experiment set at 0.5%, many particle interactions were observed. For a selected volumetric flowrate (Q) of 0.0102 ml/min, the Reynolds number based on capillary diameter was approximately 0.5, and the residence time of a fluid element traveling at the average fluid velocity is approximately 30 s in a 70-mm-long, 279-μm-diameter capillary. (The translation stage's travel is limited to 70 mm by the motor controller because the stage travel is mechanically limited to 80 mm.) Both the rotational Peclet number (Pe_r) and translational Peclet number (Pe_t) in these experiments are of the order of 10^8, thus the influence of Brownian motion on the rotation of the doublets is expected to be very small.

2.2 Experimental Setup. This experiment is designed to capture video data of the rotational motion of relatively large particulate doublets ($d_p/D \sim \mathcal{O}(0.2)$) flowing through a capillary tube. The particles were captured on video by translating the capillary tube in the direction opposite to the flow, thus allowing some of the particles to be tracked with a video microscopy system as they passed through the capillary (Fig. 4). The translation velocity of the stage is adjustable so particles traveling in different radial locations and hence different speeds could be tracked.

Particle-laden fluid was poured into the reservoir, and the fluid was drawn through a capillary tube and into a syringe by the syringe pump. The microscope stage was translated by a stepper motor. When the stage reached its travel limit, the stage returned to its start position to begin another run and follow another set of particles. To minimize settling over the long term, a small paddle in the reservoir was swept once through the reservoir while the stage returned to its start position.

2.3 Data Collection. The procedure for collecting data was as follows. First, a suspension of approximately 10 ml of 0.5% concentration of PSL particles and water-glycerine was poured into the reservoir. The syringe pump was turned on and set to draw the particles through the capillary at 0.0102 ml/min. Then, the microscope stage and hence the capillary were translated using the motion control system at a velocity equal to the negative of the velocity of the particles (adjustable depending on where observations were to be made). Standard video microscopy was used with a fluorescent filter matched to the spectra of the particles. Once the stage translated to the end of its travel, the stage was returned to its starting point near the entrance to the capillary, and then the process of tracking a new set of particles began.

The motion of many particles was captured using the above technique. The video of doublets that appeared to rotate near the plane of the field of view of the microscope ($\theta \sim 90$ deg) was digitized into avi format with a resolution of 640×480 pixels. For each doublet of interest, the avi file was parsed into a series of individual bitmap images with the same resolution, where each image is separated by 1/30 of a second. A resolution of 640×480 pixels corresponds to approximately 1.25 μm per pixel; however, given the optical distortion discussed below, this (centerline) resolution served primarily as an estimate of that within the remainder of the channel.

The series of consecutive bitmap images (similar to the one shown in Fig. 5) for each rotating doublet was analyzed in AutoCAD. The diameter of the capillary is known to be 279 μm; this known diameter was used to calibrate the image and hence the measurement of doublet radial position.

The radial position of a doublet was measured in AutoCAD by drawing a three point circle on the perimeter of each particle that forms the doublet. A line was then drawn to connect the centers of each particle, and the midpoint of that line taken as the center of the doublet. The distance from the center of the doublet to the

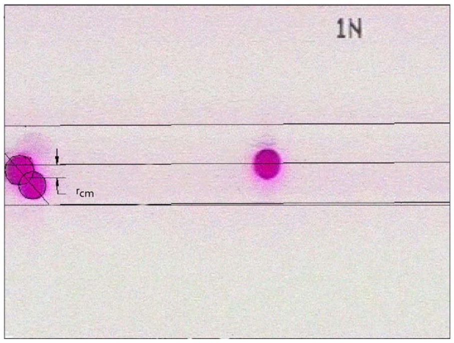

Fig. 5 Example of video frame analyzed in AutoCAD

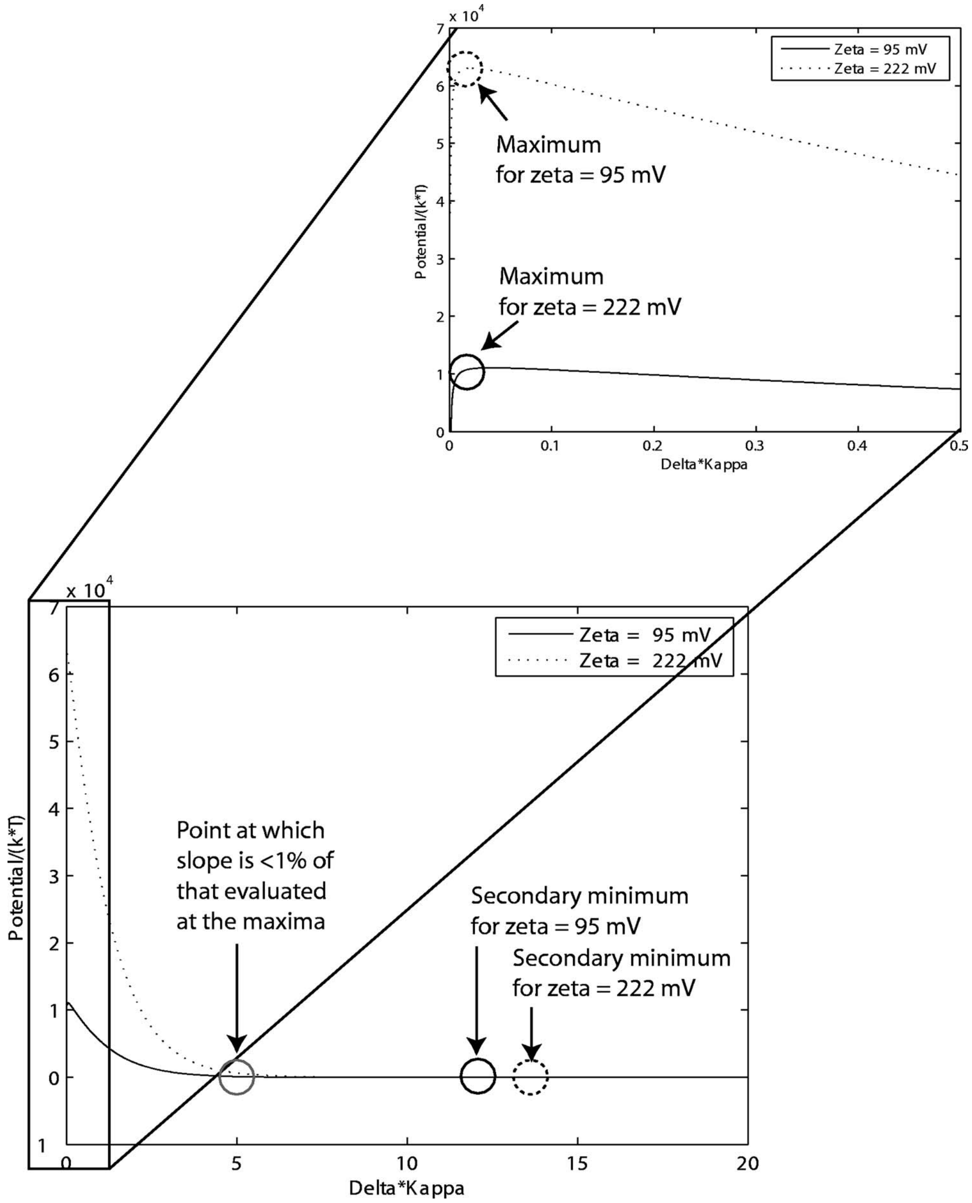

Fig. 6 Energy versus particle separation distance based on DLVO model (Eq. (15)) for 48 μm PSL particles of −95 mV and −222 mV

center of the capillary is measured. Manual measurements were used rather than an automated edge-detection algorithm given that doublets rotating with anything other than $\theta=90$ deg have some overlap in the image. Each particle has a diameter of approximately 38 pixels so even with an uncertainty of ± 2 pixels, the radial position of the particle/doublet would be located to within approximately 2–4% of the capillary radius.

Since the capillary has two curved interfaces: (1) the interface between the water-glycerine solution and the inner capillary wall, and (2) the interface between the outer capillary wall and the air, the optical distortion according to Snell's law should be considered. Snell's law is applied to the geometry of this system to provide map the radial distance observed at the objective ($r_{\text{perceived}}$) to the actual radial distance inside the capillary (r_{actual}). Details of the mapping can be found in Ref. [15]. A series of points (at r_{actual}) was mapped to the points observed at the objective ($r_{\text{perceived}}$) and a nonlinear regression with residual sum of squares equal to 1.74×10^{-5} was used to fit the following relationship between r_{actual} and $r_{\text{perceived}}$:

$$r_{\text{actual}} = \left(\frac{\frac{r_{\text{perceived}}}{R}}{1.296\frac{r_{\text{perceived}}}{R} - 1.127\frac{r_{\text{perceived}}}{R}^{1/2} + 1.083} \right) R \quad (12)$$

The actual inner radius of the capillary was 140 μm. However, because of the tight curvature near the edges, it was estimated that only 125 μm were visible. This corresponds to a perceived radius ($r_{\text{perceived}}$) of 200 μm and a perceived diameter ($D_{\text{perceived}}$) of 400 μm. Equation (12) is used along with the perceived capillary diameter ($D_{\text{perceived}}$) and the capillary diameter measured in AutoCAD to determine the actual radial position of a doublet in micrometers.

For each doublet, an average radial position ($\bar{r}_{\text{c.m.}}$) of the center of mass of the doublet is calculated from the measured radial position for each bitmap image. The average radial position ($\bar{r}_{\text{c.m.}}$) is used in Eq. (9) or (10) to determine the average centroid radial position for each doublet ($\bar{r}_{\text{centroid}}$).

The orientation data for each doublet are compared to the theory for rotating spheroids by plotting the data along with Eq. (4) on an orientation (ϕ) versus nondimensional time plot. The orientation values for each doublet range from 1 deg to 360 deg. Since the first point of each doublet rotation is arbitrary, it was "located" along the tG (nondimensional time, t^*) axis by placing the nondimensional time value for the first data point of each new revolution on the theory line derived using Eq. (4). Each subsequent data point, after the first point to start a new rotation, is plotted based on its orientation value (ϕ) and its corresponding nondimensional time value (tG_i). The corresponding nondimensional time value is found by taking the previous value (tG_{i-1}) and adding the time difference between data points (1/30 s) multiplied by the appropriate shear rate (G):

$$tG_i = tG_{i-1} + \frac{G}{30} \tag{13}$$

The error between the data and theory is quantified for the ϕ versus tG curve. The square root of the sum of the squares of the distance between each data point and the theory is used to determine the rms error for each doublet.

$$E_G = \sum_{i}^{N} \frac{\sqrt{(tG_{\text{theory}}(\phi_i) - tG(\phi_i))^2}}{N} \tag{14}$$

The total number of data points is (N). The shear rate at either the center of mass ($G_{\text{c.m.}}$) or at the centroid of shear (G_{centroid}) can be used for the shear rate (G) in Eqs. (13) and (14). A discussion of the use of these two different shear rates follows in Sec. 3.

2.4 Primary or Secondary Doublets. Primary doublets are defined as doublets in which the particles are in direct contact with each other; secondary doublets are defined as doublets in which the particles rotating around each other are separated by a small distance. There is a corresponding difference in equivalent axis ratio r_e and hence rotational period between primary doublets and secondary doublets. The separation distance in a secondary doublet may be estimated based on standard DLVO theory, which describes the energy between two particles. The particle interaction energies are classified as van der Waals (Φ_{vdw}) and electrostatic (Φ_{es}). DLVO energy (Φ_{DLVO}) is the sum of the electrostatic energy and the van der Waals energy.

$$\Phi_{\text{DLVO}} = \Phi_{\text{vdw}} + \Phi_{\text{es}} \tag{15}$$

The van der Waals force is always attractive and the electrostatic force is always repulsive for particles of the same material. The van der waals energy (Φ_{vdw}) between two spherical particles has been shown to follow [16]

$$\Phi_{\text{vdw}} = -\frac{Aa_1a_2}{6(a_1+a_2)\delta} \tag{16}$$

where a_1 and a_2 are the particles' radii (a), δ is the distance between them (Fig. 2), and A is the Hamaker constant.

For electrostatic interactions between spherical particles, electrostatic energy (Φ_{es}) takes the form [16]

$$\Phi_{\text{es}} = \frac{\epsilon}{4}\left(\frac{a_1a_2}{a_1+a_2}\right)\left[2\zeta_1\zeta_2 \ln\frac{1+\exp^{-\kappa\delta}}{1-\exp^{-\kappa\delta}} + (\zeta_1^2+\zeta_2^2)\ln(1-\exp^{-2\kappa\delta})\right] \tag{17}$$

where a_1 and a_2 are radii of the particles, δ is the separation distance, ζ_1 and ζ_2 are zeta potentials of the particles, κ^{-1} is the Debye length, and ϵ is the permittivity of the suspending fluid. Both of the above expressions are only valid for thin double layers ($\kappa a \gg 1$).

Table 1 Tabulation of doublet classification as primary (*P*) or secondary (*S*), centroidal radial position ($\bar{r}_{\text{centroid}}$), shear rate calculated at the centroidal radial position (G_{centroid}), and rms error calculated using Eq. (14) assuming that all doublets are primary.

No.	Classification	$\bar{r}_{\text{centroid}}$ (μm)	G_{centroid} (s^{-1})	E_G ($tG_{\text{theor.}}=tG_{\text{primary}}$)
1	*P*	44.0	25.1	0.48
2	*P*	96.1	54.9	1.10
3	*P*	98.6	56.3	0.51
7	*S*	81.6	46.6	3.75
9	*S*	91.9	52.5	2.66
13	*S*	89.9	51.4	2.36
14	*S*	88.5	50.6	2.60
15	*S*	68.3	39.0	3.49
16	*S*	84.2	48.1	2.40

The inverse Debye length κ is defined as follows:

$$\kappa = \sqrt{\frac{2nZ^2e^2}{\epsilon kT}} \tag{18}$$

where n is the concentration of ions in the fluid, Z is the number of charges per ion, e is the charge per electron, k is Boltzmann's constant, and T is the fluid temperature. Here, κ is found to be 3.39 μm^{-1} so the Debye length ($1/\kappa$) is approximately 300 nm, and it is reasonable to approximate the electrical double layer as thin ($\kappa a \gg 1$).

The zeta potential (ζ) of these 48 μm PSL particles suspended in the neutrally buoyant water-glycerine solution was measured using a Rank Brothers electrophoresis apparatus MK II (Rank Brothers Ltd., Cambridge, England), one of the few instruments available for measuring ζ of these particles with a size not typically classified as colloidal [17]. The Rank Brothers instrument measures the electrophoretic velocity of the particles, which was converted to a zeta potential using O'Brien and White's method [18]. Two solutions are possible, namely, zeta potentials of −95 mV and −222 mV.

The DLVO model shows that electrostatic repulsion forces are expected to dominate the van der Waals attraction forces for all but the shortest separation distances. The predicted interaction energy between the particles Φ versus separation distance δ is shown in Fig. 6. Φ is nondimensionalized by Boltzmann's constant (k) and temperature T, and the separation distance is nondimensionalized by Debye length (κ^{-1}). Secondary minima for the two different possible zeta potentials are located at $\kappa\delta \sim 11.6$ (−95 mV) and $\kappa\delta \sim 13.6$ (−222 mV).

The distinction between a primary and a secondary doublet cannot be determined optically because the separation distance between the particles is very small compared to the particles' diameter. However, given the difference in equivalent axis ratio, doublets in flows with smaller d_p/D ratios have previously been classified as primary or secondary based on their rotational periods [11]. Herein, a similar classification is suggested even though the shear rate is not assumed to be constant over the height of the doublet (where height refers to $a_1+a_2+\delta$ for a doublet at ϕ =0 deg).

3 Results and Discussion

Nine doublets are analyzed (refer to Table 1). Once the orientation (ϕ) versus nondimensional time (tG) curves were produced, it became obvious that some of the doublets followed the theory for primary doublets (r_e=1.982) and others appeared to be secondary doublets because their nondimensional period was longer. The ϕ versus tG data for all doublets were plotted with r_e =1.982 (corresponding to a primary doublet or "touching" particles). The root-mean-square error between the theoretical versus

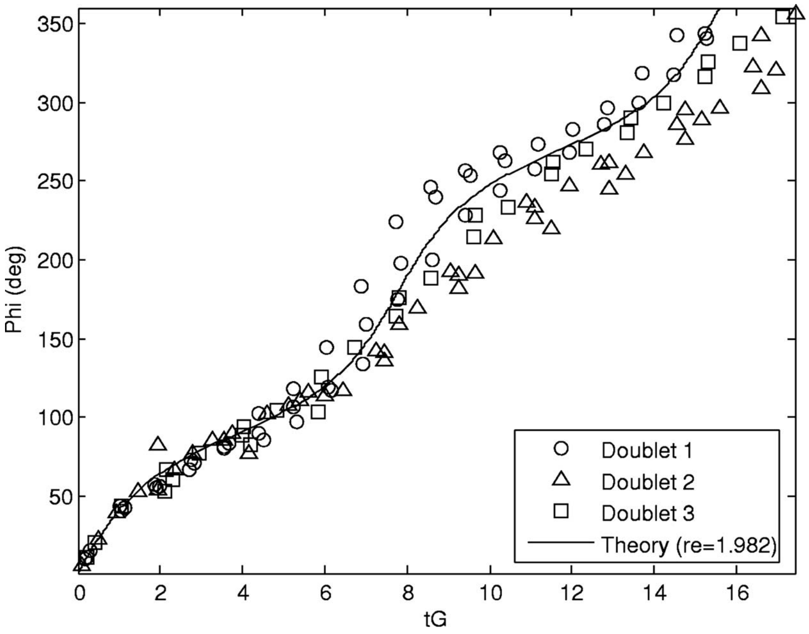

Fig. 7 ϕ **versus** tG **for observed doublets classified as primary** $(r_e=1.982)$

measured orientation for each data point in each doublet was calculated using Eq. (14) assuming that all doublets are primary and are shown in Table 1. The experimentally measured doublets were classified as the doublets whose "primary" rms error was less than 1.6. A rms error of 1.6 was used as the cutoff because it is 10% of the nondimensional period of a primary doublet. Therefore, all doublets classified as primary have a nondimensional period within 10% of the primary doublet theory developed by Van De Ven and Mason [5].

The remainder of the doublets had nondimensional periods greater than the primary doublets. Assuming that the separation distance δ in a secondary doublet is defined by the estimated secondary minimum on the DLVO curves (Fig. 6), the equivalent axis ratio would be in the range of 3.8–4.0. However, this estimated r_e is significantly larger than the r_e that provides the best fit of the orientation versus nondimensional time data for the nonprimary doublets (r_e=3.165). An equivalent axis ratio of 3.165 corresponds to a separation distance of $\kappa\delta \sim 5$ (1.5 μm). Here, a single value of r_e is calculated based on a best fit of the data. It is known that r_e (or, for that matter, nondimensional period) depends on surface charge and electrolyte concentration. Van de Ven and Mason [11] related the spread in equivalent axis ratio to the possible spread in zeta potential and particle size between separate doublets suspended in an electrolyte. Based on their data, a spread of approximately 10% in zeta potential would lead to a spread of only 0.5% in nondimensional period. Particle size was also found to have only a very small effect on the distribution of nondimensional period. Van de Ven and Mason [11] also surmised that a nonuniformity of surface charge could result in torques that influence the rotation causing variation in nondimensional period (and hence r_e) for nominally identical rotating doublets.

For the present case, the estimated mean separation distance of $\kappa\delta \sim 5$ is not strictly the secondary minimum estimated from the DLVO theory. However, it is noted that there is a relatively long and flat section of the DLVO curve for $\kappa\delta > 5$, and the negative slope of this curve at $\kappa\delta \sim 5$ is less than 1% of the slope of the curve just after the maximum ($\kappa\delta \sim 0.1$). Similar to Van de Ven and Mason [11], it is suggested that the separation distance estimated by DLVO theory may have some limitations and that, in fact, the separation distance may be better estimated by starting with the measured rotational period of the secondary doublets. One difference is that herein, the particles are not strictly colloidal, so it is not unexpected that the DLVO theory may be limited in its application, especially at such large separation distances. Other factors that may limit the use of DLVO theory in this system are its high sensitivity to estimates of physical parameters of the system and that it does not account for possible nonuniformities of charge distribution.

Table 1 shows which doublets were classified as primary (r_e =1.982) and which were classified as secondary (r_e=3.165). Figure 7 contains the orientation versus nondimensional time plot for the doublets classified as primary, and Fig. 8 contains the orientation versus nondimensional time plot for the doublets classified as secondary. Three of the doublets are primary and six are secondary. For each doublet, the radial location of the centroid of the shear across the doublet ($\bar{r}_{\text{centroid}}$) is listed along with the shear rate at that radial location (G_{centroid}) in Table 1.

Because of the differences in nondimensional rotation periods and the fact that the data collapse reasonably well onto these two curves, the data suggest that two different types or doublets are formed. It was found that about one-third of the doublets closely followed a theoretical prediction of rotational motion for primary doublets. The other two-thirds were found to have longer nondimensional periods, corresponding to a theoretical prediction of rotational motion for secondary doublets. In the course of data collection, one doublet formation was observed, as was one doublet destruction.

The uncertainty in radial position is primarily due to the relatively large depth of focus of the 2× microscope objective. This objective provided a large field of view, allowing the particles/doublets to be tracked over a longer time period, but it also had a large depth of focus (212 μm). Some additional uncertainty in R is attributed to the manufacturing limits in producing glass capillaries and manufacturer's specifications. Depth was measured in the direction of the X axis in Fig. 1.

Only doublets that appeared to rotate at or near $\theta \sim 90$ deg are considered in these experiments, which reduces the possible uncertainty in radial position. Without a three-dimensional perspective, it is not possible to precisely determine θ for each doublet. However, the authors only analyzed doublets that *appeared* to rotate at or near θ=90 deg. Considering the projection of doublets

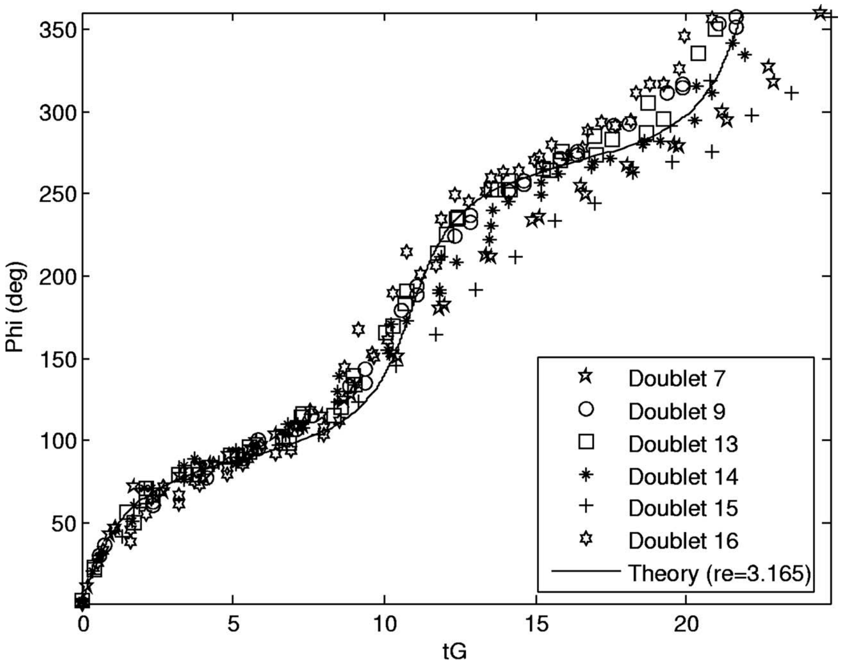

Fig. 8 ϕ **versus** tG **for observed doublets classified as secondary** (r_e=3.165)

with a range of θ orientations and comparing these projections to the actual images of the analyzed doublets, it is estimated then that θ is most likely to be in the range of 60–120 deg; otherwise, the perspective in the projected plane would make it prohibitive to measure ϕ (ϕ would be ill defined). (Van De Ven and Mason [11] estimated that the θ range for their experiment was 90 ± 60 deg.) Equation (5) predicts periodic motion in θ, which may appear as a slight wobble for projections of doublets located off $\theta \sim 90$ deg. Given the possible range of $\theta = 90 \pm 30$ deg, the uncertainty in radial position is at most +12 μm. Since the radial center of mass of the doublet is actually measured on the projection of the doublet in the $\theta = 90$ deg plane, any deviation from $\theta = 90$ deg actually reflects a radial center of mass greater than that measured; hence, the related uncertainty in radial position is quoted as only positive meaning that the related uncertainty in shear rate is biased toward greater shear rates. The uncertainty in the radius of the capillary is 9 μm (Fiber Optic Center, New Bedford, NJ).

Two effects on the prediction of rotation rate are of specific interest in the current work, namely, (i) the effect of classifying the doublets as primary or secondary, and (ii) the effect of using the shear rate at the center of mass ($G_{\text{c.m.}}$) versus the shear rate at the centroid of shear (G_{centroid}). In order to quantify these two effects, a root-mean-square error (E_G, refer to Eq. (14)) representing the error between the measured and the predicted position for all data points for each doublet is calculated. The quantity tG_{theory} in the equation for E_G (Eq. (14)) depends on r_e (and thus classification as primary or secondary). The quantity tG representing the measured point relies on the value of G used in the nondimensionalization, where G can be either the shear rate at the center of mass of the doublet ($G_{\text{c.m.}}$) or the shear rate at the centroid of shear (G_{centroid}). Thus, the rms error E_G for each doublet depends on *both* the doublet classification and the choice of G for nondimensionalization.

In order to quantify both of the effects named above, the rms error for each doublet is calculated (a) assuming that all doublets are primary (r_e=1.982) and with $G = G_{\text{centroid}}$; (b) assuming that the doublets can be properly classified as primary (r_e=1.982) or secondary (r_e=3.165) based on the rms error as discussed earlier; and using $G = G_{\text{c.m.}}$, and (c) assuming that the doublets can be properly classified as primary or secondary and using $G = G_{\text{centroid}}$. A mean rms error ($\overline{E_G}$, Eq. (19)) is calculated for each of the above cases: (a), (b), and (c), where $\overline{E_G}$ is

$$\overline{E_G} = \frac{\sum_i^M \left[\sum_i^N \frac{\sqrt{(tG_{\text{theory}}(\phi_i) - tG(\phi_i))^2}}{N} \right]}{M} \qquad (19)$$

The total number of data points for each doublet is N, and the total number of doublets is M.

It is determined that a 15% reduction in $\overline{E_G}$ occurs between cases (a) and (b) and that a 61% reduction in $\overline{E_G}$ occurs between cases (a) and (c). This reduction in mean rms error between the measured data and theoretical predictions for the case where the doublets are classified as primary or secondary *and* the shear rate used for nondimensionalization is that at the centroid of shear supports the two hypotheses that (i) the doublets can be classified as primary or secondary and (ii) the best choice for shear rate in nondimensionalization for "large" d_p/D doublets is indeed the shear rate at the centroid of shear rather than the shear rate at the center of mass of the doublet.

4 Summary and Conclusions

The motion of PSL particles suspended in a water-glycerine solution was captured using video microscopy as the particle-fluid suspension was drawn through a glass capillary tube. Particles were tracked as they moved through the capillary tube by translating the tube in the opposite direction of the particle-fluid flow. Particle tracking enabled individual particle interactions to be studied for a longer period of time when compared with conventional microscopy.

The rotational motion of relatively large d_p/D ratio doublets (d_p/D=0.17) was studied in Poiseuille flow in a capillary at Re <1. It was shown that rotational motion of these doublets agrees reasonably well with the theory presented by Van De Ven and Mason [5,11] when the radial position used to determine the shear rate is equal to the radial position of the centroid of shear across the height of the doublet. One-third of the doublets were shown to be primary doublets and the other two-thirds were shown to fit the theory for secondary doublets. Secondary doublets, or doublets in which the particles are slightly separated from each other, have a longer period of rotation, since the equivalent axis ratio is higher than for primary doublets. The separation distance in a secondary doublet was estimated using DLVO theory. However, given the suggested limitations in applicability of strict DLVO theory to the current system, the separation distance is better estimated by considering the average rotational period of doublets classified as nonprimary.

The primary contribution to the uncertainty within the experiments is expected to be due to the relatively large depth of focus of the objective. Even so, the doublet orientation versus nondimensional time data were found to agree quite well with the doublet rotational motion equations developed by Van De Ven and Mason [5,11], when the shear rate imposed on the doublet was calculated based on the location of the centroid of shear rather than the location of the center of the doublet. The data suggest that the doublets can be classified as primary or secondary based on their nondimensional rotational period.

It is determined that the minimum mean rms error between the measured data and theoretical predictions occurs for the case where the doublets are classified as primary or secondary and the shear rate used for nondimensionalization is that at the centroid of shear. This result supports the two hypotheses that (i) the doublets can be classified as primary or secondary and (ii) the best choice for shear rate in nondimensionalization for large d_p/D doublets is indeed the shear rate at the centroid of shear rather than the shear rate at the center of mass of the doublet.

Acknowledgment

This material is based on the work supported by the National Science Foundation under Grant No. 0348149. The authors would like to thank Dr. Allen Kimel and Dr. Darrell Velegol for their help and expertise in the field of colloidal science.

Nomenclature

A = Hamaker constant
D = capillary diameter
E_G = statistical measure of error between experimental data and theoretically predicted orientation as a function of time for one doublet
$\overline{E_G}$ = statistical measure of error between experimental data and theoretically predicted orientation as a function of time for all doublets
G, $G_{\text{c.m.}}$ = shear rate, shear rate at center of mass of doublet
G_{centroid} = shear rate at centroid of shear on doublet
Q = volume flowrate
M = total number of doublets analyzed
N = total number of data points for one doublet
Pe_t, Pe_r = Peclet number (translational, rotational)
Re = Reynolds number
R = $D/2$, capillary radius
T = temperature
Z = number of charges per ion
a, a_1, a_2, a_{ee} = radius of particle, radius of particle 1, radius of particle 2, semiaxis of revolution of equivalent ellipsoid (for doublet)
b_{ee} = semiaxis of equatorial diameter of equivalent ellipsoid (for doublet)
d_p = diameter of particle
e = charge per electron
h = center-to-center distance between spheres in a doublet
k = Boltzmann's constant
n = concentration of ions in fluid
r_e = equivalent ellipsoidal axis ratio ($=a_{ee}/b_{ee}$)
r, $r_{\text{c.m.}}$, $\bar{r}_{\text{c.m.}}$ = radial location, radial location of center of mass of doublet, average radial location of center of mass of doublet
$r_{\text{centroid}}, \bar{r}_{\text{centroid}}$ = radial location of centroid of shear on a doublet, average radial location of centroid of shear on a doublet
$r_{\text{perceived}}, r_{\text{actual}}$ = radial locations observed and corrected for curved glass viewing surface
t, t^* = time, nondimensional time
δ, δ^* = separation distance between particles, nondimensional separation distance used in calculation of r_e
κ = inverse Debye length
ϕ, θ = spherical polar coordinates
ω = $d\phi/dt$, rotation rate
ζ, ζ_1, ζ_2 = zeta potential, zeta potential of Particle 1, zeta potential of Particle 2
$\Phi_{\text{DLVO}}, \Phi_{\text{vdw}}, \Phi_{\text{es}}$ = particle interaction energies: sum of interaction energies, van der Waals energy, electrostatic energy

References

[1] Nguyen, N.-T., and Wereley, S., 2002, *Fundamentals and Applications of Microfluidics, Microelectromechanical Systems Series*, Artech House, Norwood, MA.
[2] Stone, H., Stroock, A., and Ajdari, A., 2004, "Engineering Flows in Small Devices: Microfluidics Toward a Lab on-a-Chip," Annu. Rev. Fluid Mech., **36**, pp. 881–411.
[3] Terray, A., Oakley, J., and Marr, W., 2002, "Fabrication of Linear Colloidal Structures for Microfluidic Applications," Appl. Phys. Lett., **81**(9), pp. 1555–1557.
[4] Jeffrey, G., 1922, "The motion of Ellipsoidal Particles Immersed in a Viscous Fluid," Proc. R. Soc. London, Ser. A, **102**(715), pp. 161–179.
[5] Van De Ven, T., and Mason, S., 1976, "The Microrheology of Colloidal Dispersions 4. Pairs of Interacting Spheres in Shear Flow," J. Colloid Interface Sci., **57**(3), pp. 505–516.
[6] Goldsmith, H., Quinn, T. A., Drury, G., Spanos, C., McIntosh, F., and Simon, S., 2001, "Dynamics of Neutrophil Aggregation in Couette Flow Revealed by Videomicroscopy: Effect of Shear Rate on Two-Body Collision Efficiency and Doublet Lifetime," Biophys. J., **81**, pp. 2020–2034.
[7] Long, M., Goldsmith, H., Tees, D., and Zhu, C., 1999, "Probabilistic Modeling of Shear-Induced Formation and Breakage of Doublets Cross-Linked by Receptor-Ligand Bonds," Biophys. J., **76**, pp. 1112–1128.
[8] Dua, A., and Cherayil, B., 2003, "Polymer Dynamics in Linear Mixed Flow," J. Chem. Phys., **119**(11), pp. 5696–5700.
[9] Lee, J., Shaqfeh, E., and Muller, S., 2007, "Dynamics of DNA Tumbling in Shear to Rotational Mixed Flows: Pathways and Periods," Phys. Rev. E, **75**, pp. 040802.
[10] Ladoux, B., and Doyle, P., 2000, "Stretching Tethered DNA Chains in Shear Flow," Europhys. Lett., **52**(5), pp. 511–517.
[11] Van De Ven, T., and Mason, S., 1976, "The Microrheology of Colloidal Dispersions 5. Primary and Secondary Doublets of Spheres in Shear Flow," J. Colloid Interface Sci., **57**(3), pp. 517–534.
[12] Goldsmith, H., and Mason, S., 1962, "The Flow of Suspensions Through Tubes 1. Single Spheres, Rods, and Discs," J. Colloid Sci., **17**, pp. 448–476.
[13] Wakiya, S., 1971, "Slow Motion in Shear Flow of a Doublet of Two Spheres in Contact," J. Phys. Soc. Jpn., **31**(5), pp. 1581–1587.
[14] Sheely, M., 1932, "Glycerol Viscosity Tables," Ind. Eng. Chem., **24**, pp. 1060–1064.
[15] McKeever, E., 2006, "Rotational Motion of Doublets in Poiseuille Flow in a Microtube," MS thesis, The Pennsylvania State University, Pennsylvania.
[16] Hogg, R., Healy, T., and Fuerstenau, D., 1966, "Mutual Coagulation of Colloidal Dispersions," Trans. Faraday Soc., **62**, pp. 1638–1651.
[17] Probstein, R., 1994, *Physiochemical Hydrodynamics*, 2nd ed., Wiley, New York.
[18] O'Brien, R., and White, L., 1978, "Electrophoretic Mobility of a Spherical Colloidal Particle," J. Chem. Soc., Faraday Trans. 2, **74**, pp. 1607–1626.

Noriyuki Shimiya
Department of Mechanical Science
and Bioengineering,
Graduate School of Engineering Science,
Osaka University,
1-3 Machikaneyama, Toyonaka,
Osaka 560-8531, Japan

Akira Fujii
Fluent Asia Pacific Co. Ltd.,
6-10-1 Nishishinjuku,
Shinjuku-ku, Tokyo, 160-0023, Japan

Hironori Horiguchi[1]
Department of Mechanical Science
and Bioengineering,
Graduate School of Engineering Science,
Osaka University,
1-3 Machikaneyama, Toyonaka,
Osaka 560-8531, Japan
e-mail: horiguti@me.es.osaka-u.ac.jp

Masaharu Uchiumi
Kakuda Space Propulsion Center,
JAXA,
1 Takakuzo, Jinjiro, Kakuda,
Miyagi 981-1526, Japan

Junichi Kurokawa
Division of Systems Research,
Faculty of Engineering,
Yokohama National University,
79-1 Tokiwadai,
Hodogaya-ku, Yokohama,
Kanagawa 240-8501, Japan

Yoshinobu Tsujimoto
Department of Mechanical Science
and Bioengineering,
Graduate School of Engineering Science,
Osaka University,
1-3 Machikaneyama, Toyonaka,
Osaka 560-8531, Japan

Suppression of Cavitation Instabilities in an Inducer by J Groove

The suppression of cavitation instabilities was attempted through the control of tip leakage vortex cavitation. The control was made by using shallow grooves, called J groove, on the casing wall. With J grooves, the onset regions of the rotating cavitation and the asymmetric cavitation could be diminished. However, a cavitation surge appeared at higher cavitation numbers. From the observation of cavitation, it was found that the cavitation surge occurred when the tip leakage vortex cavitation started to interact with the leading edge of the next blade. This type of cavitation surge could be avoided by extending the leading edge of the J groove upstream. However, in this case, another type of cavitation surge occurred at much lower cavitation numbers, which was caused by the cavitation between the blade surface and the tip leakage vortex cavitation. These results highlight the importance of the tip leakage vortex cavitation for cavitation instabilities.
[DOI: 10.1115/1.2829582]

Introduction

Cavitation instabilities such as the rotating cavitation (RC) and the cavitation surge (CS) occur in turbopump inducers for rocket engines and cause shaft vibrations and blade stress fluctuations. One of the effective methods for the suppression of the cavitation instabilities is to expand the casing diameter upstream of the inducer inlet [1]. However, there are certain cases in which cavitation instabilities cannot be suppressed perfectly. So, alternative methods for the suppression of cavitation instabilities are needed to realize reliable turbopumps.

One of the authors, Kurokawa, proposed the method using shallow grooves, named J groove, on the casing wall for the suppression of flow instabilities due to the positive slope of performance curve in a mixed flow pump [2]. A J groove was also applied to an inducer with larger blade angle [3]. For this case, the CS was suppressed almost completely. Our research group tried to suppress the cavitation instabilities in an inducer with a smaller blade angle for a rocket engine by a J groove on the casing wall near the inducer inlet for the development of a new method for the suppression of the cavitation instabilities [4]. In an inducer with a smaller blade angle, the RC was suppressed by a J groove, but the CS occurred at higher cavitation numbers [4].

The present paper reports about further attempts to suppress

---

[1] Corresponding author.

Contributed by the Fluids Engineering Division of ASME for publication in the JOURNAL OF FLUIDS ENGINEERING. Manuscript received November 6, 2006; final manuscript received August 24, 2007; published online January 25, 2008. Review conducted by Steven Ceccio. Paper presented at the Sixth International Symposium on Cavitation (CAV2006), Wageningen, The Netherlands, September 11–15, 2006.

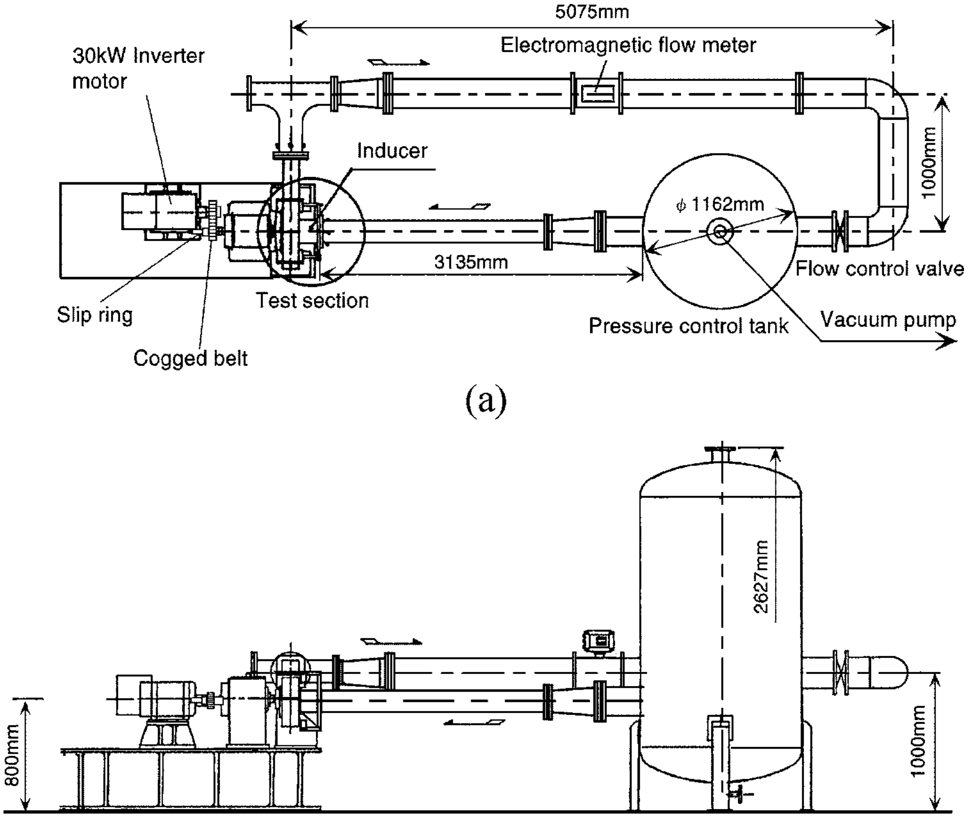

(a)

(b)

Fig. 1 Test facility: (*a*) top view and (*b*) side view

cavitation instabilities by J grooves and discusses about the correlation between tip leakage cavitation and cavitation instabilities.

Experimental Facilities

Figure 1 shows the cavitation tunnel used in the present study. This tunnel is a closed-loop-type tunnel, and the cavitation number is adjusted by changing the pressure of the air in the upper part of a tank by a vacuum pump. The working fluid is water, and experiments are performed after the deaeration of water. Figure 2 shows the sketch of a test inducer, and Table 1 shows principal dimensions.

Pressure fluctuation was measured at the inlet of the inducer by means of four pressure transducers flush mounted on the casing wall, as shown in Fig. 3, placed at intervals of 90 deg circumferentially. A type of these transducers is strain gauge type (Kyowa PGM-5KC), and their resonance frequency is 34 kHz. The rated capacity is 500 kPa, and the uncertainty is ±7.5 kPa (±1.5% of the rated capacity). The type of cavitation instability was determined from the phase difference of the signals from these pressure transducers. Casings were made of clear acrylic resin for visual observation and laser Doppler velocimeter (LDV) measurements. The rotational speed was 3000 rpm (50 Hz).

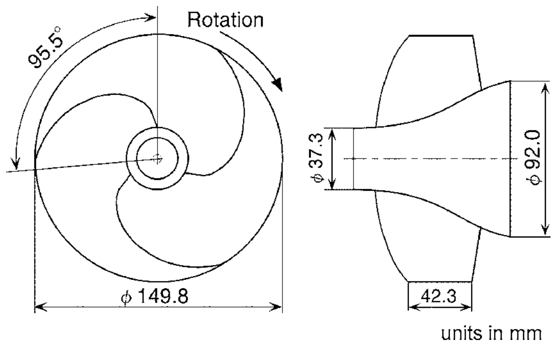

Fig. 2 Sketch of test inducer

Results and Discussions

Figure 3 shows a cross section of the inducer and the J groove. The shape and arrangement of the J groove were decided in consideration of the previous research [3]. From the research [3], it was suggested that the larger area ratio of 0.68 of the groove, defined as $WN/(\pi D_c)$, was better than 0.57 for the suppression of the cavitation instability. Here, W is the width of the groove, N is the number of grooves, and D_c is the diameter of casing. Moreover, a wider width of 12 mm of the groove was better than 6 mm. Therefore, we adopted the larger area ratio of 0.68 by setting the wider width 10 mm of the groove. As a result, the number of grooves is 32. The axial length of J grooves upstream and downstream from the leading edge of the inducer, L_1 and L_2,

Table 1 Principal dimensions of test inducer

Number of blades	3
Tip diameter, D (mm)	149.8
Inlet tip blade angle, β_{t1}	7.5 deg
Outlet tip blade angle, β_{t2}	9.0 deg
Hub/tip ratio at the inlet	0.25
Hub/tip ratio at the outlet	0.51
Solidity at the tip	1.91
Design flow coefficient, ϕ_d	0.078

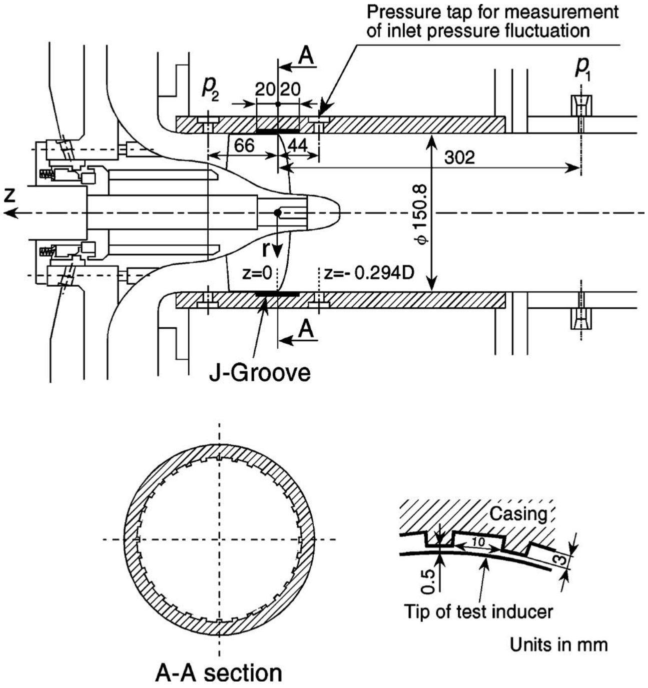

Fig. 3 Cross section of the inducer and J groove

are both 20 mm. The depth of the groove is 3 mm. This groove is called JG1(20,20) in the present study. Figure 4 shows the occurrence regions of cavitation instabilities on the suction performance curves, without and with JG1(20,20) [4]. The horizontal axis shows a cavitation number σ defined as $(p_1-p_v)/(\rho U_t^2/2)$, where p_v is a vapor pressure. The vertical axis shows a static pressure coefficient ψ_s defined as $(p_2-p_1)/(\rho U_t^2)$. The locations of the measurement of inlet and outlet pressures, p_1 and p_2, are shown in Fig. 3. U_t is a tip speed of the impeller. The pressures, p_1 and p_2, are measured by two differential pressure gauges (Kyowa PD-2KA and PDU-5KA) whose rated capacities are 200 kPa and 500 kPa, respectively. Their uncertainties are $\pm 0.3\%(\pm 600\text{ Pa})$ and $\pm 0.2\%(\pm 1\text{ kPa})$. The frequency response range of both gauges is about 0–30 Hz. ϕ is a flow coefficient defined as v_1/U_t, where v_1 is a mean axial velocity at the z plane, which crosses the root of the leading edge. In the case with JG1(20,20), the RC and the asymmetric cavitation (AC) observed without the groove were almost suppressed. However, the CS appeared at higher cavitation numbers.

Velocity distributions at the inducer inlet were obtained by 1D LDV (Kanomax, probe: FLVP-K (Model 1884), laser unit: FLV8851, signal processing board: Model 8007). About 1000 data were averaged at each measurement point. Figures 5(*a*) and 5(*b*) show axial and tangential velocity distributions at the design flow coefficient, which are measured at $z/D=-0.294$ and a certain circumferential location. The horizontal axis r/R shows a nondimensional radial location, where r is a radial location and R is the tip radius of the impeller. The data in the case without a J groove were obtained by a pitot tube with three holes by Maekawa [5]. With a J groove, backflow and prerotation in the vicinity of the casing wall disappear. This shows that J groove can suppress prerotation and backflow in the upstream.

Figure 6 shows the cavities at the design flow coefficient $\phi=0.078$ and the cavitation number $\sigma=0.120$, with and without JG1(20,20). With a J groove, the tip cavitation rolls up into a vortex and detaches from the blade surface. The tip leakage vortex cavitation bends to a circumferential direction near the leading edge of the J groove and extends toward the leading edge of the next blade. With a J groove, the cavity length is larger than that without a J groove. When the cavitation number decreases, the tip vortex cavitation becomes longer, and the CS starts to occur at the cavitation number where the tip leakage vortex cavitation starts to interact with the leading edge of next blade [4]. This suggests that the CS at the higher cavitation numbers with JG1(20,20) is caused by the interaction. Since the tip leakage vortex cavitation is bent to a circumferential direction near the leading edge of the grooves, it is expected that the interaction and hence the CS can be avoided by extending the groove upstream.

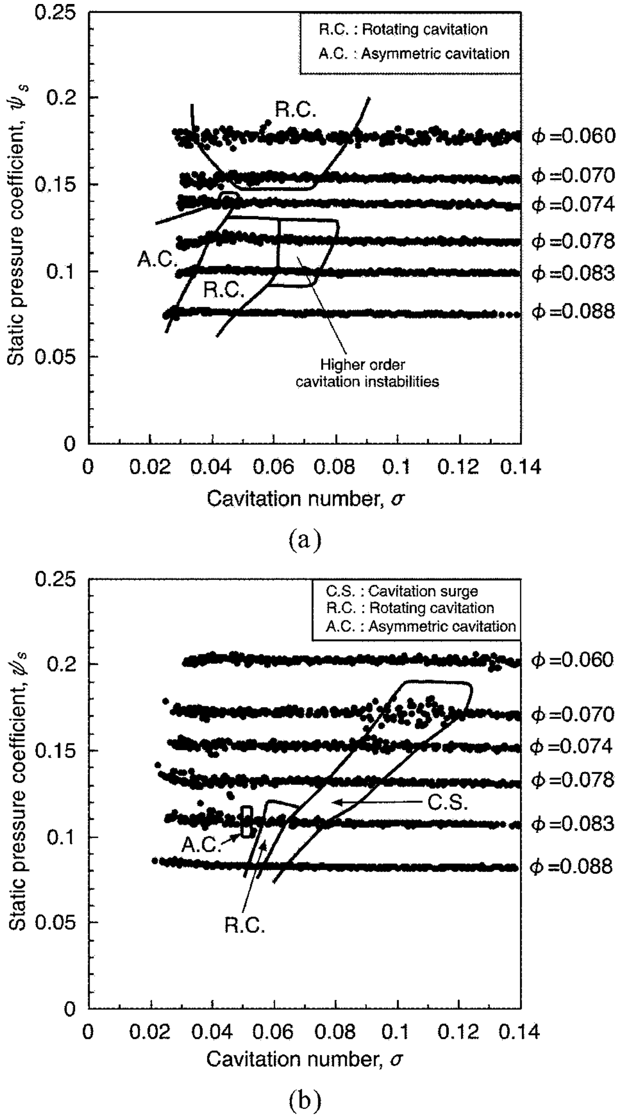

Fig. 4 The occurrence regions of cavitation instabilities on the suction performance curves at various flow coefficients. The rotational speed is 3000 rpm. (*a*) Without a J groove. (*b*) With JG1(20,20).

Figure 7 shows the cross section of a new casing with a J groove with the leading edge extended upstream by 20 mm. This groove is called JG2(40,20). The width, the depth, and the number of the J grooves of JG2(40,20) are the same as those of JG1(20,20). The occurrence regions of the cavitation instabilities in the case with JG2(40,20) is shown in Fig. 8 on the suction performance curves. Comparing Fig. 8 with Fig. 4(*b*), the occurrence region of the CS at higher cavitation numbers and RC is decreased in the case with JG2(40,20). The AC was suppressed completely. However, at lower cavitation numbers ($\sigma \leqq 0.04$), another type of CS appeared.

Figures 9(*a*) and 9(*b*) show photographs of a tip cavitation in

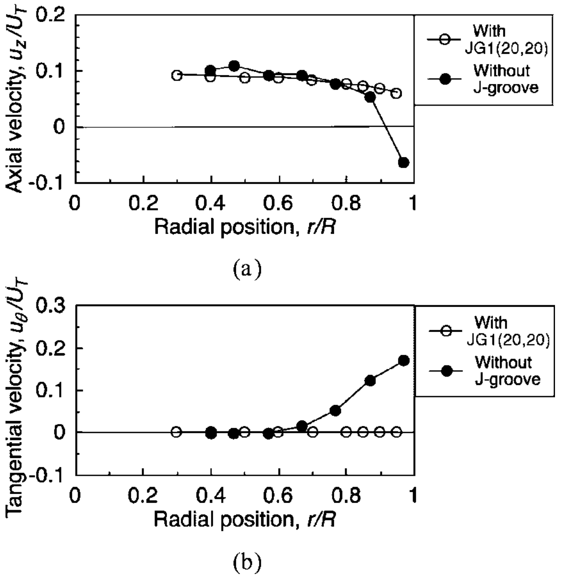

Fig. 5 Velocity distributions at the inlet of the inducer ($z/D=-0.294$) in noncavitating condition. $\phi=0.078$, 2000 rpm. (*a*) Axial velocity. (*b*) Tangential velocity.

the case with JG1(20,20) and JG2(40,20), respectively, at the lower flow coefficient ($\phi=0.060$) where the effect of the J groove is remarkable. The cavitation number σ is 0.180. In these figures, it is found that the tip leakage vortex cavitation extends more upstream in the case with JG2(40,20), as expected. Therefore, the interaction between the tip leakage vortex cavitation and the leading edge of the next blade does not occur in the case with JG2(40,20), and the CS at higher cavitation number is avoided. For both cases, a ring vortex can be observed at internal radial locations between the leading edges of the blades and the grooves.

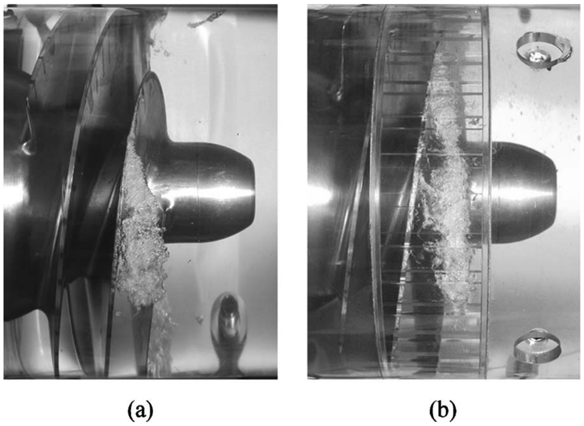

Fig. 6 Tip cavitation in the inducer without and with JG1(20,20). $\phi=0.078$, $\sigma=0.120$, 3000 rpm. (*a*) Without a J groove. (*b*) With JG1(20,20).

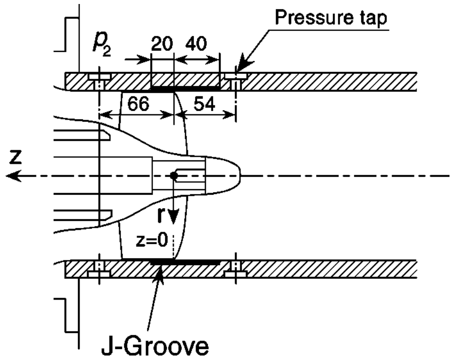

Fig. 7 Cross section of JG2(40,20)

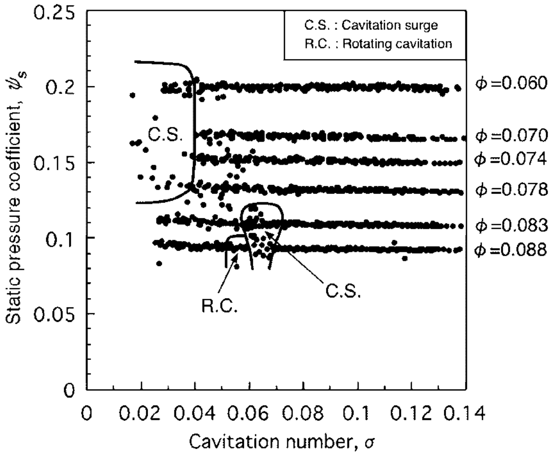

Fig. 8 The occurrence regions of cavitation instabilities on the suction performance curves at various flow coefficients in the case with JG2(40,20). The rotational speed is 3000 rpm.

Next, we think about the CS at higher flow coefficients ($\phi=0.083-0.088$) and higher cavitation numbers ($\sigma=0.055-0.065$). Figure 10 shows the photographs of tip cavitation under the CS in the case with JG2(40,20) at $\phi=0.088$ and $\sigma=0.065$. The tip leakage vortex cavitation does not extend upstream due to reduced blade loading near the leading edge. The interaction of the tip vortex cavitation with the next blade is clear, and this is the reason why the CS could not be avoided at a higher flow rate. Figure 11 shows the spectra of inlet pressure fluctuation in the case with JG2(40,20) at $\phi=0.088$. The spectra were produced by the signals from a certain transducer at the inlet, and the signals were averaged 16 times over the period of 0.8 s. The vertical axis is a fluctuating pressure coefficient $\Delta\psi$ defined as $\Delta p/(\rho U_t^2)$. f_n is a frequency of the impeller rotation. The frequency of the CS at the higher flow coefficients and $\sigma \fallingdotseq 0.060-0.070$ was about 13 Hz at 3000 rpm (50 Hz). The fluctuation of the cavity length in the CS was also observed in JG1(20,20), and its frequency is the same as the frequency in JG2(40,20).

Now, we focus on the CS at the lower flow coefficients ($\phi \leqq 0.078$) and lower cavitation numbers ($\sigma \leqq 0.040$). Figure 12 shows a photograph of the tip cavitation just before the occurrence of the CS at $\phi=0.078$ and $\sigma=0.050$. As shown in Fig. 9(*b*), the

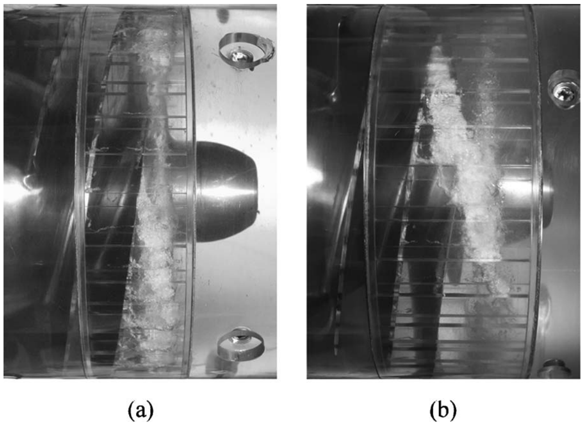

Fig. 9 Tip cavitation in the inducer for $\phi=0.060$ and $\sigma=0.180$. (*a*) JG1(20,20). (*b*) JG2(40,20).

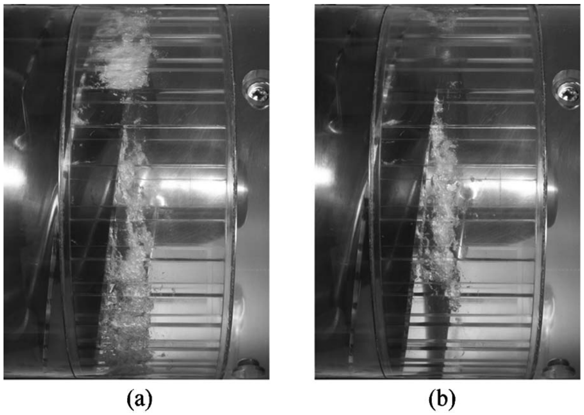
(a) (b)

Fig. 10 Tip cavitation under the CS with JG2(40,20) for $\phi = 0.088$ and $\sigma = 0.065$. (*a*) With a longer cavity. (*b*) With a shorter cavity.

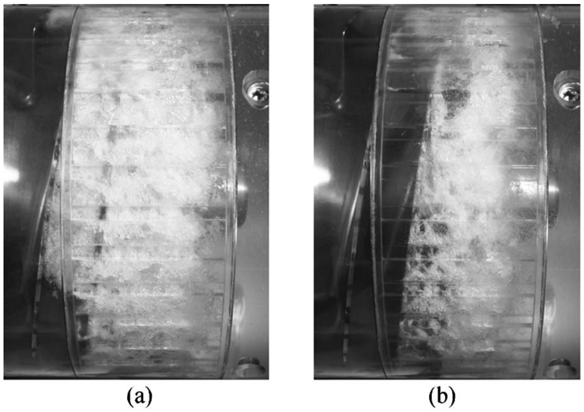
(a) (b)

Fig. 13 Tip cavitation under the CS in the case with JG2(40,20) for $\phi = 0.078$ and $\sigma = 0.030$ (*a*) With a heavier cavity. (*b*) With a lighter cavity.

interference between the tip leakage vortex cavitation and the leading edge of the next blade can be avoided. However, when the cavitation number decreases, the cavitation between the tip leakage vortex cavitation and the blade surface, which is shown by a circle in Fig. 12, develops and approaches the leading edge. The CS shown in Fig. 13 occurs when this tip leakage cavity starts to interact with the leading edge of the next blade. This suggests that the CS at the lower cavitation numbers ($\sigma \leqq 0.040$ in Fig. 8) is caused by the interference of the leading edge of the next blade with the cavitation between the tip leakage vortex and the blade surface. Figure 14 shows the spectra of the inlet pressure fluctuation at the design flow coefficient ($\phi = 0.078$). The frequency of the CS at $\sigma \fallingdotseq 0.030$ is about 5 Hz, which is significantly lower than the frequency 13 Hz of the CS at higher cavitation numbers.

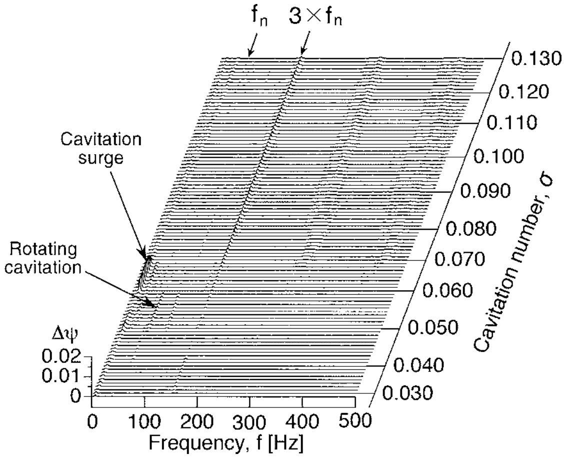

Fig. 11 Spectra of inlet pressure fluctuation in the case with JG2(40,20) for $\phi = 0.088$ and 3000 rpm

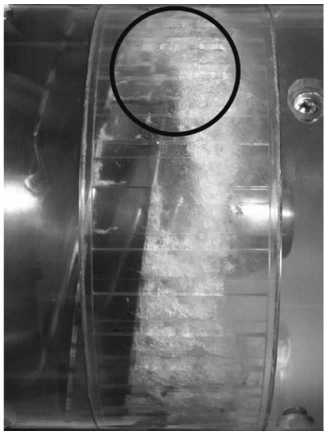

Fig. 12 Tip cavitation in the inducer in the case with JG2(40,20) for $\phi = 0.078$ and $\sigma = 0.050$

The cavity between the tip leakage vortex cavitation and the blade surface mainly occurs in the grooves, as shown in Figs. 12 and 13. From these results, it is expected that the displacement of the trailing edge of the J groove upstream could delay the interference of the cavity with the leading edge of the next blade. Thus, the trailing edge of the J groove was moved upstream by 10 mm. The cross section of the new casing is shown in Fig. 15, and the groove is called JG3(40,10). The width, the depth, and the number of grooves of JG3(40,10) are the same as those of JG1(20,20) and JG2(40,20).

Occurrence regions of cavitation instabilities with JG3(40,10) is shown in Fig. 16. Comparing with Fig. 8, it is found that the occurrence region of the CS at lower cavitation numbers is extended. Figure 17 shows photographs of the tip cavitation at $\phi = 0.060$ and $\sigma = 0.150$. The angle of the tip leakage vortex cavitation from the blade surface is smaller for the case with JG3(40,10) as compared with JG2(40,20) caused by the decrease of the flow rate of backflow in the J groove. Figure 18 shows a photograph of

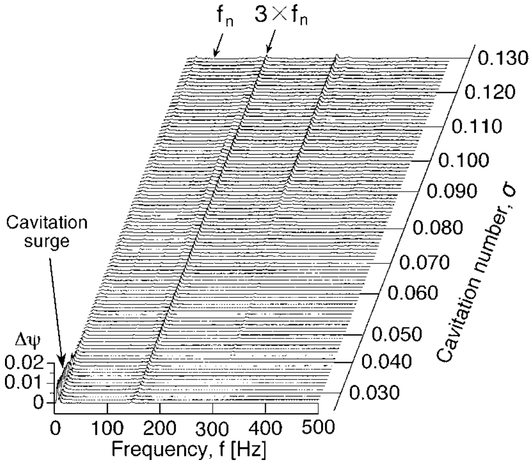

Fig. 14 Spectra of inlet pressure fluctuation in the case with JG2(40,20) for $\phi = 0.078$ and 3000 rpm

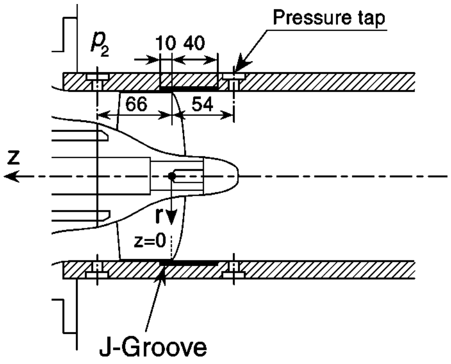

Fig. 15 Cross section of JG3(40,10)

the tip cavitation at $\phi=0.078$ and $\sigma=0.050$ just before the occurrence of the CS. A comparison with Fig. 12 shows that the cavity is closer to the leading edge for JG3(40,10).

In an inducer with a larger blade angle, the CS was suppressed completely by increasing the width of the J groove [3]. Based on this fact, a new casing with increased groove width (15 mm) and decreased number (24) was tested. The area ratio of the groove $WN/(\pi D_c)$ is 0.76. The axial location of the J groove was the same as JG3(40,20). The occurrence region of the CS was almost the same as JG3(40,10).

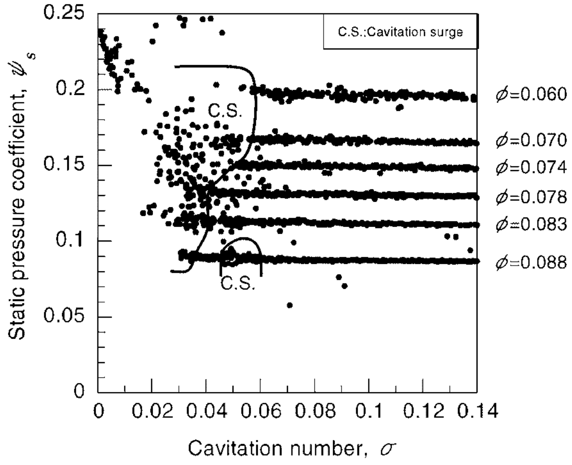

Fig. 16 The occurrence regions of cavitation instabilities on the suction performance curves at various flow coefficients in the case with JG3(40,10). The rotational speed is 3000 rpm.

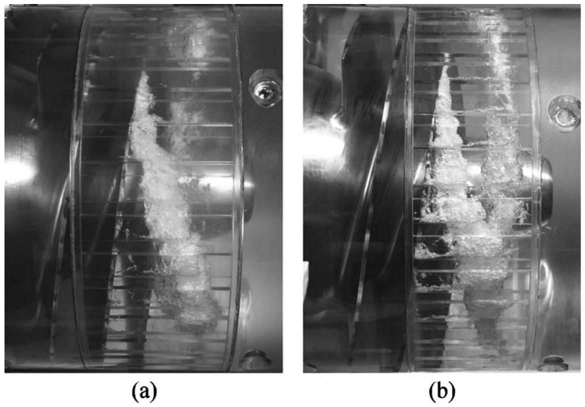
(a) (b)

Fig. 17 Tip cavitation in the inducer for $\phi=0.060$ and $\sigma=0.150$. (*a*) JG2(40,20). (*b*) JG3(40,10).

Fig. 18 Tip cavitation in the inducer in the case with JG3(40,10) for $\phi=0.078$ and $\sigma=0.050$

Conclusions

The relation between cavitation instabilities and tip leakage vortex cavitation is discussed by controlling the latter by a J groove. The results can be summarized as follows.

(1) The occurrence region of the RC and the AC could be decreased by J grooves.
(2) Prerotation and backflow in the upstream were diminished by the J groove.
(3) The CS in higher cavitation numbers in the case with a J groove was caused by the interference of the tip leakage vortex cavitation with the leading edge of the next blade. Since the cavity length of the tip leakage vortex cavitation became longer and the tip leakage vortex cavitation was bent to a circumferential direction near the leading edge of the grooves, the interference occurred.
(4) The CS in higher cavitation numbers in the case with a J groove could be almost suppressed by extending J groove upstream. This is because the tip leakage vortex cavitation could extend upstream, and it did not interact with the leading edge of the next blade.
(5) When the cavitation number was decreased, the CS occurred in lower cavitation numbers in the casing with a J groove extended upstream. This was caused by the interference of the leading edge of the next blade with the cavitation between the tip leakage vortex cavitation and the blade surface.
(6) To suppress the cavitation between the tip leakage vortex cavitation and the blade surface, the J groove whose trailing edge was moved upstream by 10 mm was used. This J groove was not effective, and the occurrence region of the CS at lower cavitation numbers was extended. This was because the interference of the tip leakage vortex cavitation with the leading edge of the next blade occurred since the flow rate of the backflow decreased and the angle of the tip leakage vortex cavitation from the blade surface became smaller.
(7) The effect of the J groove is larger at the lower flow coefficients than at the design flow coefficient because the tip leakage vortex cavitation extends upstream and does not interact with the leading edge of the next blade.
(8) At higher flow coefficients, the tip leakage vortex cavitation develops in the circumferential direction with or without a J groove and starts to interact with the leading edge of the next blade. As a result, the cavitation instabilities are not suppressed at higher flow coefficients.

As mentioned above, it was found that the interference of the tip leakage vortex cavitation with the leading edge of the next blade is closely related to the occurrence of cavitation instabilities. By a two-dimensional stability analysis, it has been shown theoretically that the interference of the blade surface cavitation on the blade surface with the next blade causes various modes of instabilities (Horiguchi et al. [6]). Based on this result, the relation between the cavitation near the tip and cavitation instabilities has been discussed. The results of the present study shows the importance of the tip leakage vortex cavitation, and it is suggested that cavitation instability can be suppressed by controlling the tip leakage vortex cavitation, not only by the J groove but also by the design of the impeller. So, we are planning to suppress the cavitation instabilities by changing the design of the inducer.

Nomenclature

D = diameter of inducer
D_c = diameter of casing
f = frequency of fluctuation
f_n = frequency of shaft rotation
L = axial length of the J groove
L_1 = axial length of the J groove upstream of the leading edge of the inducer
L_2 = axial length of the J groove downstream of the leading edge of the inducer
N = number of grooves
p_1 = inlet pressure
p_{1t} = inlet total pressure
p_2 = outlet pressure
p_v = vapor pressure
Δp = pressure fluctuation
r = radial position
R = radius of the inducer
U_t = tip speed $= \pi D f_n$
u_z = axial velocity
u_θ = tangential velocity
v_1 = mean axial velocity at the inducer inlet = flow rate/inlet area
W = width of the groove
z = axial position measured downstream from the tip leading edge
β_{t1} = inlet blade angle at the tip
β_{t2} = outlet blade angle at the tip
ρ = density
σ = cavitation number $= (p_1 - p_v)/(\rho U_t^2/2)$
ϕ = flow coefficient $= v_1/U_t$
ϕ_d = design flow coefficient
ψ_s = static pressure coefficient $= (p_2 - p_1)/(\rho U_t^2)$
$\Delta\psi$ = fluctuating pressure coefficient $= \Delta p/(\rho U_t^2)$

References

[1] Kamijo, K., Yoshida, M., and Tsujimoto, Y., 1993, “Hydraulic and Mechanical Performance of LE-7 LOX Pump Inducer,” J. Propul. Power, **9**(6), pp. 819–826.

[2] Saha, S. L., Kurokawa, J., Matsui, J., and Imamura, H., 2000, “Suppression of Performance Curve Instability of a Mixed Flow Pump by Use of J-Groove,” ASME Trans. J. Fluids Eng., **122**(3), pp. 592–597.

[3] Choi, Y. D., Kurokawa, J., and Imamura, H., 2007, “Suppression of Cavitation in Inducers by J-Grooves,” ASME Trans. J. Fluids Eng., **129**(1), pp. 15–22.

[4] Fujii, A., Uchiumi, M., Kurokawa, J., and Tsujimoto, Y., 2006, “Suppression of Rotating Cavitation in an Inducer by J-Groove,” Trans. Jpn. Soc. Mech. Eng., Ser. B, **72**(722), pp. 2496–2504 (in Japanese).

[5] Maekawa, Y., 1996, “Experimental Study of Unsteady Cavitation in an Inducer,” MS thesis, Osaka University (in Japanese).

[6] Horiguchi, H., Watanabe, S., and Tsujimoto, Y., 2000, “A Linear Stability Analysis of Cavitation in a Finite Blade Count Impeller,” ASME Trans. J. Fluids Eng., **122**(4), pp. 798–805.

M. Anderson
Department of Mechanical Engineering,
University of Idaho,
Moscow, ID 83844
e-mail: anderson@uidaho.edu

C. Richards
School of Mechanical and Materials Engineering,
Washington State University,
Pullman, WA 99164
e-mail: cill@wsu.edu

R. Richards
School of Mechanical and Materials Engineering,
Washington State University,
Pullman, WA 99164

D. Bahr
School of Mechanical and Materials Engineering,
Washington State University,
Pullman, WA 99164

Lumped Parameter Analysis of an Enclosed Incompressible Squeeze Film and a Central Gas Bubble

A lumped-parameter dynamic model for an enclosed incompressible squeeze film with a central gas bubble has been derived. A new approach was applied to derive closed-form expressions for the lumped-parameter mass and damping coefficients caused by liquid motion. It was assumed that plate motions were small and the fluid behaved as a continuum. The values of the lumped-parameter mass and damping were found to depend on the aspect ratio and nondimensional squeeze-film thickness. The nondimensional thickness was given by the ratio of the actual squeeze-film thickness to the viscous penetration depth of the liquid. A nondimensional squeeze-film thickness of a value of 5 was found to divide between categories of thick and thin incompressible squeeze films. Amplification of the liquid mass and damping over and above squeeze films open to the atmosphere at the edges was found. The amplification was attributed to converging flow caused by enclosed boundaries. Comparisons between the lumped-parameter model predictions and finite-element computations showed a surprising degree of accuracy for the lumped-parameter model despite large liquid velocities in the squeeze film. [DOI: 10.1115/1.2829587]

1 Introduction

Many microelectromechanical system (MEMS) devices contain a squeeze film. A squeeze film of some degree will be present in a device if two parts move relative to one another in near proximity when immersed in a fluid. The categories of squeeze films are determined by the geometry of the gap, the relative motion between the moving parts, and the nature of the fluid. The fluid in the squeeze film can take the form of a rarified gas, a compressible gas or liquid, or an incompressible liquid. Although some may consider that the term “squeeze film” is limited to a situation when fluid compressibility is important, the term is also used in the lubrication literature for films containing an incompressible fluid.

In this paper, an enclosed system of cylindrical geometry consisting of a planar incompressible liquid squeeze film with a central gas bubble is considered. This configuration comprises the simplified dynamic elements of MEMS liquid-vapor phase change actuators [1–5]. These thermally driven actuators generally consist of a cavity bounded on the bottom by a relatively stiff boundary on which a heater is fabricated and on the top by a compliant elastic element. The elastic element is typically a membrane, although cantilevers have been used as well [3]. Materials used for the upper membrane include silicon [1,3,4], silicon nitride [1], and silicone rubber [5]. The cavity is filled with a volatile liquid such as methanol, fluorinert, or pentane. Heat addition leads to vaporization of the liquid and subsequent displacement of the upper membrane due to the increased pressure in the cavity. These actuators are used in a variety of applications, which include, but are not limited to, valves [2,4], pumps [5], and heat engines [6]. In addition to this class of devices, the dynamics of the liquid in this geometry may also be applicable to MEMS devices that use a circular diaphragm to pump liquids [7,8]. A simple lumped-parameter model of a liquid squeeze film with this geometry does not presently exist.

Dynamic models related to the enclosed incompressible squeeze film with a central gas bubble have appeared in the literature. Hashemi and Roylance [9] derived a lumped-parameter dynamic model for an incompressible fluid between two parallel circular plates (without a central gas bubble), and open to the atmosphere at the edges. Turns [10] and Usha and Sridharan [11] analyzed an incompressible squeeze film between two annular circular plates, with the interior and exterior edges of the liquid open. Hashimoto [12], Haber and Etsion [13], and later Usha and Vimala [14] considered an incompressible squeeze layer with a central air bubble, but left the outside edge of the liquid squeeze film open. The works [10–14] predicted squeeze film forces and motions, but did not specify closed-form expressions for the lumped-parameter mass, damping, and stiffness for the dynamic system.

The present work takes the previous analyses one step further, to enclose the outside edge of the liquid-bubble system, and derive expressions for a lumped-parameter dynamic model. The analysis assumes small plate movements, and that the fluids behave in the continuum limit. A special focus is placed upon the computation of lumped-parameter mass and damping effect of the liquid, because these quantities influence the dynamic behavior of devices that contain a squeeze film, and they can reach significant magnitudes for small geometries.

Unlike use of the successive approximation [9,10,15], the Reynolds lubrication equation [16], or similar techniques [11,12,14], the present analysis used a new approach to characterize the squeeze-film motion of the liquid. Full-field expressions for liquid velocity that satisfy mass conservation and the appropriate boundary conditions were determined. The pressure in the liquid was determined by direct integration. Closed-form expressions for the equivalent mass and damping caused by the incompressible liquid were then obtained from the liquid pressure in association with the stiffness coefficient for the central gas bubble. This approach does not assume that the Reynolds squeeze number is small and that the liquid velocity is parabolic in profile.

Contributed by the Fluids Engineering Division of ASME for publication in the JOURNAL OF FLUIDS ENGINEERING. Manuscript received April 4, 2007; final manuscript received September 21, 2007; published online January 25, 2008. Review conducted by Joseph Katz.

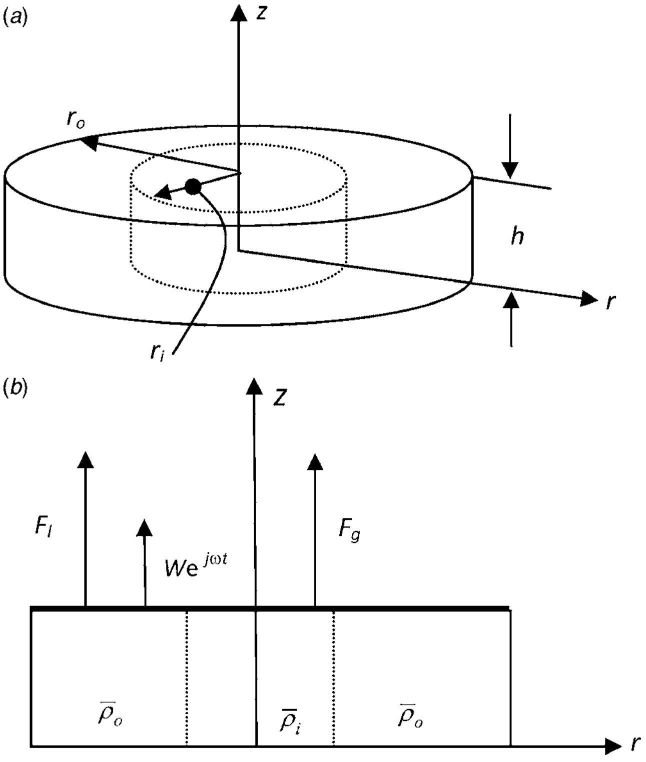

Fig. 1 Cavity geometry. (*a*) Isometric view and (*b*) side view.

2 Deriving a Lumped-Parameter Model

Consider a closed cylindrical cavity of radius r_o and height h shown in Fig. 1. The coordinates (r,z) are located on the axis of the cavity, with $z=0$ at the bottom. An incompressible liquid occupies the annulus $r_i<r<r_o$, and a noncondensable gas occupies the center $0<r<r_i$. A cross section of the cavity is shown in part (b) of Fig. 1. The ambient densities of the liquid and gas are $\bar{\rho}_i$ and $\bar{\rho}_o$ in the center $0<r<r_i$ and annulus $r_i<r<r_o$, respectively. Surface tension required to statically maintain the shape of the bubble is neglected.

The top boundary of the cavity is assumed to take the form of a rigid, massless disk. The disk is allowed to move harmonically in the z direction with velocity $We^{j\omega t}$, where ω is the circular frequency, under the assumption that $|W/\omega| \ll h$. As such, a linearized analysis is then performed. The force required to cause the motion of the upper boundary is $Fe^{j\omega t}$. In Fig. 1, the force $Fe^{j\omega t}$ is shown to be decomposed into the sum $Fe^{j\omega t}=F_l e^{j\omega t}+F_g e^{j\omega t}$, where $F_l e^{j\omega t}$ and $F_g e^{j\omega t}$ are the forces exerted on the disk by the liquid and gas respectively. The relationship between the force $Fe^{j\omega t}$ and the velocity $We^{j\omega t}$ contains the model representing the dynamics of the liquid and the compressibility of the gas.

2.1 Gas Bubble. To model the gas bubble, it is necessary to account for radial and vertical contributions to changes in the bubble volume. In the bubble, conservation of mass requires

$$\pi r_i^2 \bar{\rho}_i h = \pi (r_i + \Delta r_i)^2 (h + \Delta h)(\bar{\rho}_i + \Delta \rho_i) \tag{1}$$

where Δr_i and Δh are variations in the bubble radius and height caused by the motion of the upper boundary $We^{j\omega t}$, and $\Delta \rho_i$ is the change in gas density caused by the associated changes in bubble volume. For small motions $|W/\omega| \ll h$, the conservation of mass equation (1) approximates to

$$\pi r_i^2 h \Delta\rho_i + \pi r_i^2 \bar{\rho}_i \Delta h + 2\pi r_i h \bar{\rho}_i \Delta r_i \approx 0 \tag{2}$$

Assuming that the acoustic wavelength is much larger than the maximal dimension of the gas bubble, the excess pressure p_i in the bubble can be computed from [17]

$$p_i = c_i^2 \Delta \rho_i \tag{3}$$

where c_i is the sound speed in the bubble. The sound speed may be either isothermal or isentropic. Replacing $\Delta\rho_i$ from Eq. (3) above yields

$$\Delta r_i = -\frac{r_i}{2\bar{\rho}_i c_i^2} p_i - \frac{r_i}{2h}\Delta h \tag{4}$$

Upon taking the time derivative, one can calculate the radial velocity of the gas u_i in the r direction at $r=r_i$ as

$$u_i\big|_{r=r_i} = -\frac{r_i}{2\bar{\rho}_i c_i^2}\frac{\partial p_i}{\partial t} - \frac{r_i}{2h} We^{j\omega t} \tag{5}$$

2.2 Inviscid Motion of the Liquid. When viscosity is neglected, the velocity field in the liquid must obey conservation of mass and vanishing velocity normal to the boundary. Assuming radial symmetry, the conservation of mass equation is

$$\frac{1}{r}\frac{\partial}{\partial r}(r u_o) + \frac{\partial w_o}{\partial z} = 0$$

where u_o is the velocity in the r direction, w_o is the velocity in the z direction, and the subscript o indicates that the velocities pertain to the section $r_i<r<r_o$ containing the liquid. The velocity must satisfy the boundary conditions

$$w_o(r,z=h) = We^{j\omega t} \quad w_o(r,z=0)=0 \quad u_o(r=r_o,z)=0$$

Expressions for the velocities u_o and w_o that satisfy these conditions are

$$w_o = \frac{z}{h} We^{j\omega t} \tag{6}$$

$$u_o = \frac{r}{2h}\left[\left(\frac{r_o}{r}\right)^2 - 1\right] We^{j\omega t} \tag{7}$$

The velocities (6) and (7) fall into the category of potential flow, as the vector curl of this field is zero.

The pressure p_o in excess of ambient can be determined from the conservation of momentum equations

$$\bar{\rho}_o \frac{\partial w_o}{\partial t} = -\frac{\partial p_o}{\partial z} \quad \bar{\rho}_o \frac{\partial u_o}{\partial t} = -\frac{\partial p_o}{\partial r}$$

where viscosity has been neglected. By direct integration of both equations using Eqs. (6) and (7) for u_o and w_o, one obtains

$$p_o(r,z,t) = -\bar{\rho}_o j\omega \frac{1}{2h}\left[z^2 + r_o^2 \ln r - \frac{r^2}{2} + C\right] We^{j\omega t} \tag{8}$$

for the excess liquid pressure p_o, where C is a constant of integration.

Boundary conditions at the interface between the gas and liquid are now applied to determine the excess pressures in the liquid p_o and gas bubble p_i. These boundary conditions are continuity in pressure and radial velocity at $r=r_i$. Requiring continuity in radial velocity by equating Eqs. (5) and (7) at $r=r_i$ determines the acoustic pressure p_i in the gas cavity to be

$$p_i = -\frac{\bar{\rho}_i c_i^2}{j\omega h}\left(\frac{r_o}{r_i}\right)^2 We^{j\omega t} \tag{9}$$

Requiring continuity in excess pressures p_o and p_i at $r=r_i$ determines the constant of integration C in Eq. (8), and the excess pressure p_o in the liquid becomes

$$p_o(r,z,t) = -\bar{\rho}_o j\omega \frac{1}{2h}\left[z^2 + r_o^2 \ln r - \frac{r^2}{2} - r_o^2 \ln r_i + \frac{r_i^2}{2}\right] We^{j\omega t} + p_i$$

$$\approx -\bar{\rho}_o j\omega \frac{1}{2h}\left[r_o^2 \ln \frac{r}{r_i} - \frac{1}{2}(r^2 - r_i^2)\right] We^{j\omega t} + p_i \qquad (10)$$

In this formulation, the z dependence of p_o has been neglected in applying the boundary condition at $r=r_i$. In the context of the central gas bubble problem, the accuracy of this assumption is dependent on the inequality

$$|p_i| \gg \frac{\bar{\rho}_o \omega h}{2}$$

Using Eq. (10) for p_i, this inequality reduces to

$$\left(\frac{\lambda_i}{h}\right)^2 \gg 2\pi^2 \frac{\bar{\rho}_o}{\bar{\rho}_i}\left(\frac{r_i}{r_o}\right)^2$$

where $\lambda_i = c_i/f$ is the acoustic wavelength in the gas cavity. Otherwise, the z dependence in liquid pressure is also neglected in analyses that use the Reynolds lubrication equation.

From the excess pressures in the liquid p_o and gas bubble p_i, it is possible to compute the force $Fe^{j\omega t}$ on the upper boundary. The force F_g on the air cavity can be found from

$$F_g = -\pi r_i^2 p_i \qquad (11)$$

The force F_l on the liquid can be found by integrating the liquid pressure p_o from Eq. (10) over the annulus area

$$F_l = -\int_{r_i}^{r_o} p_o(r, z=h) 2\pi r dr = j\omega \bar{\rho}_o \frac{\alpha}{2h} We^{j\omega t} - \pi(r_o^2 - r_i^2) p_i$$

where

$$\alpha = 2\pi\left[\frac{r_o^4}{2}(\ln r_o - \ln r_i) - \frac{1}{8}(3r_o^2 - r_i^2)(r_o^2 - r_i^2)\right]$$

$$= \pi r_o^4\left[\ln\left(\frac{r_o}{r_i}\right) - \frac{1}{4}\left(3 - \frac{r_i^2}{r_o^2}\right)\left(1 - \frac{r_i^2}{r_o^2}\right)\right]$$

The total force $Fe^{j\omega t}$ required to cause the motion $We^{j\omega t}$ then is

$$Fe^{j\omega t} = F_l e^{j\omega t} + F_g e^{j\omega t} = j\omega\left[\frac{\bar{\rho}_o \alpha}{2h}\right] We^{j\omega t} + \frac{\pi r_o^2 \bar{\rho}_i c_i^2}{j\omega h}\left(\frac{r_o}{r_i}\right)^2 We^{j\omega t}$$

where Eq. (9) has been used for the acoustic pressure p_i in the gas. The impedance caused by the liquid and gas is given by a mass m and stiffness s of

$$m = \frac{\bar{\rho}_o \alpha}{2h} \qquad (12)$$

$$s = \frac{\pi r_o^2 \bar{\rho}_i c_i^2}{h}\left(\frac{r_o}{r_i}\right)^2 \qquad (13)$$

Note that the lumped-parameter mass m is in a large part determined by the aspect ratio r_o/h of the cavity.

2.3 Viscous Motion of the Liquid. The liquid in the cavity must meet no-slip boundary conditions, conservation of mass $\nabla \cdot \mathbf{v}_0 = 0$, and satisfy the linearized conservation of momentum equations including viscous components

$$\bar{\rho}_o \frac{\partial u_o}{\partial t} = -\frac{\partial p_o}{\partial r} + \mu \frac{\partial}{\partial r}\left[\frac{1}{r}\frac{\partial}{\partial r}(r u_o)\right] + \mu \frac{\partial^2 u_o}{\partial z^2}$$

$$\bar{\rho}_o \frac{\partial w_o}{\partial t} = -\frac{\partial p_o}{\partial z} + \mu \frac{1}{r}\frac{\partial}{\partial r}\left(r \frac{\partial w_o}{\partial r}\right) + \mu \frac{\partial^2 w_o}{\partial z^2} \qquad (14)$$

where μ is the shear viscosity of the liquid. To accomplish this analysis, it is convenient to decompose the fluid velocities into mutually exclusive potential and rotational components as

$$u_o = \tilde{u}_o + \hat{u}_o \quad w_o = \tilde{w}_o + \hat{w}_o$$

where the $\sim$ and $\wedge$ superscripts denote the potential and rotational components, respectively. Using this decomposition, the conservation of momentum equations (13) and (14) are satisfied by separately requiring that

$$\bar{\rho}_o \frac{\partial \tilde{u}_o}{\partial t} = -\frac{\partial p_o}{\partial r} \qquad (15a)$$

$$\bar{\rho}_o \frac{\partial \hat{u}_o}{\partial t} = \mu \frac{\partial}{\partial r}\left[\frac{1}{r}\frac{\partial}{\partial r}(r\hat{u}_o)\right] + \mu \frac{\partial^2 \hat{u}_o}{\partial z^2} \qquad (15b)$$

$$\bar{\rho}_o \frac{\partial \tilde{w}_o}{\partial t} = -\frac{\partial p_o}{\partial z} \qquad (16a)$$

$$\bar{\rho}_o \frac{\partial \hat{w}_o}{\partial t} = \mu \frac{1}{r}\frac{\partial}{\partial r}\left(r \frac{\partial \hat{w}_o}{\partial r}\right) + \mu \frac{\partial^2 \hat{w}_o}{\partial z^2} \qquad (16b)$$

Both the potential and rotational components include the effect of liquid inertia. The potential quantities $\tilde{u}_o$ and $\tilde{w}_o$ together with the rotational terms $\hat{u}_o$ and $\hat{w}_o$ meet the no-slip boundary conditions

$$\tilde{u}_o + \hat{u}_o = 0 \quad \text{at } z = 0, h \qquad (17)$$

$$\tilde{w}_o + \hat{w}_o = 0 \quad \text{at } z = 0 \qquad (18)$$

$$\tilde{w}_o + \hat{w}_o = We^{j\omega t} \quad \text{at } z = h \qquad (19)$$

It is shown in the Appendix that the following expressions for the velocity components $\tilde{u}_o$, $\tilde{w}_o$, $\hat{u}_o$, and $\hat{w}_o$ satisfy conservation of momentum (13) and (14), conservation of mass, and the boundary conditions (17)–(19)

$$\tilde{u}_o = \frac{r}{2h}\left[\left(\frac{r_o}{r}\right)^2 - 1\right]\Gamma We^{j\omega t} \qquad (20)$$

$$\tilde{w}_o = \left\{\frac{z}{h} - \left[\frac{2l_v}{(1+j)h}\frac{1 - \cosh\left[\frac{(1+j)}{l_v}h\right]}{\sinh\left[\frac{(1+j)}{l_v}h\right]}\right]\right\}\Gamma We^{j\omega t} \qquad (21)$$

$$\hat{u}_o = -\frac{r}{2h}\left[\left(\frac{r_o}{r}\right)^2 - 1\right] \times \left[\frac{\sinh\left[\frac{(1+j)}{l_v}z\right] + \sinh\left[\frac{(1+j)}{l_v}(h-z)\right]}{\sinh\left[\frac{(1+j)}{l_v}h\right]}\right]\Gamma We^{j\omega t} \qquad (22)$$

$$\hat{w}_o = -\frac{l_v}{(1+j)h}\left[\frac{\cosh\left[\frac{(1+j)}{l_v}z\right] - \cosh\left[\frac{(1+j)}{l_v}(h-z)\right]}{\sinh\left[\frac{(1+j)}{l_v}h\right]}\right]\Gamma We^{j\omega t} \qquad (23)$$

where $l_v = \sqrt{2\mu/\omega\bar{\rho}_o}$ is the viscous penetration depth [18] in the liquid at frequency ω and

$$\Gamma = \left[1 + \frac{2l_v}{(1+j)h}\frac{1 - \cosh\left[\frac{(1+j)}{l_v}h\right]}{\sinh\left[\frac{(1+j)}{l_v}h\right]}\right]^{-1}$$

The viscous penetration depth l_v is a measure of the diffusion of momentum into the liquid caused by a boundary oscillating at frequency ω.

The excess pressure p_o in the liquid is now determined. Given that the rotational velocity components $\hat{u}_o$ and $\hat{w}_o$ satisfy Eqs. (15b) and (16b), the excess pressure may be computed from the potential velocity components $\tilde{u}_o$ and $\tilde{w}_o$ by integrating Eqs. (15a) and (16a). Upon integrating Eqs. (15a) and (16a), and applying the boundary condition that $p_o(r,z,t)=p_i$ at $r=r_i$, the pressure $p_o(r,z,t)$ in the liquid cavity is computed as

$$p_o(r,z,t) = -\bar{\rho}_o j\omega \frac{1}{2h}\left[r_o^2 \ln\frac{r}{r_i} - \frac{r^2}{2} + \frac{r_i^2}{2} + z^2 + z\frac{l_v}{(1+j)h}\frac{1-\cosh\left[\frac{(1+j)}{l_v}h\right]}{\sinh\left[\frac{(1+j)}{l_v}h\right]}\right]\Gamma W e^{j\omega t} + p_i$$
$$\approx -\bar{\rho}_o j\omega \frac{1}{2h}\left[r_o^2 \ln r - \frac{r^2}{2} - r_o^2 \ln r_i + \frac{r_i^2}{2}\right]\Gamma W e^{j\omega t} + p_i \tag{24}$$

where the z dependence in the excess pressure p_o has been neglected.

As before, the force on the upper boundary disk $Fe^{j\omega t}$ is found by integrating the excess pressures p_o and p_i over the upper boundary area. After performing this step, the force $Fe^{j\omega t}$ is computed to be

$$F = j\omega\frac{\bar{\rho}_o\alpha}{2h}\Gamma W e^{j\omega t} + \frac{\pi r_o^2 \bar{\rho}_i c_i^2}{j\omega h}\left(\frac{r_o}{r_i}\right)^2 W e^{j\omega t}$$

Then, the mass m and damping coefficients b become

$$m = \frac{\bar{\rho}_o \alpha}{2h}\,\mathrm{Re}\{\Gamma\} \tag{25}$$

$$b = \frac{\bar{\rho}_o \omega\alpha}{2h}\,\mathrm{Im}\{\Gamma\} \tag{26}$$

2.4 Limiting Cases. The analysis in Sec. 2.3 gives complicated expressions for the lumped-parameter mass and damping caused by the liquid squeeze film. Considerable simplification and physical insight are obtained by deriving two limiting forms of the velocities $\tilde{u}_o$, $\tilde{w}_o$, $\hat{u}_o$, $\hat{w}_o$ and the liquid mass m and damping b. Limits are calculated in terms of the ratio of the cavity thickness to viscous penetration depth h/l_v. The square of the ratio, $(h/l_v)^2$, corresponds to one-half of the Reynolds squeeze number given by $\mathrm{Re}=\bar{\rho}_i h^2\omega/\mu$ [19,20].

In the limit of a thick cavity, $h/l_v \gg 1$, one calculates the velocity components $\tilde{u}_o$, $\tilde{w}_o$ $\hat{u}_o$, $\hat{w}_o$ from Eqs. (20)–(23) to be

$$\tilde{u}_o = \frac{r}{2h}\left[\left(\frac{r_o}{r}\right)^2 - 1\right]\left[1 + \frac{2l_v}{(1+j)h}\right] W e^{j\omega t} \tag{27}$$

$$\tilde{w}_o = \frac{z}{h}\left[1 + \frac{2l_v}{(1+j)h}\right] U e^{j\omega t} - \left[\frac{l_v}{(1+j)h}\right] W e^{j\omega t} \tag{28}$$

$$\hat{u}_o = -\frac{r}{2h}\left[\left(\frac{r_o}{r}\right)^2 - 1\right]\left[e^{-(1+j)(z/l_v)} + e^{-(1+j)[(h-z)/l_v]}\right]\left[1 + \frac{2l_v}{(1+j)h}\right] W e^{j\omega t} \tag{29}$$

$$\hat{w}_o = -\frac{l_v}{(1+j)h}\left[-e^{-(1+j)(z/l_v)} + e^{-(1+j)[(h-z)/l_v]}\right] W e^{j\omega t} \tag{30}$$

The rotational velocities $\hat{u}_o$ and $\hat{w}_o$ (Eqs. (29) and (30)) contain thin viscous boundary layer components. Likewise, the lumped-parameter mass m and damping coefficient b are calculated from Eqs. (25) and (26) to be

$$m = \frac{\bar{\rho}_o}{2h}\left[\left(1 + \frac{l_v}{h}\right)\alpha\right] \tag{31}$$

$$b = \frac{\bar{\rho}_o \omega}{2h}\left[\frac{l_v}{h}\alpha\right] \tag{32}$$

The mass m approaches the inviscid form (12) in the limit $h/l_v \to \infty$. Note that the damping coefficient b is proportional to $\omega^{1/2}$.

In the limit of a thin cavity, i.e., $h/l_v \ll 1$, the radial velocity $u_o = \tilde{u}_o + \hat{u}_o$ becomes

$$u_o = \frac{r}{2h}\left[\left(\frac{r_o}{r}\right)^2 - 1\right] 6\left[\frac{z}{h} - \left(\frac{z}{h}\right)^2\right] W e^{j\omega t} \tag{33}$$

Its shape in the z direction is parabolic as expected. In this limit, the lumped-parameter mass m and damping coefficient b are computed as

$$m = \frac{\bar{\rho}_o}{2h}\left[\frac{6}{5}\alpha\right] \tag{34}$$

$$b = \frac{\bar{\rho}_o \omega}{2h}\left(\frac{l_v}{h}\right)^2 [6\alpha] \tag{35}$$

In this case, the damping coefficient b is independent of circular frequency ω.

3 Accuracy of the Analytical Model

The accuracy of the analytical models developed in Sec. 2 for the motion of the liquid was explored by comparing to a corresponding finite-element solution of the isothermal Navier–Stokes equations. Specifically, a commercial software package, COMSOL [21], was used to solve

$$\bar{\rho}_o \frac{\partial \mathbf{v}}{\partial t} + \bar{\rho}_o \mathbf{v}\cdot\nabla\mathbf{v} = \nabla p_i + \frac{4}{3}\mu\nabla(\nabla\cdot\mathbf{v}) - \mu\nabla\times\nabla\times\mathbf{v} \tag{36}$$

where $\mathbf{v}$ is the liquid velocity subject to $\nabla\cdot\mathbf{v}=0$. These equations were solved in the time domain. This version of the Navier–Stokes equations is inclusive of the set (14), but in addition includes the nonlinear convective inertial component $\bar{\rho}_o\mathbf{v}\cdot\nabla\mathbf{v}$. Consequently, this comparison not only verifies the analytical solutions to the set (13) and (14), but also reveals the accuracy of assuming small-amplitude liquid movements.

Consider the computations of radial velocity u_o shown in Figs. 2 and 3. The intent of the figures is to explore the accuracy of the thick (Fig. 2) and thin (Fig. 3) cavity limits of radial liquid motion by comparing to a corresponding finite-element computation. Common to both figures is a cavity of dimensions $h=200$ μm, $r_o=5$ mm, $r_i=2.5$ mm, and water as the liquid medium ($\bar{\rho}_o = 1000$ kg/m^3, $\mu=0.001$ kg/ms). In each computation, the velocity of the upper boundary was adjusted such that displacement amplitude $\Delta h = |W|/\omega$ was 5% of the nominal cavity depth h. A normal velocity of $|W|\sin(2\pi f t)$ for the upper boundary was specified in the time domain finite-element solution. For these computations, a boundary condition of $p_i=0$ was specified at $r=r_i$. The

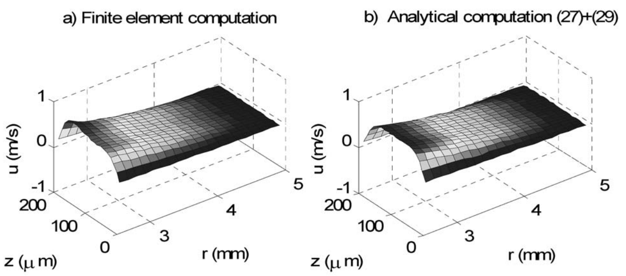
a) Finite element computation

b) Analytical computation (27)+(29)

c) Radial velocity extracted from surface plots at given radius *r*

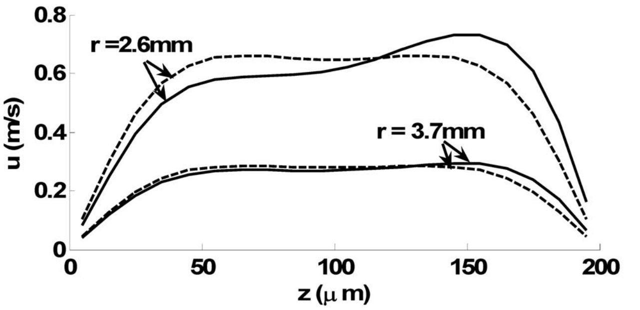

Fig. 2 Radial liquid velocity for a thick cavity $h \gg l_v$, $h=200\ \mu m$, $r_i=2.5$ mm, $r_o=5$ mm, $W=-j0.0314$ m/s, $f=500$ Hz, and time $t=8.6$ ms: (*a*) and (*b*) surface plots and (*c*) solid line, finite element; dashed line, analytical model

finite element solution was generated for several cycles to reach steady state, and was compared with the analytical models (27) and (29) and Eq. (33) for radial velocity u_o at the same time instant. In the surface plots (parts (*a*) and (*b*) of Figs. 2 and 3), it is evident that the analytical models (27) and (29) and Eq. (33) gave results that were quite similar to the finite-element computations, and distinguished the radial velocity profile between the thick and thin nondimensional cavity thickness cases. Radial velocities extracted from the surface plots are shown in part (c) of Figs. 2 and 3 at selected radii *r*. For the thick cavity case shown in Fig. 2 part (c), the quantitative agreement in radial velocity was quite good, even though the maximum velocity exceeded 0.6 m/s. The main departure appeared to be an asymmetry with respect to the *z* coordinate in the radial velocity predicted by the finite-element computations. Presumably, this was caused by the presence of a pressure gradient $\partial p_i/\partial z$ in the finite-element model (36). The pressure gradient $\partial p_i/\partial z$ was neglected in the analytical derivations contained in Secs. 2.2–2.4. Consequently, the analytical predictions were symmetric with respect to the *z* coordinate. For the thin cavity example shown in part (*c*) of Fig. 3, the quantitative agreement was not quite as good, with a difference of 23% in radial velocity along the centerline ($z=100\ \mu$m) and near the inner boundary $r=2.6$ mm. However, the analytical model and finite-element computations shared the parabolic velocity profile that would be expected in the thin cavity case.

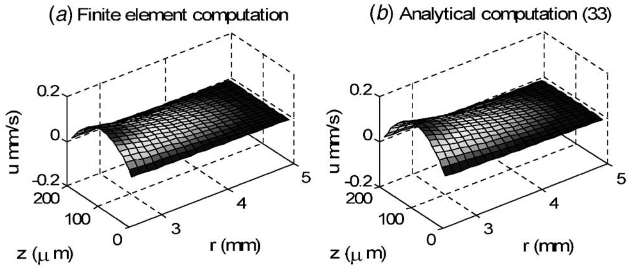
(*a*) Finite element computation

(*b*) Analytical computation (33)

(*c*) Radial velocity extracted from surface plots at given radius *r*

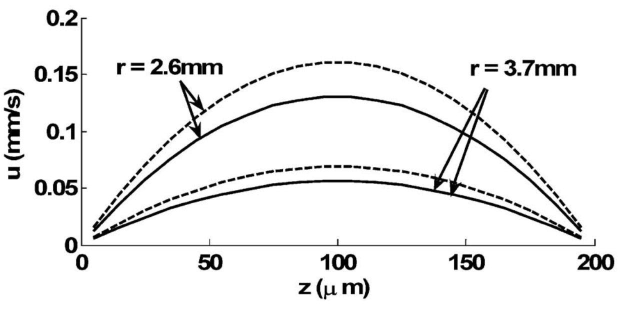

Fig. 3 Radial liquid velocity for a thin cavity $h \ll l_v$, $h=200\ \mu m$, $r_i=2.5$ mm, $r_o=5$ mm, $W=-j6.28\ \mu m/s$, $f=0.1$ Hz, and time $t=43$ s: (*a*) and (*b*) surface plots and (*c*) solid line, finite element; dashed line, analytical model

In general, one can assess the accuracy of the small-amplitude assumption contained in the analytical models by computing conservation of mass flux at the liquid boundaries. By equating the mass fluxes at the top boundary and the inner radius $r=r_i$, one obtains

$$\pi\lfloor r_o^2-(r_i+\Delta r_i)^2\rfloor \Delta h=\pi\lfloor (r_i+\Delta r_i)^2\rfloor h \tag{37}$$

Solving for the displacement of the upper boundary Δh, one calculates

$$\Delta h=\Delta r_i\left(1+\frac{\Delta r_i}{r_i}\right)\left\{\frac{r_i}{2h}\left[\left(\frac{r_o}{r_i}\right)^2-1\right]-\frac{r_i}{2h}\left[2\frac{\Delta r_i}{r_i}+\left(\frac{\Delta r_i}{r}\right)^2\right]\right\}^{-1} \tag{38}$$

For

$$\frac{\Delta r_i}{r_i} \ll 1 \tag{39a}$$

$$\left(\frac{r_o}{r_i}\right)^2-1 \gg 2\frac{\Delta r_i}{r_i}+\left(\frac{\Delta r_i}{r_i}\right)^2 \tag{39b}$$

the time derivative of Eq. (38) reduces to Eq. (7) determined for the radial liquid velocity in the small-amplitude liquid motion case. These requirements are quite lax, and do not include a limitation on the aspect ratio r_o/h of the cavity. For example, with $r_o/r_i=2$, the second condition (39*b*) reduces to $\Delta r_i/r_i \ll 3/2$, say, $\Delta r_i/r_i < 0.015$. When applied to the conditions used to generate Fig. 2(*a*), an upper boundary displacement amplitude consisting of 5% of the nominal cavity depth $h=200\ \mu$m translates into a radial amplitude of $\Delta r_i=0.188$ mm using the linearized analysis (7). This radial displacement is well within the limits of Eqs. (39*a*) and (39*b*), so it is to be expected that the linearized analysis is a good approximation of the finite-element solution of the isothermal Navier–Stokes equations (36) in the computation shown in Fig. 2. The linearized analysis remained valid even though the aspect ratio of the cavity was $r_o/h=25$ and the radial fluid velocity exceeded 0.5 m/s.

4 Physics of the Enclosed Squeeze Film

Lumped-parameter formulas for mass *m*, damping *b*, and stiffness *s* for the enclosed incompressible squeeze film driven by harmonic squeezing motion at frequency ω at the boundary were derived in Sec. 2. When accounting for liquid inertia while neglecting viscous effects, the lumped-parameter mass *m* of the liquid was given by Eq. (12). In this situation, the lumped-parameter damping coefficient *b* was zero. When viscous effects were added to inertial effects in liquid motion, the lumped-parameter mass *m* and damping coefficient *b* of the liquid were given by Eqs. (25) and (26). These expressions were valid for motions of the upper boundary at arbitrary frequency ω. At high frequencies, the nondimensional thickness of the squeeze film h/l_v is large. In this case, the limiting forms of the lumped-parameter mass *m* and

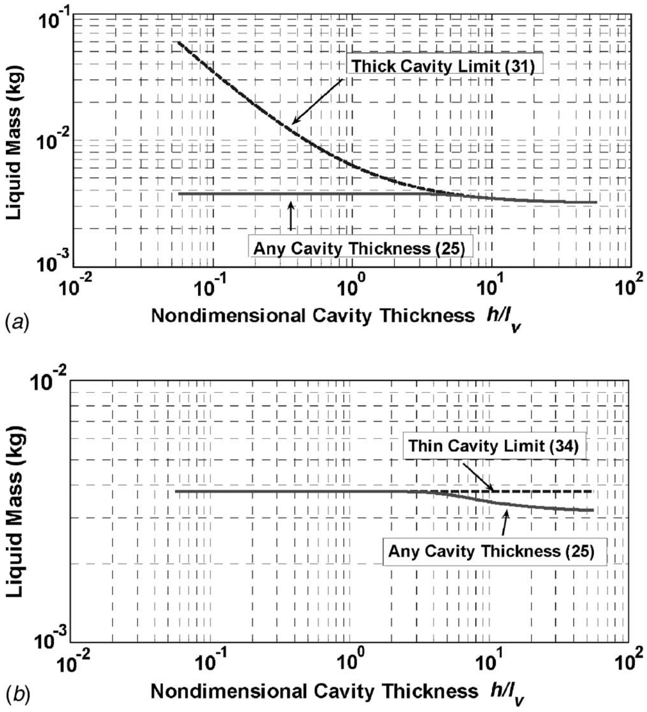

Fig. 4 Accuracy for thick- and thin-cavity limits for liquid mass: (*a*) thick-cavity limit and (*b*) thin-cavity limit

damping b for the liquid were given by Eqs. (31) and (32). At low frequencies, the nondimensional thickness of the squeeze film h/l_v is small. In this case, the limiting forms of the lumped-parameter mass m and damping b for the liquid were given by Eqs. (34) and (35). In the following, the lumped-parameter mass and damping for motion of the incompressible liquid are discussed.

The limiting cases for the thick ($h/l_v \gg 1$) and thin ($h/l_v \ll 1$) cavities span the behavior of the enclosed squeeze film. Consider the plots of squeeze-film mass m and damping coefficient b shown in Figs. 4 and 5. For this squeeze film, the liquid was assumed to be water ($\bar{\rho}_o = 1000\ \text{kg/m}^3$, $\mu = 1.00 \times 10^{-3}$ kg/ms); the thickness h, outer radius r_o, and bubble radius r_i were $h = 100\ \mu$m, $r_o = 5$ mm, and $r_i = 2$ mm. Computations were performed over a frequency $f = \omega/2\pi$ range spanning 0.1 Hz–100 kHz. Over this frequency range, the nondimensional squeeze-film thickness h/l_v ranges from $0.056 < h/l_v < 56$ in order of increasing frequency. The resulting values of lumped-parameter mass m and damping b were plotted on the vertical axis versus the nondimensional squeeze-film thickness h/l_v on the horizontal axis. In part (a) of Fig. 4, the mass m given by the general formula (25) and the approximation (31) for a thick cavity is shown. The two expressions for the mass are seen to agree for $h/l_v > 5$. In part (b) of Fig. 4, the mass m given by the general formula (25) and the approximation (34) for a thin cavity $h/l_v \ll 1$ is shown. For $h/l_v < 5$, the two expressions agree. In Fig. 5, the damping coefficient b given by the general formula (26), and the thick (32) and thin (35) cavity limits are shown. For $h/l_v > 5$, it is evident that the general formula (26) and thick cavity limit (32) predict increasing damping proportional to $\omega^{1/2}$ and that the thin cavity limit (35) agrees with the general formula (26) for $h/l_v < 5$. A damping coefficient proportional to $\omega^{1/2}$ is expected for viscous diffusion processes, such as boundary friction that contributes to attenuation of sound in a waveguide [18]. These computations show that the behavior of the squeeze film is determined by the thickness of the cavity h relative to the viscous penetration depth l_v and that a suitable dividing value for nondimensional cavity thickness is $h/l_v = 5$.

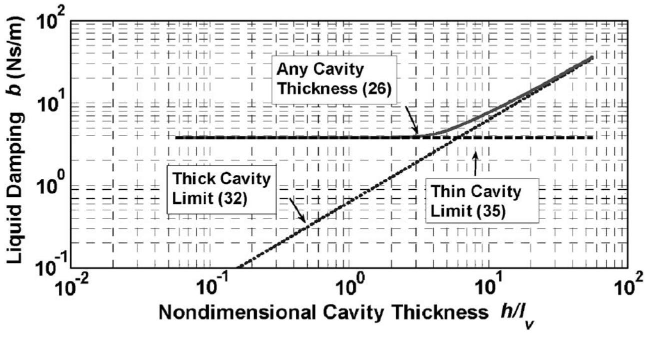

Fig. 5 Accuracy for thick- and thin-cavity limits for liquid damping

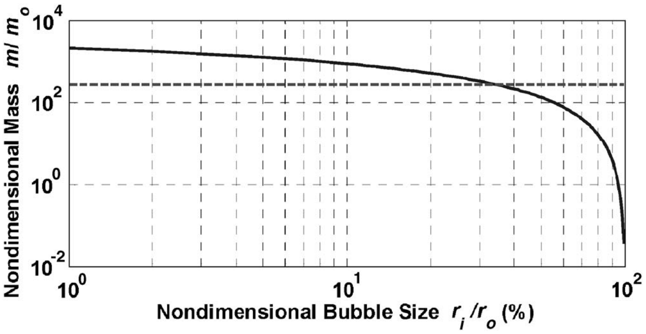

Fig. 6 Liquid mass versus bubble size

The effects of the enclosed geometry can be assessed by comparing the lumped-parameter mass in the enclosed geometry to a squeeze film that is open at the edges. The lumped-parameter mass m of a squeeze film between two parallel circular plates without a central bubble, but open to ambient pressure at the outer boundary $r = r_o$, can be computed with the inviscid assumption using the methods from Sec. 2.2. In the computation, the radial velocity u_o at the center $r = 0$ and the excess pressure p_o at the edge $r = r_o$ are required to vanish. The result is that the lumped-parameter mass m for a squeeze film between two circular parallel plates without a central bubble and open at the edges was computed to be

$$m = \frac{\bar{\rho}_o}{2h} \frac{\pi r_o^4}{4} \tag{40}$$

Computations contained in Fig. 6 are intended to quantify the amplification of lumped-parameter mass m for the enclosed and open geometries relative to the static mass of the liquid. For these computations, the outer radius was $r_o = 5$ mm, the cavity thickness was $h = 75\ \mu$m, and the liquid was assumed to be water with density and viscosity previously cited above. The lumped-parameter mass m for the enclosed geometry was computed using the inviscid model (12), the bubble diameter r_i was allowed to range from $0 < r_i < 2.5$ mm, and the lumped-parameter mass was normalized to the static mass of the liquid $m_o = \bar{\rho}_o \pi (r_o^2 - r_i^2)$ in the annulus defined by $r_i < r < r_o$. The normalized lumped-parameter mass m/m_o for the enclosed geometry was plotted on the vertical axis against nondimensional bubble diameter r_i/r_o in units of percent on the horizontal axis. The lumped-parameter mass m for a squeeze film between circular parallel plates without a central bubble was computed with Eq. (40), and normalized against the static mass $m_o = \bar{\rho}_o \pi r_o^2$ for the liquid between the two plates. The normalized lumped-parameter mass m/m_o for the squeeze film between parallel circular plates is shown in Fig. 6 with a dashed line. When the nondimensional bubble diameter was less than

30%, it is apparent that the amplification of the lumped-parameter mass m for the enclosed squeeze film with a central bubble exceeded that of a squeeze film between parallel circular plates. A physical interpretation for this behavior is that the enclosed boundary $r=r_o$ prevents diverging fluid flow, while converging flow at the inner boundary $r=r_i$ is necessary. For nondimensional bubble sizes larger than 30%, the nondimensional mass of the enclosed squeeze film is lower than the squeeze film between parallel circular plates. An interpretation for this behavior is that the cross section of the enclosed squeeze film has a smaller aspect ratio than the squeeze film between circular parallel plates with no central bubble.

The present analysis shows that the behavior of the incompressible squeeze-film is determined by the nondimensional squeeze-film thickness h/l_v, and it can be shown that analysis using the Reynolds lubrication equation or similar approach is a special case. Using the methods from Secs. 2.3 and 2.4 that account for viscous and inertial effects, the lumped-parameter mass m and damping b for squeeze film between two parallel circular plates without a central bubble, but open to ambient pressure at the outer boundary $r=r_o$, can be computed. In the limit of a thin cavity, $h/l_v \ll 1$, the lumped-parameter mass m and damping coefficient b in this situation were determined to be

$$m=\frac{\bar{\rho}_o}{2h}\frac{3\pi r_o^4}{10} \tag{41}$$

$$b=\frac{3}{2}\frac{\mu\pi r_o^4}{h^3} \tag{42}$$

This result is identical to the lumped-parameter mass m and damping b that can be extracted from computations contained in Ref. [9]. In Ref. [9], a successive approximation approach with an assumed parabolic profile for the radial velocity was used. At higher frequencies (i.e., a thick cavity $h/l_v \gg 1$), the present analysis shows that the radial velocity will depart from the parabolic profile and will become similar to what would be expected for the inviscid case, i.e., plug flow, with the addition of viscous boundary layers at the boundaries to maintain no-slip boundary conditions. In this circumstance, the lumped-parameter mass and damping are different than would be determined using the Reynolds lubrication equation or similar approach.

5 Summary and Conclusions

Lumped-parameter mass, damping, and spring coefficients were computed for the motion of an enclosed annular incompressible liquid squeeze film and central gas bubble caused by vertical harmonic displacements of the upper boundary. A full-field velocity technique was used to perform the derivations that characterized the motion of the liquid. For the liquid squeeze film, lumped-parameter expressions for mass and damping at arbitrary frequencies, and limiting cases of thick and thin cavities were derived.

These computations show that the behavior of an incompressible squeeze film for periodic motions is determined by the thickness h of the cavity relative to the viscous penetration depth l_v. A suitable dividing value for nondimensional cavity thickness is $h/l_v=5$. It was apparent that the enclosed geometry can magnify the lumped-parameter mass of a liquid squeeze film relative to an open squeeze film between two parallel plates. The magnification was attributed to the enclosed geometry forcing converging flow on the liquid. A linearized analysis was used to generate these conclusions. The accuracy of the linearized analysis was shown to be limited to radial movements of the liquid that are a small fraction of the inner radius of the cavity, and the accuracy was not limited by the aspect ratio of the cavity.

Nomenclature

b = lumped-parameter damping coefficient (N s/m)
C = constant of integration, see Eq. (8)
c_i = sound speed in bubble (m/s)
f = frequency (Hz)
F = complex amplitude of total force on disk (N)
F_g = complex amplitude of force of gas on disk (N)
F_l = complex amplitude of force of liquid on disk (N)
h = cavity thickness (m)
Δh = vertical displacement of disk (m)
j = $\sqrt{-1}$ (dimensionless)
l_v = viscous penetration depth (m)
m = lumped-parameter mass (kg)
m_o = static mass of liquid in annulus (kg)
p_i = pressure fluctuations from ambient in bubble ($\mathrm{N/m^2}$)
p_o = pressure fluctuations from ambient in liquid ($\mathrm{N/m^2}$)
r = radial coordinate (m)
r_i = bubble radius (m)
Δr_i = radial displacement of bubble boundary (m)
Re = reynolds squeeze number (dimensionless)
r_o = outer radius of cavity (m)
s = lumped-parameter stiffness (N/m)
t = time (s)
W = complex amplitude of upper disk velocity (m/s)
u_i = radial velocity in bubble (m/s)
u_o = radial component of velocity in liquid (m/s)
$\tilde{u}_o$ = potential component of u_o (m/s)
$\hat{u}_o$ = rotational component of u_o (m/s)
w_o = vertical component of velocity in liquid (m/s)
$\tilde{w}_o$ = potential component of w_o (m/s)
$\hat{w}_o$ = rotational component of w_o (m/s)
$\mathbf{v}$ = vector velocity in liquid (m/s)
z = vertical coordinate (m)
α = coefficient defined before Eq. (12)
Γ = coefficient defined after Eq. (23)
λ_i = acoustic wavelength in bubble (m/s)
μ = shear viscosity in liquid ($\mathrm{N\,s/m^2}$)
$\Delta\rho_i$ = density fluctuations in bubble ($\mathrm{kg/m^3}$)
$\bar{\rho}_i$ = ambient density of gas in bubble ($\mathrm{kg/m^3}$)
$\bar{\rho}_{oi}$ = density of incompressible liquid in annulus ($\mathrm{kg/m^3}$)
ω = circular frequency (rad/s)

Appendix

An expression for the potential velocity $\tilde{u}_o$ that will satisfy conservation of momentum (15a) is

$$\tilde{u}_o=\frac{r}{2h}\left[\left(\frac{r_o}{r}\right)^2-1\right]\Gamma e^{j\omega t} \tag{A1}$$

where Γ is an unyet undetermined coefficient. The rotational velocity $\hat{u}_o$ that satisfies conservation of momentum (15b) and the no-slip condition (17) is

$$\hat{u}_o=-\frac{r}{2h}\left[\left(\frac{r_o}{r}\right)^2-1\right]\frac{\sinh\left[\frac{(1+j)}{l_v}z\right]+\sinh\left[\frac{(1+j)}{l_v}(h-z)\right]}{\sinh\left[\frac{(1+j)}{l_v}h\right]}\Gamma e^{j\omega t} \tag{A2}$$

where $l_v=\sqrt{2\mu/\omega\bar{\rho}_o}$ is the viscous penetration depth in the liquid at frequency ω. Given the rotational velocity component $\hat{u}_o$, conservation of mass determines $\hat{w}_o$ to be

$$\hat{w}_o = -\frac{l_v}{(1+j)h}\frac{\cosh\left[\frac{(1+j)}{l_v}z\right] - \cosh\left[\frac{(1+j)}{l_v}(h-z)\right]}{\sinh\left[\frac{(1+j)}{l_v}h\right]}\Gamma e^{j\omega t} \tag{A3}$$

which in turn satisfies conservation of momentum (16*b*). To meet the boundary conditions (18) and (19), the potential velocity $\hat{w}_o$ must take the form given by

$$\hat{w}_o = zAe^{j\omega t} + Be^{j\omega t} \tag{A4}$$

where A and B are as yet undetermined coefficients. Applying conservation of mass to the potential components $\hat{u}_o$ (Eq. (A2)) and $\hat{w}_o$ (Eq. (A3)) results in the following constraint:

$$Ah = \Gamma \tag{A5}$$

Application of the boundary conditions (18) and (19) yields the following two constraints:

$$Ahe^{j\omega t} + Be^{j\omega t} - \frac{l_v}{(1+j)h}\frac{\cosh\left[\frac{(1+j)}{l_v}h\right] - 1}{\sinh\left[\frac{(1+j)}{l_v}h\right]}\Gamma e^{j\omega t} = We^{j\omega t} \tag{A6}$$

$$Be^{j\omega t} - \frac{l_v}{(1+j)h}\frac{1 - \cosh\left[\frac{(1+j)}{l_v}h\right]}{\sinh\left[\frac{(1+j)}{l_v}h\right]}\Gamma e^{j\omega t} = 0 \tag{A7}$$

Using Eqs. (A5)–(A7), the coefficients A, B, and Γ can be determined.

References

[1] Whalen, S., Richards, C., Bahr, D., and Richards, R., 2007, "Characterization of a Liquid-Vapor Phase-Change Actuator With Microcapillary Wick," Sens. Actuators, A, **134**, pp. 201–212.
[2] Bergstom, P., Ji, J., Liu, Y., Kaviany, M., and Wise, K., 1995, "Thermally Driven Phase Change Microactuation," J. Microelectromech. Syst., **4**, pp. 10–17.
[3] Lin, L., and Pisano, A., 1994, "Thermal Bubble Powered Actuators," Microsyst. Technol., **1**, pp. 51–58.
[4] Rich, C., and Wise, K., 2003, "A High-Flow Thermopneumatic Microvalve With Improved Efficiency and Integrated State Sensing," J. Microelectromech. Syst., **12**(2), pp. 201–208.
[5] Sim, W., Yoon, H., Jeong, O., and Yang, S., 2003, "A Phase-Change Type Micropump With Aluminum Flap Valves," J. Micromech. Microeng., **13**, pp. 286–294.
[6] Weiss, L., Cho, J., McNeil, K., Richards, C., Bahr, D., and Richards, R., 2006, "Characterization of a Dynamic Micro Heat Engine With Integrated Thermal Switch," J. Micromech. Microeng., **16**, pp. S262–S269.
[7] Nguyen, N., Huang, X., and Chuan, T., 2002, "MEMS-Micropumps: A Review," ASME J. Fluids Eng., **124**, pp. 384–392.
[8] Woias, P., 2005, "Micropumps-Past, Progress and Future Prospects," Sens. Actuators B, **105**, pp. 28–38.
[9] Hashemi, S., and Roylance, B., 1989, "Analysis of an Oscillatory Oil Squeeze Film Including Effects of Fluid Inertia," Tribol. Trans., **32**, pp. 461–468.
[10] Turns, S., 1983, "Annular Squeeze Films With Inertia Effects," ASME J. Lubr. Technol., **105**, pp. 361–363.
[11] Usha, R., and Sridharan, R., 1998, "An Investigation of a Squeeze Film Between Two Plane Annuli," ASME J. Tribol., **120**, pp. 610–615.
[12] Hashimoto, H., 1995, "Squeeze Film Characteristics Between Parallel Circular Plates Containing a Single Central Air Bubble in the Inertial Flow Regime," ASME J. Tribol., **117**, pp. 513–518.
[13] Haber, S., and Etsion, I., 1985, "Analysis of an Oscillatory Oil Squeeze Film Containing a Central Gas Bubble," ASLE Trans., **28**, pp. 253–260.
[14] Usha, R., and Vimala, P., 2000, "Inertia Effects in Circular Squeeze Films Containing a Central Air Bubble," Fluid Dyn. Res., **26**, pp. 149–155.
[15] Kuzma, D., 1967, "Fluid Inertia Effects in Squeeze Films," Appl. Sci. Res., **18**, pp. 15–20.
[16] Hori, Y., 2006, *Hydrodynamic Lubrication*, Springer, Berlin.
[17] Kinlser, L., Frey, A., Coppens, A., and Sanders, V., 2000, *Fundamentals of Acoustics*, 4th ed., Wiley, New York.
[18] Pierce, A., 1981, *Acoustics: An Introduction to Its Physical Principles and Applications*, McGraw-Hill, New York.
[19] Langlois, W., 1962, "Isothermal Squeeze Films," Q. Appl. Math., **20**, pp. 131–150.
[20] Starr, J., 1990, "Squeeze-Film Damping in Solid-State Accelerometers," *Technical Digest, 1990 Solid-State Sensor and Actuator Workshop, IEEE*, pp. 44–47.
[21] Spear, M., 2004, "Multiphysics Modeling," Process Eng., **85**, pp. 20–22.

Frequency in Shedding/ Discharging Cavitation Clouds Determined by Visualization of a Submerged Cavitating Jet

Ezddin A. F. Hutli
M.Sc.
Ph.D. Student

Milos S. Nedeljkovic
Professor Dr. Ing.
Mem. ASME

Faculty of Mechanical Engineering,
University of Belgrade,
Belgrade 11120, Serbia

Visualization of a highly submerged cavitating water jet was done by high-speed camera photography in order to study and understand the jet structure and the behavior of cloud cavitation within time and space. The influencing parameters, such as injection pressure, nozzle diameter and geometry, and nozzle direction (convergent and divergent), were experimentally proven to be very significant. Periodical shedding and discharging of cavitation clouds have been also analyzed and the corresponding frequency was determined by cloud shape analysis. Additionally, the dependence of this frequency on injection pressure and nozzle geometry has been analyzed and a simple formula of correspondence has been proposed. The formula has been tested on self-measured and literature data. The recordings of sonoluminescence phenomenon proved the bubble collapse everywhere along the jet. [DOI: 10.1115/1.2813125]

Keywords: cavitating jet, cavitation cloud, shedding and discharging frequency, vapor cavity, cavitation number

1 Introduction

Flow visualization is an important tool in fluid dynamics research and it has been used extensively in the fields of engineering, physics, medical science, meteorology, oceanography, sport, aerodynamics, etc. Over the past few years, cavitating fluid jets have received considerable attention, primarily with laboratory experiments, in order to understand their behavior and to determine the feasibility of their use in a variety of situations. Recently, these testing and evaluation efforts have proven certain applications of the cavitating jet, which include cleaning paint and rust from metal surfaces, underwater removal of marine fouling, removal of high explosives from munitions, and augmenting the action of deep-hole mechanical bits used to drill for petroleum or geothermal energy resources; it is widely used in cutting, penning, and flushing. Thus, the cavitating fluid jet method is indeed commercially attractive [1–5].

The concept of using cavitating fluid jets to enhance the erosive action of a relatively low velocity fluid stream has been given considerable exposure over the past few years. Since nothing is known on the unsteady behavior of rapid fracture and breakoff of the cavitating jet, as well as on the development and collapse of cavitation clouds on the impinging surface, investigations must concentrate on these subjects in order to understand their mechanisms. If the unsteady behavior and the jet structure are clarified in detail, expectedly, the jet working capacity may be drastically improved [1,2]. Cavitation clouds behave stochastically both in time and space, with a very rapid change within microseconds [6–14].

Many researchers have made an effort to observe and visualize the cavitating jet in order to understand its behavior, formation mechanisms of cloud cavitation, and stability of cavitation characteristics, Soyama et al. [1,6] reported that cavitation cloud shedding and the breakdown of the cavitating jet cloud in water took place periodically with a frequency in the range of 0.5–2 kHz. This frequency depends on the injection pressure of the cavitating jet and/or the cavitation number but does not depend on the nozzle geometry. The time period (interval) between one discharge and the next is scarcely dependent on nozzle geometry, but significantly on the injection pressure (a direct proportion is stated). In addition, they reported that the cloud breakoff could be related to a time-dependent feature of the streamwise pressure gradient. Ganippa et al. [14], concluded from their experimental results and observations using different nozzle inclinations that the cavitation structure and its distribution within the hole play a vital role on the spray pattern and atomization in the fuel injection system of the diesel engine and it is very sensitive to the sac and hole geometry. In addition, inception bubbles grew intensively in the shear layer and developed into cloudlike coherent structures. They also found that instabilities of the shear layer caused breaking off of the cloud cavitation structures, which subsequently led to shedding of the cavitation cloud. Soyama [15] optimized the cavitating jet in air, using high-speed photography observations. His results revealed that the cavitating jet in air under high impact conditions showed periodic phenomena—the cavitation cloud in a low-speed water jet shedded periodically, the low-speed water jet had a wavy surface with a frequency related to that of the cloud shedding, and the frequency of the wavy pattern of low-speed water jet decreased with increasing low-speed water jet injection pressure. Keiichi and Yasuhiro [16] investigated cavitation inside a circular-cylindrical nozzle mounted in a cavitation tunnel. They reported that the periodic shedding of the large scale vortex cavity exists in a transition cavitation stage from a subcavitation to a supercavitation state. This periodic shedding is dependent on the formation and coalescence of microvortex cavities on the separated shear layer and the reentrant motion after shedding. In addition, they reported that the Strouhal number can be estimated by analyzing motions of the vortex cavities on the separated shear layer and the reentrant flow. Yamauchi et al. [17] studied the structure of the jet intensively, but they also proposed a formula for the dependence of the vortex ring cavitation frequency on upstream pressure and other influencing parameters. This implementation idea was also used in this paper.

In this paper, an attempt is made to understand the behavior of

---

Contributed by the Fluids Engineering Division of ASME for publication in the Journal of Fluids Engineering. Manuscript received September 23, 2006; final manuscript received July 11, 2007; published online January 31, 2008. Review conducted by Theodore Heindel.

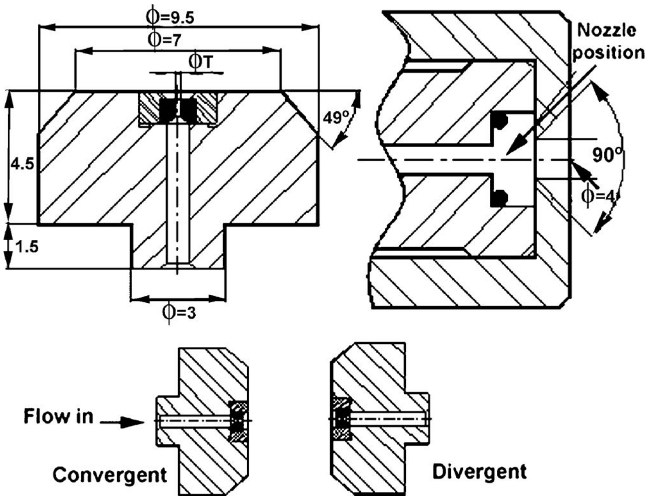

Fig. 1 Nozzle geometry (mm). From left to right: nozzle geometry, nozzle holder, ways of nozzle installation.

severely erosive cavitation clouds by collecting visual information on a high-speed submerged water jet using a PHOTRON APX (high-speed video camera, 100,000 frames/s). Visualizations were done for different hydrodynamic conditions and with different techniques in order to be able to understand the jet behavior and its composition. Figure 1 shows the nozzle geometry (convergent and divergent conicity) and nozzle holder used in this work.

2 Experimental Setup and Measurement Procedure

The experimental setup for jet performance investigation is a closed hydraulic loop shown on Fig. 2. A high-speed submerged cavitating jet is produced in the test chamber by adjusting appropriate hydrodynamic conditions and the final outflow to the test chamber through the nozzle. Jet impacts the sample located $L = 25.67$ mm away from the nozzle—Fig. 3 (left down).

2.1 Error Analysis of the Measured Quantities (Experimental Uncertainty).

The upstream pressure (P_1) and downstream pressure (P_2) were measured at the inlet and outlet of the test chamber, respectively. The pressure transducers were calibrated by the manufacturer and accuracy certificates were issued for a maximum error of $+0.2/-0.21\%$FS. As the flow rate was determined using P_1 and P_2 values from previous nozzle calibration, its determination uncertainty is also of the order of $\pm 0.3\%$FS. Uncertainty in time could not be determined since fast camera shots were made in order of microseconds and factory claimed values were taken as such. Lengths and widths of clouds were measured from the photographs with a precision of 0.1 mm. Values of the results of formula proposed in Sec. 3.3 and in Tables 1–3 are mostly of the order of magnitude $\pm 3\%$ since they use rounded values of k for certain nozzle geometry. The crucial analysis of uncertainty of determination (indirect measurement) of frequency is given in Fig. 8 where the quality of the fit of the curve determined using the least squares method is described by appropriate R^2 factor.

3 Visualization of Cavitating Jets Using a Photron APX Camera

Use of high-speed photography in this paper allowed careful observation of the aspects of cavitation clouds. It was used with convergent and divergent types of cylindrical nozzles.

High-speed photography was achieved using a Photron APX camera with a Corodin flash lamp system. The model 359 flash lamp system is designed to operate a flash lamp at pulse duration of 0.5–11 ms. The system is triggered by a +30 V pulse signal, which comes from a pulse generator. Three windows were used in the test chamber in order to get successful visualization of a cavitating jet (see Fig. 2, right). The light to the downstream chamber in the test system was supplied through two coaxial windows and observations (camera) were made through the third window (upper window). The camera was moved in different directions in order to optimize light scattering from cavities. The system installation is shown in Fig. 3 (left-up).

The fast camera system applied allows for very good performance visualizations with very high frame rates. However, the

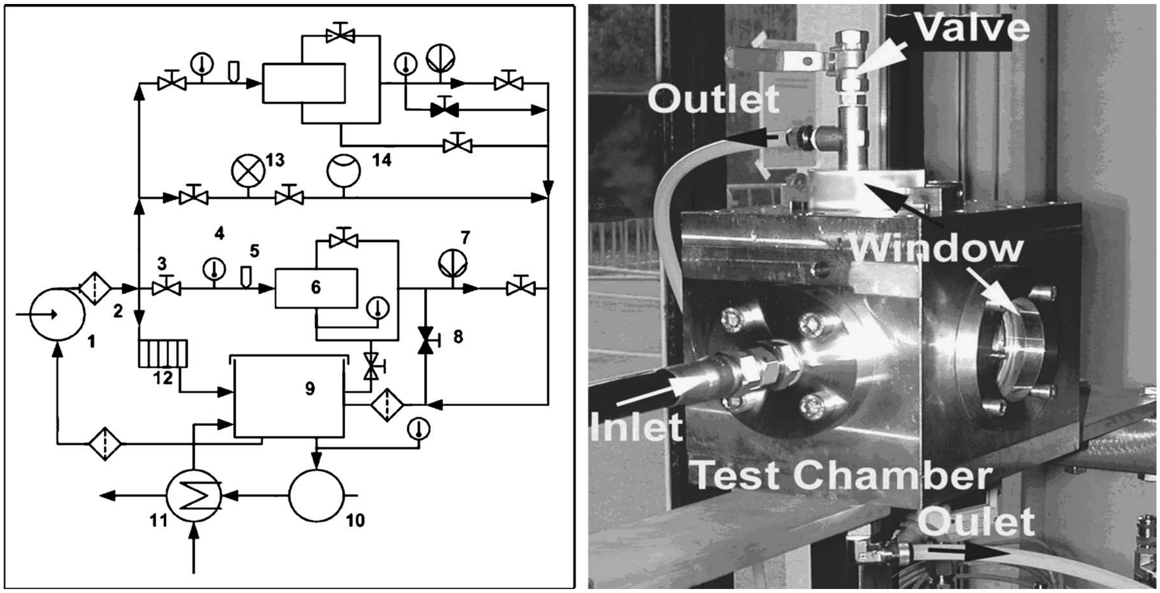

Fig. 2 (Left) Schematic diagram of a cavitating jet machine. (1) plunger pump, (2) filter, (3) regulation valve, (4) temperature sensor, (5) high-pressure transducer, (6) test chamber, (7) valve, (8) low-pressure transducer, (9) safety valve, (10) tank, (11) circulation pump, (12) heat exchanger, (13) energy destroyer in the bypass, and (14) pressure gauge. (Right) the test chamber.

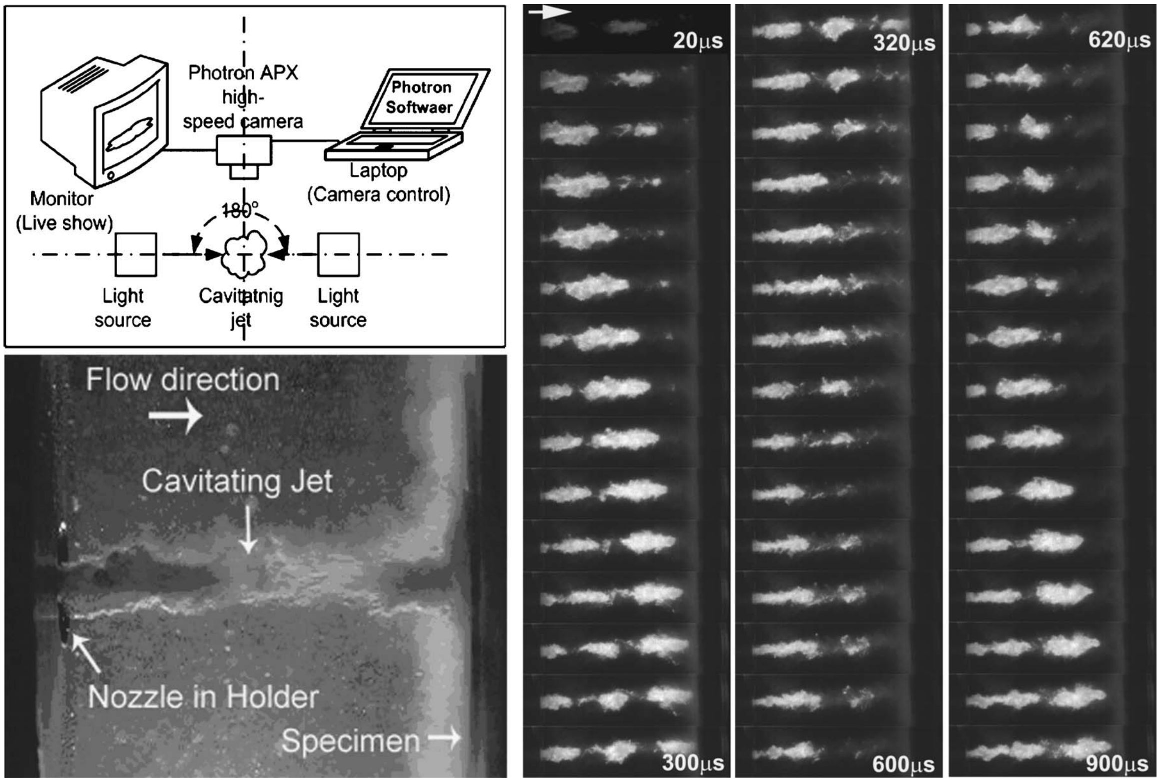

Fig. 3 (Left-up) Visualization system, (Left-down) cavitating jet striking the specimen, and (Right) group of jet images obtained under the following conditions: convergent nozzle ($D_{out}=0.45$ mm). $P_1=105$ bars, $P_2=2.06$ bars, $V_J=124$ m/s, $\sigma=0.02568$, $T=18.5°C$, $X/d=57.044$. Camera: FASTCAM-APX 120K, frame rate: 50,000 fps, shutter frequency: 1/250,000 s, resolution: 256×64, number of pictures in a film: 300 frames.

photo resolution was the restriction factor for operating with the highest frame rates. As an example, Fig. 3 (right) shows visualization with the higher frame rate (the interval time between any two frames in consequence is 20 μs), but then the resolution had to be lowered to 256×64. Normally visualizations were recorded with lower frame rates but with better resolution 512×128 (Figs. 4 and 5 as examples).

Analyses of jet shape and frequency could be made from the groups of jet images recorded by the fast camera system. Recordings were performed after a certain time, which allowed achievement of "steady" conditions (steady state of the main flow conditions in the test-rig and steady readings of the instruments, although the phenomenon is unsteady in nature but with a certain frequency).

Table 1 Numerical calculation of experimental data from Refs. [1,6]

P_1 (bar)	50	300	700
k	0.05	0.05	0.05
t_p (ms)	0.35	0.87	1.32
f (s^{-1})	2860	1150	760

Table 2 Numerical calculation of a convergent nozzle

p_1 (bar)	105	177
K	0.0154	0.0154
t_p (μs)	158	205
f (s^{-1})	6335	4880

Table 3 Numerical calculation of a divergent nozzle

p_1 (bar)	90.5	267
K	0.0147	0.0147
t_p (μs)	140	240
f (s^{-1})	7140	4170

3.1 Shedding and Discharging Phenomenon. Since the cavitating jet is always accompanied by several types of cavitation continuously moving and changing in shape or type [1,6], it is necessary to first clarify the aspects of clouds developed along the free jet injected from a convergent or divergent conical nozzle.

The term shedding represents the moment of starting of a new cavity going out at the nozzle lip, while the term discharging represents the breakoff moment of the cavitating jet. The discharging moment is in fact the starting moment of the end of the cavity life. Shedding and discharging moments are periodical in nature and very close to each other, so practically only one (the same) appearance frequency exists for this phenomenon.

Visualization of shedding/discharging phenomenon may be noticed in photos primarily through periodic changes in jet shape, both in length and width.

3.1.1 Analysis of Cloud Length. Figure 4 shows high-speed photographs taken at typical injection pressures of $P_1=105$ bars and 177 bars, respectively, for a convergent nozzle mounted ($D_{in}=1$ mm, $D_{out}=0.45$ mm). For comparison, Fig. 5 shows the same, at typical injection pressures of $P_1=90.5$ bars and 267 bars, respectively, but now with a divergent nozzle mounted $D_{in}=0.45$ mm, $D_{out}=1$ mm). In all images the flow is from left to right, the time passes from above to below and from left to right, and the interval between two frames is about 42 μs.

In all figures, the cloud length was determined by measuring the distance from the nozzle lip to the first breakoff point (PHOTOSHOP software was used for this purpose). This value was ad-

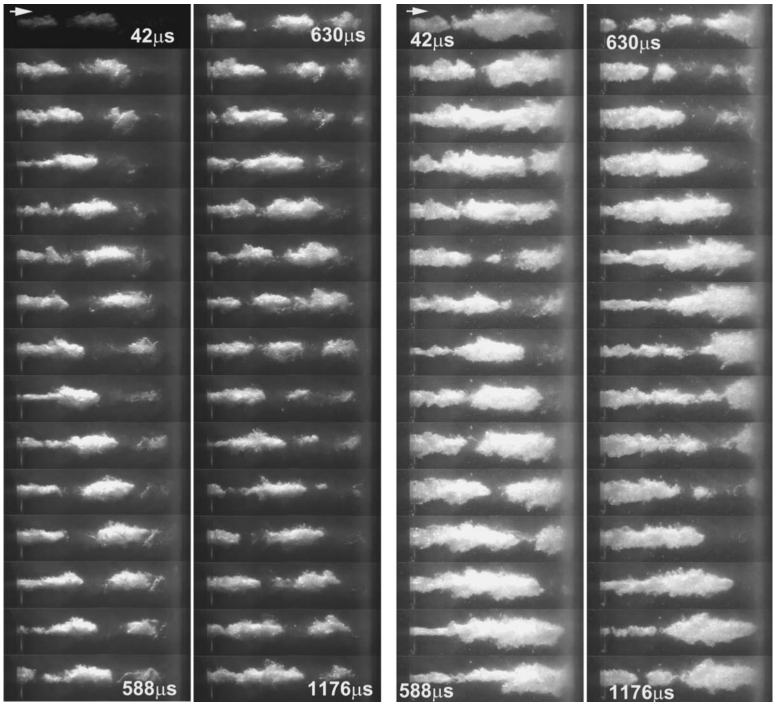

Fig. 4 (Left-two columns) Conditions: P_1=105 bars, P_2=2.06 bars, V_J=124 m/s, σ=0.02568, T=18.5°C. (Right-two columns) Conditions: P_1=177 bars, P_2=2.06 bars, V_J=162 m/s, σ=0.0155, T=18.5°C. Convergent nozzle. X/d=57.044, frame rate: 24,000 fps, shutter frequency: 1/250,000 s, resolution 512×128, and number of frames in a film: 300 frames.

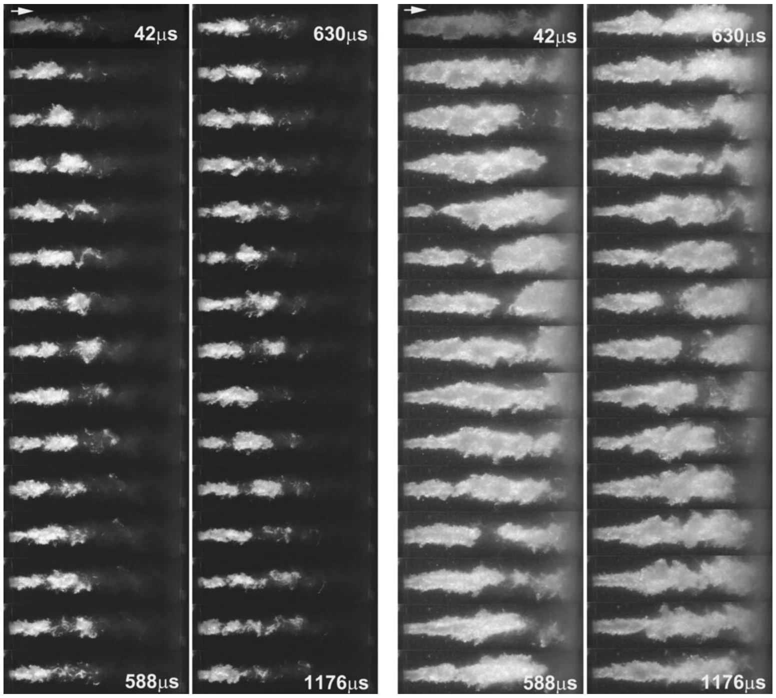

Fig. 5 (Left-two columns) Conditions: P_1=90.5 bars, P_2=1.89 bars, V_J=18.2 m/s, σ=1.142, T=20°C. (Right-two columns) Conditions: P_1=267 bars, P_2=1.89 bars, V_J=31.5 m/s, σ=0.37, T=20°C. Divergent nozzle. X/d=25.67, frame rate: 24,000 fps, shutter frequency: 1/250,000 s, resolution: 512×128, and number of frames in a film: 300 frames.

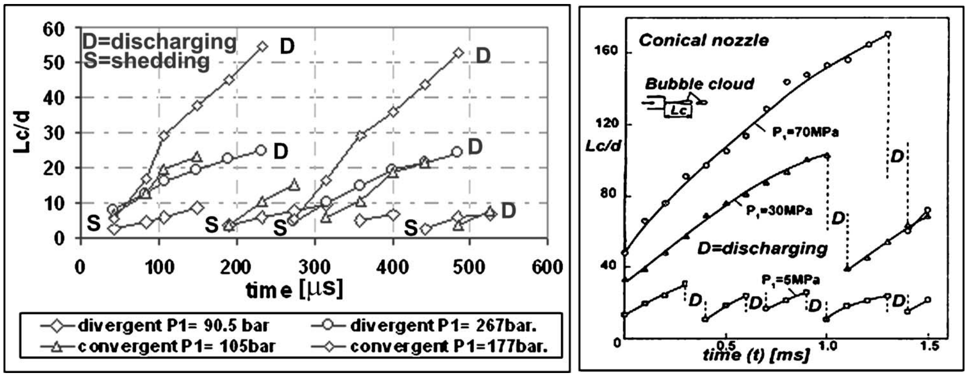

Fig. 6 The variation of cloud cavitation length (L_c) with upstream pressure and nozzle geometry. *S* is shedding, *D* is discharging. (Left) authors' data: (Right) data from Refs. [1,6].

equately scaled and then made dimensionless by division with d (nozzle outlet diameter). Figure 6 (left) shows the results. Looking at the change of this length in time, it may be noticed that a certain period of time corresponding to the frequency of change of this length exists. Thus, the cloud length may be treated as a good parameter for frequency estimation. This was also most probably done in papers [1,6] Fig. 6 (right).

3.1.2 Analysis of Jet Width. Considering the jet width the following analysis was done. Along the jet length three locations (x/d) were chosen to measure the change of jet width with time. The width was measured from the pictures (using PHOTOSHOP software), adequately scaled and then made dimensionless. Figure 7 shows the results. Looking at the changes of the widths in time, it may also be noticed that a certain period of time corresponding to the frequency of their change exists. Thus, the cloud width may also be treated as a good parameter for frequency estimation. To the authors' best knowledge, this procedure has not been tried yet in literature.

The diagrams presented also show that the jet width behavior is globally regular, i.e., periodic in nature in all positions along the jet length. Additional analysis has been done to prove this statement and to find the frequency of the periodic regularity. As just an example, Fig. 8 shows a fitting curve approximation of the measured data (*TableCurve2D* software was used for that purpose).

3.2 Shedding/Discharging Frequency of Cavitation Clouds. In order to clarify the relation, which obviously exists between the injection pressure and cloud shedding frequency, the groups of images given in Figs. 4 and 5 were analyzed. The length of the cavitation cloud, as well as its width, is increased with the upstream pressure increase. The breaking-off point is shifted downstream as P_1 increases, and the jet penetrations increase as P_1 increases.

Cavitation is clearly seen to have the form of white clouds. For any value of the injection pressure P_1, clouds are obviously repeatedly breaking off and shedding off. Downstream from the breakoff point, a single cavity has developed with a smooth surface of a rhomboic shape (Figs. 4 (left) and 5 (left)). This presumes that the velocity is very high in the jet axis. As the distance of the breakoff point (length of the first part of the jet L_c) progressively increases, the downstream part of the cloud is rapidly divided into small groups of very fine bubbles after the breakoff (cascade bubbles).

As a submerged cavitating jet is a two phase flow, the sound (wave) velocity within the jet has to be very low [1,6]. The cloud breakoff is related to the streamwise pressure gradient and takes place intermittently and at different distances. The pressure field around the jet is very unstable, as a result of movement (compression and expansion) of waves in and out of the jet. Waves are generated through the collapse of bubbles (happening all the way along the jet path, as shown in Fig. 9) and bubble rebounding (increasing or decreasing of the bubble size). Cloud deceleration also leads to pressure instability [1].

With a further increase in time, the upstream part of the cloud rapidly develops again (frames with time may be followed in any group of pictures in any figure), and cloud breakoff begins. So generally speaking it may be said that cloud cavitation is periodical in shedding off and in breaking off regardless of the nozzle geometry, but its frequency is dependent on nozzle geometry.

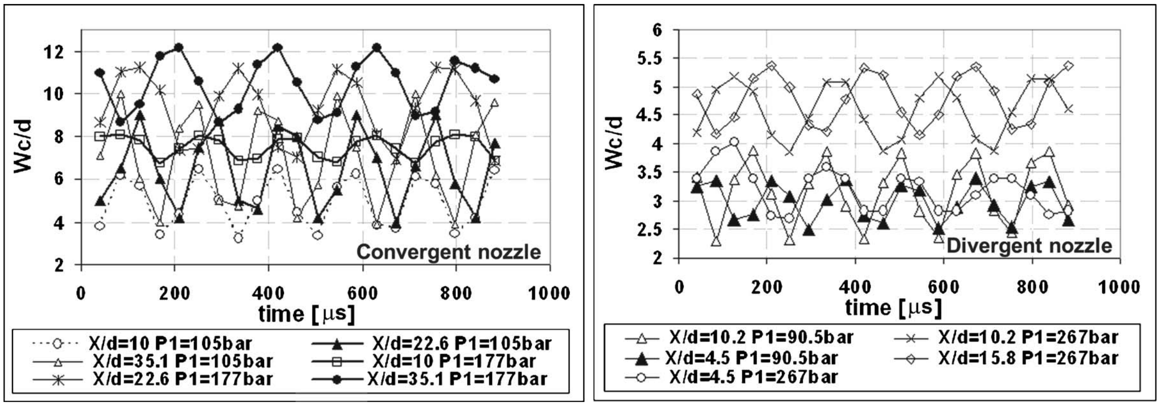

Fig. 7 Cavitating water jet cloud width (W_c) behavior at different values of x/d; (Left) convergent nozzle; (Right) divergent nozzle

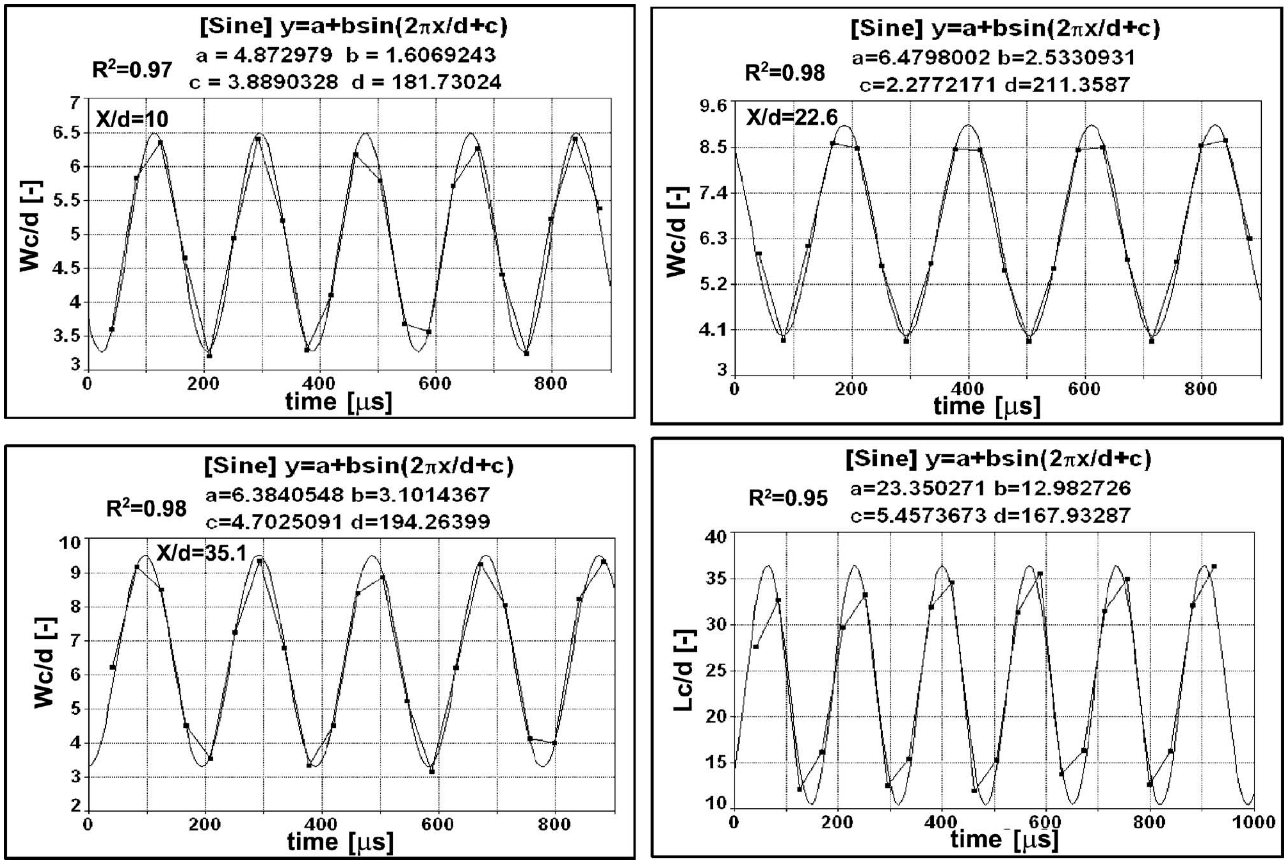

Fig. 8 The first three diagrams represent cavitating water jet cloud width (W_c) behavior at different values of x/d for convergent nozzle at injection pressure $P_1=105$ bars. The fourth diagram represents the cloud length (L_c) change with the time (measured along the center of the jet). The pattern is a sine wave for all and with the same frequency.

As P_1 increases, the number of gaseous cavitation bubbles increases and sustains in the test section without collapsing (they move as floating bubbles in the test chamber). This can be seen for the case of a convergent nozzle at $P_1=177$ bars (Fig. 4) and for the case of a divergent nozzle at $P_1=267$ bars (Fig. 5). These bubbles appear as white spots in the images and their density (number of bubbles) depends on the upstream pressure value. For elimination of this kind of bubbles, the pressure in the test chamber (P_2) must be changed.

The shedding frequency (cavitation cloud shedding/discharging) is a strong function of the injection (upstream) pressure P_1, decreasing when the injection pressure increased. This allowed for easier repetition of cavitating jet breakoff formation (cloud cavitation) at low upstream pressures, since the jet life is a function of P_1 and the standoff distance. From Fig. 6, it is noted that the jet is more stable at high upstream pressures.

Figure 6 shows the streamwise length L_c between the nozzle exit and the appearance of the first breakoff point (cloud end). This length may be graphically determined from the movie photos with respect to time, where it is noted that the time for discharge points almost corresponds to the time of breakoff points. At any P_1 the periodical breakoff of the cavitation cloud may be clearly observed.

The average cloud cavitation life time t_c as a function of the upstream pressure can be determined from Fig. 6. The values of t_c are weakly dependent on nozzle geometry, but they significantly change with P_1 (a similar result was obtained in Refs. [1,14,15]). In short, the higher P_1 is, the longer t_c is, as well as the range between the maximum and the minimum value of L_c. This fact suggests that the velocity effects, which result from changing of P_1, have to be considerable (as approved in the erosion tests where the erosion rate increased with P_1 and the velocity in-

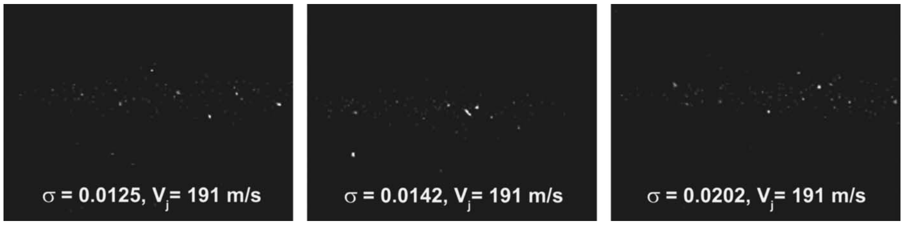

Fig. 9 An attempt to observe the luminescence phenomenon in a cavitating jet. The flow from left to right. Conditions: $P_1=213$ bars, $V_J=191$ m/s, $T=22°C$ ($\sigma=0.0125$, $\sigma=0.0142$, and $\sigma=0.0207$ starting from left to right).

crease). The cloud lifetime t_c is quite different from the fluctuating period of the plunger pump used to feed the jet, since t_c is in the order of microseconds.

As it may be seen, the frequency (time period of jet width change) has been matched very well with a sine periodic (wave form) function. The frequencies determined by the matching (fitting) curve in all positions along the jet length were very close to each other, meaning that this represents the frequency of the cavitating jet. This frequency is practically the same one as the one determined by measuring the cloud length with its breakoff point.

3.3 Formula for Frequency Determination. Reference [17] served as an idea how to connect frequency and pressure. So, in this paper a simplified proposition of an interdependence formula is given. Namely, the dependence of the time period (frequency) on upstream pressure may be expressed as

$$tp = \frac{1}{f} = k\sqrt{P_1}$$

where k is the constant influenced mostly by nozzle shape. The formula gives values for tp in microseconds when pressure P_1 is put in bars.

The formula was tested on data shown in the paper and proved to be very useful. It worked for frequencies determined from jet width change and also for frequencies determined from cloud length change. It also gave good results when applied to time periods measured directly from diagrams in some other papers [1,6].

3.4 Numerical Examples. If we apply the formula to data from Refs. [1,6], we get results shown in Table 1. Where the value of k for a certain conical nozzle was determined by a vice versa calculation knowing tp and P_1 from the diagram of cloud-length dependence on time with P_1 as the parameter (shown at right of Fig. 6 in this paper).

For the nozzle used in Ref. [17], the value of k was found using the values of Strouhal's number, standoff distance, density (not by pressure and time period), and it was found to be nearly 0.134.

For the data given in this paper, the formula gives the results in Tables 2 and 3.

It may be seen that the order of magnitude for k is 0.015 in this paper and in Ref. [17], but it is higher in Ref. [6] because the nozzle used there was much bigger.

4 Sonoluminescence in a Cavitating Jet

An attempt to record the sonoluminescence phenomenon associated with the collapse of bubbles in a cavitating jet was also made. Recordings were made for different values of the cavitation number (σ=0.0125, σ=0.0142, and σ=0.0207) at a constant exit jet-velocity $V_J = 191$ m/s and working fluid temperature $T = 22°$C. Figure 9 shows the results.

The aim is to show that the cavitating jet contains cavity bubbles along its path and the bubble collapse process may take place anywhere in and around the jet from its starting point until the end point in the jet path. An intensified charge coupled device (CCD) camera recorded the light emission simultaneously.

The intensified camera used (4-QUIK-05) has a standard video output, which can be set to interlaced or noninterlaced operation. The microchannel plate (MCP) intensifier has a maximum gain of more than 10,000, which should be sufficient to ensure that a recorded photon "spot" will have a pixel brightness ten units above the noise level in the CCD. The noise level in the CCD typically did not extend above 29 on a scale of 255 brightness levels (the noise level is determined from the image histogram taken while the intensifier is operated at zero gain). Thus all levels below 29 were rejected in the measurements taken. The output of the camera was recorded with the aid of frame grabber software (MATROX INTELLICAM).

No clear differences could be seen between the first and the second images in Fig. 9 but a difference between the first two images and the third one could be seen. In order to achieve better results and for an analytic study of sonoluminescence phenomenon, light emission must be recorded simultaneously by an intensified CCD camera and photomultiplier tubes connected with an electrometer or galvanometer (analog ampere meter) in order to make a correlation between the output voltage and the luminescence density and the side effects of the cavitation such as cavitation erosion, cavitation noise, and vibration.

5 Conclusions

Both gaseous and vaporous types of cavitation were observed in the present study. These two types of cavitation were quite distinct in appearance in the origin (root), in the creation mechanism, in the way of existence (individual or in a cluster), and in the lifetime. The jet life (penetration, width, spreading angle, shedding frequency, etc.) was strongly dependent on hydrodynamic conditions. The morphology of jet cloud movement of the generated cavitation differed according to the shape and size of the nozzle. The cavitation clouds always behaved stochastically both in time and in space, with a very rapid change within microseconds (the result as in Refs. [1–8,11]). Jet cloud length and width may be used as parameters for shedding/discharging frequency determination. The length of cloud cavitation L_c increases with the P_1 increase.

A formula has been proposed for time period (frequency) determination based on the upstream pressure value and nozzle geometry. The values of t_c scarcely change with the nozzle geometry, but they significantly change with the P_1 and are quite different from the fluctuating period of the feed pump. The sonoluminescence phenomenon, associated with the collapse of bubbles in a cavitating jet, can be used as an indicator for the distribution of cavity bubbles along the jet. In addition, it shows that the collapse process happens all along the jet and is related to the pressure line distribution in the jet path.

Nomenclature

σ = cavitation number, defined as $\sigma = p_{\text{ref}} - p_v / 1/2\rho u^2_{\text{ref.}}$
p_{ref} = reference pressure (bar)
$p_v(T)$ = saturation (vapour) pressure (bar)
$\rho(T)$ = density of the liquid (kg/m^3)
T = temperature (°C)
L_c = length of the cloud (mm)
$t_c = tp$ = cavitation cloud lifetime (period) (μs)
u_{ref} = reference velocity (m/s)$= V_J = Q/A$ (flow rate/area of nozzle outlet cross section)
P_1 = upstream (injection) pressure (bar)
P_2 = downstream pressure (bar)
D_{in} = inlet nozzle diameter (mm)
D_{out} or d = outlet nozzle diameter (mm)
W_C = width of jet (mm)
D, S = points of discharge and shedding

References

[1] Soyama, H., Yamauchi, Y., Adachi, Y., Adachi, Y., and Oba, R., 1994, "High-Speed Cavitation-Cloud Observations Around High-Speed Submerged Water Jets," *Second International Symposium on Cavitation*, Tokyo Japan, pp. 225–230.

[2] Vijay, M. M., Zou, C., and Tavoularis, S., 1991, "A Study of The Characteristics of Cavitating Water Jets by Photography And Erosion," *Jet Cutting Technology—Proceedings of Tenth International Conference*, Elsevier Science, pp. 37–67.

[3] Soyama, H., Adachi, Y., Yamauchi, Y., and Oba, R., 1994, "Cavitation-Noise-Characteristics Around High Speed Submerged-Water-Jets," JSME Int. J., Ser. B, **60**(517), pp. 730–735.

[4] Conn, A. F., Johnson, V. E., Lindenmuth, W. T., Jr., and Fredrick, G. S., 1981, "Some Industrial Applications of Cavitating Fluid Jets Flow," *Proceedings of*

the First U.S. Water Jet Conference Golden, Colorado, www.wjta.org/Book%201/5_2a_Conn,_JohnsonLindenmu.pdf.

[5] Yamaguchi, A., and Shimizu, S., 1987, "Erosion Due to Impingement of Cavitating Jet," ASME Trans. J. Fluids Eng., **109**, pp. 442–447.

[6] Soyama, H., Yamauchi, Y., Adachi, Y., Adachi, Y., and Oba, R., 1995, "High-Speed Cavitation-Cloud Observations Around High-Speed Submerged Water Jets," JSME Int. J., Ser. B, **38**(2), pp. 245–251.

[7] Ito, Y., Ogata, H., Oba, R., and Ikeda, R., 1988, "Stereo-Observation of Cavitation Bubbles on A Clark-Y 11.7% Hydrofoil," Trans. ASME, Ser. B, **54**(500), pp. 763–769.

[8] Soyama, H., Ikohagi, T., and Oba, R., 1994, "Observation of the Cavitating Jet in a Narrow Watercourse," *Proceedings of the 29th Cavitation and Multiphase Flow Forum*, O. Furuya and J. Katz, eds., ASME-FED-194, pp. 79–82.

[9] Caron, J. F., Farhat, M., and Avellan, F., 1995, "Physical Investigation of the Cavitation Phenomenon," *Proceedings of the 6th International Symposium on Fluid Control, Measurement and Visualization* (Flucome, 2000), August 13–17, Sherbrooke, Canada.

[10] Koivula, T., 2000, "On Cavitation in Fluid Power," *Proceedings of First FPNI-PhD Symposium*, Hamburg, Germany, pp. 371–382.

[11] Oba, R., 1994, "The Sever Cavitation Erosion," *Second International Symposium on Cavitation*, Tokyo Japan, pp. 1–8.

[12] Clanet, C., and Lasheras, J. C., 1997, "Depth Penetration of Bubbles Entrained by a Plunging Water Jet," Phys. Fluids **9**(7), pp. 1864–1866.

[13] Soyama, H., Lichtarowicz, A., and Lampard, D., 1998, "Useful Correlations for Cavitating Jets," 3rd International Symposium on Cavitation, Grenoble, France, pp. 17–24.

[14] Ganippa, L. C., Bark, G., Andersson, S., and Chomiak, J., 2001, "Comparison Of Cavitation Phenomena In Transparent Scaled-Up Single-Hole Diesel Nozzles," CAV2001, Session A9.005, California, (http://cav.2001.library.calteh.edu/).

[15] Soyama, H., 2005, "High-Speed Observation of a Cavitating Jet in Air," ASME Trans. J. Fluids Eng., **127**, pp. 1095–1101.

[16] Keiichi, S., and Yasuhiro, S., 2002, "Unstable Caviitation Behavior in a Circular-Cylindrical Orifice Flow," JSME Int. J., Ser. B, **45**(3), pp. 638–645.

[17] Yamauchi, Y., Kawano, S., Soyama, H., Sato, K., Matsudaira, Y., Ikohagi, T., and Oba, R., 1996, "Formation of Process of Vortex Ring Cavitation in High-Speed Submerged Water Jet," JSME Int. J., Ser. B, **62**(593), pp. 72–78.

Influence of Wall Inclination Angles on the Onset of Gas Entrainment During Single and Dual Discharges From a Reservoir

M. Ahmed
Department of Mechanical Engineering,
Assiut University,
Assiut 71516, Egypt
e-mail: aminism@aun.edu.eg

A theoretical analysis was carried out to predict the influences of wall inclination angles of large reservoirs on the onset of gas entrainment during single and dual discharges from a stratified two-phase region. The findings reveal that when the wall inclination angle differs from zero, along with low values of Froude number, two distinct flow regimes occur: the gas-entrainment and no gas-entrainment regimes. A new criterion has been developed to predict the critical Froude number at the transition from the gas-entrainment to the no-gas-entrainment regime. The critical Froude number is defined as a function of the wall inclination angle for a single discharge. For dual discharge, the critical Froude number is found to be dependent on the wall inclination angle, the separating distance between the centerlines of the two branches, as well as the Froude number of the second branch. Furthermore, four different flow regions are mapped, representing the flow regime, as well as the two-phase flow for each branch. These maps serve to predict the flow regions, mass flow rates, and quality during single and dual two-phase discharges. For the gas-entrainment regime, the predicted values of the critical height at the onset of gas entrainment are compared with the experimental data reported in literatures. Comparisons showed good concurrence between the measured and predicted results. Furthermore, the influence of the wall inclination angle on the flow regions, the predicted critical height, and the location of the gas entrainment are presented and discussed at different values of independent variables.

[DOI: 10.1115/1.2813124]

Keywords: *gas entrainment, dual discharge, theoretical analysis*

1 Introduction

Many industrial applications involve a two-phase discharge from large reservoirs, pipes, or manifolds through single and multiple branches. One crucial application is related to the topic of nuclear reactor safety, in connection with the postulated loss of coolant accidents. It is of great importance to determine the flow rate and the quality of the discharging flows in the design and performance predictions of such systems.

In the case of a single discharge from a large channel containing a stratified two-phase flow, Zuber [1] indicated that two individual phenomena occur depending on the location of the gas-liquid interface relative to the break. If the horizontal gas-liquid interface is located above the break, the gas may be entrained by a vortex, or a vortex-free flow, through the break into the predominantly liquid flow (onset of gas entrainment (OGE)). On the other hand, if the horizontal gas-liquid interface is located below the break, the liquid may be entrained in the predominating gas flow through the break (onset of liquid entrainment (OLE)). Detailed experimental data and correlations were developed for the OGE through a general oriented single branch (e.g., Smoglie and Reimann [2], Schrock et al. [3], Yonomoto and Tasaka [4,5], Micaelli and Memponteil [6], and Hassan et al. [7]).

Xue and Yue [8], Miloh and Tyvand [9], Lubin and Springer [10], Zhou and Graebel [11], and Haugen and Tyvand [12] investigated liquid flow as resulting from side and bottom submerged point sink. These studies showed that the dip formation at the free surface occurs at a specific value of a dimensionless parameter, which is related to the sink strength, and the height above the point sink. A similar type of study conducted by Forbes and Hocking [13–15], Vanden Broeck and Keller [16,17] considered liquid flow due to submerged point sink.

For the theoretical study of the OGE from a stratified two-phase region, Ahmed et al. [18] developed a new criterion for the OGE. This criterion was based on the instability of inviscid liquid surface accelerated vertically when the effect of lighter density fluid is ignored. Accordingly, the critical height at the OGE during a single discharge from a side branch was theoretically predicted. Applying the criterion during discharge from a single side-oriented branch at moderate Froude numbers was theoretically studied based on an axisymmetric flow assumption, as indicated by Ahmed et al. [19]. This assumption is revised in this paper by considering a three-dimensional flow rather than an axisymmetric flow.

For dual discharges from a stratified two-phase region, Parrott et al. [20] and Parrott [21] experimentally investigated the OGE from a stratified two-phase region, during dual discharge, through vertically aligned branches located on the sidewall of a reservoir. Hassan [22] studied the onsets of gas and liquid entrainment, mass flow rate, and quality during discharge from two horizontal branches with centerlines falling in a common horizontal plane located on the side of a high-pressure reservoir containing a stratified two-phase mixture. Maier et al. [23,24] performed experi-

---

Contributed by the Fluids Engineering Division of ASME for publication in the Journal of Fluids Engineering. Manuscript received July 14, 2006; final manuscript received July 16, 2007; published online February 8, 2008. Review conducted by Joseph Katz.

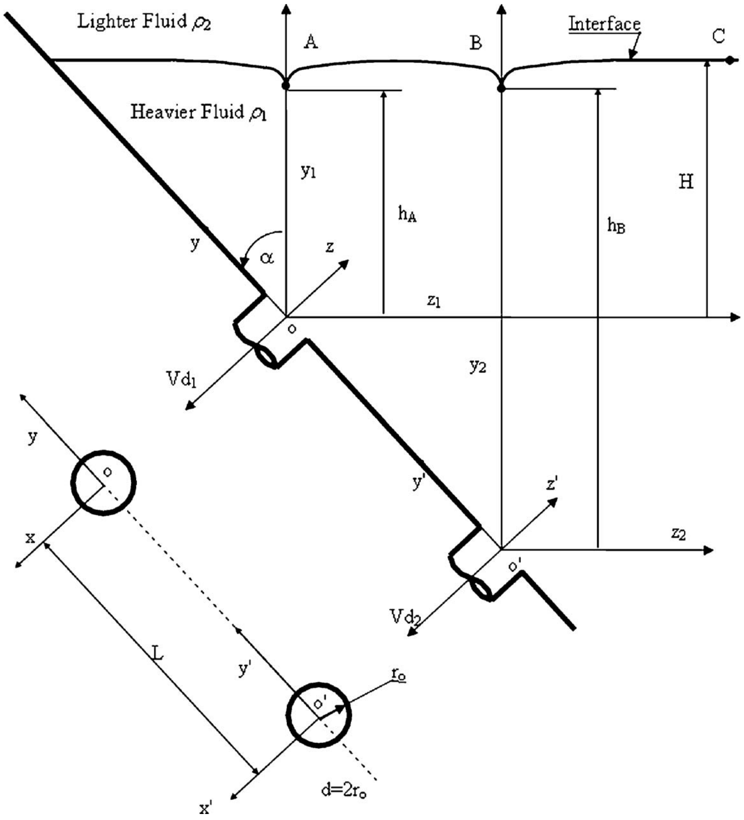

Fig. 1 Geometry and the coordinate system for finite-branch analysis

mental work on the onset of both gas and liquid entrainment during dual discharges through two horizontal branches with centerlines falling in a common plane, with variable inclinations, in order to determine the critical height and location of the onset. Moreover, Maier [25] mentioned that four distinguishable modes of gas entrainment were observed. These modes can be defined as initial vortex entrainment, continuous vortex entrainment, initial depression entrainment, and continuous depression entrainment.

Regarding the theoretical prediction of the critical height at the OGE from a stratified two-phase region through dual branches, Ahmed et al. [26] developed theoretical models using their criterion to investigate the OGE through two vertically aligned side branches. More recently, Ahmed [27] revised the previously mentioned criterion to predict the OGE by considering the density of lighter fluid. He reported that comparisons with the experimental data of Maier [25] illustrated a good agreement between the experimental and predicted critical height, as well as the onset location.

The objective of the present research is to investigate the influence of wall inclination angles of large reservoirs on the OGE during single and dual discharges from a stratified two-phase region from a large reservoir. The transition from a gas-entrainment to a no-gas-entrainment regime at low values of Froude numbers and wall inclination angles $\alpha > 0$ has been studied, utilizing a new criterion to predict the critical Froude number at the transition. In the case of the gas-entrainment regime, the influence of wall inclination angle on the flow regions, the predicted critical height, the location of gas entrainment at different values of the Froude number of each branch, and the separating distance between the branches are investigated.

2 Theoretical Analysis

The configuration shown in Fig. 1 is composed of stratified layers of two immiscible fluids having densities ρ_1 and ρ_2, where ρ_1 is the density of the heavier fluid, and ρ_2 is the density of the lighter fluid. These fluids are contained in a large reservoir whose wall is inclined at an angle α from the vertical axis. Two branches are mounted on the inclined wall, separated by a distance L, center to center. The mass flow rate of the upper and the lower branch is $\dot{m}_1$ and $\dot{m}_2$, respectively. There is a critical height H, as shown in Fig. 1, at which the lighter fluid begins to flow into one of the two branches. This phenomenon, defined as the OGE, may occur at the upper branch, lower branch, or simultaneously at both branches. This is dependent on $\dot{m}_1$, $\dot{m}_2$, α, and L. Furthermore, decreasing $\dot{m}_1$ and/or $\dot{m}_2$ to beyond a certain value ends the occurrence of gas entrainment (no-gas-entrainment regime). This transition from gas-entrainment to no-gas-entrainment regime may also take place at the upper branch, lower branch, or simultaneously at both branches. The purpose of this analysis is, first, to predict H and the branch at which the onset occurs and, second, to predict the mass flow rate and the branch at which the transition from gas-entrainment to no-gas-entrainment regime takes place. The analysis presented in this paper is based on the following assumptions.

1. The two fluids are considered to be inviscid, homogeneous, and incompressible.
2. The flow of the higher density fluid is considered to be irrotational, vortex-free, and quasisteady. Therefore, the transient behavior of the interface is not considered in this study.
3. The lower density fluid is considered stagnant.
4. The surface tension effect is ignored.
5. The change in the surface elevation is considered to be very small, which can be reasonably neglected.

Points A and B, as shown in Fig. 1, represent the onset locations at the interface that lie vertically above the branch center. To the best of the author's knowledge, there is no experimental or analytical evidence for defining the location of the onset as a function of the Froude number. As previously reported by Yildirim et al. [28], it was found experimentally that the location of the onset is dependent on the branch orientation. For a horizontal branch, the onset occurs close to the upper edge, and as the branch orientation changes toward a bottom branch orientation, the onset location is shifted to the center of the branch. The experimental work reported in Ref. [28] also showed that the branch inlet is placed away from the wall to avoid the effect of the wall. If the branch inlet was located at the wall, the onset location would be closer to the center, as is the case for a horizontal branch mounted on a vertical wall. Furthermore, in the case of a horizontal branch, the current prediction of critical height, which is based on having the onset location at the branch center, shows a good agreement with experimental data for a wide range of Froude numbers between $0.1 \leq \mathrm{Fr} \leq 100$, as will be shown later in Fig. 11. The figure shows that there is no significant difference between measured and predicted values within the four orders of magnitude of the Froude number considered.

In brief, it was found that considering that the onset occurs at the branch center for the worst case (wall inclination angle $\alpha=0$) shows a good agreement between predicted and measured values, which are independent of the Froude number. In the current investigation, small branches are mounted on an inclined wall where the onset point will be at the center or very close to the center. Therefore, assuming that the onset occurs at the branch center is reasonable and consistent with the findings reported in literatures [18,26,27].

The assessment of neglecting the surface tension can be explained as follows: The effect of surface tension is typically considered at two locations along the gas-liquid interface: at the onset point and at the wall-liquid-gas interface. At the onset point, the surface tension force will be created if there is a significant change or deformation of gas-liquid interface curvature. At low Froude numbers where the inertia force is weak, the change of interface elevation is very small since we are looking for the state of marginal entrainment. Consequently, there is no significant change of interface curvature. This is especially true since we have a semi-infinite or finite extended interface. Accordingly, there is no significant effect of surface tension force, and the effect of surface tension can be reasonably neglected in the model formulation.

The other effect of surface tension is due to the contact angle at the wall-liquid-gas interface (the meniscus effect). Based on the Young–Laplace equation, the maximum height of the meniscus occurs in the case of a vertical wall (i.e., $\alpha=0$) and decreases with the increasing wall inclination angle, as indicated by Daves and Rideal [29] and Croxton [30]. In the current study, the wall angle is assumed to vary between 0 deg and 90 deg (i.e., $0 \leq \alpha \leq 90$ deg), and there is no meniscus effect as α approaches 90 deg. Therefore, the worst case for this effect occurs when $\alpha=0$ (vertical wall). It was found that for this case, the model correctly predicts the physical limitation of the critical height at very low values of Froude number (i.e., Froude number approaches zero), as indicated in Ref. [18]. In addition, the maximum calculated meniscus height using the Young–Laplace equation is 3.27 mm corresponding to a contact angle of 74 deg as reported by Parrott [21]. Therefore, when $\alpha > 0$, the meniscus height will be much smaller than 3.0 mm and the meniscus effect can be neglected. That is, when the wall inclination angle is greater than zero, the meniscus effect will be very small. Therefore, the effect of surface tension can be reasonably neglected (Fig. 1). Moreover, several previous studies (e.g., Ref. [11]) have shown that this assumption is still valid even for bounded flow with tracking of the interface and in the case of the OGE in the vortex flow regime where the flow is bounded and the change of surface curvature is significant, as indicated by Hite and Mih [31] and Jain and Raju [32].

The analysis technique consists of three main steps as follows:

(a) Determine the velocity of the onset points A and B by considering the equilibrium condition of the interface, as shown in Sec. 2.1.

(b) Determine the velocity field of the higher density fluid using two different models: a simplified point-sink model, as shown in Sec. 2.2, and a more accurate, finite-branch model, as shown in Sec. 2.3. The critical height and the branch at which the OGE regime occurs can be determined by knowing the velocity field.

(c) Determine the critical Froude number at the transition from gas-entrainment to no-gas-entrainment regime using the finite-branch analysis, as shown in Sec. 2.4.

2.1 Equilibrium of the Interface.

In order to develop an analytical expression of the velocity at point A, by applying the Bernoulli equation on a streamline coincident with the interface from the heavier fluid side between points A and C of Fig. 1, we obtain

$$P_{\mathrm{C}} + \frac{1}{2}\rho_1 V_{\mathrm{C}}^2 + \rho_1 g H = p_{\mathrm{A}} + \frac{1}{2}\rho_1 V_{\mathrm{A}}^2 + \rho_1 g h_{\mathrm{A}} \tag{1}$$

On the side of the stagnant, lighter fluid, the hydrostatic equilibrium gives

$$p_{\mathrm{C}} + \rho_2 g H = p_{\mathrm{A}} + \rho_2 g h_{\mathrm{A}} \tag{2}$$

When $H=H_{\mathrm{OGE}}$, $V_{\mathrm{C}}=0$, the velocity of the liquid at point A may be given as

$$V_{\mathrm{A}}^2 = 2g\frac{\Delta\rho}{\rho_1}[H_{\mathrm{OGE}} - h_{\mathrm{A}}] \tag{3}$$

Again, by applying the Bernoulli equation on a streamline coincident with the interface from the heavier fluid side between points B and C as presented in Fig. 1, and following the same procedure, the velocity of the liquid at point B may be given as

$$V_{\mathrm{B}}^2 = 2g\frac{\Delta\rho}{\rho_1}[H_{\mathrm{OGE}} - (h_{\mathrm{B}} - L\cos\alpha)] \tag{4}$$

where P_{A} is the static pressure of the interface at point A and P_{B} is the static pressure of the interface at point B. ρ_1 is the density of the heavier fluid, ρ_2 is the density of the lighter fluid, and $\Delta\rho$ is the difference between the heavier and lighter densities. H is the vertical distance between the upper branch centerline and the interface at point C, and H_{OGE} is the critical height corresponding to the OGE. h_{A} is the vertical distance between the upper branch centerline and the interface at point A. h_{B} is the vertical distance between the upper branch centerline and the interface at point B, as defined in Fig. 1. The criterion used to predict the critical height at the OGE was previously reported by Ahmed [27] and was based on the concept of Taylor's instability theory. It can be written as follows:

$$[a]_{\mathrm{A}} = -g\left[\frac{\Delta\rho}{\rho_1}\right] \tag{5}$$

This means that if the acceleration of point A (onset point at the interface) due to branch discharge exceeds the reduced acceleration of gravity, the surface becomes unstable. This instability results in a catastrophic change in the interface shape, which quickly extends the formed dip toward the branch exit (OGE).

2.2 Point-Sink Analysis.

Each branch is simulated as a three-dimensional point sink with corresponding strengths M_1 or M_2. By assuming that the lighter density fluid has a density nearly equal to that of the heavier fluid, that is, ρ_2/ρ_1 being nearly equal to 1, the heavier fluid is then a semi-infinite medium extending over $-\infty \leq x \leq \infty$, $-\infty \leq y \leq \infty$, and $0 \leq z \leq \infty$. Relating the sink strengths M_1 and M_2, and the mass flow rates $\dot{m}_1$ and $\dot{m}_2$, results in the following correlations:

$$\dot{m}_1 = 2\pi\rho_1 M_1 \quad \dot{m}_2 = 2\pi\rho_1 M_2 \tag{6}$$

2.2.1 Onset of Gas Entrainment at the Upper Branch. Regarding the upper branch, the velocity field of the heavier fluid can be determined by following Schetz and Fuhs [33] formulations. The potential function Φ is illustrated by

$$\Phi = \Phi_1 + \Phi_2 = \frac{M_1}{\sqrt{x^2+y^2+z^2}} + \frac{M_2}{\sqrt{x^2+(y+L)^2+z^2}} \tag{7}$$

The criterion used to predict the critical height at the OGE at the upper branch is shown in Eq. (5) as follows:

$$[a]_{\mathrm{A}} = -g\left[\frac{\Delta\rho}{\rho_1}\right]$$

At point A, the acceleration (a) of the fluid particle can be written as

$$[a]_{\mathrm{A}} = \frac{\partial V_{y1}}{\partial t} + V_{x1}\frac{\partial V_{y1}}{\partial x_1} + V_{y1}\frac{\partial V_{y1}}{\partial y_1} + V_{z1}\frac{\partial V_{y1}}{\partial z_1} \tag{8a}$$

where

$$\begin{aligned} &\frac{\partial V_{y1}}{\partial t} = 0 && \text{quasisteady assumption} \\ &V_{x1} = 0 && \text{boundary condition (at } x = 0, V_{x1} = 0) \\ &V_{z1} = 0 && \text{at the onset} \end{aligned}$$

Then, the final acceleration of the fluid particle at point A can be written as

$$[a]_{\mathrm{A}} = \left\{\left(\frac{\partial\Phi}{\partial y_1}\right)\left(\frac{\partial^2\Phi}{\partial y_1^2}\right)\right\}_{\mathrm{A}} \tag{8b}$$

To determine the acceleration of point A in terms of (x_1, y_1, z_1), the coordinate system (x, y, z) is transformed to (x_1, y_1, z_1), as shown in Fig. 1: This can be represented by a matrix of the form

$$\begin{bmatrix} x \\ y \\ z \end{bmatrix} = \begin{bmatrix} 1 & 0 & 0 \\ 0 & \cos\alpha & -\sin\alpha \\ 0 & \sin\alpha & \cos\alpha \end{bmatrix}\begin{bmatrix} x_1 \\ y_1 \\ z_1 \end{bmatrix}$$

Therefore,

$$\left[\frac{\partial\Phi}{\partial y_1}\right]_{\mathrm{A}} = \Phi_y|_{\mathrm{A}}\cos\alpha + \Phi_z|_{\mathrm{A}}\sin\alpha \tag{9}$$

$$\left[\frac{\partial^2\Phi}{\partial y_1^2}\right]_{\mathrm{A}} = \Phi_{yy}|_{\mathrm{A}}\cos\alpha^2 + \Phi_{zz}|_{\mathrm{A}}\sin\alpha^2 + 2\,\Phi_{yz}|_{\mathrm{A}}\sin\alpha\cos\alpha \tag{10}$$

where Φ_y is the first derivative of the potential function with respect to y. Φ_{yy} is the second derivative of the potential function with respect to y. Φ_z is the first derivative of the potential function with respect to z. Φ_{zz} is the second derivative of the potential function with respect to z. Φ_{yz} is the second derivative of the potential function with respect to y and z. Substituting Eqs. (9) and (10) in Eq. (8b) leads to the criterion of the OGE at the upper branch as follows:

$$\frac{\mathrm{Fr}_1^2}{h_{\mathrm{A}}^{*5}} + \mathrm{Fr}_1\mathrm{Fr}_2\left[\frac{h_{\mathrm{A}}^* + L^*\cos\alpha}{h_{\mathrm{A}}^{*3}(h_{\mathrm{A}}^{*2} + 2h_{\mathrm{A}}^*L^*\cos\alpha + L^{*2})^{3/2}} + \frac{h_{\mathrm{A}}^{*2} + 2h_{\mathrm{A}}^*L^*\cos\alpha + 0.5L^{*2}(3\cos^2\alpha - 1)}{h_{\mathrm{A}}^{*2}(h_{\mathrm{A}}^{*2} + 2h_{\mathrm{A}}^*L^*\cos\alpha + L^{*2})^{5/2}}\right] \\ \times\mathrm{Fr}_2^2\left[\frac{(h_{\mathrm{A}}^* + L^*\cos\alpha)(h_{\mathrm{A}}^{*2} + 2h_{\mathrm{A}}^*L\cos\alpha + 0.5L^{*2}(3\cos^2\alpha - 1))}{(h_{\mathrm{A}}^* + 2h_{\mathrm{A}}^*L^*\cos\alpha + L^{*2})^4}\right] - 1 = 0 \tag{11}$$

where $\mathrm{Fr}_1 = \dot{m}_1/\pi\sqrt{2gr_0^5\rho_1\Delta\rho}$, $\mathrm{Fr}_2 = \dot{m}_2/\pi\sqrt{2gr_0^5\rho_1\Delta\rho}$, $h_{\mathrm{A}}^* = h_{\mathrm{A}}/r_0$, and $L^* = L/r_0$.

By substituting Eq. (9) in Eq. (3), the dimensionless critical height (H_{OGE}/d) corresponding to the OGE at point A can be written as follows:

$$\left.\frac{H_{\mathrm{OGE}}}{d}\right|_{\mathrm{A}} = \frac{h_{\mathrm{A}}^*}{2} + \frac{1}{8}\left[\frac{\mathrm{Fr}_1}{h_{\mathrm{A}}^{*2}} + \mathrm{Fr}_2\left(\frac{h_{\mathrm{A}}^* + L^*\cos\alpha}{(h_{\mathrm{A}}^{*2} + 2h_{\mathrm{A}}^*L^*\cos\alpha + L^{*2})^{3/2}}\right)\right]^2 \tag{12}$$

For any specific value of Fr_1, Fr_2, L^*, and α, the height above the branch h_{A}^* can be estimated by solving Eq. (11) using an iterative procedure. Consequently, the critical height $H_{\mathrm{OGE}}/d|_{\mathrm{A}}$ at the onset of the upper branch can be determined from Eq. (12).

2.2.2 Onset of Gas Entrainment at the Lower Branch. The critical height at the OGE of the lower branch can be determined using the same procedure as for the upper branch. The criterion of the OGE at the lower branch can be demonstrated as follows:

$$\begin{aligned} &\frac{\mathrm{Fr}_1\mathrm{Fr}_2}{2}\left[\frac{3(h_{\mathrm{B}}^* - L^*\cos\alpha)^2}{h_{\mathrm{B}}^{*2}(h_{\mathrm{B}}^{*2} - 2h_{\mathrm{B}}^*L^*\cos\alpha + L^{*2})^{5/2}}\right. \\ &\quad - \frac{1}{h_{\mathrm{B}}^{*2}(h_{\mathrm{B}}^{*2} + 2h_{\mathrm{B}}^*L^*\cos\alpha + L^{*2})^{3/2}} \\ &\quad \left. + \frac{2(h_{\mathrm{B}}^* - L^*\cos\alpha)}{h_{\mathrm{B}}^{*3}(h_{\mathrm{B}}^{*2} - 2h_{\mathrm{B}}^*L^*\cos\alpha + L^{*2})^{3/2}}\right] + \frac{\mathrm{Fr}_2^2}{h_{\mathrm{B}}^{*5}} \\ &\quad - \frac{\mathrm{Fr}_1^2}{2}\left[\frac{h_{\mathrm{B}}^* - L^*\cos\alpha}{(h_{\mathrm{B}}^{*2} - 2h_{\mathrm{B}}^*L^*\cos\alpha + L^{*2})^3}\right. \\ &\quad \left. - \frac{3(h_{\mathrm{B}}^* - L^*\cos\alpha)^3}{(h_{\mathrm{B}}^{*2} + 2h_{\mathrm{B}}^*L^*\cos\alpha + L^{*2})^4}\right] - 1 = 0 \end{aligned} \tag{13}$$

where $h_{\mathrm{B}}^* = h_{\mathrm{B}}/r_0$. The dimensionless critical height (H_{OGE}/d) at the OGE at point B can be expressed as follows:

$$\left.\frac{H}{d}\right|_{\mathrm{B}} = \left[\frac{h_{\mathrm{B}}^{*} - L^{*}\cos\alpha}{2}\right] + \frac{1}{8}\left[\frac{\mathrm{Fr}_1}{h_{\mathrm{B}}^{*2}} + \mathrm{Fr}_2\left(\frac{h_{\mathrm{B}}^{*} + L^{*}\cos\alpha}{(h_{\mathrm{B}}^{*2} - 2h_{\mathrm{B}}^{*}L^{*}\cos\alpha + L^{*2})^{3/2}}\right)\right]^2 \qquad (14)$$

Again, by knowing Fr_1, Fr_2, L/d, and α, the height above the branch h_{B}^{*} can be calculated by solving Eq. (13) using an iterative procedure. By identifying the value of h_{B}^{*}, the critical height $H_{\mathrm{OGE}}/d|_{\mathrm{B}}$ corresponding to the OGE at the lower branch can be determined from Eq. (14).

The critical height corresponding to the gas entrainment for both branches can be calculated as follows: If $H_{\mathrm{OGE}}/d|_{\mathrm{A}} > H_{\mathrm{OGE}}/d|_{\mathrm{B}}$, the OGE occurs at the upper sink, and the critical height will be $H_{\mathrm{OGE}}/d = H_{\mathrm{OGE}}/d|_{\mathrm{A}}$. If $H_{\mathrm{OGE}}/d|_{\mathrm{B}} > |H_{\mathrm{OGE}}/d|_{\mathrm{A}}$, the OGE occurs at the lower sink, and the critical height will be $H_{\mathrm{OGE}}/d = H_{\mathrm{OGE}}/d|_{\mathrm{B}}$. If $H_{\mathrm{OGE}}/d|_{\mathrm{A}} = H_{\mathrm{OGE}}/d|_{\mathrm{B}}$, the OGE occurs at the upper sink and the lower sink at the same time, and $H_{\mathrm{OGE}}/d = H_{\mathrm{OGE}}/d|_{\mathrm{A}} = H_{\mathrm{OGE}}/d|_{\mathrm{B}}$.

2.2.3 Onset of Gas Entrainment in the Case of a Single Branch. The critical height for the onset of entrainment in the case of a single branch can be obtained by inserting $\mathrm{Fr}_2=0$, $\mathrm{Fr}_1=\mathrm{Fr}$, and $h_{\mathrm{A}}^{*}=h^{*}$ into Eqs. (11) and (12). The final analytical equation of the OGE can be expressed in the following form:

$$\frac{\mathrm{Fr}^2}{h^{*5}} - 1 = 0 \qquad (15)$$

The critical height corresponding to the OGE can be written as

$$\frac{H_{\mathrm{OGE}}}{d} = \frac{h^{*}}{2} + \frac{1}{8}\left[\frac{\mathrm{Fr}}{h^{*2}}\right]^2 \qquad (16)$$

By substituting Eq. (15) in Eq. (16), the critical height can be written as

$$\frac{H_{\mathrm{OGE}}}{d} = 0.625\mathrm{Fr}^{0.4} \qquad (17)$$

Based on Eq. (17), the critical height at the OGE was found to be independent of the wall inclination angle. This result is not acceptable from the physical point of view and the reasons for the independency of the point-sink analysis on the wall inclination angle will be explained and discussed latter in Sec. 3. Furthermore, as Fr approaches zero, the critical height converges to zero. However, for the branch of a finite size, the correct value should be $d/2$. Therefore, the accuracy of the point-sink analysis is questionable and we cannot rely on it. This is why the finite-branch analysis will be developed for single and dual branches, as shown in the following section. In the finite-branch analysis, all previously mentioned assumptions will be considered, as well as the significance of the branch size.

2.3 Finite-Branch Analysis. In this analysis, the real dimensions of the branches are considered. By implementing the origin at (O), the heavier fluid is a semi-infinite medium extending over $-\infty \leqslant x \leqslant \infty$, $-\infty \leqslant y \leqslant \infty$, and $0 \leqslant z \leqslant \infty$. The flow is caused by the two discharges with uniform velocity V_{d1} from branch 1, located at $y=x=z=0$, and the velocity V_{d2} from branch 2, located at $y=-L$, $x=z=0$.

2.3.1 Onset of Gas Entrainment at the Upper Branch. In this case, the continuity equation in Cartesian coordinates can be written in dimensionless form as follows:

$$\frac{\partial V_x^{*}}{\partial x^{*}} + \frac{\partial V_y^{*}}{\partial y^{*}} + \frac{\partial V_z^{*}}{\partial z^{*}} = 0 \qquad (18)$$

where V_x^{*}, V_y^{*}, and V_z^{*} are the dimensionless velocity components in x^{*}, y^{*}, and z^{*} directions. By introducing a dimensionless scalar potential function Φ^{*}, $V_x^{*}=\partial\Phi^{*}/\partial x^{*}$, $V_y^{*}=\partial\Phi^{*}/\partial y^{*}$, and $V_z^{*}=\partial\Phi^{*}/\partial z^{*}$. Therefore, Eq. (18) can be written as follows:

$$\nabla^2\Phi^{*} = \frac{\partial^2\Phi^{*}}{\partial x^{*2}} + \frac{\partial^2\Phi^{*}}{\partial y^{*2}} + \frac{\partial^2\Phi^{*}}{\partial z^{*2}} = 0 \qquad (19)$$

with the following boundary conditions:

(a) At $z^{*}=0$,

$$\frac{\partial\Phi^{*}}{\partial z^{*}} = -V_{d_1}^{*} \quad -\sqrt{1-y^{*2}} \leqslant x^{*} \leqslant \sqrt{1-y^{*2}},$$

$$-1 \leqslant y^{*} \leqslant 1$$

$$= -V_{d_2}^{*} \quad -\sqrt{1-(y^{*}-L^{*})^2} \leqslant x^{*} \leqslant +\sqrt{1-(y^{*}-L^{*})^2},$$

$$-L^{*}-1 \leqslant y^{*} \leqslant -L^{*}+1$$

$$= 0 \quad \text{for other values of } x^{*} \text{ and } y^{*}$$

(b) At $x^{*}=0$,

$$\frac{\partial\Phi^{*}}{\partial x^{*}} = 0 \quad \text{at all values of } y^{*} \text{ and } z^{*}$$

(c) At $x^{*} \to \pm\infty$, $y^{*} \to \pm\infty$, $z^{*} \to +\infty$, Φ^{*} is finite, where

$$x^{*} = \frac{x}{r_0} \quad y^{*} = \frac{y}{r_0} \quad z^{*} = \frac{z}{r_0} \quad V_x^{*} = \frac{V_x}{\sqrt{V_{d_1}^2 + V_{d_2}^2}}$$

$$V_y^{*} = \frac{V_y}{\sqrt{V_{d_1}^2 + V_{d_2}^2}} \quad V_z^{*} = \frac{V_z}{\sqrt{V_{d_1}^2 + V_{d_2}^2}}$$

$$V_{d_1}^{*} = \frac{V_{d_1}}{\sqrt{V_{d_1}^2 + V_{d_2}^2}} \quad V_{d_2}^{*} = \frac{V_{d_2}}{\sqrt{V_{d_1}^2 + V_{d_2}^2}}$$

$$\nabla\Phi^{*} = \frac{\nabla\Phi}{\sqrt{V_{d_1}^2 + V_{d_2}^2}}$$

The solution of Eq. (19), subjected to the boundary conditions given by (a), (b), and (c), was obtained using the method of separation of variables as follows:

$$\Phi^{*}(x^{*},y^{*},z^{*}) = \int_0^{\infty}\int_0^{\infty} \frac{\cos(\beta y^{*})\cos(\lambda x^{*})e^{-z^{*}\sqrt{\lambda^2+\beta^2}}}{\lambda\sqrt{\lambda^2+\beta^2}}\left[\frac{2V_{d_2}^{*}}{\pi^2}\int_{-L^{*}-1}^{-L^{*}+1} \sin(\lambda\sqrt{1-(y^{*}-L^{*})^2})\sin(\beta y^{*})dy^{*} + \frac{2V_{d_1}^{*}}{\pi^2}\int_{-1}^{1} \sin(\lambda\sqrt{1-y^{*2}})\sin(\beta y^{*})dy^{*}\right]d\lambda d\beta + \int_0^{\infty}\int_0^{\infty} \frac{\sin(\beta y^{*})\cos(\lambda x^{*})e^{-z^{*}\sqrt{\lambda^2+\beta^2}}}{\lambda\sqrt{\lambda^2+\beta^2}}$$

$$\left[\frac{2V_{d_2}^*}{\pi^2}\int_{-L^*-1}^{-L^*+1}\sin(\lambda\sqrt{1-(y^*-L^*)^2})\sin(\beta y^*)dy^*+\frac{2V_{d_1}^*}{\pi^2}\int_{-1}^{1}\sin(\lambda\sqrt{1-y^{*2}})\sin(\beta y^*)dy^*\right]d\lambda d\beta \tag{20}$$

In this analysis, the criterion used to predict the critical height at the OGE at the upper branch, as shown in Eq. (5), can be written in dimensionless form as follows:

$$[a^*]_{\mathrm{A}}=-g^*\left[\frac{\Delta\rho}{\rho_1}\right] \tag{21}$$

where $g^*=gr_0/\sqrt{V_{d_1}^2+V_{d_2}^2}$. The final dimensionless acceleration of fluid particle at point A can then be written in terms of a dimensionless potential function Φ^* as

$$[a^*]_{\mathrm{A}}=\left\{\left(\frac{\partial\Phi^*}{\partial y_1^*}\right)\left(\frac{\partial^2\Phi^*}{\partial y_1^{*2}}\right)\right\}_{\mathrm{A}[x_1^*=z_1^*=0,y_1^*=h_{\mathrm{A}}^*]} \tag{22}$$

where $\partial\Phi^*/\partial y_1^*$ and $\partial^2\Phi^*/\partial y_1^{*2}$ are previously defined by Eqs. (9) and (10). Then, by incorporating $\partial\Phi^*/\partial y_1^*$ and $\partial^2\Phi^*/\partial y_1^{*2}$ into Eq. (22), the result is such that the criterion of the OGE at the upper branch can be demonstrated in nondimensional form as follows:

$$\mathrm{Fr}_1^2[f_1]+\mathrm{Fr}_1\mathrm{Fr}_2[f_2]+\mathrm{Fr}_2^2[f_3]+2\pi^2=0 \tag{23}$$

From Eq. (3), the critical height corresponding to the OGE at the upper branch H_{OGE} will be written as

$$\left.\frac{H_{\mathrm{OGE}}}{d}\right|_{\mathrm{A}}=\frac{h_{\mathrm{A}}^*}{2}+\frac{1}{2}\left[\mathrm{Fr}_1^2\left(\frac{f_4}{2\pi}\right)^2+\mathrm{Fr}_1\mathrm{Fr}_2\left(\frac{f_4f_5}{2\pi^2}\right)+\mathrm{Fr}_2^2\left(\frac{f_5}{2\pi}\right)^2\right] \tag{24}$$

where

$$\begin{aligned}f_1=&(I_1I_3)\cos^3\alpha+(I_1I_7)\cos\alpha\sin^2\alpha+2(I_1I_9)\cos^2\alpha\sin\alpha\\&+(I_5I_3)\cos^2\alpha\sin\alpha+(I_5I_7)\sin^3\alpha+2(I_5I_9)\sin^2\alpha\cos\alpha\end{aligned} \tag{25}$$

$$\begin{aligned}f_2=&(I_1I_4+I_2I_3)\cos^3\alpha+(I_1I_8+I_2I_7)\cos\alpha\sin^2\alpha\\&+2(I_1I_{10}+I_2I_9)\cos^2\alpha\sin\alpha+(I_5I_4+I_6I_3)\cos^2\alpha\sin\alpha\\&+(I_5I_8+I_6I_7)\sin^3\alpha+2(I_5I_{10}+I_6I_9)\sin^2\alpha\cos\alpha\end{aligned} \tag{26}$$

$$\begin{aligned}f_3=&(I_2I_4)\cos^3\alpha+(I_2I_8)\cos\alpha\sin^2\alpha+2(I_2I_{10})\cos^2\alpha\sin\alpha\\&+(I_6I_4)\cos^2\alpha\sin\alpha+(I_6I_8)\sin^3\alpha+2(I_6I_{10})\sin^2\alpha\cos\alpha\end{aligned} \tag{27}$$

$$f_4=I_1\cos\alpha+I_5\sin\alpha \tag{28}$$

$$f_5=I_2\cos\alpha+I_6\sin\alpha \tag{29}$$

The values of I_1–I_{10} are defined in the Appendix. The procedures to calculate the critical height, as defined in Eq. (24), which corresponds to the OGE at the upper branch for the specific values of the independent variables Fr_1, Fr_2, L/d, and α, can be summarized as follows:

1. Calculate the integral functions I_1, I_2, $I_3,\ldots$, and I_{10} using the numerical integration technique. To avoid the semi-infinite integrals, all doubly infinite domains of integration were transformed to finite integrals. Each integral is then computed used an adaptive quadrature technique. Regarding the adaptive technique, it is well known that if the estimated errors exceed the requested relative error, further subdivision is conducted until the requested accuracy is achieved, as indicated by Stroud [34]. The singularities are dealt with mathematically. A computer code was developed to compute these integrals.
2. Solve Eq. (23) using an iterative procedure to obtain the value of h_{A}^*.
3. Substitute h_{A}^* in Eq. (24) in order to determine the critical height at the OGE.

2.3.2 Onset of Gas Entrainment at the Lower Branch. The critical height at the OGE can be obtained by following the same technique as for the upper branch, which is demonstrated in Sec. 2.3.1. The final analytical equation that represents the criterion of the onset of gas-entrainment at the lower branch can be expressed in the following form:

$$\mathrm{Fr}_2^2[f_6]+\mathrm{Fr}_1\mathrm{Fr}_2[f_7]+\mathrm{Fr}_1^2[f_8]+2\pi^2=0 \tag{30}$$

The critical height corresponding to the OGE at the lower branch H_{OGE} can be written as follows:

$$\begin{aligned}\left.\frac{H_{\mathrm{OGE}}}{d}\right|_{\mathrm{B}}=&\left[\frac{h_{\mathrm{B}}^*-L^*\cos\alpha}{2}\right]+\frac{1}{2}\left[\mathrm{Fr}_2^2\left(\frac{f_9}{2\pi}\right)^2+\mathrm{Fr}_1\mathrm{Fr}_2\left(\frac{f_9f_{10}}{2\pi^2}\right)\right.\\&\left.+\mathrm{Fr}_1^2\left(\frac{f_{10}}{2\pi}\right)^2\right]\end{aligned} \tag{31}$$

where:

$$\begin{aligned}f_6=&(I_{11}I_{13})\cos^3\alpha+(I_{11}I_{17})\cos\alpha\sin^2\alpha+2(I_{11}I_{19})\cos^2\alpha\sin\alpha\\&+(I_{15}I_{13})\cos^2\alpha\sin\alpha+(I_{15}I_{17})\sin^3\alpha+2(I_{15}I_{19})\sin^2\alpha\cos\alpha\end{aligned} \tag{32}$$

$$\begin{aligned}f_7=&(I_{11}I_{14}+I_{12}I_{13})\cos^3\alpha+(I_{11}I_{18}+I_{12}I_{17})\cos\alpha\sin^2\alpha\\&+2(I_{11}I_{20}+I_{12}I_{19})\cos^2\alpha\sin\alpha+(I_{15}I_{14}+I_{16}I_{13})\cos^2\alpha\sin\alpha\\&+(I_{15}I_{18}+I_{16}I_{17})\sin^3\alpha+2(I_{15}I_{20}+I_{16}I_{19})\sin^2\alpha\cos\alpha\end{aligned} \tag{33}$$

$$\begin{aligned}f_8=&(I_{12}I_{14})\cos^3\alpha+(I_{12}I_{18})\cos\alpha\sin^2\alpha+2(I_{12}I_{20})\cos^2\alpha\sin\alpha\\&+(I_{16}I_{14})\cos^2\alpha\sin\alpha+(I_{16}I_{18})\sin^3\alpha+2(I_{16}I_{20})\sin^2\alpha\cos\alpha\end{aligned} \tag{34}$$

$$f_9=I_{11}\cos\alpha+I_{15}\sin\alpha \tag{35}$$

$$f_{10}=I_{12}\cos\alpha+I_{16}\sin\alpha \tag{36}$$

The values of I_{11}–I_{20} are defined in the Appendix. In a similar way to the previous procedures for the upper branch, the critical height corresponding to the OGE of the lower branch can be determined.

Based on the calculated values of $H_{\mathrm{OGE}}/d|_{\mathrm{A}}$ and $H_{\mathrm{OGE}}/d|_{\mathrm{B}}$, two objectives are considered. The first one is to locate the branch or branches in which the OGE will occur, and the second one is to determine the critical height corresponding to this onset. For a specific value of Fr_1, Fr_2, L/d, and α, the critical height corresponding to the OGE for both branches can be calculated as previously demonstrated in Sec. 2.2.2.

2.3.3 Onset of Gas Entrainment in the Case of a Single Branch. The critical height for the OGE in the case of a single branch can be obtained by inserting $\mathrm{Fr}_2=0$, $\mathrm{Fr}_1=\mathrm{Fr}$, and $h_{\mathrm{A}}^*=h^*$ in Eqs. (23) and (24). The final analytical equation of the OGE can be expressed in the following form:

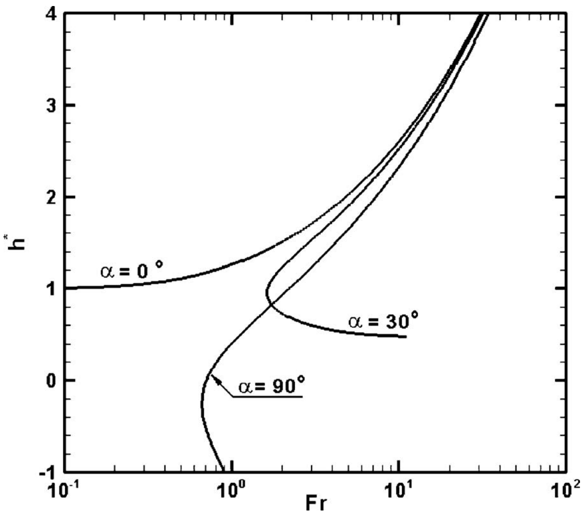

Fig. 2 Influence of the wall inclination (α) on the critical Froude number for a single branch

$$\mathrm{Fr}^2[f_1] + 2\pi^2 = 0 \qquad (37)$$

The critical height corresponding to the OGE can be written as:

$$\left.\frac{H_{\mathrm{OGE}}}{d}\right| = \frac{h^*}{2} + \frac{1}{2}\left[\mathrm{Fr}^2\left(\frac{f_4}{2\pi}\right)^2\right] \qquad (38)$$

The previous analysis, shown in Secs. 2.1 and 2.2, is aimed to determine the critical height and the branch at which the OGE occurs. The second objective of this research is to find the value of Fr or ($\dot{m}$) of each branch at which the OGE no longer occurs. In the following section, new criterion has been developed to predict the transition from gas-entrainment to no-gas-entrainment regime. By using this criterion, the prediction of the value of Fr, at which the transition takes place, is illustrated.

2.4 Criterion of the Transition From Gas-Entrainment to No-Gas-Entrainment Regime. The finite-branch analysis is extended to determine the value of Fr for each branch at which the OGE no longer occurs. Single and dual branches are considered in the following analysis.

2.4.1 Single Discharge. In the case of a single discharge, to determine the values of Fr in which the gas entrainment no longer occurs or to end the gas entrainment, the variation of Fr versus the height above the branch (h^*) is investigated. Figure 2 represents the behavior of Fr as a function of (h^*), at different values of the wall inclination angle α, as described by Eq. (37). Based on Fig. 2, at $\alpha=0$ deg, by decreasing Fr to zero, the value of (h^*) approaches 1. Consequently, by using Eq. (38), the critical height (H_{OGE}) at the OGE is equal to $d/2$. This means that only one regime can occur at $\alpha=0$, which is the gas-entrainment regime. However, at $\alpha=30$ deg, by decreasing Fr down to around 1.63, the value of (h^*) decreases, and there is no corresponding value of (h^*) with further decreases of Fr beyond 1.63. This indicates that there is no existing solution for the OGE (Eq. (37)) at $\alpha=30$ deg. Furthermore, at $\alpha=90$ deg, it is also clear from Fig. 2 that the value of (h^*) reduces when Fr is decreased down to around 0.7, and with further decreases of Fr beyond 0.7, there is no corresponding value of (h^*). As pointed out earlier, it also means that there is no existing solution for the onset of the gas entrainment (Eq. (37)) at $\alpha=90$ deg.

The main objective of Fig. 2 is to find the minimum value of Fr where no solution exists for the onset equation (Eq. (37)). Based on Fig. 2, one can draw the following: For the wall inclination angle of 30 deg, it was found that the minimum value of Fr is 1.63 (Fr=1.63) and that with any further decrease of Fr there is no solution for the onset equation. At Fr=2 and the wall inclination angle of 30 deg, only the onset flow regime exists because the value of Fr is greater than 1.63. Moreover, there are two roots (two values of h^*) of the onset equation (Eq. (37)). The first root is equal to 1.23 ($h^*=1.23$), which corresponds to the critical height of $H_{\mathrm{OGE}}/d=0.75$. The second root is 0.72, and it is rejected (physically impossible). Also, the height of the edge at the top of the branch is $(d/2)\cos 30=0.445d$, where $H_{\mathrm{OGE}}/d=0.75$ and $h^*=1.23$ ($h=0.615d$). Both the values of h^* and H_{OGE} are greater than the height of the branch edge. More details are shown in Fig. 4(*b*), where the variation of the critical height (H_{OGE}/d) corresponding to minimum Fr (or the minimum critical height) versus wall inclination angle is presented.

For a wall inclination angle of 90 deg, the value of minimum Fr is 0.7 (Fr=0.7), where the value of h^* is less than zero (−0.03). The corresponding value of the critical height (H_{OGE}/d) is equal to 0.25, and it is far away from the physical limit of the critical height (H_{OGE}/d), which is zero. At Fr=0.8, only the onset flow regime exists because the value of Fr is greater than 0.7. Also, there are two roots of the onset equation (Eq. (37)). The first root is accepted ($h^*=0.2, H_{\mathrm{OGE}}/d=0.31$), and the second root (−0.8) is rejected (physically impossible). Fortunately, the case where $\alpha=90$ deg was considered as a benchmark for the numerical solution of this model. The reason is that an analytical solution can be developed for this case that leads to a simple algebraic expression to calculate the values of h^* and, consequently, the critical height at any value of Fr. Based on the above explanation, Fig. 2 shows a good agreement with the physics of the problem.

In conclusion, decreasing Fr below a specific value results in no existing solution for the OGE equation (Eq. (37)). This value of Fr depends on the wall inclination angle α and can be defined as the critical Froude number ($\mathrm{Fr}_{\mathrm{critical}}$), and the value of ($h^*$) corresponding to ($\mathrm{Fr}_{\mathrm{critical}}$) can be defined as ($h^*_{\mathrm{min}}$). Also, the value of ($\mathrm{Fr}_{\mathrm{critical}}$) can be determined where $\partial h^*/\partial \mathrm{Fr}=\infty$ or $\partial \mathrm{Fr}/\partial h^*=0$.

In order to understand this phenomenon further, an investigation of the variation of the relative acceleration (a_R) with Fr is explained. The relative acceleration can be defined as the acceleration of the point at the interface directly above the branch (onset point), divided by the acceleration required for the onset to occur at the same point

$$a_R = \frac{-a}{g(\Delta\rho/\rho_1)} = \frac{-a^*}{g^*(\Delta\rho/\rho_1)}$$

where a^* is defined by Eq. (22). It was found that at $\alpha=0$, $a_R=1$ for all values of Fr, whereas at $\alpha>0$, $a_R=1$ for any value of $\mathrm{Fr}\geqslant\mathrm{Fr}_{\mathrm{critical}}$ and at $\mathrm{Fr}<\mathrm{Fr}_{\mathrm{critical}}$, the value of $a_R<1$ for any value of (h^*), and approaches zero as Fr approaches zero.

The conclusion can be summarized as follows: As the Froude number decreases beyond the critical value, it was found that there is no existing solution for the onset of the gas entrainment (Eq. (37)), and the acceleration of the point at the free surface that lies directly above the branch is less than the acceleration required for the onset to occur, i.e., $a_R<1$. This means that there is no occurrence of the OGE. The reason is that the developed criterion for the OGE was based on the onset of instability study of Taylor [35]. Taylor stated that the initial stability of the upper surface of a liquid would pass over into instability if the liquid was given a downward acceleration greater than that of gravity. In addition, Zhou and Graebel [11] indicated that when the downward acceleration of the free surface exceeds the gravitational acceleration, a dip appeared in the free surface. They reported that the dip formation was due to the instability of the free surface, which was analogous to Taylor's instability theory. Based on the concept of Taylor's instability theory, the criterion to predict the OGE from a stratified two-phase region is shown by Eq. (5) as follows: $[a]=-g[\Delta\rho/\rho_1]$. If the acceleration of the onset point is less than

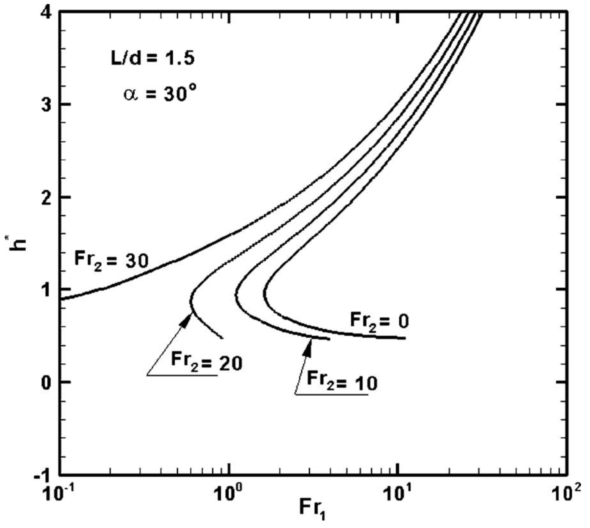

Fig. 3 Influence of Fr_2 on the critical value of Fr_1 at $L/d=1.5$ and $\alpha=30$ deg

the reduced acceleration of gravity ($a_R<1$), the interface will be stable based on Taylor's instability theory. This means that no gas entrainment will occur.

For any value of a wall inclination angle α greater than zero, the value of ($\mathrm{Fr}_{\mathrm{critical}}$) at the transition from gas-entrainment to no-gas-entrainment regime, where $h^*=h^*_{\min}$ and $\partial h^*/\partial \mathrm{Fr}=\infty$ or $\partial \mathrm{Fr}/\partial h^*=0$, can be determined by solving Eqs. (37)–(39),

$$\left.\frac{\partial \mathrm{Fr}}{\partial h^*}\right|_{h^*=h^*_{\min}} = \frac{\pi}{\sqrt{2}}\frac{1}{\sqrt{f_1^3}}\frac{\partial f_1}{\partial h^*} = 0 \tag{39}$$

By solving Eq. (39), the value of $h^*=h^*_{\min}$ is obtained, and this value $h^*=h^*_{\min}$ will then be substituted in Eq. (37) to determine the value of the critical Froude number ($\mathrm{Fr}_{\mathrm{critical}}$), and substituted in Eq. (38) to find the critical height.

2.4.2 Dual Discharge. In the case of a dual discharge, to determine the values of Fr in which the gas entrainment no longer occurs or to end the gas entrainment at the upper branch or at the lower branch, the same procedure as for a single branch can be followed. For the upper branch, the criterion for the OGE is shown in Eq. (23) as follows:

$$\mathrm{Fr}_1^2[f_1] + \mathrm{Fr}_1\mathrm{Fr}_2[f_2] + \mathrm{Fr}_2^2[f_3] + 2\pi^2 = 0$$

The behavior of Fr_1, as a function of h^*_{A}, while varying the values of Fr_2 (0, 10, 20, and 30), at $\alpha=30$ deg and $L/d=1.5$, as demonstrated in Eq. (23), is shown in Fig. 3. Based on this figure, at $\mathrm{Fr}_2=30$, decreasing Fr_1 to zero results in a decrease of the height h^*_{A} to about 0.9. This indicates that only one regime can be defined at $\mathrm{Fr}_2=30$, which is the gas-entrainment regime. However, at $\mathrm{Fr}_2=0$, 10, and 20, by decreasing Fr_1, the value of h^*_{A} decreases to $h^*_{\mathrm{A\,min}}$, and there is no corresponding value of h^*_{A} with further decreases of Fr_1. As previously indicated, this means that there is no existing solution for the onset of the gas entrainment (Eq. (23)) at $\mathrm{Fr}_2=0$, 10, and 20. The conclusion based on Fig. 3 is that at Fr_2 varying from 0 to 20, there are critical values of Fr_1 in which there is no existing solution for the onset equation (Eq. (23)), where at this point $\partial h^*_{\mathrm{A}}/\partial \mathrm{Fr}_1=\infty$ or $\partial \mathrm{Fr}_1/\partial h^*_{\mathrm{A}}=0$ and $h^*_{\mathrm{A}}=h^*_{\mathrm{A\,min}}$.

Acquiring a deeper understanding of this phenomenon necessitates an investigation of the variation of a_R versus Fr_1. At $\mathrm{Fr}_1 \geqslant \mathrm{Fr}_{1\mathrm{critical}}$, the value of a_R was found to be equal to 1 for any value of $\mathrm{Fr}_1 \geqslant \mathrm{Fr}_{1\mathrm{critical}}$. However, at $\mathrm{Fr}_1 < \mathrm{Fr}_{1\mathrm{critical}}$, the value of a_R was found to be less than 1 for any value of h^*_{A}, and it approaches zero as Fr_1 approaches zero. In conclusion, when the Froude number decreases beyond the critical value, it was found that there is no existing solution for the onset of the gas entrainment (Eq. (23)), and the acceleration of point A is less than the acceleration required for the onset to occur, i.e., $a_R<1$. Consequently, there is no occurrence of OGE.

The value of the ($\mathrm{Fr}_{1\mathrm{critical}}$) at the transition from gas-entrainment to no-gas-entrainment regime, as previously pointed out, satisfied two conditions, which are the onset equations Eq. (23) and $\partial h^*_{\mathrm{A}}/\partial \mathrm{Fr}_1=\infty$ or $\partial \mathrm{Fr}_1/\partial h^*_{\mathrm{A}}=0$ at $h^*_{\mathrm{A}}=h^*_{\mathrm{A\,min}}$. To determine $\partial \mathrm{Fr}_1/\partial h^*_{\mathrm{A}}$, one should start from Eq. (23), and write Fr_1 as a function of Fr_2, f_1, f_2, and f_3. This can be accomplished by solving Eq. (23) in Fr_1, and then by differentiating Fr_1 with respect to h^*_{A}. The final equation of $\partial \mathrm{Fr}_1/\partial h^*_{\mathrm{A}}=0$ can be written as

$$\begin{aligned}\left.\frac{\partial \mathrm{Fr}_1}{\partial h^*_{\mathrm{A}}}\right|_{h^*_{\mathrm{A}}=h^*_{\mathrm{A\,min}}} = -&\frac{\mathrm{Fr}_2(\partial f_2/\partial h^*_{\mathrm{A}})}{2f_1} \\ &+\frac{\mathrm{Fr}_2 f_2(\partial f_1/\partial h^*_{\mathrm{A}})}{2f_1^2} \pm \left\{\frac{\mathrm{Fr}_2^2 f_2(\partial f_2/\partial h^*_{\mathrm{A}})}{2f_1^2}\right. \\ &-\frac{\mathrm{Fr}_2^2 f_2^2(\partial f_1/\partial h^*_{\mathrm{A}})}{2f_1^3} - \frac{\mathrm{Fr}_2^2(\partial f_3/\partial h^*_{\mathrm{A}})}{f_1} \\ &\left.+\frac{\mathrm{Fr}_2^2 f_3(\partial f_1/\partial h^*_{\mathrm{A}})}{f_1^2} + \frac{2\pi^2(\partial f_1/\partial h^*_{\mathrm{A}})}{f_1^2}\right\} \\ &\times\left[\frac{1.0}{\sqrt{\mathrm{Fr}_2^2 f_2^2/f_1^2 - 4\mathrm{Fr}_2^2 f_3/f_1 - 8\pi^2/f_1}}\right] = 0\end{aligned} \tag{40}$$

The procedures to calculate the critical Froude number ($\mathrm{Fr}_{1\mathrm{critical}}$) and the corresponding critical height, where the transition from gas-entrainment to no-gas-entrainment regime of the upper branch for specific values of independent variables Fr_2, L/d, and α, can be summarized as follows.

1. Calculate the integral functions $I_1, I_2, \ldots, I_{10}$ using the numerical integration technique as indicated by Stroud [34].
2. Calculate the integral functions $\partial I_1/\partial h^*_{\mathrm{A}}$, $\partial I_2/\partial h^*_{\mathrm{A}}, \ldots$, $\partial I_{10}/\partial h^*_{\mathrm{A}}$.
3. Calculate the integral functions $\partial f_1/\partial h^*_{\mathrm{A}}$, $\partial f_2/\partial h^*_{\mathrm{A}}$, and $\partial f_3/\partial h^*_{\mathrm{A}}$.
4. Solve Eq. (40) using the iterative procedure to obtain the value of $h^*_{\mathrm{A\,min}}$.
5. Determine the critical Froude number ($\mathrm{Fr}_{1\mathrm{critical}}$) at the transition from gas-entrainment to no-gas-entrainment regime by solving the onset Eq. (23).
6. Solve Eq. (24) to determine the value of critical height.

With regard to the lower branch, in order to calculate the critical Froude number, the same procedure must be followed, as previously illustrated, for the determination of the critical Froude number of the upper branch. The value of the ($\mathrm{Fr}_{2\mathrm{critical}}$) at the transition from gas-entrainment to no-gas-entrainment regime satisfied two conditions, which are the onset Eq. (30) and $\partial h^*_{\mathrm{B}}/\partial \mathrm{Fr}_2=\infty$ or $\partial \mathrm{Fr}_2/\partial h^*_{\mathrm{B}}=0$ at $h^*_{\mathrm{B}}=h^*_{\mathrm{B\,min}}$. The final equation of $\partial \mathrm{Fr}_2/\partial h^*_{\mathrm{B}}=0$ can be written as

$$\begin{aligned}\left.\frac{\partial \mathrm{Fr}_2}{\partial h^*_{\mathrm{B}}}\right|_{h^*_{\mathrm{B}}=h^*_{\mathrm{B\,min}}} = -&\frac{\mathrm{Fr}_1(\partial f_7/\partial h^*_{\mathrm{B}})}{2f_6} \\ &+\frac{\mathrm{Fr}_1 f_7(\partial f6/\partial h^*_{\mathrm{B}})}{2f_6^2} \pm \left\{\frac{\mathrm{Fr}_1^2 f_7(\partial f_7/\partial h^*_{\mathrm{B}})}{2f_6^2}\right. \\ &-\frac{\mathrm{Fr}_1^2 f_7^2(\partial f_6/\partial h^*_{\mathrm{B}})}{2f_6^3} - \frac{\mathrm{Fr}_1^2(\partial f_8/\partial h^*_{\mathrm{B}})}{f_6} \\ &\left.+\frac{\mathrm{Fr}_1^2 f_8(\partial f_6/\partial h^*_{\mathrm{B}})}{f_6^2} + \frac{2\pi^2(\partial f_6/\partial h^*_{\mathrm{B}})}{f_6^2}\right\}\end{aligned}$$

$$\times \frac{1.0}{\sqrt{\mathrm{Fr}_1^2 f_7^2/f_6^2 - 4\mathrm{Fr}_1^2 f_8/f_6 - 8\pi^2/f_6}}\Bigg] = 0 \qquad (41)$$

The procedures to calculate the critical Froude number corresponding to the transition from gas-entrainment to no gas-entrainment regime of the lower branch can be determined in a similar way to the previous procedures for the upper branch.

3 Results and Discussion

The influence of the wall inclination angle α on the critical Froude number at the transition from gas-entrainment to no-gas-entrainment regime and on the flow regions is presented for a single discharge, followed by the comparison between predicted and available experimental results during the gas-entrainment regime. For dual discharges, the influence of the wall inclination angle on the flow region and the critical height at different values of L/d, Fr_1, and Fr_2 are clearly presented and discussed.

The objective of this research is to investigate how the wall inclination angle affects the values of critical height, the predicted flow regions for each branch, as well as the critical Froude number at the transition from gas-entrainment to no-gas-entrainment regime. In order to validate the present developed models, comparisons between the theoretically predicted results and the available experimental results will be provided. The available sets of the experimental data for single and dual discharges were obtained by Parrott [21], Maier [25], Hassan [22], and Lubin and Springer [10].

3.1 Single Discharge.

For a single discharge, Fig. 4(a) shows the variation of the critical Froude number representing the mass flow rate that ends the occurrence of the gas-entrainment (no-gas-entrainment regime), with the wall inclination angle α. Based on the figure, it is clear that when only a gas-entrainment regime occurs, the value of Fr_c approaches zero as the wall inclination angle decreases to zero. However, increasing the wall inclination angle tends to increase the critical Froude number up to 1.66, at a wall inclination angle of approximately 35 deg. Further increase of the wall inclination angle beyond 35 deg results in the decrease of the critical Froude number to about 0.7 at the horizontal wall (α=90 deg). The same trend was observed with regard to the variation of the minimum critical height with a wall inclination angle, as shown in Fig. 4(b). At a wall inclination angle of zero, the critical height is 0.5. By increasing the wall inclination angle, the critical height increases until α=24 deg, where the maximum critical height is shown, and then the critical height decreases to 0.25 at α=90 deg.

The conclusion is that for the wall inclination angle α, if $\mathrm{Fr} < \mathrm{Fr}_c$, the branch velocity is not enough to cause the acceleration of the point at the interface directly above the branch to reach the required acceleration, $g(\Delta\rho/\rho_1)$ for the onset to occur. Consequently, no gas entrainment will occur during these flow conditions. This flow regime is consistent with both the reverse jet regime defined by Zhou and Grabel [11] during the withdrawal of liquid from an open tank through a hole centered on the bottom and the subcritical regime defined by Xue and Yue [8]. As indicated in both cases, the downward acceleration of the free surface directly above the branch is never close to the magnitude of gravity through the evolution. However, if $\mathrm{Fr} > \mathrm{Fr}_c$, there is a corresponding value of the critical height H_{OGE}/d, where the onset will occur.

During the gas-entrainment regime, the comparisons between the predicted critical height at the OGE by the current developed models and the available experimental results are carried out at different values of wall inclination angles (0 deg and 90 deg), as shown in Fig. 5. It was found that at $\mathrm{Fr} > 1$, there is a good concurrence between the experimental and the predicted values of both models. The results of the finite-branch analysis demonstrate that at α=0, the critical height corresponding to the OGE approaches the branch radius, as Fr_1 approaches zero. At α =90 deg, it predicts a no-gas-entrainment regime at $\mathrm{Fr}_1 \sqcup 0.7$. Furthermore, the predicted critical height at $\mathrm{Fr} < 10$ slightly decreases as the wall inclination angle increases, and this effect is insignificant with further increase of the Froude number. However, based on the point-sink analysis, the predicted critical height approaches zero as the Froude number approaches zero, and it is independent of the wall inclination angle.

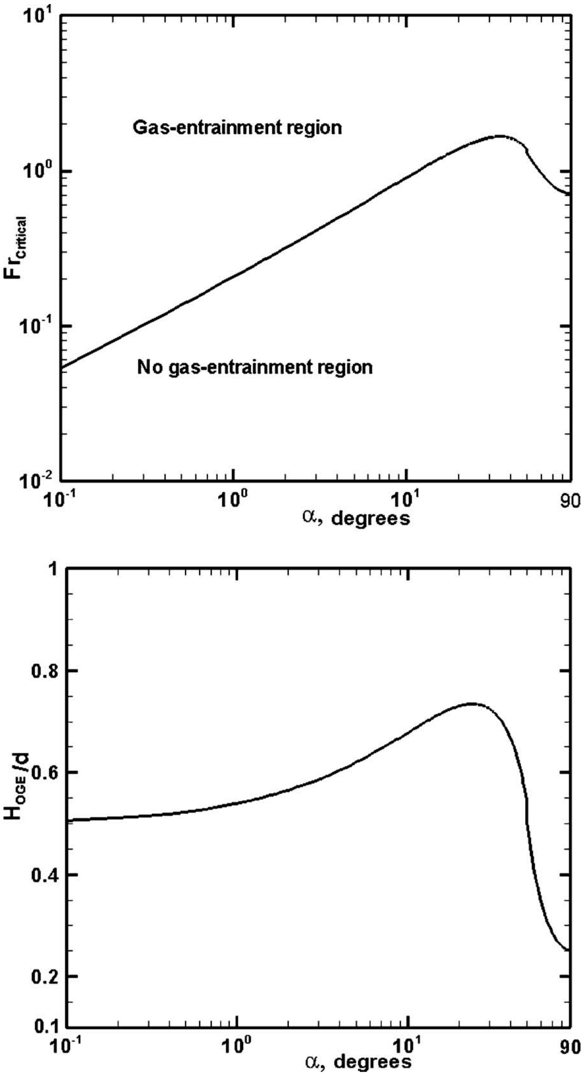

Fig. 4 (*a*) Variation of the critical Froude number ($\mathrm{Fr}_{\mathrm{critical}}$) versus the wall inclination under the upper figure as shown on the web ready text file. (*b*) Variation of the critical height (H_{OGE}/d) versus the wall inclination angle α in the case of a single discharge under the lower figure as shown on the web ready text file.

Figure 6 shows the influence of the wall inclination angle on the variation of (h/H_{OGE}) versus Fr. As illustrated in Fig. 6, at α=0 deg, the results of the finite-branch analysis approach the physically implied limit of h/H_{OGE}=1 as Fr approaches zero, while at α=90 deg, h/H_{OGE} approaches 0.0 at Fr=0.7. The higher the Froude number, the less the influence of the wall inclination angle; consequently, the values of h/H_{OGE} for the different angles converge to approximately the same value as predicted by point sink (=0.8).

Figure 7 demonstrates the influence of the wall inclination angle on the variation of the absolute value of dimensionless velocity $|V_A/V_d|$ of the onset point A versus Fr. At low values of Fr, the variation of α from zero to α=90 deg increases the value of

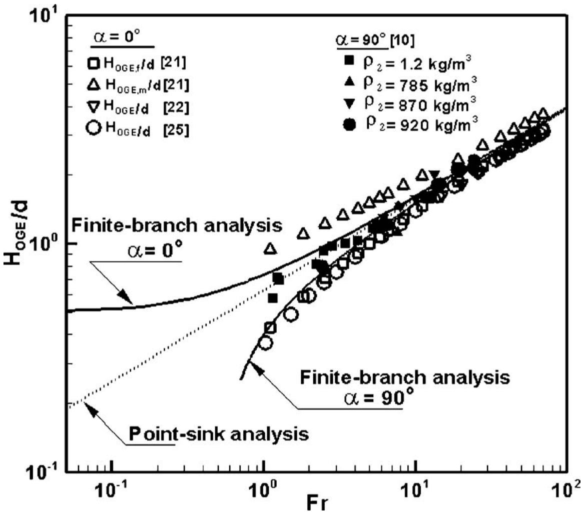

Fig. 5 Comparisons between predicted and measured critical height at different values of α (0 deg and 90 deg)

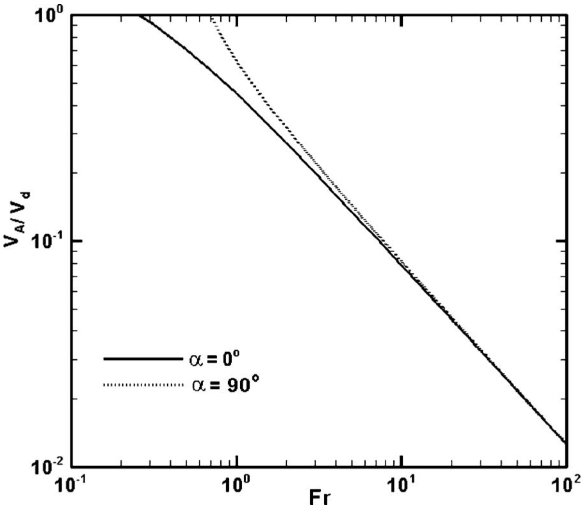

Fig. 7 Influence of the wall inclination angle on the variation of the absolute value of (V_A/V_d) versus Fr

dimensionless velocity of the onset point A. However, as Fr increases, the influence of α becomes insignificant. Also, at $\alpha = 90$ deg, the dimensionless velocity approaches unity (the applied boundary condition) at $h=0$.

Based on Figs. 5–7, the point-sink analysis results, such as H_{OGE}/d and h/H_{OGE}, are independent of the wall inclination angle α and cannot be used to predict the transition from onset to no-onset flow regime. The independency of the wall inclination angle is most likely due to assumptions associated with the point-sink analysis where the flow velocity is radial and a function of both the sink strength and the radial distance from the point sink. Therefore, changing the angle will not allow us to vary the velocity and the acceleration as long as the radial distance is fixed.

Using the finite-branch analysis, the potential function, the solution of the continuity equation, is mainly a function of the wall inclination angle α, the branch velocity V_d, and the height between the interface and branch centerline h, as shown in Fig. 1. Consequently, the vertical velocity and acceleration of the point in the interface directly above the branch were found to be a function of the wall inclination angle α, the branch velocity V_d, and the height between the interface and branch centerline h. As previously indicated, during the onset regime, the acceleration of the point in the interface directly above the branch must be equal to $g(\Delta\rho/\rho_1)$. At any value of Fr, varying the wall inclination angle results in changing the value of h to keep the values of acceleration constant. Consequently, the critical height H_{OGE}/d, as well as the interface h/H_{OGE}, will be dependent on the inclination angle α, as shown in Figs. 5 and 6. Furthermore, varying the wall inclination angle means a change in the direction of branch velocity V_d with respect to the vertical velocity of the interface directly above the branch. Accordingly, this leads to a variation in the velocity of the interface directly above the branch, as shown in Fig. 7. However, at higher Fr, the influence of the wall inclination angle becomes insignificant since increasing Fr will directly increase the value of h. This will make the integral functions insensitive to the variation of the wall inclination angle α. To conclude, varying the wall inclination angle not only changes the liquid-wall interaction boundary conditions but also changes the direction of branch velocity. In the case of dual discharge, the results are discussed in the following section.

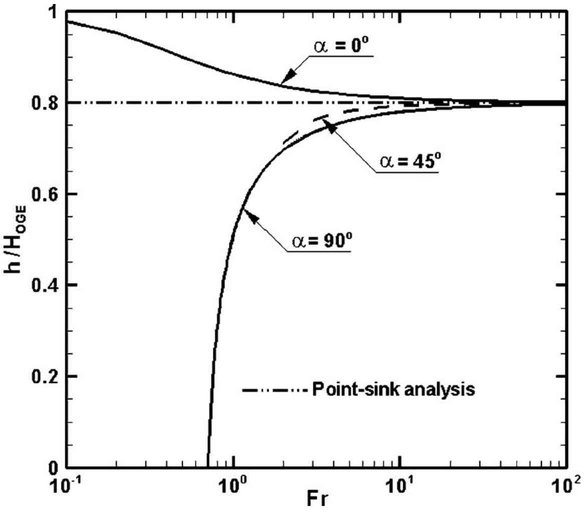

Fig. 6 Influence of the wall inclination angle on the variation of (h/H) versus Fr

3.2 Dual Discharge

3.2.1 Flow Regions. As previously stated, decreasing Fr_1 and/or Fr_2 beyond a certain value ends the occurrence of the gas-entrainment (no-gas-entrainment regime). This transition from gas-entrainment to no-gas-entrainment regime may take place at the upper branch, lower branch, or simultaneously at both branches, and is dependent on Fr_1, Fr_2, L/d, and α. Four different flow regions, as well as a two-phase flow, can be identified representing the flow regime of each branch. These regions can be defined as follows:

1. Region I: The OGE occurs at the upper branch.
2. Region II: The OGE occurs at the lower branch.
3. Region III: The value of the critical height of the upper branch (H_{OGE}/d) is less than the physical limitations of the upper branch $[(d/2)\cos\alpha]$, and this results in a two-phase flow at the upper branch, combined with the OGE that occurs at the lower branch.
4. Region IV: There is no OGE at both the upper and the lower branches.

The operating conditions describing the flow regions are mapped in Fig. 8 at different values of the wall inclination angles (α), with $L/d=1.5$. Figures 8(*a*)–8(*c*) show the influence of the wall inclination angle α on the variation of the flow regions. Based on Fig. 8(*a*), where the inclination angle $\alpha=0.1$ deg, it was observed that

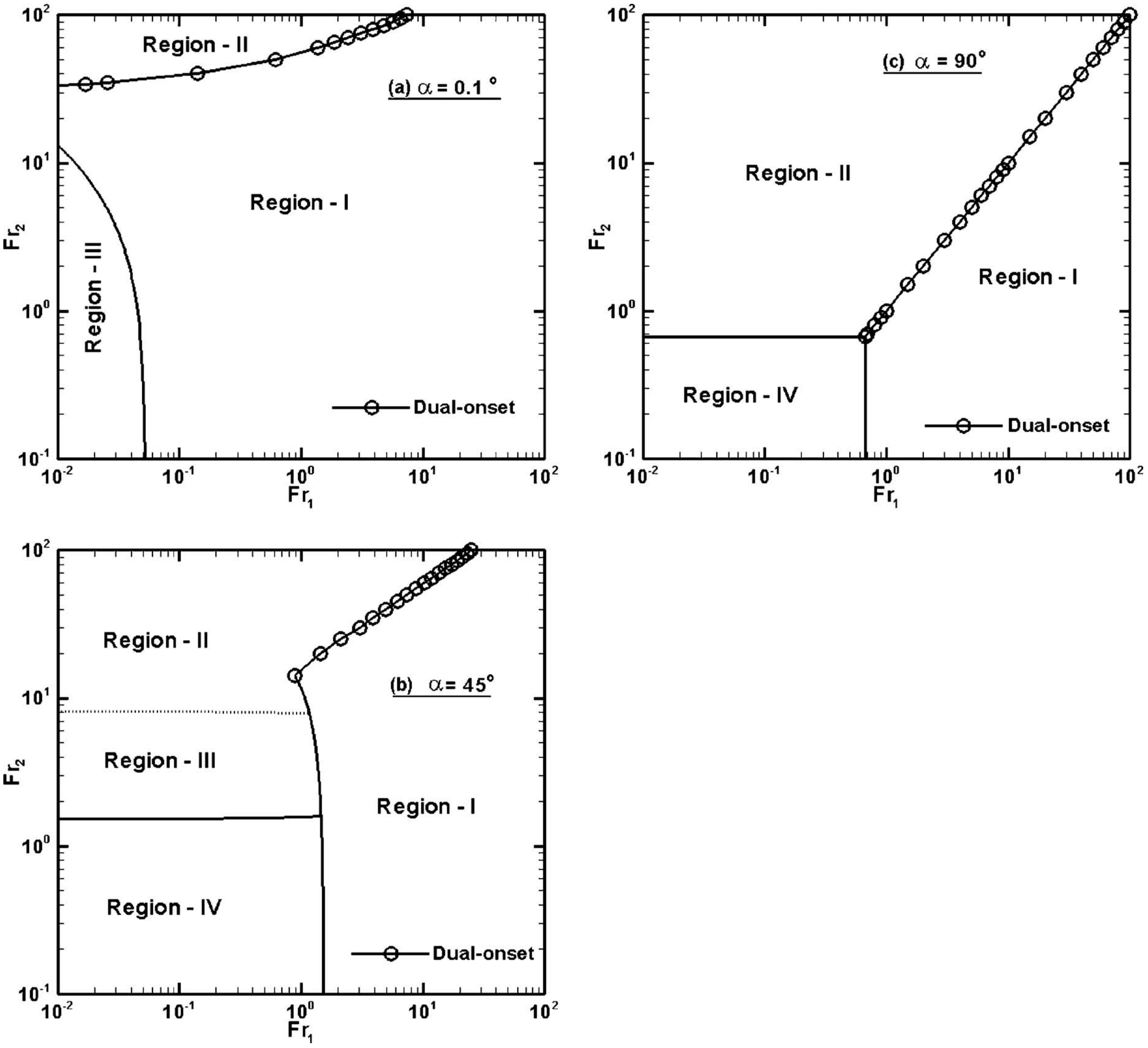

Fig. 8 Influence of the wall inclination angle (α) on flow regions at $L/d=1.5$ for (*a*) $\alpha=0.1$ deg, (*b*) $\alpha=45$ deg, and (*c*) $\alpha=90$ deg

most of the figure domain is dominated by Region I, where the gas entrainment occurs only at the upper branch. For the value of $Fr_2 > 35$ and Fr_1 ranging from 0.01 to 7, Region II is bound by the curve that represents the dual onset points of the two branches, where $[H_{OGE}/d]_A=[H_{OGE}/d]_B=[H_{OGE}/d]$. Region III is bound by the vertical axis Fr_2 and the curve representing the critical value of Fr_1 at the transition from the gas-entrainment regime to no-gas-entrainment regime for the upper branch. It is worth mentioning that at a wall inclination angle of 0 ($\alpha=0$), only Region I appears for the whole domain for Fr_1, ranging from 0.01 to 100, and for Fr_2, ranging from 0.1 to 100. This implies that the OGE occurs only at the upper branch.

Figure 8(*b*) represents the predicted flow regions at a wall inclination α of 45 deg. In Region I, for $Fr_1 \geq 2.0$, Fr_2 ranges from 0.1 to 20, and for $Fr_2 \geq 30$, Fr_1 ranges from 2 to 25. In Region II, for $Fr_2 \geq 8$, Fr_1 ranges from 1 to 25. In Region III, for $Fr_1 \leq 1.5$, Fr_2 ranges from 1.8 to 8. Region IV is bound by $Fr_1 \leq 1.5$ and $Fr_2 \leq 1.5$. At a wall inclination angle (α) of 90 deg, there are only three different flow regions, Region I, Region II, and Region IV, while Region III no longer occurs, as indicated by Fig. 8(*c*). Region IV is bound by $Fr_1 \leq 0.7$ and $Fr_2 \leq 0.7$. Region II is bounded by $Fr_2 \geq 0.7$ and the line $Fr_1=Fr_2$, and Region I is bound by $Fr_1 \geq 0.7$ and the line $Fr_2=Fr_1$.

The conclusion based on Figs. 8(*a*)–8(*c*) can be explained as follows: at $\alpha=0$ deg, only Region I occurs. This means that the OGE occurs only at the upper branch for the whole range of Fr_2. However, at $\alpha=90$ deg, the OGE occurs at the branch that has a higher Fr, and simultaneously in both branches if $Fr_1=Fr_2$. This is referred to as both branches having the same height from the interface and each branch behaving as an independent single one. Increasing the wall inclination angle ($0\ \text{deg} < \alpha < 90\ \text{deg}$) changes the height of each branch from the interface and increases the influence of the lower branch. Consequently, Fr_2 must be greater than Fr_1 for the onset to occur in the lower branch; the higher the h_B, the higher the Fr_2 is required for the onset to occur at the lower branch. Moreover, increasing L/d for $0\ \text{deg} < \alpha < 90\ \text{deg}$, results in an increase of the value of Fr_2 required for the onset to occur at the lower branch since it increases the value of h_B. Consequently, it increases the domain of Region I and decreases the domain of Region II.

3.2.2 Critical Height. The influence of the wall inclination angle on the behavior of the critical height as a function of Fr_1 at $L/d=1.5$ and $Fr_2=40$ is presented in Fig. 9. Based on the figure, at $\alpha=0$, the onset occurs only at the upper branch for all values of Fr_1 (Region 1). Increasing the wall inclination results in the onset

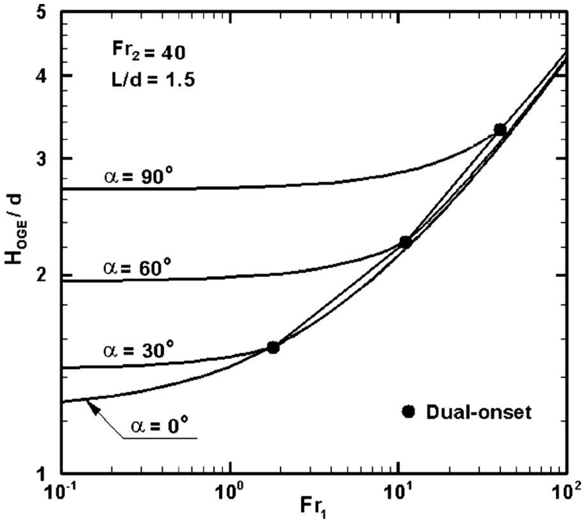

Fig. 9 Influence of the wall inclination angle on the critical height

at the lower branch for low values of Fr_1. There is a slight increase in (H_{OGE}/d) as Fr_1 increases up to the dual onset point. Beyond this point, the onset shifts to the upper branch and (H_{OGE}/d) increases significantly with Fr_1. The value of Fr_1 required for the dual onset to occur increases with the increase of the wall inclination angle. During the onset at the lower branch where $\mathrm{Fr}_1 < \mathrm{Fr}_2$, the critical height increases with the increasing wall inclination angle. However, during the onset at the upper branch, the influence of the wall inclination angle on the critical height is insignificant.

The variation of critical height (H_{OGE}/d) versus the wall inclination angle (α) for $\mathrm{Fr}_2=60$ at different values of Fr_1 and L/d is shown in Fig. 10. At $\mathrm{Fr}_2=60$ and $L/d=1.5$, Fig. 10(*a*) shows the effect of Fr_1 on the variation of (H_{OGE}/d) versus the wall inclination angle. Based on this figure, it is clear that at $\mathrm{Fr}_1=0.1$, the OGE only occurs at the upper branch for $0 \leq \alpha \leq 0.01$. However, for all values of $\alpha > 0.01$, the onset occurs at the lower branch. Increasing Fr_1 to 2 will lead to the dual onset occurrence at the value of $\alpha=\alpha_d=10.5$. For $\alpha < 10.5$, the OGE occurs at the upper branch, while for $\alpha > 10.5$, the OGE occurs at the lower branch. By increasing Fr_1 up to 60 (i.e., $\mathrm{Fr}_1=\mathrm{Fr}_2$), the value of the wall inclination angle at the dual onset point increases to the upper value of 90 deg. At $\alpha < \alpha_d$, the onset only occurs at the upper branch where there is a gentle variation of (H_{OGE}/d) with increasing α, and at $\alpha > \alpha_d$, the onset only occurs at the lower branch where the value of (H_{OGE}/d) rises with the increase of the wall inclination angle. At $\mathrm{Fr}_1 > \mathrm{Fr}_2$, the OGE occurs at the upper branch for all values of the wall inclination angle (α).

A similar trend was noticed in the variation of (H_{OGE}/d) versus the wall inclination angle (α) at $L/d=4$, and for the values of Fr_1, ranging from 2 to 80, as shown in Fig. 10(*b*). However, at $\mathrm{Fr}_1=2$ and 10, the values of (H_{OGE}/d) slightly decrease with the increasing wall inclination angle until $\alpha=\alpha_d$, where the dual onset occurs. Furthermore, at $\mathrm{Fr}_1=0.1$, different flow regions are observed. At α values from 0 deg to 0.89 deg, the OGE only occurs at the upper branch, but by increasing the value of α, the gas entrainment no longer occurs at this branch; instead, the OGE only occurs at the lower branch at α varied from 1 deg to 90 deg. Within the range of the wall inclination angle, two different flow regions can be predicted. Region II occurs at a wall inclination angle ranging from 90 deg to approximately 42 deg, where the critical height at the OGE at the lower branch is equal to the physical limitation of the upper branch $[(d/2)\cos\alpha]$. Finally, the comparison between Figs. 10(*a*) and 10(*b*) indicated that by increasing L/d, the value of α_d corresponding to the dual onset location increases, while the value of critical height (H_{OGE}/d) decreases.

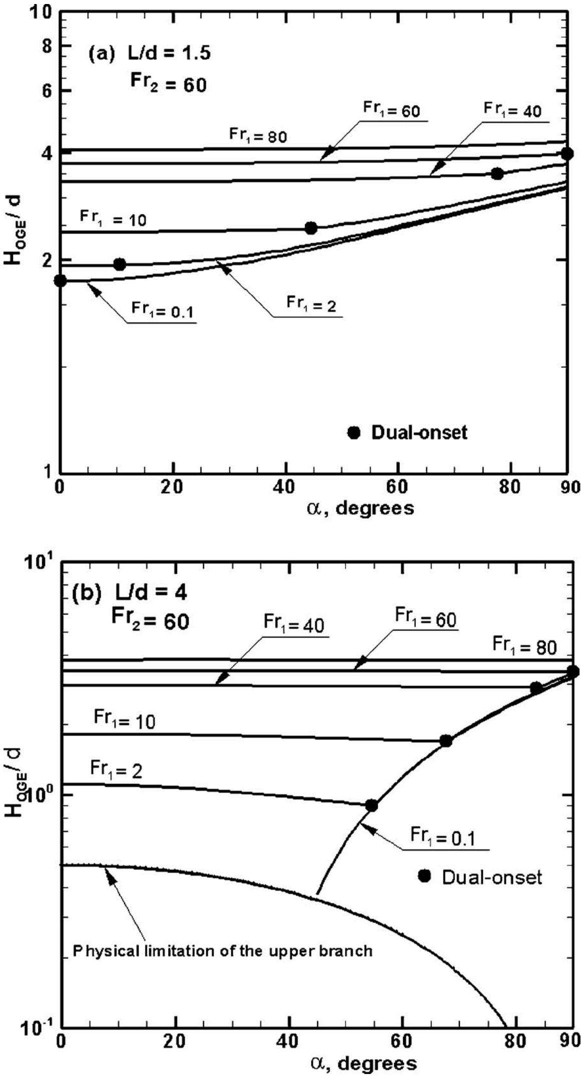

Fig. 10 Variation the critical height versus the wall inclination for $\mathrm{Fr}_2=60$ at different values of L/d: (*a*) $L/d=1.5$ and (*b*) $L/d=4$

The conclusion based on Figs. 9 and 10 is that the influence of the wall inclination angle α on the critical height depends on Fr_1, Fr_2, and L/d as follows: If $\mathrm{Fr}_1 > \mathrm{Fr}_2$, the OGE only occurs at the upper branch and the wall inclination angle has no effect on the flow regions. The reason is that the acceleration at the interface directly above the lower branch never reaches $g(\Delta\rho/\rho_1)$ due to the fact that $h_{\mathrm{B}} > h_{\mathrm{A}}$ for all values of α ranging from 0 deg to 90 deg. However, increasing the wall inclination angle slightly increases or decreases the critical height, depending on the value of L/d, as shown in Figs. 10(*a*) and 10(*b*). At a low value of L/d, increasing the angle α slightly increases the critical height due to the contribution of the lower branch in increasing the acceleration of the interface above the upper branch. However, a higher value of L/d results in the opposite effect of wall inclination on the critical height. This means that the lower branch has an opposing effect on the gas entrainment in the upper branch. Whether the lower branch aids or opposes the OGE at the upper branch at any value of L/d may be attributed to the hydrodynamic pressure distribution within the flow field between the two branches. Maier et al. [23] noticed a similar trend when investigating the OLE from two branches mounted on a vertical wall.

If $\mathrm{Fr}_1=\mathrm{Fr}_2$, the onset occurs at the upper branch for $\alpha < 90$ deg, whereas at $\alpha=90$ deg the onset occurs at both branches simultaneously. The same trend was noticed regarding the influence of the wall inclination angle on the critical height as previously explained. If $\mathrm{Fr}_1<\mathrm{Fr}_2$, two scenarios occur: onset at the upper branch followed by onset at the lower branch, where the location of the dual onset point (α_d) depends on L/d, Fr_1, and Fr_2. During the first scenario, $\alpha<\alpha_d$, whether the critical height increases or decreases with increasing wall inclination angle depends on L/d, as previously mentioned. Moreover, during the second scenario, $\alpha>\alpha_d$, by increasing the wall inclination angle, the critical height significantly increases. The reason is that increasing α will increase the height of the interface directly above the branch as a result of reducing the value of $(L\cos\alpha)$. Consequently, the critical height H_{OGE}/d increases, as shown by Eq. (31).

3.2.3 Comparisons With Experimental Data. During the gas-entrainment regime, the influence of the Froude number of each branch, Fr_1 and Fr_2, the distance between the branch centerlines (L/d) on the critical height, and the flow regions are presented as follows: comparisons between the predicted critical height and the available experimental measurements at $\alpha=0$ by Parrott [21] and different values of L/d are presented in Figs. 11 and 12. Figure 11 shows the comparison between the present theoretical results and the experimental data when $L/d=1.5$ and $\mathrm{Fr}_2=31.43$, as shown in Fig. 11(*a*), and Fr_2 is set to 43.99, as shown in Fig. 11(*b*), for low values of $\mathrm{Fr}_1 \geqslant 0.1$. Based on the figures, one can observe that there is good concurrence between measured and predicted results by both finite-branch and point-sink models.

Figure 12 shows the comparison between the predicted and the experimental results at $L/d=4.5$ when $\mathrm{Fr}_2=56.67$. The models were found to be consistent with the average value of $(H_{\mathrm{OGE},f}/d)$ and $(H_{\mathrm{OGE},m}/d)$. However, at low values of the Froude number $(\mathrm{Fr}_1<1)$, there is a clear difference between the predicted critical height of the finite-branch model and point-sink model. Based on Figs. 11 and 12, the conclusion is that the comparison between the predicted results of both models and the measured results show a good concurrence. Moreover, the predicted critical heights by the finite-branch model demonstrate conformity with the predicted critical height by the point-sink model at $L/d=1.5$. However, increasing L/d to 4.5 increases the difference between predicted critical heights, at low values of Fr_1, in both models.

At $\alpha=0$ deg, the OGE occurs only at the upper branch for all independent variables. However, the experimental results of Parrott [21] show different flow regions that occur at $\alpha=0$ deg, as shown in Fig. 13(*a*). The differences between measured and predicted results are most likely due to inviscid flow assumptions in which the viscous effect is neglected and the slip condition is applied to the wall-liquid interaction. Consequently, the interaction between the onset point (A) and the interface is considered directly adjacent to the wall. As a further step toward improving the finite-branch model, shifting point A away from the wall is therefore suggested so that the line connected between point A and the branch centerline makes an angle of approximately 0.05 deg. Based on this suggestion, the flow regions are presented and compared with the available experimental data of Parrott [21], where the phenomena of no-gas-entrainment regime was reported for the upper branch, and other flow regions, in the case of a dual discharge, as shown in Fig. 13(*b*). It is evident that Regions I and II, based on Fig. 13(*b*), are well predicted, whereas the dual onset locations are underpredicted by the finite-branch model. The conclusion based on Fig. 13 is that a further investigation of the interface interaction with the onset point is necessary to estimate how much shift of the point (A) from the wall will correctly predict the experimental results. Moreover, experimental measure-

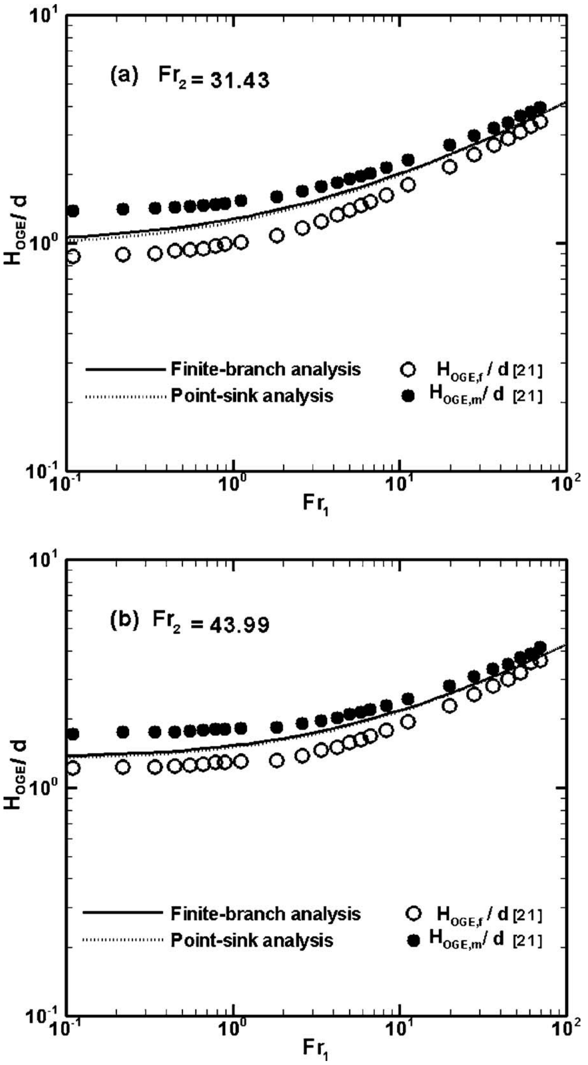

Fig. 11 Comparison between predicted and experimental critical height at different values of Fr_2, for $L/d=1.5$, and (*a*) $\mathrm{Fr}_2=31.43$ and (*b*) $\mathrm{Fr}_2=43.99$

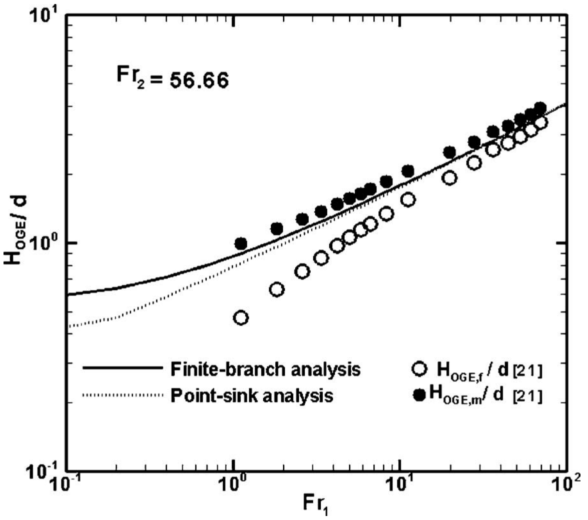

Fig. 12 Comparison between predicted and experimental critical height at different values of Fr_2, for $L/d=4.5$

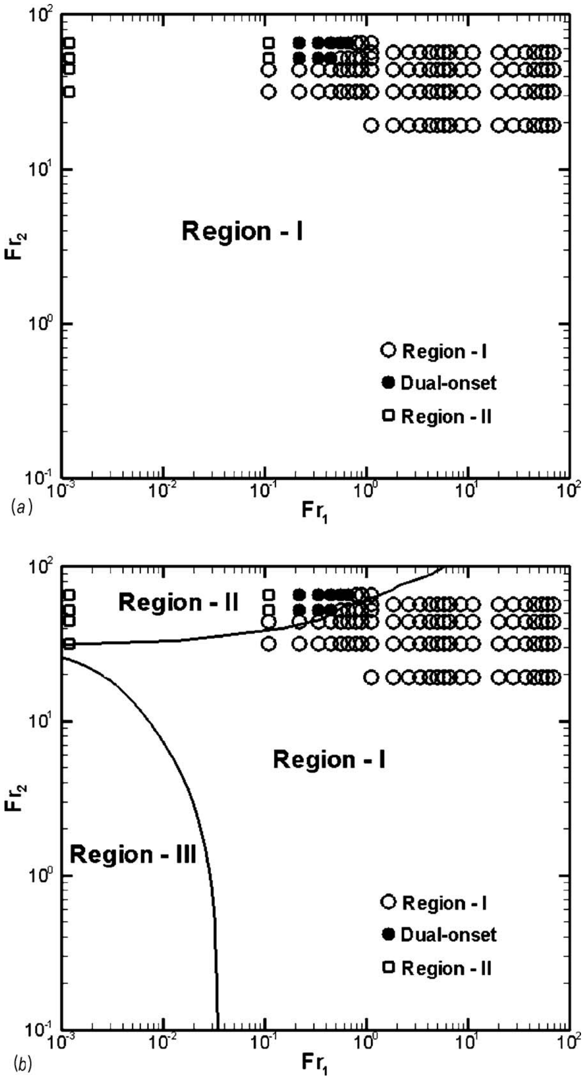

Fig. 13 (*a*) Comparison between predicted and experimental results at $L/d=1.5$ and $\alpha=0$ under the upper figure as shown on the web ready text file. (*b*) Comparison between predicted and experimental results at $L/d=1.5$ and $\alpha=0$ when shifting the onset point under the lower figure as shown on the web ready text file.

ments of the critical Froude number at varying wall inclination angles will greatly help to confirm the no-gas-entrainment regime as well as the different predicted flow regions for single and dual discharges.

In the current investigation, the wall inclination angle varies between 0 deg and 90 deg ($0 \leqslant \alpha \leqslant 90$ deg). The only available experimental data are at $\alpha=0$ deg, and $\alpha=90$ deg, which are in a good concurrence with the predicted values. Since there is no available experimental data for an inclined wall, these two cases ($\alpha=0$ deg and 90 deg) represent the limits of the model and have already shown to validate the proposed model. However, as in any scientific endeavor, particularly analytical/computational modeling work, the model presented in this paper, despite being limited in some aspects, can be further validated, refined, and extended as more experimental data become available.

4 Conclusion

In light of the current study, some important observations can be made.

1. For a vertical wall, the gas-entrainment regime is predicted at all values of Froude numbers, whereas for an inclined wall ($\alpha > 0$), along with low values of the Froude number, two distinct flow regimes are predicted: the gas-entrainment and no-gas entrainment regimes.
2. The critical Froude number at the transition from gas-entrainment to no-gas-entrainment regime is shown to be a function of a wall inclination angle for a single discharge. For dual discharge, the critical Froude number is found to be dependent on the wall inclination angle, the separating distance between the centerlines of the two branches, as well as the Froude number of the other branch.
3. Four different flow regions are mapped, representing the flow regime for each branch as well as the two-phase flow. Increasing the wall inclination angle α results in a decrease of the domain of Region I, where the OGE occurs at the upper branch, and an increase of the domain of Region II, where the OGE occurs at the lower branch. Furthermore, at a wall inclination equal to 0 deg and 90 deg, the same flow regions are predicted and independent of L/d. For 0 deg $< \alpha < 90$ deg, increasing L/d results in an increase in the value of Fr_2 at the dual onset point, a decrease of the domain of Region I, and an increase of the domain of Region II.
4. The point-sink analysis, for the single branch, cannot predict the transition from gas-entrainment to no-gas-entrainment regime since the onset of the gas-entrainment equation is independent of the wall inclination angle α.

In the gas-entrainment regime, the critical height at the OGE and the onset location are found to be dependent on Fr_1, Fr_2, L/d, and α. If $\mathrm{Fr}_1 > \mathrm{Fr}_2$, the OGE only occurs at the upper branch and independently of L/d and α, whereas the critical height decreases slightly with increasing L/d. The variation of the critical height with α is shown to be dependent on the value of L/d. If $\mathrm{Fr}_1 = \mathrm{Fr}_2$, the same trend is observed and the dual onset occurs at $\alpha = 90$ deg for all values of L/d. If $\mathrm{Fr}_1 < \mathrm{Fr}_2$, two scenarios occur: onset at the upper branch followed by the onset at the lower branch, where the location of the dual onset point depends on L/d, Fr_1, and Fr_2. In both scenarios, the critical height depends on the wall inclination angle. Experimental efforts are essential in order to define the interaction between the onset point and the interface in the case of a vertical wall. Moreover, experimental measurements of the critical Froude number at varying wall inclination angles will greatly help to verify the no-gas-entrainment regime for single and dual discharges, as well as the predicted flow regions.

Acknowledgment

The author gratefully acknowledges the financial support for this research from the Department of Mechanical Engineering, Assiut University, Egypt. Thanks are also due to the anonymous reviewers for their valuable suggestions and critical review to improve the manuscript. The author also thanks Dr. Mahmoud Halfawy at the National Research Council of Canada for his valuable feedback and Dr. Khaled Ahmed for his help during the preparation of this manuscript.

APPENDIX: THE INTEGRAL FUNCTIONS I_1–I_{20}

$$I_1 = -\frac{4}{\pi}\int_0^\infty \int_0^\infty \int_{-1}^{1} \frac{\beta e^{-h_A^* \sin\alpha\sqrt{\lambda^2+\beta^2}}}{\lambda\sqrt{\lambda^2+\beta^2}} \sin(\lambda(\sqrt{1-y^{*2}})) \times \sin(\beta(h_A^* \cos\alpha - y^*))dy^* d\lambda d\beta$$

$$I_2 = -\frac{4}{\pi}\int_0^\infty \int_0^\infty \int_{-L^*-1}^{-L^*+1} \frac{\beta e^{-h_A^* \sin\alpha\sqrt{\lambda^2+\beta^2}}}{\lambda\sqrt{\lambda^2+\beta^2}} \sin(\lambda(\sqrt{1-(y^*-L^*)^2})) \times \sin(\beta(h_A^* \cos\alpha - y^*))dy^* d\lambda d\beta$$

$$I_3 = -\frac{4}{\pi}\int_0^\infty \int_0^\infty \int_{-1}^{+1} \frac{\beta^2 e^{-h_A^* \sin\alpha\sqrt{\lambda^2+\beta^2}}}{\lambda\sqrt{\lambda^2+\beta^2}} \sin(\lambda(\sqrt{1-y^{*2}})) \times \cos(\beta(h_A^*\cos\alpha - y^*))dy^* d\lambda d\beta$$

$$I_4 = -\frac{4}{\pi}\int_0^\infty \int_0^\infty \int_{-L^*-1}^{-L^*+1} \frac{\beta^2 e^{-h_A^* \sin\alpha\sqrt{\lambda^2+\beta^2}}}{\lambda\sqrt{\lambda^2+\beta^2}} \times \sin(\lambda(\sqrt{1-(y^*-L^*)^2}))\cos(\beta(h_A^*\cos\alpha - y^*))dy^* d\lambda d\beta$$

$$I_5 = -\frac{4}{\pi}\int_0^\infty \int_0^\infty \int_{-1}^{+1} \frac{e^{-h_A^* \sin\alpha\sqrt{\lambda^2+\beta^2}}}{\lambda} \times \sin(\lambda(\sqrt{1-y^{*2}}))\cos(\beta(h_A^*\cos\alpha - y^*))dy^* d\lambda d\beta$$

$$I_6 = -\frac{4}{\pi}\int_0^\infty \int_0^\infty \int_{-L^*-1}^{-L^*+1} \frac{e^{-h_A^* \sin\alpha\sqrt{\lambda^2+\beta^2}}}{\lambda} \times \sin(\lambda(\sqrt{1-(y^*-L^*)^2}))\cos(\beta(h_A^*\cos\alpha - y^*))dy^* d\lambda d\beta$$

$$I_7 = \frac{4}{\pi}\int_0^\infty \int_0^\infty \int_{-1}^{+1} \frac{\sqrt{\lambda^2+\beta^2} e^{-h_A^* \sin\alpha\sqrt{\lambda^2+\beta^2}}}{\lambda} \times \sin(\lambda(\sqrt{1-y^{*2}}))\cos(\beta(h_A^*\cos\alpha - y^*))dy^* d\lambda d\beta$$

$$I_8 = \frac{4}{\pi}\int_0^\infty \int_0^\infty \int_{-L^*-1}^{-L^*+1} \frac{\sqrt{\lambda^2+\beta^2} e^{-h_A^* \sin\alpha\sqrt{\lambda^2+\beta^2}}}{\lambda} \times \sin(\lambda(\sqrt{1-(y^*-L^*)^2}))\cos(\beta(h_A^*\cos\alpha - y^*))dy^* d\lambda d\beta$$

$$I_9 = \frac{4}{\pi}\int_0^\infty \int_0^\infty \int_{-1}^{+1} \frac{\beta e^{-h_A^* \sin\alpha\sqrt{\lambda^2+\beta^2}}}{\lambda} \times \sin(\lambda(\sqrt{1-y^{*2}}))\sin(\beta(h_A^*\cos\alpha - y^*))dy^* d\lambda d\beta$$

$$I_{10} = \frac{4}{\pi}\int_0^\infty \int_0^\infty \int_{-L^*-1}^{-L^*+1} \frac{\beta e^{-h_A^* \sin\alpha\sqrt{\lambda^2+\beta^2}}}{\lambda} \times \sin(\lambda(\sqrt{1-(y^*-L^*)^2}))\sin(\beta(h_A^*\cos\alpha - y^*))dy^* d\lambda d\beta$$

$$I_{11} = -\frac{4}{\pi}\int_0^\infty \int_0^\infty \int_{-1}^{+1} \frac{\beta e^{-h_B^* \sin\alpha\sqrt{\lambda^2+\beta^2}}}{\lambda\sqrt{\lambda^2+\beta^2}} \times \sin(\lambda(\sqrt{1-y'^{*2}}))\sin(\beta(h_B^*\cos\alpha - y'^*))dy'^* d\lambda d\beta$$

$$I_{12} = -\frac{4}{\pi}\int_0^\infty \int_0^\infty \int_{L^*-1}^{L^*+1} \frac{\beta e^{-h_B^* \sin\alpha\sqrt{\lambda^2+\beta^2}}}{\lambda\sqrt{\lambda^2+\beta^2}} \times \sin(\lambda(\sqrt{1-(y'^*-L^*)^2}))\sin(\beta(h_B^*\cos\alpha - y'^*))dy'^* d\lambda d\beta$$

$$I_{13} = -\frac{4}{\pi}\int_0^\infty \int_0^\infty \int_{-1}^{+1} \frac{\beta^2 e^{-h_B^* \sin\alpha\sqrt{\lambda^2+\beta^2}}}{\lambda\sqrt{\lambda^2+\beta^2}} \times \sin(\lambda(\sqrt{1-y'^{*2}}))\cos(\beta(h_B^*\cos\alpha - y'^*))dy'^* d\lambda d\beta$$

$$I_{14} = -\frac{4}{\pi}\int_0^\infty \int_0^\infty \int_{L^*-1}^{L^*+1} \frac{\beta^2 e^{-h_B^* \sin\alpha\sqrt{\lambda^2+\beta^2}}}{\lambda\sqrt{\lambda^2+\beta^2}} \times \sin(\lambda(\sqrt{1-(y'^*-L^*)^2}))\cos(\beta(h_B^*\cos\alpha - y'^*))dy'^* d\lambda d\beta$$

$$I_{15} = -\frac{4}{\pi}\int_0^\infty \int_0^\infty \int_{-1}^{+1} \frac{e^{-h_B^* \sin\alpha\sqrt{\lambda^2+\beta^2}}}{\lambda} \times \sin(\lambda(\sqrt{1-y'^{*2}}))\cos(\beta(h_B^*\cos\alpha - y'^*))dy'^* d\lambda d\beta$$

$$I_{16} = -\frac{4}{\pi}\int_0^\infty \int_0^\infty \int_{L^*-1}^{L^*+1} \frac{e^{-h_B^* \sin\alpha\sqrt{\lambda^2+\beta^2}}}{\lambda} \times \sin(\lambda(\sqrt{1-(y'^*-L^*)^2}))\cos(\beta(h_B^*\cos\alpha - y'^*))dy'^* d\lambda d\beta$$

$$I_{17} = \frac{4}{\pi}\int_0^\infty \int_0^\infty \int_{-1}^{+1} \frac{\sqrt{\lambda^2+\beta^2} e^{-h_B^* \sin\alpha\sqrt{\lambda^2+\beta^2}}}{\lambda} \times \sin(\lambda(\sqrt{1-y'^{*2}}))\cos(\beta(h_B^*\cos\alpha - y'^*))dy'^* d\lambda d\beta$$

$$I_{18} = \frac{4}{\pi}\int_0^\infty \int_0^\infty \int_{L^*-1}^{L^*+1} \frac{\sqrt{\lambda^2+\beta^2} e^{-h_B^* \sin\alpha\sqrt{\lambda^2+\beta^2}}}{\lambda} \times \sin(\lambda(\sqrt{1-(y'^*-L^*)^2}))\cos(\beta(h_B^*\cos\alpha - y'^*))dy'^* d\lambda d\beta$$

$$I_{19} = \frac{4}{\pi}\int_0^\infty \int_0^\infty \int_{-1}^{+1} \frac{\beta e^{-h_B^* \sin\alpha\sqrt{\lambda^2+\beta^2}}}{\lambda} \times \sin(\lambda(\sqrt{1-y'^{*2}}))\sin(\beta(h_B^*\cos\alpha - y'^*))dy'^* d\lambda d\beta$$

$$I_{20} = \frac{4}{\pi}\int_0^\infty \int_0^\infty \int_{L^*-1}^{L^*+1} \frac{\beta e^{-h_B^* \sin\alpha\sqrt{\lambda^2+\beta^2}}}{\lambda} \times \sin(\lambda(\sqrt{1-(y'^*-L^*)^2}))\sin(\beta(h_B^*\cos\alpha - y'^*))dy'^* d\lambda d\beta$$

References

[1] Zuber, N., 1980, "Problems in Modeling of Small Breaks LOCA," Nuclear Regulatory Commission, Report No. NUREG–0724.

[2] Smoglie, C., and Reimann, J., 1986, "Two-Phase Flow Through Small Breaks in a Horizontal Pipe With Stratified Flow," Int. J. Multiphase Flow, **12**, pp. 609–625.

[3] Schrock, V. E., Revankar, S. T., Mannheimer, R., Wang, C. H., and Jia, D., 1986, "Steam-Water Critical Flow Through Small Pipes From Stratified Upstream Regions," *Proceeding of the Eighth International Heat Transfer Conference*, San Francisco, CA, Vol. 5, pp. 2307–2311.

[4] Yonomoto, T., and Tasaka, K., 1988, "New Theoretical Model for Two-Phase Flow Discharged From Stratified Two-Phase Region Through Small Break," J. Nucl. Sci. Technol., **25**, pp. 441–455.

[5] Yonomoto, T., and Tasaka, K., 1991, "Liquid and Gas-Entrainment to a Small Break Hole From a Stratified Two-Phase Region," Int. J. Multiphase Flow, **17**, pp. 745–765.

[6] Micaelli, J. C., and Memponteil, A., 1989, "Two-Phase Flow Behavior in a Tee-Junction—The Cathare Model," *Proceedings of the Fourth International Topical Meeting on Nuclear Reactor Thermal-Hydraulics*, Karlsruhe, Germany, Oct. 10–13, Vol. 2, pp. 1024–1030.

[7] Hassan, I. G., Soliman, H. M., Sims, G. E., and Kowalski, J. E., 1998, "Two-Phase Flow From a Stratified Region Through a Small Side Branch," J. Fluids Eng., **120**, pp. 605–612.

[8] Xue, M., and Yue, D. P., 1998, "Nonlinear Free Surface Flow Due to an Impulsively Started Submerged Point Sink," J. Fluid Mech., **364**, pp. 325–347.

[9] Miloh, T., and Tyvand, P. A., 1993, "Nonlinear Transient Free Surface Flow and Dip Formation Due to Point Sink," Phys. Fluids A, **5**(6), pp. 1368–1375.

[10] Lubin, B. T., and Springer, G. S., 1966, "The Formation of a Dip on the Surface of a Liquid Draining From a Tank," J. Fluid Mech., **29**, pp. 385–390.

[11] Zhou, Q. N., and Graebel, W. P., 1990, "Axisymmetric Draining of a Cylindrical Tank With a Free Surface," J. Fluid Mech., **221**, pp. 511–532.

[12] Haugen, K. B., and Tyvand, P. A., 2003, "Free Surface Evolution Due to an Impulsive Bottom Sink at Uniform Depth," Phys. Fluids, **15**(3), pp. 742–751.

[13] Forbes, L. K., and Hocking, G. C., 2005, "Flow Due to a Sink Near a Vertical Wall in Infinitely Deep Fluid," Comput. Fluids, **34**, pp. 684–704.

[14] Forbes, L. K., and Hocking, G. C., 2003, "On the Computation of Steady Axisymmetric Withdrawal From a Two-Layer Fluid," Comput. Fluids, **32**, pp. 385–401.

[15] Forbes, L. K., and Hocking, G. C., 1998, "Withdrawal From a Two-Layer Inviscid Fluid in a Duct," J. Fluid Mech., **361**, pp. 275–296.

[16] Vanden Broeck, J.-M., and Keller, J. B., 1997, "An Axisymmetric Free Surface With a 120 Degree Angle Along a Circle," J. Fluid Mech., **342**, pp. 403–409.

[17] Vanden Broeck, J.-M., and Keller, J. B., 1987, "Free Surface Flow Due to a Sink," J. Fluid Mech., **175**, pp. 109–117.

[18] Ahmed, M., Hassan, I., and Esmail, N., 2003, "Modeling of the Onset of Gas Entrainment Through a Finite-Side Branch," ASME J. Fluids Eng., **125**, pp. 902–909.

[19] Ahmed, M., Hassan, I., and Esmail, N., 2004, "Theoretical Analysis of the Onset of Gas Entrainment From a Stratified Region Through a Single-Oriented Branch at Moderate Froude Numbers," Can. J. Chem. Eng., **82**(6), pp. 1175–1182.

[20] Parrott, S. D., Soliman, H. M., Sims, G. E., and Krishnan, V. S., 1991, "Experiments on the Onset of Gas Pull-Through During Dual Discharge From a Reservoir," Int. J. Multiphase Flow, **17**, pp. 119–129.

[21] Parrott, S. D., 1993, "Experiments on the Onsets of Gas Pull-Through and Liquid Entrainment During Dual Discharge From a Large Reservoir," MS thesis, University of Manitoba, Winnipeg, MB, Canada.

[22] Hassan, I. G., 1995, "Single, Dual and Triple Discharge From a Large Stratified, Two Phase Region Through Small Branches," Ph.D. thesis, University of Manitoba, Winnipeg, MB, Canada.

[23] Maier, M. R., Soliman, H. M., Sims, G. E., and Armstrong, K. F., 2001, "Onsets of Entrainment During Dual Discharge From a Stratified Two-Phase Region Through Horizontal Branches With Centerlines Falling in an Inclined Plane: Part 1. Analysis of Liquid Entrainment," Int. J. Multiphase Flow, **27**, pp. 1011–1028.

[24] Maier, M. R., Soliman, H. M., Sims, G. E., and Armstrong, K. F., 2001, "Onsets of Entrainment During Dual Discharge From a Stratified Two-Phase Region Through Horizontal Branches With Centerlines Falling in an Inclined Plane: Part 2. Experiments on Gas and Liquid Entrainment," Int. J. Multiphase Flow, **27**, pp. 1029–1049.

[25] Maier, M. R., 1998, "Onsets of Entrainment During Dual Discharge From a Stratified Two-Phase Region Through Horizontal Branches With Centerlines Falling in an Inclined Plane," MS thesis, University of Manitoba, Winnipeg, MB, Canada.

[26] Ahmed, M., Hassan, I., and Esmail, N., 2004, "The Onset of Gas Pull-Through During Dual Discharge From Stratified Two-Phase Region-Theoretical Analysis," Phys. Fluids, **16**(9), pp. 3385–3392.

[27] Ahmed, M., 2006, "Theoretical Analysis of the Onset of Gas-Entrainment From a Stratified Two-Phase Region Through Two Side Oriented Branches Mounted on a Vertical Wall," ASME J. Fluids Eng., **128**, pp. 131–141.

[28] Yildirim, N., Kocabas, F., and Gulcan, S., 2000, "Flow-Boundary Effects on Critical Submergence of Intake," J. Hydraul. Eng., **126**(4), pp. 288–297.

[29] Daves, J. T., and Rideal, E. K., 1963, *Interfacial Phenomena*, Academic, London.

[30] Croxton, C. A., 1986, *Fluid Interfacial Phenomena*, Wiley, New York.

[31] Hite, J., and Mih, W., 1994, "Velocity of Air-Core Vortices at Hydraulic Intakes," J. Hydraul. Eng., **120**(3), pp. 284–297.

[32] Jain, A., and Raju, K., 1978, "Air Entrainment in Radial Flow Towards Intakes," J. Hydr. Div., **104**(HY9), pp. 1323–1329.

[33] Schetz, J. A., and Fuhs, A. E., 1996, "Handbook of Fluid Dynamics and Fluid Machinery," *Fundamentals of Fluid Mechanics*, Wiley, New York, Vol. 1.

[34] Stroud, A. H., 1971, *Approximate Calculation of Multiple Integrals*, Prentice-Hall, Englewood Cliffs, NJ.

[35] Taylor, G. I., 1950, "The Instability of Liquid Surfaces When Accelerated in a Direction Perpendicular to their Planes,"-I, Proc. R. Soc. London, Ser. A, **201**, pp. 192–196.

J.-C. Jouhaud[1]
Senior Researcher
Centre Européen de Recherche et de Formation
Avancée en Calcul Scientifique (CERFACS),
42 Avenue Gaspard Coriolis,
31057 Toulouse Cedex, France
e-mail: jjouhaud@cerfacs.fr

P. Sagaut
Professor
Institut Jean Le Rond d'Alembert,
Université Pierre et Marie Curie,
4 place Jussieu-case 162,
F-75252 Paris Cedex 05, France
e-mail: pierre.sagaut@upmc.fr

B. Enaux
Ph.D student

J. Laurenceau
Ph.D student

Centre Européen de Recherche et de Formation
Avancée en Calcul Scientifique (CERFACS),
42 Avenue Gaspard Coriolis,
31057 Toulouse Cedex, France

Sensitivity Analysis and Multiobjective Optimization for LES Numerical Parameters

Accuracy and reliability of large-eddy simulation data in a really complex industrial geometry are invesigated. An original methodology based on a response surface for LES data is introduced. This surrogate model for the full LES problem is built using the Kriging technique, which enables a low-cost optimal linear interpolation of a restricted set of large-eddy simulation (LES) solutions. Therefore, it can be used in most realistic industrial applications. Using this surrogate model, it is shown that (i) optimal sets of simulation parameters (subgrid model constant and artificial viscosity parameter in the present case) can be found; (ii) optimal values, as expected, depend on the cost functional to be minimized. Here, a realistic approach, which takes into account experimental data sparseness, is introduced. It is observed that minimization of the error evaluated using a too small subset of reference data may yield a global deterioration of the results.
[DOI: 10.1115/1.2829602]

Keywords: kriging, surrogate model, large-eddy simulation, multiobjective optimization, error estimation

1 Introduction

Large-eddy simulation (LES) [1,2] is now commonly recognized as a reliable numerical approach for the prediction of complex turbulent flows. The assessment of quality and reliability of LES results is an important issue, since error estimation and control is a necessary step toward an increased use of LES for practical applications. Several works dealing with the analysis of numerical schemes within the LES framework [3–6] and subgrid modeling error [7,8] have been performed during the past decade. Most of them put the emphasis on the improvement of the computed results on simple test flows, but the issue of estimating the error on complex flows is still an important open issue.

A priori and a posteriori error estimation for LES has recently been addressed in a few research works. While some adjoint-based error estimation techniques have been implemented for grid refinement by Hoffman and Johnson (see Ref. [9] for a global survey of this approach), simplest methods for computing an error index have been proposed [10,11]. Another strategy is the error map approach proposed by Geurts and co-workers [7,8,12] which is certainly the most used one. Following this approach, the response surface of the LES computation is drawn by running a large set of simulations, varying the values of the computational setup parameters. This approach yielded very interesting results in isotropic turbulence, making it possible to derive optimal trajectories for the setup parameters, which lead to the lowest possible error.

The underlying idea here is not to compute the local sensitivity of the LES solution with respect to the setup parameters (as for the adjoint-based approach) but to parametrize the space of possible solutions spanned by the numerical tool (including the numerical scheme, boundary and initial conditions, subgrid model, etc.). The number of samples required can be dramatically reduced considering advanced response surface techniques. Pseudospectral modeling can be performed using the generalized polynomial chaos approach if the density probability of the possible variations of the setup parameters is prescribed. The first use of this technique to analyze LES sensitivity is very recent [13]. Another popular approach for response surface building is the Kriging method [14], which is an optimal linear approximation technique. This technique is now more and more popular in the field of aerodynamics, and was used to analyze Reynolds averaged Navier–Stokes (RANS) solution sensitivity and optimality [15] or for surrogate model based shape optimization [16].

The search for the minimal errors solution requires the foreknowledge of a reference solution, and is therefore not possible in all realistic configurations. Therefore, the estimation of error is not always possible, and it must be replaced by an evaluation of the robustness of the solution. Robustness is an important feature of the solution in engineering applications, since a very sensisitive solution, i.e., a solution that varies a lot if setup parameters undergo small variations are of restricted interest for practical purposes.

The goal of the present paper is twofold: (i) to assess the possibility of building reliable Kriging-based response surface for LES of complex flows and (ii) to derive optimal LES solutions in realistic applications at affordable cost. The selected case is the LES of jet in crossflow (JICF) on unstructured grids, including wall heat transfer. The main features of the numerical method are presented in Sec. 2. The flow configuration and the numerical setup are displayed in Sec. 3. The construction of the Kriging surface response (considering variations of both the subgrid and the artificial viscosities), the analysis of the solution sensitivity, and the definition of optimal LES solutions are discussed in Sec. 4. It is worth noting that the different error norms (or equivalently cost functions) are introduced, which require different amount of

---

[1] Corresponding author.

Contributed by the Fluids Engineering Division of ASME for publication in the JOURNAL OF FLUIDS ENGINEERING. Manuscript received June 11, 2007; final manuscript received August 30, 2007; published online January 25, 2008. Review conducted by Ugo Piomelli.

data related to a reference solution. The optimized LES solutions are presented in Sec. 5. Conclusions are drawn in Sec. 6.

2 Governing Equations

The aim of the LES is to resolve the large scale of the turbulence while the small ones are modeled because of their universality. It is one of the main discrepancies with the RANS simulation where all scales are modeled. Consequently, the LES will be easier to use in industrial complex configurations in which the large scales are dominant. Moreover, the unsteady behavior of the JICF will be predicted more precisely by an unsteady LES approach.

2.1 Physical Model. The removal of small scales in LES-type simulations is often modeled as the application of a filtering operator to the continuity equation, the transport equations of momentum, energy, and species. In this case, a Favre filtering is used:

$$\bar{\rho}\tilde{f}(\mathbf{x},t) = \overline{\rho f(\mathbf{x},t)} = \int_{-\infty}^{+\infty} \rho f(\mathbf{x}',t)\mathcal{G}(\mathbf{x}'-\mathbf{x})d\mathbf{x}' \tag{1}$$

where $\mathcal{G}$ is the filter function, ρ is the density, and f can be either the velocity vector, the energy, or the mass fraction of species. It leads to the following equations:

$$\begin{gathered}
\frac{\partial\bar{\rho}}{\partial t} + \frac{\partial}{\partial x_i}(\bar{\rho}\tilde{u}_i) = 0 \\
\frac{\partial}{\partial t}(\bar{\rho}\tilde{u}_j) + \frac{\partial}{\partial x_i}(\bar{\rho}\tilde{u}_i\tilde{u}_j) = -\frac{\partial\bar{p}}{\partial x_j} + \frac{\partial\bar{\tau}_{jk}}{\partial x_k} - \frac{\partial}{\partial x_i}(\bar{\rho}\tilde{T}_{ij}) \\
\frac{\partial}{\partial t}(\bar{\rho}\tilde{E}) + \frac{\partial}{\partial x_i}(\bar{\rho}\tilde{u}_i\tilde{E}) = -\frac{\partial\bar{q}_j}{\partial x_j} + \frac{\partial}{\partial x_j}[\overline{(\tau_{ij} - p\,\delta_{ij})u_i}] - \frac{\partial}{\partial x_j}(\bar{\rho}\tilde{Q}_j) \\
- \frac{\partial}{\partial x_j}(\bar{\rho}\tilde{T}_{ij}\tilde{u}_i) \\
\frac{\partial}{\partial t}(\bar{\rho}\tilde{Y}_\alpha) + \frac{\partial}{\partial x_i}(\bar{\rho}\tilde{u}_i\tilde{Y}_\alpha) = -\frac{\partial\bar{J}_i^\alpha}{\partial x_i} - \frac{\partial}{\partial x_i}(\bar{\rho}\tilde{F}_i^\alpha)
\end{gathered} \tag{2}$$

where

$$\tau_{ij} = \mu\left(\frac{\partial u_i}{\partial x_j} + \frac{\partial u_j}{\partial x_i}\right) - \frac{2}{3}\mu\frac{\partial u_k}{\partial x_k}\delta_{ij} \quad q_i = -\lambda\frac{\partial T}{\partial x_i} \quad J_i^\alpha = -\rho D^\alpha\frac{\partial Y_\alpha}{\partial x_i} \tag{3}$$

The terms $\tilde{T}_{ij}$ and $\tilde{F}_i$ need to be modeled to close the LES equations. To realize that, an eddy viscosity is introduced to replace the subgrid scales action:

$$\tilde{T}_{ij} = (\widetilde{u_iu_j} - \tilde{u}_i\tilde{u}_j) = -2\nu_t\tilde{S}_{ij} + \frac{1}{3}\tilde{T}_{kk}\delta_{ij} \tag{4}$$

with

$$\tilde{S}_{ij} = \frac{1}{2}\left(\frac{\partial\tilde{u}_i}{\partial x_j} + \frac{\partial\tilde{u}_j}{\partial x_i}\right) - \frac{1}{3}\frac{\partial\tilde{u}_k}{\partial x_k}\delta_{ij} \tag{5}$$

So it remains just to define the subgrid scale turbulent viscosity ν_t. In this study, the standard Smagorinsky model is used [17]:

$$\nu_t = (C_S\Delta)^2\sqrt{2\tilde{S}_{ij}\tilde{S}_{ij}} \tag{6}$$

with C_S=0.18 the standard value of the model constant. The cutoff length Δ is taken equal to the cubic root of the control cell volume.

2.2 Flow Solver. The simulation is performed with the turbulent compressible Navier–Stokes code AVBP developed at CERFACS. This solver uses structured, unstructured, and hybrid grids to resolve complex configurations to model unsteady flows thanks to the LES approach. In order to handle such grids, the CFD code AVBP is based on a cell-vertex finite-volume approximation. Furthermore, the LES approach employs the second order scheme of Lax–Wendroff for spatial discretization, and for time integration an explicit method is used.

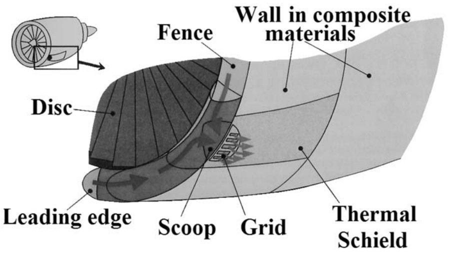

Fig. 1 Schematic illustration of the engine antiicing system

As it was said previously, AVBP uses a numerical discretization, which is spatially centered. These types of schemes are known to be subject to small oscillations (wiggles) in the solution variations. In order to solve this problem, a common practice is to add an artificial viscosity to smooth the gradients. The use of artificial viscosity is triggered by a wiggle detector based on pressure. Several artificial viscosity models are used in AVBP and all are based on a combination of two operators: the second order artificial viscosity operator, which smoothes gradients and introduces an artificial dissipation, and the fourth-order artificial viscosity operator, which allows to control high frequency wiggles. In this paper, the influence of the second operator is more investigated. It is based on this principle, as follows:

- First, a cell contribution of the fourth order artificial viscosity is computed on each vertex of the cell Ω_j:

$$R_{k\in\omega_j} = \frac{1}{N_v}\frac{V_{\Omega_j}}{\Delta t_{\Omega_j}}\text{smu4}[(\boldsymbol{\nabla}\omega)_{\Omega_j}.(\mathbf{x}_{\Omega_j} - \mathbf{x}_k) - (\omega_{\Omega_j} - \omega_k)] \tag{7}$$

  with smu4 the fourth oder artificial viscosity constant, which is tunable by the user.
- Then every cell contributions are added what gives the nodal value:

$$d\omega_k = \sum_j R_{k\in\omega_j} \tag{8}$$

3 Computational Setup

The selected case presented in this document is the interaction between a hot JICF (see Margason [18] for a detailed review on JICF's and their applications) and the wall of a turbofan engine nacelle. The interaction takes place on the leading edge of the nacelle where hot air is injected through the wall of the nacelle in order to avoid icing on the exterior (see Fig. 1). The hot air is collected in a scoop and ejected on the leading edge of the nacelle to form the JICF. Since the velocities are of the order of tens of m s^{-1}, temperature can be considered as a passive scalar.

The objective of engine designers is to determine the essential characteristics of the jet and its development, and not to simulate the flow around the turbofan engine. The jet is thus studied in the simplified geometry of the flat plate configuration. This choice is justified by the fact that the nacelle has relatively low curvature and the jet diameter is very small in comparison with the dimension of the turbofan engine. The zone where the jet mixes with the cross flow can then be regarded as quasiplanar. Experimental data

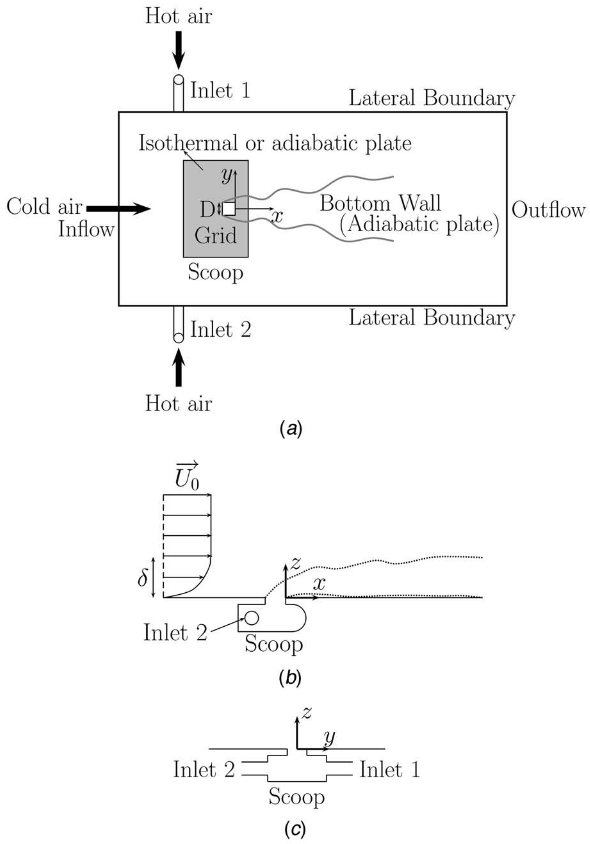

Fig. 2 Computational domain considered for LES: (*a*) Top view, (*b*) lateral view, and (*c*) front view.

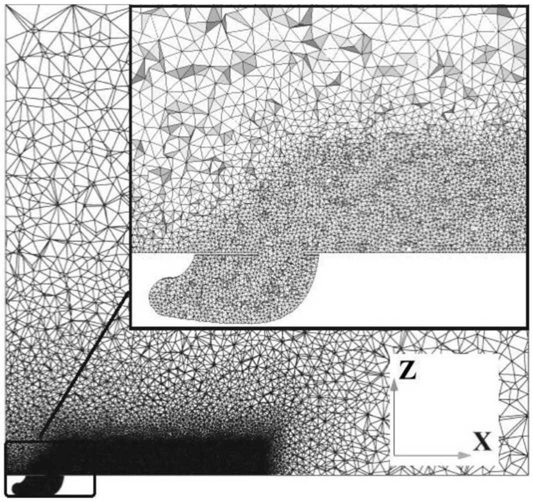

Fig. 3 Fine mesh used for the LES computations

to be used in the validation of the numerical methods for this industrylike configuration were obtained using an apparatus located at ONERA.

As is shown on Fig. 2, the computational domain is composed of one jet injected vertically, whose injection diameter D measures 30 mm and the exit is flushed to the flat plane. The jet inlet is located $X/D=2.8$ downstream the main inlet of the domain, and $X/D=33.3$ upstream of the outlet. Each lateral face is located $Y/D=27.8$ of the jet inlet, and the domain size is $37.2D \times 46.5D \times 33.3D$. So the spreading of the jet is not restricted by the domain. On this domain a fine mesh composed of 2,740,000 cells is used (Fig. 3). It is refined along the jet directory. To keep a relatively reasonable number of cells, a wall law is used for the bottom wall. Consequently, the grid has a first cell from the bottom wall whose the height corresponds to $\Delta y^+=150$.

Thanks to experimental measurements, the flow in the main section is fixed by imposing the velocity profile with a boundary layer profile at the inlet of the domain. The initial boundary layer height is $\delta=2D$ and the freestream velocity is $U_0=47.1$ m s^{-1}. At the injection pipes, which compose the jet scoop, a mean turbulent pipe profile is applied, using a standard 1/7 power law approximation (Table 1). For these inlets, "injection of turbulence" is not employed because it would be negligible in front of the turbulence generated by the shear of the two fluids. All these velocity profiles agree with the mass flux of the experiments.

Because of acoustic wave reflections due to the compressible flow solver, a boundary condition of relaxation is applied on the velocity, the temperature, and the mass fraction of the species for the inlets. The same boundary condition is applied for the outlet but just on the pressure. With regard to the plate, which is divided in two parts, a no-slip isothermal wall law condition is applied on the so-called "grid," and on the remainder part a no-slip adiabatic wall law condition is used. At the lateral surfaces, a symmetry condition is used, and a wall-slip-adiabatic condition is forced at the top surface. The use of a wall-slip adiabatic condition on the top surface is valid in this case because it is placed sufficiently far from the jet exit. So it seems reasonable to consider that no fluid leaves this wall, and there is not a reflection of energy back into the domain: the use of Navier–Stokes compressible boundary conditions (NSCBCs) (see Poinsot et al. [19] and Polifke et al. [20]) on this surface is thus not necessary.

4 Definition of the Optimization Problem

4.1 Optimization Framework. The present numerical method involves artificial dissipation. It is known that numerical dissipation and subgrid model induced dissipation are in competition, and that they must be tuned in and ad hoc, case-dependent way to recover the best possible results (e.g., Refs. [21,22]). It is chosen in the present work to retain both the Smagorinsky constant C_S and the artificial fourth-order dissipation parameter smu4 as optimization parameters.

Cost function evaluations require expensive LES simulations that is why the optimization method was to provide results in as few evaluations as possible excluding genetic algorithms and most global optimization methods. Despite gradient methods converge quickly to a local minima, these methods cannot treat multiple cost functions and were not adapted to this problem. Response surface based optimization seemed the best method to solve this low-dimensional problem. Once the sample database computed and the inexpensive response surfaces built, a Pareto front of solution can easily be plotted by a simple exploration of the domain of solution. Moreover, as the problem depends on two variables the robustness of solutions can be assessed by plotting the cost functions on the whole domain.

4.2 Space of Possible Solutions and Solution Sensitivity. A range of ±30% around the standard values $C_s=0.18$, smu4 $=0.01$ was studied. As only two parameters were considered, a sufficient exploration of the research space was possible to build

Table 1 Inlet characteristics

Patch	Velocity	Temperature	Pressure
Inlet1 and Inlet2	$\lvert V\rvert=53.1$ m s^{-1}	$T=363$ K	$P=98{,}701$ Pa
Inflow	$U_0=47.1$ m s^{-1}	$T_0=293$ K	$P_0=98{,}701$ Pa

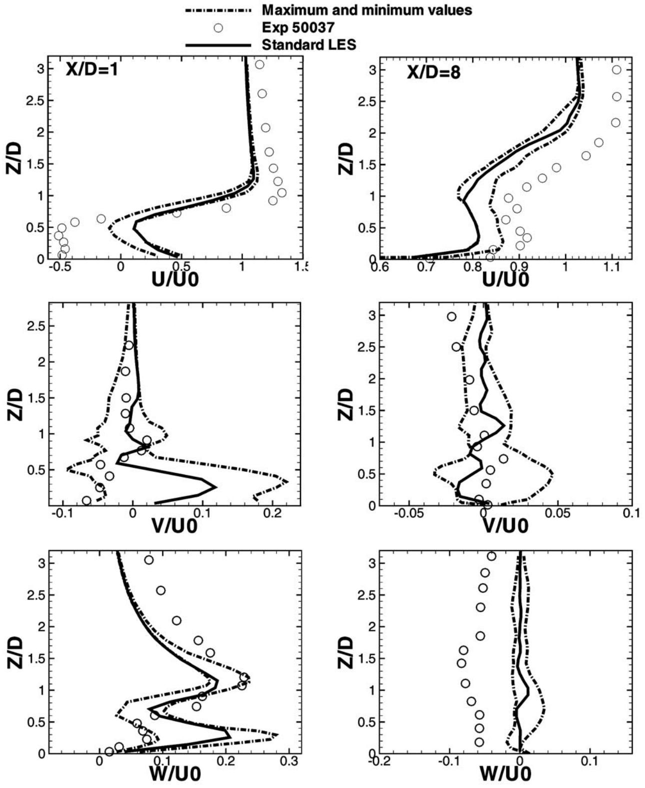

Fig. 4 Range of velocity response in the damping parameter space

globaly precise response surfaces using four points per direction for the sample database. The space filling distribution method was a 16-point uniform grid sampling.

- For Smagorinsky constant, $0.126 \leqslant C_s \leqslant 0.234$ with a step of 0.036.
- For the fourth-order smoothing constant, $0.007 \leqslant \text{smu4} \leqslant 0.013$ with a step of 0.002.

The sensitivity of the mean flow with respect to these two parameters is illustrated in Figs. 4 and 5, which compare the standard LES solution, the experimental data, and the extreme values found exploring the response surface built for the mean flow solution at each grid point. The sensitivity of the solution is directly related to the differences between the two extrema profiles. The robustness of the solution is observed to depend on both the location and the physical variable under consideration.

The figures reveal the existence of two different cases. In the first case, the reference data lie between the two extrema and it may be possible to tune the setup parameters to match the experimental data, leading to a very accurate LES solution at the considered location. In the second case, the experimental data are outside the response surface, meaning that the exact solution does not belong to the space of solutions spanned by the LES method used here.

4.3 Cost Functions for Multidisciplinary Optimization.

We now address the issue of defining and computing the optimal LES solution. To this end, some cost functions to be minimized must be defined, the optimal LES solution being the one that minimizes one or several cost functions.

4.3.1 Definition of Cost Functions. A total of four cost functions were computed. Mean and mean squared error were computed along two planar cut at locations $X/D=1$ and $X/D=8$.

The following total cost function is used in the following:

$$F^{(l)} = \frac{\sqrt{\sum_i \alpha_i E_i^2}}{\sum_i \alpha_i} = \sqrt{\frac{1}{2}(E_u^{(l)} + E_V^{(l)} + E_W^{(l)})^2 + \frac{1}{2}E_\eta^{2(l)}} \qquad (9)$$

where in L_1 norm,

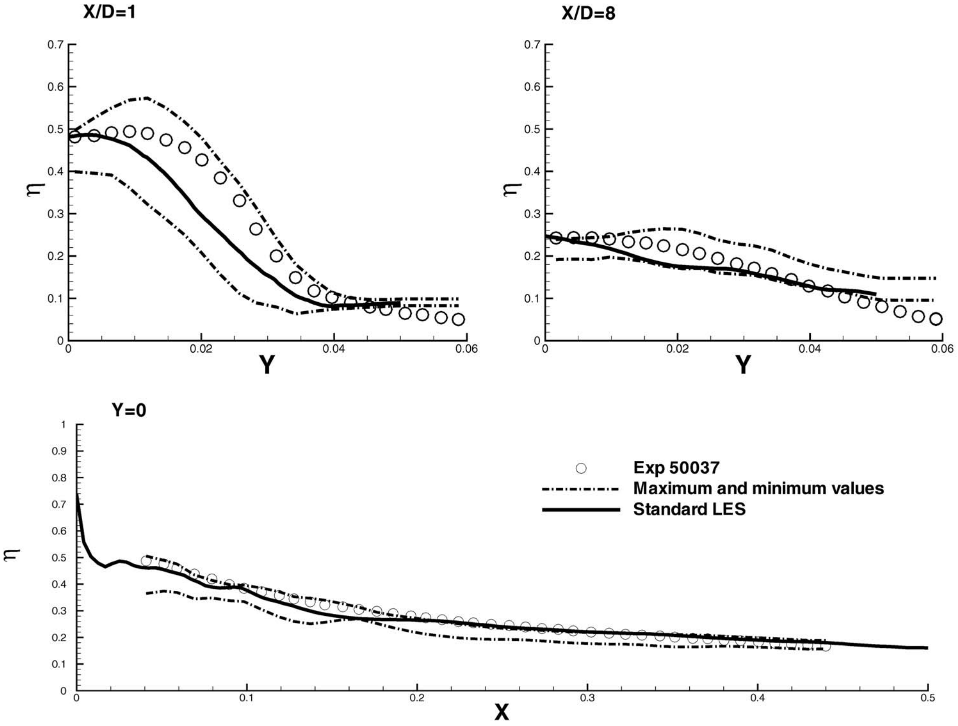

Fig. 5 Range of cooling effectiveness response in the damping parameter space

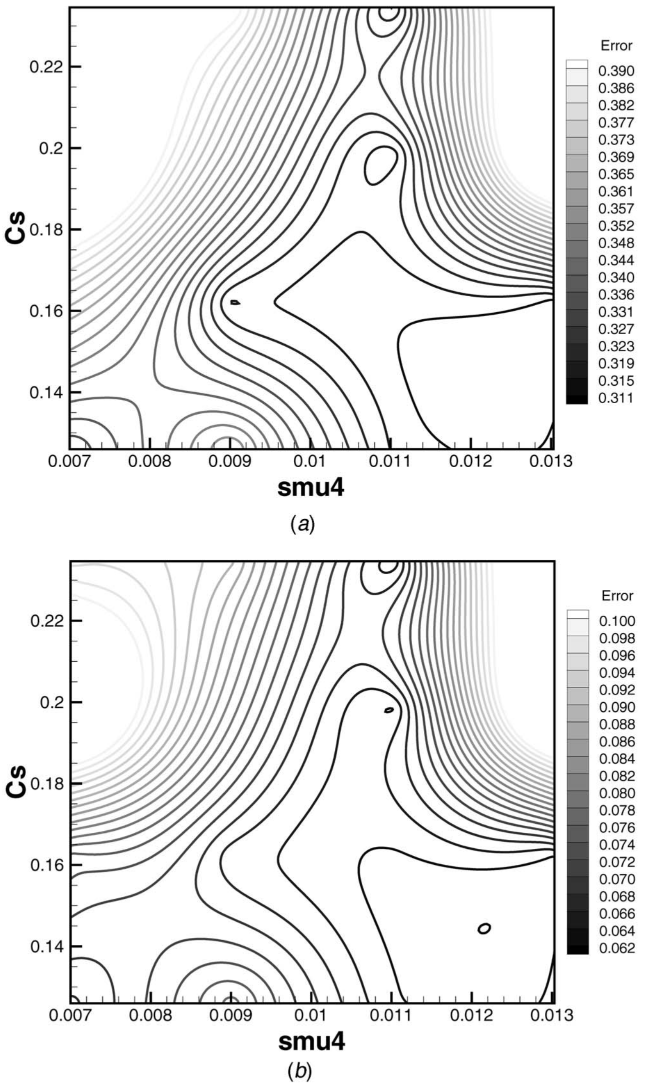

(*a*)

(*b*)

Fig. 6 Ordinary Kriging for the plane *X*/*D*=1. Cost function: (*a*) $F^{(1)}$ and (*b*) $F^{(2)}$.

$$
\begin{aligned}
E_U^{(1)} &= \frac{1}{\Delta z}\int_0^{\Delta z} \frac{|U_{\text{num}} - U_{\text{exp}}|}{\|\vec{U}_{\text{exp}}\|_{\max}} dz \\
E_V^{(1)} &= \frac{1}{\Delta z}\int_0^{\Delta z} \frac{|V_{\text{num}} - V_{\text{exp}}|}{\|\vec{U}_{\text{exp}}\|_{\max}} dz \\
E_W^{(1)} &= \frac{1}{\Delta z}\int_0^{\Delta z} \frac{|W_{\text{num}} - W_{\text{exp}}|}{\|\vec{U}_{\text{exp}}\|_{\max}} dz \\
E_\eta^{(1)} &= \frac{1}{\Delta y}\int_0^{\Delta y} \frac{|\eta_{\text{num}} - \eta_{\text{exp}}|}{\eta_{\text{exp}_{\max}}} dz
\end{aligned}
\tag{10}
$$

or in L_2 norm,

$$
E_U^{(2)} = \frac{1}{\Delta z}\int_0^{\Delta z} \left(\frac{U_{\text{num}} - U_{\text{exp}}}{\|\vec{U}_{\text{exp}}\|_{\max}}\right)^2 dz
$$

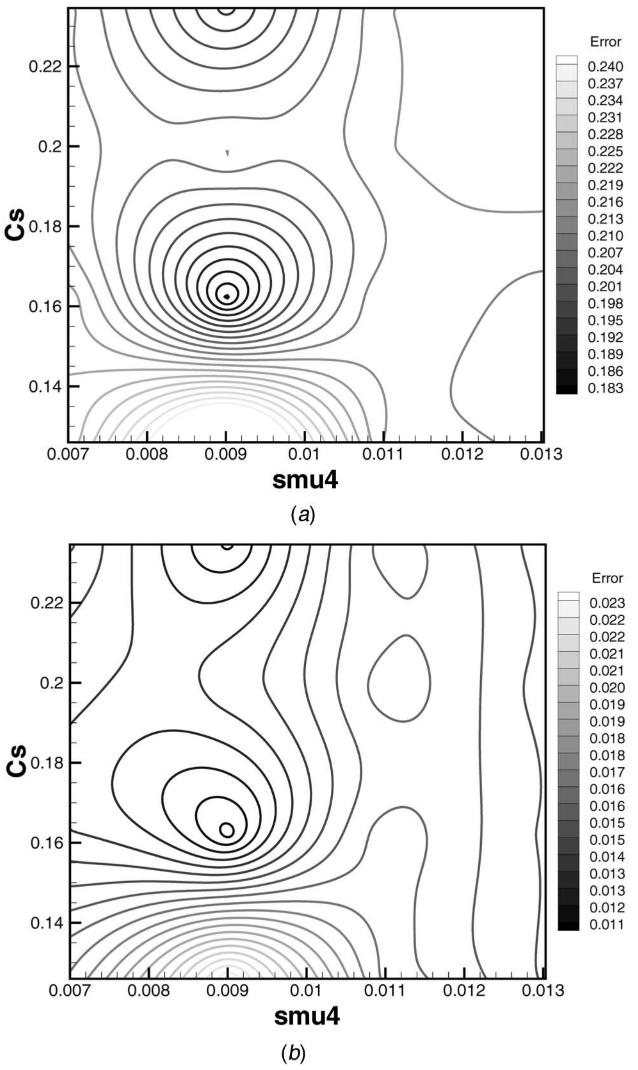

(*a*)

(*b*)

Fig. 7 Ordinary Kriging for the plane *X*/*D*=8. Cost function: (*a*) $F^{(1)}$ and (*b*) $F^{(2)}$.

$$
\begin{aligned}
E_V^{(2)} &= \frac{1}{\Delta z}\int_0^{\Delta z} \left(\frac{V_{\text{num}} - V_{\text{exp}}}{\|\vec{U}_{\text{exp}}\|_{\max}}\right)^2 dz \\
E_W^{(2)} &= \frac{1}{\Delta z}\int_0^{\Delta z} \left(\frac{W_{\text{num}} - W_{\text{exp}}}{\|\vec{U}_{\text{exp}}\|_{\max}}\right)^2 dz \\
E_\eta^{(2)} &= \frac{1}{\Delta y}\int_0^{\Delta y} \left(\frac{\eta_{\text{num}} - \eta_{\text{exp}}}{\eta_{\text{exp}_{\max}}}\right)^2 dz
\end{aligned}
\tag{11}
$$

where the thermal efficiency is defined as

$$
\eta = \frac{\langle T_w \rangle - T_0}{T_j - T_0} \tag{12}
$$

with $\langle T_w \rangle, T_j$, and T_0 the temporally averaged local wall temperature, the jet temperature, and the temperature of the cross flow upstream of the jet exit, respectively.

The cost function (9), which allows to test the sensitivity to the damping parameters, is well adapted to the configuration. Indeed, it is possible to test the sensitivity of the mixing prediction to these parameters via the effectiveness (E_η) and also the sensitivity of the velocity predictions (E_U, E_V, E_W). Moreover, thanks to non-

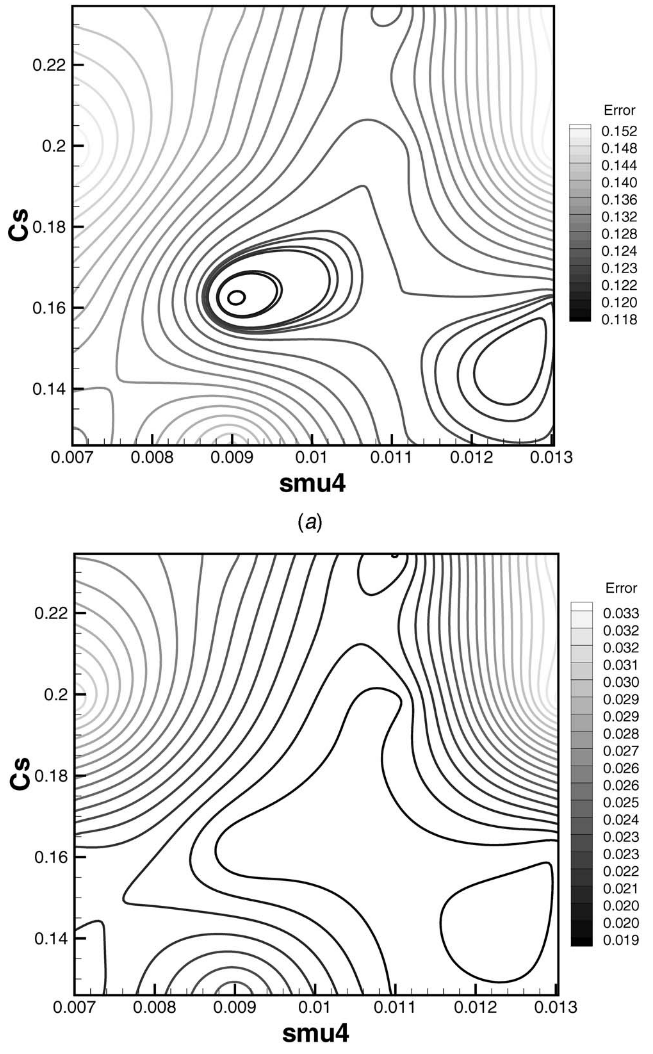

(*a*)

(*b*)

Fig. 8 Ordinary Kriging for the planes *X/D*=1 and *X/D*=8 (L_1 norm). Cost function: (*a*) $F^{(1)}$, and (*b*) $F^{(2)}$.

dimensional errors and the fact that E_V and $E_W \ll E_U$, the sensitivity to the viscosity parameters takes into account as much the mixing prediction as the velocity ones (particularly the U field).

The Eq. (9) can be thus simplified:

$$F^{(l)} \simeq \sqrt{\frac{1}{2}E_U^{2(l)} + \frac{1}{2}E_\eta^{2(l)}} \qquad (13)$$

4.4 Response Surface Construction Using the Kriging Method. Originally developed for application in geostatistics [14], the Kriging method was extended to various applications including computer experiments (design and analysis of computer experiments) [23]. Among all techniques available to predict functions at unknown locations from data observed at sampled locations (polynomial surfaces, artificial neural networks, etc.), the Kriging is a linear unbiased statistical predictor. Linear estimators express unknown values from linear combination of sample points. As the model is unbiased, the model cannot be fitted by minimizing least squares error as for polynomial regression, but rather using a statistical likelihood maximization.

General Kriging model is a sum of a polynomial regression model plus a Gaussian process. Most of the time as no assumption can be made a priori on the global trend of the studied function, a constant is used for the regression part (ordinary Kriging).

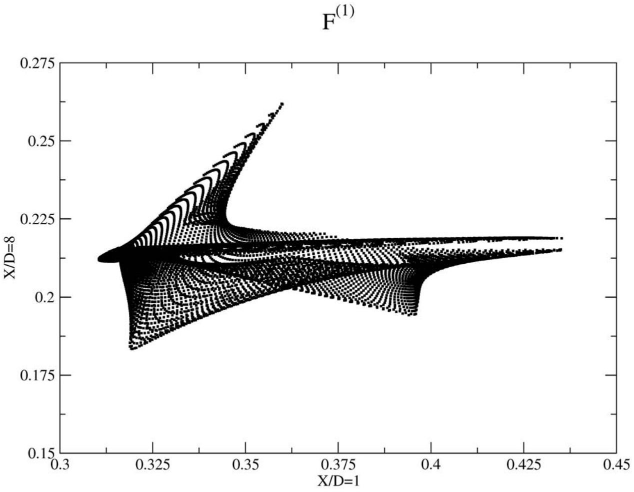

Fig. 9 Pareto front for $F^{(1)}$ function

Given n samples $X_s^T=\{s^1,\ldots,s^i,\ldots,s^n\}$ in the parameter space $S \subset \mathbb{R}^2$ and the evaluation of the studied function f at those control points $F_s^T=\{f(s^1),\ldots,f(s^i),\ldots,f(s^n)\}$, the linear predictor at a location $x \in S$ is

$$\hat{f}(x) = \sum_{i=1}^{n} \gamma_i(x) f(s^i) = \Gamma^T(x)F(X_s) \qquad (14)$$

with $\{\gamma_i(x)\}$ the weighting functions respecting the isotropic stationary model assumption and the unbiasedness constraints.

The model being stationary, the covariance C of the surface function f between two locations (s^i,x) depends only on the distance between these two locations and the variance σ^2 of the samples.

$$C[f(s^i),f(x)] = E[(f(s^i)-E(f(s^i)))(f(x)-E(f(x)))] = C(|s^i - x|) \qquad (15)$$

Covariances are usually represented as a matrix called the covariance matrix:

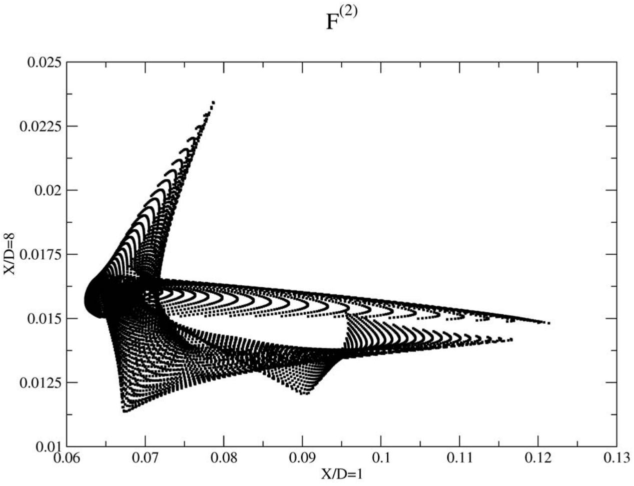

Fig. 10 Pareto front for $F^{(2)}$ function

Table 2 Kriging minima for the two different cost functions

	Plane	C_s	smu4
$F^{(1)}$	$X/D=1$	0.1465	0.01237
	$X/D=8$	0.1622	0.00901
	Global	0.1622	0.00901
$F^{(2)}$	$X/D=1$	0.1444	0.01213
	$X/D=8$	0.1622	0.00901
	Global	0.1449	0.01234

$$\underset{\sim}{C} = \begin{pmatrix} \sigma^2 & C(\|s^1 - s^2\|) & \cdots & C(\|s^1 - s^n\|) \\ C(\|s^2 - s^1\|) & \sigma^2 & \cdots & C(\|s^2 - s^n\|) \\ \vdots & \vdots & \ddots & \vdots \\ C(\|s^n - s^1\|) & C(\|s^n - s^2\|) & \cdots & \sigma^2 = C(0) \end{pmatrix} \tag{16}$$

The covariance vector $\vec{c}$ at unknown location is

$$\mathbf{c}(x) = \begin{pmatrix} C(\|x - s^1\|) \\ C(\|x - s^2\|) \\ \vdots \\ C(\|x - s^n\|) \end{pmatrix} \tag{17}$$

The estimated value $\hat{f}(x)$ will most likely differs from the actual value $f(x)$ and the difference is called the estimation error:

$$e(x) = \hat{f}(x) - f(x) \tag{18}$$

To obtain an optimal function estimator, the weighting functions $\Gamma(x)$ are computed so as to minimize the variance of the error or equivalently the mean squared error (MSE) of $\hat{f}(x)$:

$$\frac{\partial}{\partial \Gamma(x_p)}[\text{MSE}(\hat{f}(x_p))] = 0 \tag{19}$$

where MSE is defined by the following formula:

$$\begin{aligned} \text{MSE}(\hat{f}(x)) &= E[(\hat{f}(x) - f(x))^2] = E[\hat{f}^2(x)] + E[f^2(x)] - 2E[f(x)\hat{f}(x)] \\ &= \sum_{i=1}^{n}\sum_{j=1}^{n} \gamma_j(x)\gamma_i(x)C(|s^i - s^j|) \\ &\quad + \sigma^2 - 2\sum_{i=1}^{n} \gamma_i(x)C(|x - s^i|) \\ &= \Gamma^T(x)\underset{\sim}{C}\Gamma(x) + \sigma^2 - 2\Gamma^T(x)\mathbf{c}(x) \end{aligned} \tag{20}$$

As a consequence, the solution of Eq. (19) is

$$\Gamma(x) = \underset{\sim}{C}^{-1}\mathbf{c}(x) \tag{21}$$

In the ordinary Kriging method, the stationary model assumption gives the following constraint:

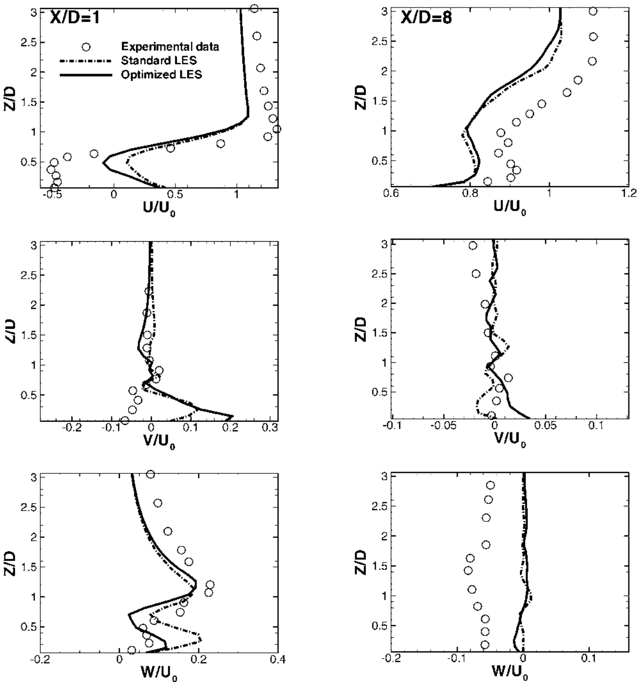

Fig. 11 Optimized profiles in the *X/D*=1 and *X/D*=8 planes (L_2 norm) for the velocity

$$\forall x \in S \quad \Gamma^T(x)I = \sum_{i=1}^{n} \gamma_i(x) = 1 \tag{22}$$

To enforce the unbiasedness constraint about the summation of the weighting coefficients, a Lagrange multiplier $\lambda(x)$ is introduced. The original problem (19) with the constraint (22) is then rewritten as

$$\frac{\partial}{\partial \Gamma(x)}\text{MSE}\hat{f}(x) + \Gamma^T(x)I\lambda(x) = 0 \tag{23}$$

leading to

$$\Gamma_+(x) = \underset{\sim}{C}_+^{-1}\mathbf{c}_+(x) \tag{24}$$

where

$$\Gamma_+(x) = \begin{pmatrix} \Gamma(x) \\ \lambda(x) \end{pmatrix} \quad \underset{\sim}{C}_+ = \begin{pmatrix} \underset{\sim}{C} & 1 \\ 1 & 0 \end{pmatrix} \quad \mathbf{c}_+(x) = \begin{pmatrix} \mathbf{c}(x) \\ 1 \end{pmatrix} \tag{25}$$

The estimator of the function $f(x)$ is then given by

$$\hat{f}(x) = \mathbf{c}^T(x)\underset{\sim}{C}^{-1}F(X_s) \tag{26}$$

In ordinary Kriging, the most widely used covariogram function is the Gaussian covariogram:

$$C(\|x - s^i\|) = \sigma^2 \exp(-\|x - s^i\|) \tag{27}$$

The linear system (24) is solved using the mathematical library of linear algebra package *LAPACK* [24].

Table 3 Relatives errors in reference simulations with the experimental profiles (cooling effectiveness η and axial velocity *U*)

	$X/D=1$		$X/D=8$		Global	
	$F^{(1)}$	$F^{(2)}$	$F^{(1)}$	$F^{(2)}$	$F^{(1)}$	$F^{(2)}$
Standard LES	0.322	6.706×10^{-2}	0.205	1.459×10^{-2}	0.123	1.969×10^{-2}
Optimized LES	0.310	6.243×10^{-2}	0.212	1.556×10^{-2}	0.121	1.877×10^{-2}

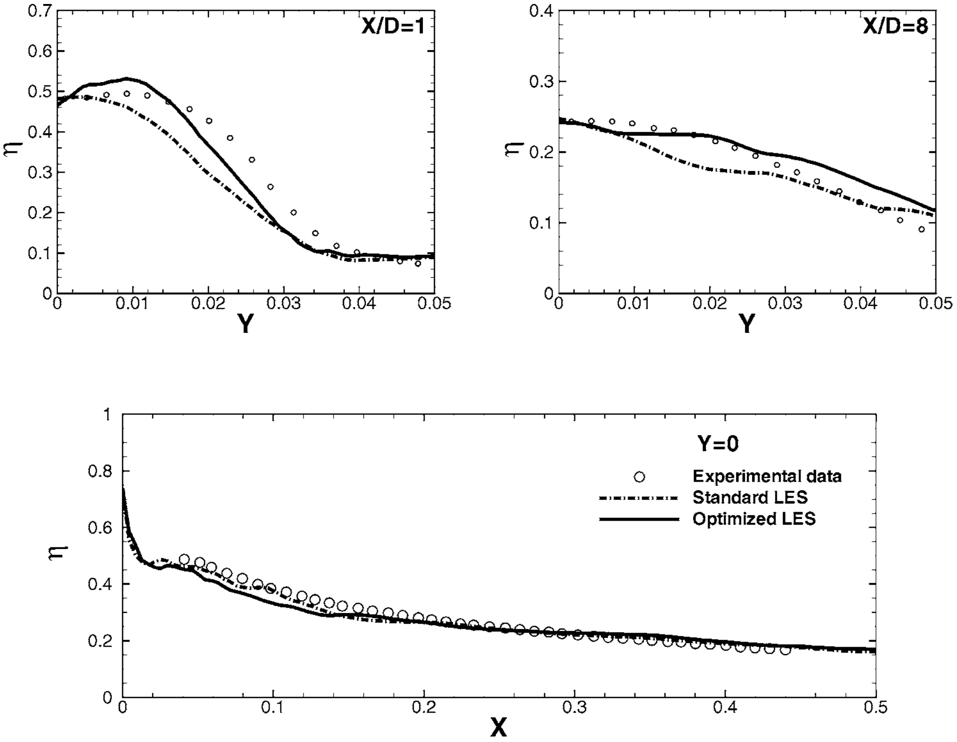

Fig. 12 Optimized profiles in the *X/D*=1 and *X/D*=8 planes (L_2 norm) for the cooling effectiveness

5 Numerical Optimization Results

The error maps constructed using the Kriging-based response surface are displayed in Figs. 6–8. Different error measures are considered, depending on the location and the norm. It is observed that the error admit several local extrema and are not convex. Therefore, simple gradient based optimization methods may be unable to obtain the best LES solution. Another interesting observation is that the minimum error is not obtained at the two locations with the same value of the parameters C_S and smu4. This lead to the conclusion that optimizing the LES setup considering a restricted subset of the reference data may lead to a solution, which is not globally fully satisfactory.

This last point is further illustrated plotting the Pareto front of the error for the two error norms (see Figs. 9 and 10). It is seen that minimizing the error at a single location can yield an error growth at the remaining one.

The values of the optimal parameters corresponding to the different cost functions are presented in Table 2, and values of the cost functions in the different cases are reported in Table 3.

The global optimal solution is compared to experimental reference data in Figs. 11 and 12. The global optimization yield a restricted local improvement of the results, and some local increase of the error can be observed. The increase of the quality of the solution on the temperature field is much more striking than on the velocity field.

6 Conclusion

A methodology for the analysis of LES result sensitivity was proposed. It is based on Kriging-based surface response, and requires the computation of a minimal set of LES solutions. The sensitivity of the results is observed to be very dependent on several parameters, such as the location and the physical variable under consideration. The construction of the surface response allows for the search of optimal LES solution. A LES solution is referred to as optimal if it corresponds to an absolute minimum of an error-based cost function. Different definitions of the cost function have been considered. It is observed that optimal values of the computional setup exhibit very large variations, showing that the concept of "best LES solution" is only a relative one in practical cases.

The complexity of the test flow induce large local variations in the sensitivity of the solution, a consequence being that the minimizing an error norm can lead to an increase of another error measure. Again, the concept of best LES solution can be questioned.

References

[1] Sagaut, P., 2005, *Large-Eddy Simulation for Incompressible Flows*, 3rd ed., Springer, New York.

[2] Geurts, B. J., 2003, *Elements of Direct and Large-Eddy Simulation*, Edwards, Ann Arbor.

[3] Ghosal, S., 1996, "An Analysis of Numerical Errors in Large-Eddy Simulations of Turbulence," J. Comput. Phys., **125**, pp. 187–206.

[4] Garnier, E., Mossi, M., Sagaut, P., Deville, M., and Comte, P., 1999, "On the Use of Shock-Capturing Schemes for Large-Eddy Simulation," J. Comput. Phys., **153**, pp. 273–311.

[5] Geurts, B. J., and Froehlich, J., 2002, "A Framework for Predicting Accuracy Limitations in Large-Eddy Simulation," Phys. Fluids, **14**(6), pp. L41–L44.

[6] Park, N., and Mahesh, K., 2007, "Analysis of Numerical Errors in Large-Eddy Simulation Using Statistical Closure Theory," J. Comput. Phys., **222**, pp. 194–216.

[7] Meyers, J., Geurts, B. J., and Baelmans, M., 2003, "Database Analysis of Errors in Large-Eddy Simulation," Phys. Fluids, **15**(9), pp. 2740–2755.

[8] Meyers, J., and Sagaut, P., 2006, "On the Model Coefficients for the Standard and the Variational Multi-Scale Smagorinsky Model," J. Fluid Mech., **569**, pp. 287–319.

[9] Hoffman, J., and Johnson, C., 2004, "Computatbility and Adaptivity in CFD," *Encyclopedia of Computational Mechanics*, E. Stein, R. de Borst, and T. J. R. Hughes eds., Wiley, New York, Vol. 3, pp. 183–206.

[10] Celik, I. B., Cehreli, Z. N., and Yavuz, I., 2005, "Index of Resolution Quality for Large-Eddy Simulations," ASME J. Fluids Eng., **127**, pp. 949–958.

[11] Freitag, M., and Klein, M., 2006, "An Improved Method to Assess the Quality of Large-Eddy Simulations in the Context of Implicit Filtering," J. Turbul., **7**(40), pp. 1–11.

[12] Meyers, J., Sagaut, P., and Geurts, B. J., 2006, "Optimal Model Parameters for Multi-Obective Large-Eddy Simulations," Phys. Fluids, **18**, p. 095103.

[13] Lucor, D., Meyers, J., and Sagaut, P., "Sensitivity Analysis of LES Using Polynomial Chaos," J. Fluid Mech., in press.

[14] Krige, D. G., 1951, "A Statistical Approach to Some Basic Mine Valuations Problems on the Witwatersrand," J. of Chem., Metal. and Mining Soc. of the South Africa, **52**, pp. 119–139.

[15] Jouhaud, J. C., Sagaut, P., and Labeyrie, B., 2006, "A Kriging Approach for CFD/Wind Tunnel Data Comparison," ASME J. Fluids Eng., **128**(4), pp. 847–855.

[16] Jouhaud, J. C., Sagaut, P., Montagnac, M., and Laurenceau, J., 2007, "A Surrogate-Model Based Multi-Disciplinary Shape Optimization Method With Application to a 2D Subsonic Airfoil," Comput. Fluids, **36**(3), pp. 520–529.

[17] Smagorinsky, J., 1963, "General Recirculation Experiments With the Primitive Equations. I. The Basic Experiment," Mon. Weather Rev., **91**(3), pp. 99–164.

[18] Margason, R. J., 1993, "Fifty Years of Jet in Crossflow," AGARD Computational and Experiments Assessment of Jets in Cross Flow, AGARD CP-534, pp. 1.1–1.12.

[19] Poinsot, T., and Lele, S. K., 1992, "Boundary Conditions for Direct Simulations of Compressible Viscous Flows," J. Comput. Phys., **101**, pp. 104–129.

[20] Polifke, W., and Wall, C., 2002, "Non-Reflecting Boundary Conditions for Acoustic Transfer Matrix Estimation With LES," *Proceedings of the Summer Program 2002*, Center for Turbulence Research, pp. 345–356.

[21] Garnier, E., Sagaut, P., and Deville, M., 2001, "A Class of Explicit ENO Filters With Application to Unsteady Flows," J. Comput. Phys., **170**, pp. 184–204.

[22] Ciardi, M., Sagaut, P., Klein, M., and Dawes, W. N., 2005, "A Dynamic Finite-Volume Scheme for Large-Eddy Simulation on Unstructured Grids," J. Comput. Phys., **210**, pp. 632–655.

[23] Sacks, J., Welch, W. J., Mitchell, T. J., and Wynn, H. P., 1989, "Design and Analysis of Computer Experiments," Stat. Sci., **4**(4), pp. 409–435.

[24] Anderson, E., Bai, Z., Bischof, C., Blackford, S., Demmel, J., Dongarra, J., Du Croz, J., Greenbaum, A., Hammarling, S., McKenney, A., and Sorensen, D., 1999, LAPACK Users' Guide, Society for Industrial and Applied Mathematics, 3rd ed., SIAM, 1999.